

Implications of Reactive Oxygen Species (ROS) in Initiating Chemical Reactions

JOMANA AL-NU' AIRAT, BSc (Hons)

This thesis is presented for the degree of

Doctor of Philosophy



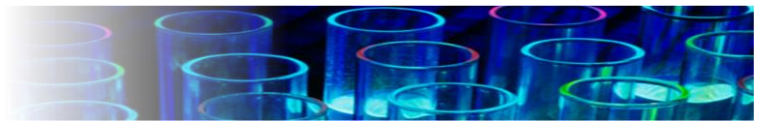
School of Engineering and Information Technology,

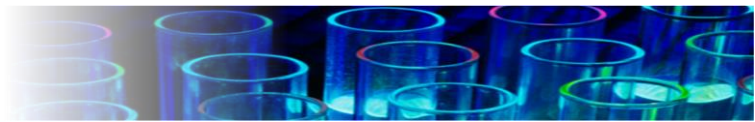
Murdoch University, Western Australia



2018

Jomana Al-Nu'airat





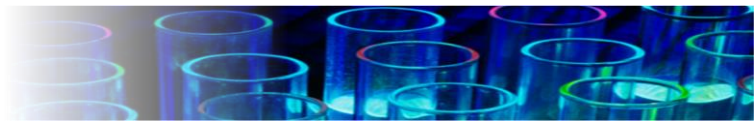
Declaration

I declare that this thesis is my own account of my research and contains as its main content work which has not previously been submitted for a degree at any tertiary education institution.

.....

Jomana N. Al-Nu'airat

September 2018



Supervisory Statement

We, the undersigned, attest that Higher Research Degree candidate, **Jomana N. Al-Nu'airat**, has devised and synthesised the experimental program, conducted experiments, analysed data, performed computational quantum-mechanical calculations and has written all papers included in this thesis. **Dr Mohammednoor Altarawneh**, **Professor Bogdan Z. Dlugogorski**, and **Dr Xiangpeng Gao** provided the necessary advice on the experimental program, project direction and assisted with the editing of the papers, consistent with normal supervisors' candidate relations.

.....

Dr Mohammednoor Altarawneh

September 2018

.....

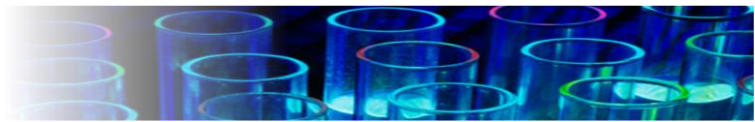
Professor Bogdan Z. Dlugogorski

September 2018

.....

Dr Xiangpeng Gao

September 2018



Dedications

To Faith, Humanity, and Love



Acknowledgments

After an intensive period of three years, today is the day: writing this note of thanks is the finishing touch on my dissertation. It has been a period of intense learning for me, not only in the scientific arena, but also on a personal level. This lovely journey would not be possible without the support and love of families, friends, colleagues and complete strangers. At the end of my journey, it is an utmost pleasure to express my thanks to all those who contributed in many ways to the success of this study.

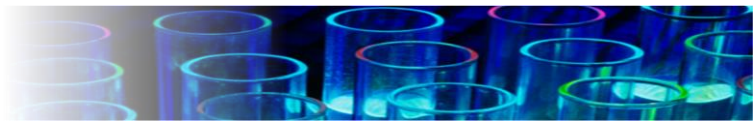
I would like to thank my supervisors Dr Mohammednoor Altarawneh, Professor Bogdan Dlugogorski, and Dr Xiangpeng Gao for their exceptional support, understanding, mentorship, encouragement, and dedication. Thank you again, you always encourage me to do better and trust me enough to discover many aspects of science by my own.

To my life-coach, my mentor Craig Moulton: because I owe it to you. Many Thanks!

I acknowledge my gratitude to my fellow student colleagues and staffs of the Fire Safety and Combustion Kinetics Research Laboratory. It was great sharing laboratory with all of you during the last three years. What a cracking place to work! I experienced exciting years of research and experiments. Most of my long night experimental adventures would not be possible without the enormous help of Gary Rodrigues and Don Snape, Murdoch security men, who make sure that I am home, safe and dry, and for our most lovely academic support officers (Rose and Emma), thank you!

I am grateful to Murdoch University for the award of a postgraduate research scholarship which provided a valuable financial support for this research. This study has also been funded by the Australian Research Council (ARC) and with grants of computing time from the National Computational Infrastructure (NCI) and the Pawsey Supercomputing Centre in Perth, Australia.

I am highly privileged to receive the School of Engineering and Information Technology's Graduate Poster Prize (2018), The three minutes thesis competition 3MT-Runner up award and People Choice award 2017, Murdoch University, Australia, The Western Australian Joint Chemical Engineering Committee (JCEC), i.e., the Institution of Chemical Engineers



(IChemE) and the Engineers Australia's (EA) selected finalist Postgraduate Research Excellence Award (2017), as well as Enlisted and participated in the 2017 Mentoring Network in Science, Technology and Engineering (IMNIS), Australia.

My forever interested, encouraging and always enthusiastic girl and boy Lujain and Abuod: they were always keen to know what their mom was doing and how I was proceeding, although it is likely that they have never grasped what it was all about! I am very grateful to my sibling and parents (Nadia, Twafiq, Najah, Samah, Suha, Reham, Ibrahim, and Hanan) and (Haiat and Nahel), who have provided me through moral and emotional support in my life. I am also indebted to my other family members and friends who have supported me along the way.

To Heather Gunnell, you gave me courage, endless support and lights in the darkest and brightest days. You are awesome! I would like to thank my secret friend "Ages" for accepting nothing less than excellence from me. My eternal cheerleader, Hanan Abu Abbas: I miss our interesting and long-lasting "roof" chats. I will always miss your screams of joy whenever a significant momentous was reached. I would also like to thank my friend Suekainah Sluiman for her wise counsel and sympathetic ear. A very special gratitude goes out to Lisa Maher, no one sing like you in the morning, you rock!

I also place on record, my sense of gratitude to one and all, who directly or indirectly, have lent their hand in this venture.

Thanks for all your encouragement!

Jomana Al-Nu'airat



Abstract

This thesis presents a series of scientific studies exploring the initiation of various chemical reactions with reactive oxygen species (ROS), mainly singlet oxygen. These studies have revealed new mechanistic insights in environmental, industrial and biological systems, have described the associated set of reactions, have illustrated the detection of new radicals i.e., environmentally persistent free radicals (EPFR), and have provided a new insight explaining the spontaneous fire in coal mines. Comprehensive experimental and quantum-mechanical calculations afforded the investigation of oxidation reactions of singlet oxygen with wastewater organic contaminants, for example, the photodegradation of *Phenol* and *Aniline* in water. Detailed experimental studies on modelled surrogates, i.e., *Anisole*, resolved the fundamentals of thermal interaction of coal with iron oxide Fe_2O_3 nanoparticles. Along the same line of interest, enhancing the combustion efficiency of fuel constitutes a mainstream strategy in the pursuit of meeting the ever-increasing energy demand. Therefore, this thesis also provides a comprehensive mechanistic and thermo-kinetic accounts underpinning the reaction of fuel surrogates, namely *Toluene*, with singlet oxygen in the internal combustion (IC) engines. Finally, this work extends insights into biological systems, mapping the *Alloxan-Glutathione* redox cycle to expose the formation of ROS, species that eventually cause necrosis of the pancreatic insulin-producing beta cells and prompt the insulin-dependent diabetes mellitus (IDDM).

The methodology involve customised LED-photoreactors, thermal packed-bed reactor, and various reaction product-monitoring systems, e.g., Fourier transform infrared spectroscopy (FTIR) to quantitate the ignition temperatures of fuel surrogates, in-situ electron paramagnetic



resonance (EPR) to elucidate the formation of environmentally-persistent free radicals (EPFR) as well as intermediate radical species, diffuse reflectance infrared Fourier transform spectroscopy (DRIFTS) to monitor the chemisorption of organic substrates on the nanoparticles, X-ray diffraction for particles characterisation, as well as broad-scan UV-Vis spectroscopy and high-performance liquid chromatography (HPLC) to identify and quantify the intermediate and product species in solutions.

Results obtained in this thesis elucidate, for the very first time, the formation of *para*-semibenzoquinone anion (PSBQ) supporting the reaction pathway leading to the formation of *para*-benzoquinone during the reaction of phenol (and aniline) with singlet oxygen. These results have practical application to quantify the degradation of organic pollutants in wastewater. Investigations regarding combustion applications shows that the presence of singlet oxygen considerably lowers the activation energy of the initiation channels of aromatic hydrocarbons (e.g., in IC engines), resulting in an energetically improved combustion process, the relative reactivity of singlet oxygen, based on the reaction rate constants, follows the order of $\text{OH} > \text{H} > \text{CH}_3 > {}^1\text{O}_2 > \text{HO}_2 > {}^3\text{O}_2$. Furthermore, the chemisorption of anisole on $\alpha\text{-Fe}_2\text{O}_3$ surfaces has been elucidated to follow a direct dissociation of the O-CH_3 (and $\text{OCH}_2\text{-H}$), leading to the formation of surface-bound phenoxy radicals and gaseous species at temperatures as low as 25 °C. This insight applies to free-radical chain reactions that induce spontaneous fires of coal, as low-ranked coal comprises ferric oxide nanoparticles, and equally, to coexistence of aromatic fuels with thermodynamically reactive Fe_2O_3 surface, e.g., in fly ash, at the cooled-down tail of combustion stacks. Results from alloxan-glutathione redox cycle clarified, for the first time, the direct synchronised generation of dialuric acid radical (DA^\cdot) and glutathione radical (GS^\cdot), assigning the nature of the mysterious “compound 305”



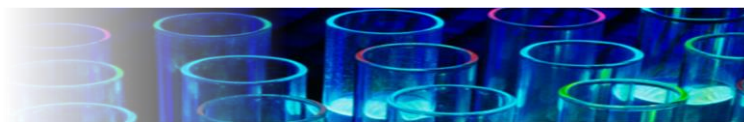
to the DA \cdot -GS \cdot complex. These results explain the alloxan-induced diabetes on precise molecular bases.

This thesis provides new perspectives on opportunities in understanding the influence of ROS, mainly singlet oxygen ($^1\text{O}_2$) and superoxide (O^{2-}) in germane chemical reactions. Such attempts will advance the existing ROS-related technologies, and improve the fundamental theories in supports of environmental management and application decisions.



Table of Contents

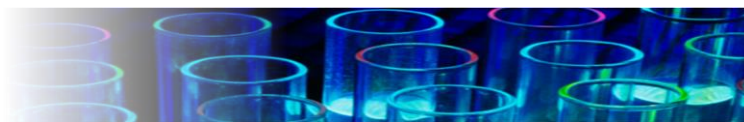
Thesis Declaration	i
Supervisory Statement	ii
Dedications	iii
Acknowledgements	iv
Abstract	vi
Table of Contents	ix
Contribution towards Publication	xiii
1. Introduction	1
1.1 Thesis Overview	3
1.2 Research Motivation and Purpose	3
1.3 Thesis Objectives	5
1.4 Thesis Outline	7
1.5 References	9
2. Comprehensive Review of Relevant Reactive Oxygen Species	12
2.1 Introduction to Reactive Oxygen Species (ROS)	14
2.1.1 Overview of ROS	14
2.1.2 Comparative assessment of ROS	15
2.2 Singlet Oxygen ($O_2\ ^1\Delta_g$) and Organic Reactions	18
2.2.1 Background of singlet oxygen $O_2\ ^1\Delta_g$	18
2.2.2 Generation of singlet oxygen 1O_2	19
2.2.3 Detection of singlet oxygen 1O_2	34
2.2.4 Role of singlet oxygen in initiation of hydrocarbon reactions	38
2.3 Research Gaps and Outlooks	41
2.4 References	43
3. Methodology	58
3.1 Experimental configurations	60
3.1.1 Overview of experimental techniques	60



3.1.2. Tubular packed-bed reactor setup	61
3.1.3. Electron paramagnetic resonance	63
3.1.4. Diffuse reflectance infrared Fourier transform spectroscopy	63
3.1.5. Photo-reactors	65
3.1.6 Analytical HPLC and UV-Vis techniques	67
3.2 Computational Details	68
3.2.1 Overview of computational method	68
3.2.2 Error estimation of M062X, B3LYP, and CBS-QB3 approaches	70
3.3 Data Analyses	73
3.4 References	74
4. Paper I: Role of Singlet Oxygen in Combustion Initiation of Aromatic Fuels	78
4.1 Introduction	81
4.2 Computational Methodology	84
4.3 Results and Discussion	86
4.3.1 Preliminary assessment of gas-phase reaction of benzene with singlet oxygen	86
4.3.2 Initial steps of gaseous reaction of toluene with singlet oxygen	88
4.3.3 Routes for formation of primary products	93
4.3.4 Thermodynamics and reaction kinetics	95
4.4 Concluding Remarks and Practical Implications	99
4.5 References	101
5. Paper II: Effect of Fe₂O₃ Nanoparticles on Combustion of Coal Surrogate (Anisole): Enhanced Ignition and Formation of Persistent Free Radicals	108
5.1 Introduction	111
5.2 Experimental and Computational Methodology	113
5.2.1 Tubular packed-bed reactor setup	113
5.2.2 Electron paramagnetic resonance	115



5.2.3 Diffuse reflectance infrared Fourier transform spectroscopy	116
5.2.4 Computational details	117
5.3 Results and Discussion	118
5.3.1 Assessment of thermal decomposition of anisole in presence of Fe ₂ O ₃	118
5.3.2 Low-temperature formation of environmentally-persistent free radicals (EPFR)	123
5.3.3 Chemisorption of anisole on oxygenated Fe ₂ O ₃ cluster	126
5.4 Conclusions	127
5.5 References	128
6. Paper III: Reaction of Aniline with Singlet Oxygen (O₂¹Δ_g)	136
6.1 Introduction	139
6.2 Methodologies	141
6.3 Results and Discussion	143
6.3.1 Preliminary Analysis of Results from M062X and B3LYP Approaches	143
6.3.2 Characterisation of Singlet Oxygen and Aniline	144
6.3.3 Reaction Mechanism	145
6.4. Conclusions	153
6.5. References	155
7. Paper IV: Reaction of Phenol with Singlet Oxygen	163
7.1 Introduction	166
7.2 Materials and Methodology	168
7.2.1 Materials	168
7.2.2 Photooxidation of phenol with singlet oxygen	167
7.2.3 Analytical techniques	172
7.2.4 Estimated LED light intensity	174
7.2.5 Computational details	175
7.3 Results and Discussion	177



7.3.1	Generation of singlet oxygen	177
7.3.2	Reaction of singlet oxygen with phenol	180
7.3.3.	Quantitative analysis of N-conversion at high temperature	181
7.3.4.	Comments on NO _x reduction and formation of N ₂	185
7.4	Conclusions	192
7.5	References	193
8.	Paper V: Alloxan – Glutathione Redox Cycle	202
8.1.	Introduction	205
8.2	Methodology	208
8.2.1	Analytical techniques	208
8.2.2	Computational details	209
8.3	Results and Discussion	212
8.3.1	Hydrogen atom transfer to alloxan	213
8.3.2	UV-Vis and EPR analysis	217
8.3.3	Oxygenation of dialuric acid and its radical	222
8.3.4	Formation of ROS	224
8.3.5	Dimerisation reactions	226
8.4	Conclusions	229
8.5	References	229
9.	Conclusions and Recommendations	238
10.	Supplementary Documents	246
Appendix I	Supporting Information for Chapter 4	248
Appendix II	Supporting Information for Chapter 5	278
Appendix III	Supporting Information for Chapter 6	281
Appendix IV	Supporting Information for Chapter 7	306



Contribution towards Publication

The work embodied in this thesis contains published joint-authored papers as listed below. I am the principal contributor in the publications. I have included as part of the thesis a written statement, endorsed by my supervisors, attesting to my significant contribution to the joint publications.

Paper I: Role of Singlet Oxygen in Combustion Initiation of Aromatic Fuels

Al-Nu'airat J; Altarawneh M.; Oluwoye I.; Gao X; Dlugogorski B. Z. *Energy and Fuel*, 2018.

Impact factor: 3.024

Paper II: Effect of Fe₂O₃ Nanoparticles on Combustion of Coal Surrogate (Anisole): Enhanced Ignition and Formation of Persistent Free Radicals

Al-Nu'airat J; Altarawneh M.; Gao X., Oluwoye I; Dlugogorski B.Z., *Proceedings of the Combustion Institute*, 2018.

Impact factor: 5.336

Paper III: Reaction of Aniline with Singlet Oxygen (O₂ ¹Δ_g)

Al-Nu'airat J.; Altarawneh M.; Gao X; Dlugogorski B. Z., *Journal of Physical Chemistry A*, 2017.

Impact factor: 2.836

Paper IV: Phenol Reaction with Singlet Oxygen (O₂ ¹Δ_g)

Al-Nu'airat J., Dlugogorski B.Z.; Gao X; Zeinali N.; Skut J.; Phillip R. Westmoreland P. R.; Altarawneh M., *Physical Chemistry Chemical Physics*, 2018.

Impact factor: 4.449

Paper V: Alloxan – Glutathione Redox Cycle

Al-Nu'airat J.; Altarawneh M.; Gao X; Dlugogorski B. Z. (**Submitted**)



The list below itemises the publications to which I have published/ joint-authored papers during the course of the PhD study and not within the scope of the thesis:

(i) **The Mechanism of Electrophilic Addition of Singlet Oxygen to Unsubstituted Pyrrole**

Zeinali N.; **Al-Nu'airat J.**; Zeng Z.; Altarawneh M.; Li D.; Skut J.; Dlugogorski B.Z., *Proceedings of the 9th Asia-Pacific Conference on Combustion, ASPACC 2017.*

(ii) **Formation of environmentally-persistent free radicals (EPFR) on α -Al₂O₃ clusters**

Assaf N.; Altarawneh M.; **Al-Nu'airat J.**; Randy M. and Dlugogorski B.Z., *RSC Advances* 2017.

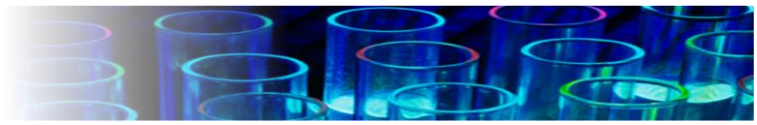
(iii) **Thermo-mechanical properties of cubic titanium nitride**

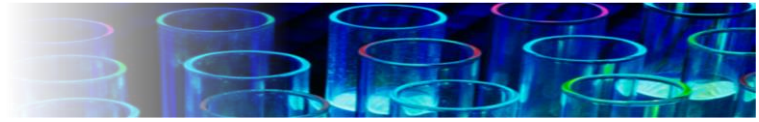
Mohammadpour E.; Altarawneh M.; **Al-Nu'airat J.**; Mondinos N.; Jiang Z.T.; Dlugogorski B.Z., *Molecular Simulation*, 2017.

(iv) **New Mechanistic Insights: Why Do Plants Produce Isoprene?**

Zeinali N.; Altarawneh M.; Li D.; **Al-Nu'airat J.**; Dlugogorski B.Z., *ACS Omega*, 2016.

Jomana Al-Nu'airat

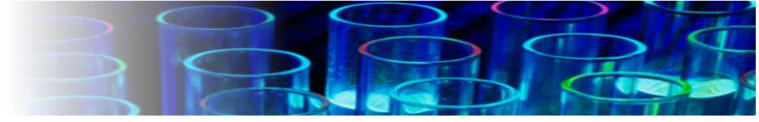


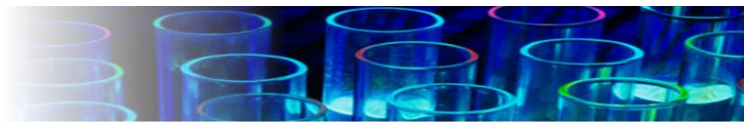


Chapter 1

Introduction

Chapter 1





1.1 Thesis Overview

Reactive oxygen species (ROS) represents the collective group of an emerging class of endogenous, highly reactive, oxygen-bearing molecules formed upon incomplete reduction of molecular oxygen. ROS remain the backbone of diverse ground-breaking technologies, driving the waves of development in environmental, biotechnology, materials, medical and defence sciences [1]. For instance, photodynamic therapy (PDT) employs the singlet oxygen, an example of ROS, for cancer treatment [2,3]. Likewise, various combustion, water and biological activities depend on the interaction of ROS with hydrocarbons as well as other functional substrates [4–6]. Arising from diverse natural and anthropogenic exogenous processes, the major environmental sources of ROS include ultraviolet light, ionising radiation, and metabolisation and oxidation of primary pollutants, resulting in various physico-chemical phenomena that require detailed understanding [4,7,8].

This thesis assembles critical scientific studies on the implications of reactive oxygen species in initiating chemical reactions. The chapters describe the elementary and practical aspects of the reaction of selected ROS with hydrocarbons, identifying and quantitating the consequential effects on pertinent industrial processes such as combustion, fire safety (coal mining), wastewater treatments, and biological systems.

1.2 Research Motivation and Purpose

As illustrated in Figure 1.1, the motivation of this work lies in understanding and resolving the effect of ROS in vital industrial activities. For example, (i) the role of singlet oxygen (an



example of ROS) in enhancing combustion of aromatic fuels in internal combustion engines, (ii) the contribution of ROS to spontaneous fires in coal mines, (iii) the primary chemistry of photo-chemically generated ROS in treating contaminated waters, and (iv) forced oxidative damages in biological cells, are narrowly described in the literature. Of particular interest to safety and economics, the reoccurrence of spontaneous fire of coal have led to closures of the mines and numerous accidental casualties [9]. Moreover, from an environmental viewpoint, the ROS-initiated low-temperature oxidation of coal instigates heavy CO₂ emissions, amounting to 30 % of all greenhouse gas emissions. This thesis seeks to expand our vision of key reactions that have been overlooked. One of the snubbed reactions is the activation of dioxygen to singlet oxygen, one of the most reactive ROS. Figure 1.1 exemplifies the application of the excitation power of singlet oxygen as one of the most attractive approaches in combustion enhancement in internal combustion (IC) engines [10–15].

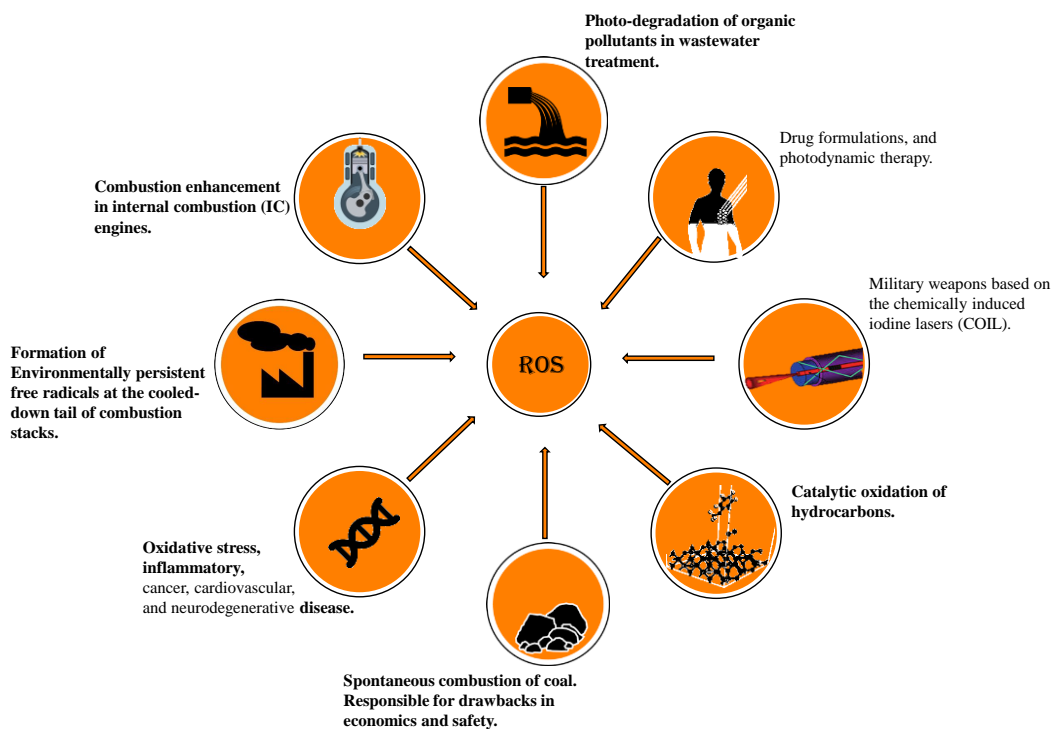
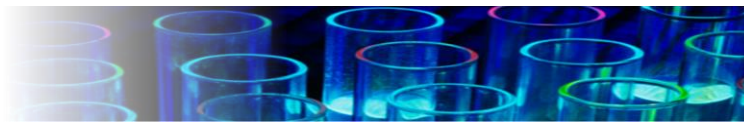


Figure 1.1 Snap-shot of some practical implications of ROS. The topics covered in the subsequent chapters of this thesis are shown in bolded font.



Therefore, the aim of this study is to characterise, both kinetically and thermodynamically, the primary reactions of some ROS with organic materials, with pivoting focus on combustion, water recycling and metabolism processes. This research links the origin of some combustion initiation reactions to the fundamental inter-play of electronically excited species of oxygen and carbonaceous materials, explaining the implications on aromatic fuels and spontaneous fires (i.e., self-heating) of coal. Similarly, the scientific work embodied in this thesis has provided a significant understanding of the reaction mechanisms ensuing during the photo-oxidative ROS- supported cleaning up of organic pollutants in wastewater and mainstream biological chemicals that are metabolized to radicals, e.g., as in alloxan-glutathione redox cycle.

1.3 Thesis Objectives

The underlying aim of this dissertation seeks new perspectives on opportunities in understanding the influence of ROS, mainly singlet oxygen ($^1\text{O}_2$), superoxide (O_2^-), as well as hydroxyl radical ($\text{HO}\cdot$), in germane chemical reactions. Such attempts will advance the existing ROS-related technologies, and improve the fundamental theories in supports of environmental management and application decisions. The following outlines the objectives of the thesis, targeting three critical thematic areas, i.e., combustion, pollutant remediation, and biological chemistry:

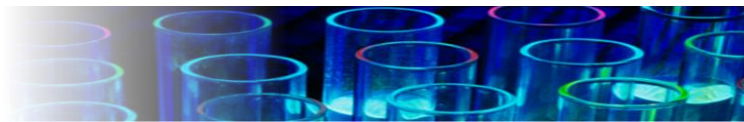
- (i) Interactions of ROS with aromatic fuels and coal surrogates in combustion scenarios: To provide the fundamental understanding of the reactions between electronically excited species of oxygen and carbonaceous fuels, with applications



to improve safety in wood, mineral and food industries. To elucidate the influence of excited oxygen species formed on the surfaces of nano-component of coal in initiating low-temperature combustion (i.e., spontaneous fire) of coal combustion; to identify and classify the toxicity of the primary products of such surface-mediated reactions. To investigate the gas-phase kinetics of reactions involving singlet oxygen and aromatic fuels, clarify the reaction intermediates, assemble the rate parameters of elementary steps, and to illustrate the relative effects in internal combustion (IC) engines.

- (ii) Photosensitised reactions of singlet oxygen with hydrocarbons in water: To resolve the photochemical activation of triplet oxygen into the singlet state using a typical photosensitiser, to study the subsequent oxidation (i.e., remediation) of organics, e.g., phenolic-based pollutants, that constitute negative impacts on public health and the environment in wastewater. To map the reaction mechanisms and develop the relevant kinetic models.

- (iii) Preliminary investigation on implications on biological systems. To illuminate the mechanistic pathways governing the alloxan–Glutathione redox cycle, resolving the formation routes of reactive oxygen species (ROS) that cause necrosis of the pancreatic insulin-producing beta cells, prompting the insulin-dependent diabetes mellitus (IDDM).



1.4 Thesis Outline

Based on the above-mentioned objectives, this thesis partitions into a variety of sections that portray the core findings as follows:

Chapter 2 presents a synopsis ROS, and a comprehensive review of the physical and chemical aspects of singlet oxygen. The chapter sets the foundational knowledge, comparing the occurrence, as well as reactivity of the major reactive oxygen species. Focusing on singlet oxygen, the chapter describes the relevant generation and detection techniques, and assembles some useful rate parameters and literature data on the physico-chemical interaction with other chemical substances. Most importantly, Chapter 2 outlines the important gaps in the literature, providing an outlook on the need for accurate thermodynamic and kinetic requirement for the interaction of singlet oxygen with a broader class of hydrocarbons (e.g., the role of different functional groups) in the gas phase and aqueous media.

Chapter 3 illustrates the main experimental and computational techniques employed within the scope of this study. Each of the thematic area, i.e., combustion, pollutant remediation and biological system employ unique experimental and computational methodologies.

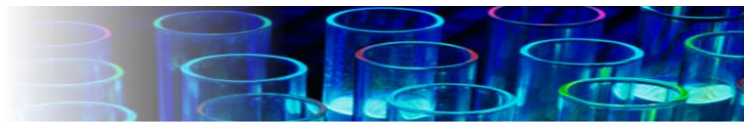
Chapter 4 explores the impact of applying singlet oxygen in oxy-fuel systems, centring the relative effect on the activation energy of the initiation reactions, the overall chain-branching mechanism, and ignition temperature. However, the underlining reaction mechanism of the surface-generated ROS. The intent of this chapter converged on the primary interaction of singlet oxygen with fuel surrogates (i.e., alkylbenzene, namely, toluene) in the gas phase, reporting the complete mechanistic and thermo-kinetic accounts.



Chapter 5 couples both experimental and computational studies to address the effect of iron oxide nanoparticle (or precisely the excited oxygen species generated on nanoparticles of iron oxide) in initiating low-temperature combustion of a coal surrogate (methoxybenzene, namely, anisole). The chapter describes the initiation steps, i.e., the fire chemistry, of self-heating of coal, elucidate the formation of persistence pollutants, and suggests new technologies for mitigation of spontaneous fires, based on quenching of the initiation reactions.

Chapters 6 and 7 engages further applications in wastewater treatments. The chapters respectively investigate dissolved organic matters (DOM, rose bengal) as an effective photochemical sensitiser that produces the singlet delta state of molecular oxygen, to remove organic pollutants (i.e., aniline and phenol) from aqueous solutions. The chapters incorporate extensive experiments and quantum-chemical modellings to resolve the exact mode of reactions, as well as the selectivity of primary products. Overall, these chapters address the photo-chemical treatments of aniline and phenol contaminants with singlet oxygen, assembling the rate constants for a detailed kinetic modelling.

Chapter 8 identifies and describes ROS mainly superoxide ($O_2^{\cdot-}$) in glutathione redox-cycle as it occurs in mammalian induced diabetes with alloxan. This chapter provides a detailed map of alloxan redox cycle with intercellular thiols (GSH) and the formation of dialuric acid radical (DA^{\cdot}), glutathione radical (GS^{\cdot}), hydrogen peroxide (H_2O_2) and hydroxyl radical (HO^{\cdot}). The experiments and theoretical works in this chapter provide insights on the ROS causing necrosis of the pancreatic insulin-producing beta cells, prompting the insulin-dependent diabetes mellitus (IDDM). This Chapter pinpoints the mechanistic pathways governing the alloxan–



GSH redox via accurate molecular modelling coupled with the experimental determination of prominent reactive species.

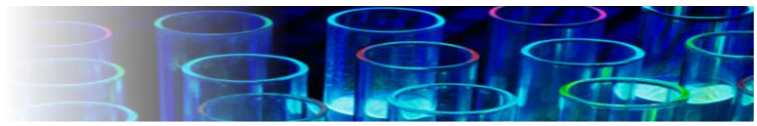
1.5 References

- [1] Nonell S, Flors C. Singlet Oxygen: Applications in Biosciences and Nanosciences. Royal Society of Chemistry; 2016.
- [2] DeRosa MC, Crutchley RJ. Photosensitized singlet oxygen and its applications. *Coordination Chemistry Reviews* 2002;233:351–371.
- [3] Gorman AA, Rodgers M a. J. Singlet molecular oxygen. *Chem Soc Rev* 1981;10:205–31. doi:10.1039/CS9811000205.
- [4] Kieber DJ, Peake BM, Scully NM. Reactive oxygen species in aquatic ecosystems. *UV Effects in Aquatic Organisms and Ecosystems* 2003:251–288.
- [5] Livingstone DR. Contaminant-stimulated reactive oxygen species production and oxidative damage in aquatic organisms. *Marine Pollution Bulletin* 2001;42:656–666.
- [6] Burns JM, Cooper WJ, Ferry JL, King DW, DiMento BP, McNeill K, et al. Methods for reactive oxygen species (ROS) detection in aqueous environments. *Aquatic Sciences* 2012;74:683–734.
- [7] Burns JM, Cooper WJ, Ferry JL, King DW, DiMento BP, McNeill K, et al. Methods for reactive oxygen species (ROS) detection in aqueous environments. *Aquatic Sciences* 2012;74:683–734.
- [8] Bartosz G. Use of spectroscopic probes for detection of reactive oxygen species. *Clinica Chimica Acta* 2006;368:53–76.
- [9] Ham B. A review of spontaneous combustion incidents, John Wiley & Sons, 2005.
- [10] Starik AM, Kozlov VE, Titova NS. On the influence of singlet oxygen molecules on characteristics of HCCI combustion: A numerical study. *Combustion Theory and Modelling* 2013;17:579–609. doi:10.1080/13647830.2013.783238.



- [11] Wu Z, Kang Z, Deng J, Hu Z, Li L. Effect of oxygen content on n-heptane auto-ignition characteristics in a HCCI engine. *Applied Energy* 2016;184:594–604. doi:10.1016/j.apenergy.2016.10.050.
- [12] Starik AM, Titova NS. On a possibility to reduce the ignition threshold for combustible mixtures by selective excitation of molecular vibrations in initial reagents. *Doklady Physics*, vol. 45, Springer; 2000, p. 5–10.
- [13] Starik AM, Titova NS. Kinetics of detonation initiation in the supersonic flow of the $H_2 + O_2$ (air) mixture in O_2 molecule excitation by resonance laser radiation. *Kinetics and Catalysis* 2003;44:28–39.
- [14] Smirnov VV, Stelmakh OM, Fabelinsky VI, Kozlov DN, Starik AM, Titova NS. On the influence of electronically excited oxygen molecules on combustion of hydrogen–oxygen mixture. *Journal of Physics D: Applied Physics* 2008;41:192001.
- [15] Starik AM, Kozlov VE, Titova NS. On the influence of singlet oxygen molecules on the speed of flame propagation in methane–air mixture. *Combustion and Flame* 2010;157:313–27. doi:10.1016/j.combustflame.2009.11.008.

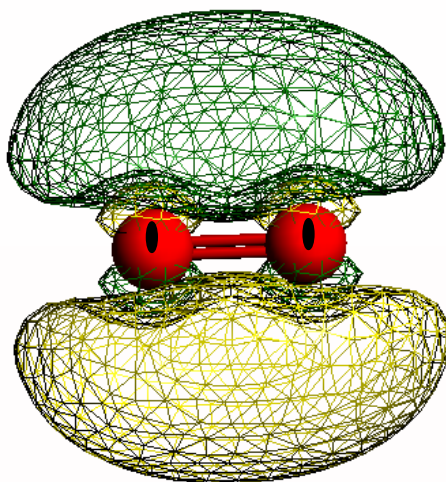
Jomana Al-Nu'airat



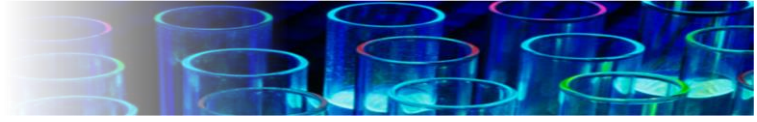


Chapter 2

Comprehensive Review of Relevant Reactive Oxygen Species



Chapter 2





2.1 Introduction to Reactive Oxygen Species (ROS)

2.1.1 Overview of ROS

Reactive oxygen species (ROS) represents a group of oxygen-derived chemically reactive (short-lived) species. ROS are relatively more reactive than the common molecular (triplet) oxygen ($O_2 \text{ } ^3\Sigma_g^-$). In 1954, Gerschman et al. [1] made one of the earliest discovery of oxygen spinoff free radicals, later termed as ROS, in X-ray beams and during oxygen poisoning activities. Common examples of ROS include singlet oxygen ($O_2 \text{ } ^1\Delta_g$), superoxide (O_2^-), hydrogen peroxide (H_2O_2), hydroxyl radical (HO), and peroxides. Arising from exogenous sources such as ionizing radiation, ultraviolet (UV) light exposure, (X, γ)-rays, and metal-catalysed reactions, ROS exist at pico-molar to micro-molar concentrations in the biosphere, i.e., the total environmental air, soil, water, and biological bodies [2–4]. However, the literature illustrates the presence of reactive oxygen species in higher concentrations in polluted environments. The typical half-life of ROS ranges from nanoseconds to hours. From the perspective of chemical functionality, ROS can exhibit both constructive (i.e., beneficial) and destructive reaction mechanisms. For instance, while ROS could initiate favourable chemical reactions, they can also act as a bane to all aerobic species. The influence of ROS span across wide applications, including metabolism activities in living organisms and energy recovery from organic fuels. In a biological context, the implication of ROS has been established in oxidative stress and cell signalling [5–8].



2.1.2 Comparative assessment of ROS

This section discusses different types of ROS, comparing their nature, reactions, products and significances. Table 2.1 lists some major ROS with their respective characteristics. Overall, ROS form as a result of electron (or energy) transfer and photolysis [3,4,9] of parent oxygen species as shown in Figure 2.1. Due to their short lifetime (except for H_2O_2) and low occurrence concentration, direct detection by ex situ analyses is quite challenging, therefore indirect in situ techniques are usually adopted. Indirect detection of ROS implements the reaction of ROS with a probe molecule (e.g., spin traps) to produce a long-lived stable product. This analyte can later be detected via ultraviolet-visible (UV-Vis), fluorescence (FL), and chemiluminescence (CL) light spectroscopic techniques. Other approaches include gas chromatography (GC), high performance liquid chromatography (HPLC), nuclear magnetic resonance (NMR) and electron paramagnetic resonance (EPR). To select a certain approach, one must consider the method sensitivity, selectivity, and the temporal resolution of the measurements.

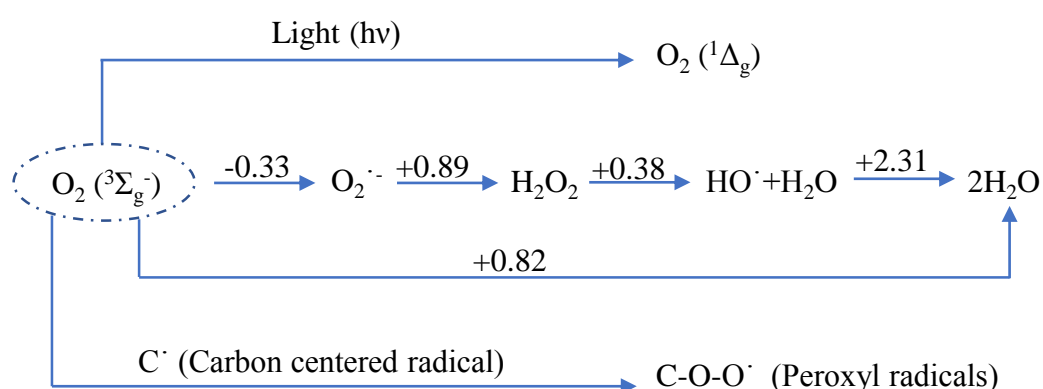


Figure 2.1. Oxygen one-electron reduction steps and respective reduction potentials. The reduction potentials are in Volts vs. NHE at pH 7.0 and 25 °C.

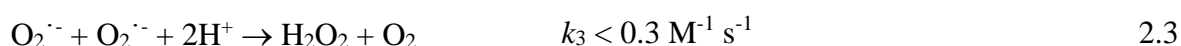
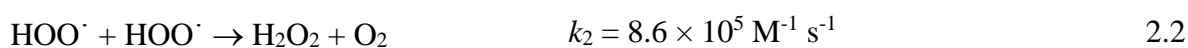
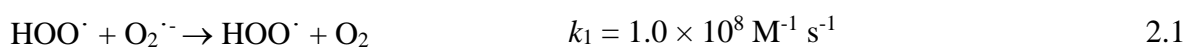


Table 2.1. Comparative summary of typical ROS species

IUPAC Name; Symbol	E ⁰ vs. NHE at pH 7.0	Typical lifetime; Generation technique	λ_{max} (absorption)	Occurrence in [C] _{ss} ; Notes
Singlet oxygen O ₂ (¹ Δ _g) [2,10–13]	0.65 V(¹ O ₂ /O ₂ ⁻)	Exists 4 μs in water and 45 min in vacuum. Produced by photosensitisation [14], electrical discharge [15], and thermally via surface-mediated reactions on transition metal oxides [16,17]. Also produced chemically by decomposition of triethylsilyl hydrotrioxide generated in situ from triethylsilane and ozone [18] Persistence ranges from 1 – 3,000 min.	1,913 nm	10 ⁻¹² to 10 ⁻¹³ M in natural water. Has application in drug formulations, photodynamic therapy and in military weapons. Can enhance initiation of chemical reaction.
Superoxide anion O ₂ ⁻ [2,19,20]	-0.33/ -0.137 V (O ₂ /O ₂ ⁻), 0.94/0.95 V (O ₂ ⁻ / H ⁺ , H ₂ O ₂)	Produced by dissolution of the alkali metals and alkaline earth metals salts, such as CsO ₂ , RbO ₂ , KO ₂ , and NaO ₂ in water [21]. Biologically, in phagocytes, O ₂ ⁻ is produced by the enzyme NADPH oxidase [22,23]. Can last 0.2 – 40 s.	240 nm	10 ⁻⁹ to 10 ⁻¹² M in natural water. Predominantly exists in the protonated hydroperoxyl form at neutral pH. The alkali salts of O ₂ ⁻ are used on the space shuttle, submarines and in firefighters' oxygen tanks [24].
Hydroxyl radical HO [•] [2,25,26]	2.18 V (HO [•] , H ⁺ /H ₂ O)	Forms during decomposition of hydroperoxide (ROOH) species, reaction of excited atomic oxygen with water, photolysis of 1-hydroxy-2(1H)-pyridinethione. UV-light dissociation of H ₂ O ₂ , and Fenton chemistry[27]. Stable ROS.	260 nm	10 ⁻¹⁵ to 10 ⁻¹⁸ M in natural water. Known as the troposphere "detergent" by decomposing pollutants and eliminating some greenhouse gases (methane and ozone) [28].
Hydrogen peroxide H ₂ O ₂ [29,30]	1.8 V (H ₂ O ₂ / H ₂ O)	Prepared industrially by hydrolysis of the ammonium peroxydisulfate, in anthraquinone processes. Direct synthesis from the elements using finely dispersed metal catalysts [31].		Sea water contains 0.5 to 14 μg/L, freshwater 1 to 30 μg/L and air 0.1 to 1 ppb [32]. Functions as strong oxidizing agent in industries. About 60 % of the world's production of hydrogen peroxide is used for pulp- and paper-bleaching [33].



As will be later discussed, this thesis provides some basis for understanding the role of ROS, mainly singlet oxygen ($O_2\ ^1\Delta_g$) and superoxide anion ($O_2^{\cdot-}$), in reactions initiation, environmental pollution and health hazards. In aqueous solution, hydroperoxyl radical (HOO^{\cdot}), $O_2^{\cdot-}$, and H_2O_2 exist in equilibrium depending on the pH. The disproportionation of superoxide species, i.e., $O_2^{\cdot-}$, occurs in a second-order spontaneous steps in Eqns 2.1 and 2.2 [34,35]. The reaction depends strongly on the pH, having a maximum global rate constant of $k \sim 1 \times 10^7\ M^{-1}\ s^{-1}$ at a pH value corresponding to the pK_a of $HOO^{\cdot}/O_2^{\cdot-}$. However, at neutral pH, the equilibrium favors the disproportionation of $O_2^{\cdot-}$ with $k = 4.0 \times 10^{20}\ M^{-1}\ s^{-1}$.



Superoxide anion can represent a reducing agent in aqueous solutions containing species such as coordinated iron complexes (hemes) in cytochromes and copper ions in proteins [36]. Superoxide anion can also act as an oxidiser in biologically-related redox reactions (e.g., with alloxan $k = 6-8 \times 10^5\ M^{-1}\ s^{-1}$ [37] ; or ascorbate, $k = 2.7 \times 10^5\ M^{-1}\ s^{-1}$ [38]) to generate H_2O_2 .

On the other hand, singlet oxygen has unique physical characteristics and functions in many areas. The study (and application) of singlet oxygen spans across photo reactions, drug formulations, combustion engines, and environmental (water) waste treatments. The broader scope of this review chapter focuses mainly on singlet oxygen, addressing the cogent aspects as compiled in the literature.



2.2 Singlet Oxygen ($O_2\ ^1\Delta_g$) and Organic Reactions

2.2.1 Background of singlet oxygen $O_2\ ^1\Delta_g$

This section expands the vision of key reaction attributes of singlet oxygen. Singlet oxygen forms as a result of molecular activation of triplet oxygen (i.e., dioxygen) – usually by photosensitisation [14], electrical discharge [15] or via surface-mediated reactions on particles such as silicon dioxide, aluminium oxide, and transition metal oxides [16,17]. It resides 95 kJ mol⁻¹ ($\Delta_G H^o_{298}$) above the ground state triplet oxygen molecule [39,40], making it kinetically unstable at ambient conditions and highly reactive against a large variety of electron-rich substrates. Singlet oxygen $O_2\ ^1\Delta_g$, as discovered by Kautsky in 1931, incurs a quantum state in which all electrons are spin paired. This astounding non-ionic and non-radical form of oxygen can diffuse through packed systems very easily with lifetime varying from seconds (in the gas phase) to a few microseconds (in water) [41].

The chemical and physical nature of $O_2\ ^1\Delta_g$ imposes some interesting behaviour in various important processes. For instance, singlet O_2 can open-up “unusual” reaction channels during oxidation of hydrocarbons, thioethers and organometallic complexes. In photosynthesis, singlet oxygen materialises from the light-harvesting chlorophyll molecules. Likewise, in mammalian biology, singlet oxygen represents one of the reactive oxygen species, responsible for oxidation of LDL cholesterol and the resultant cardiovascular effects. Singlet oxygen can react with water to form the rather unusual molecule trioxidane (H-O-O-O-H). Furthermore, when singlet oxygen is presented in combustion media, such as H_2-O_2 [42–45], CH_4-O_2 [46–48], and $CO-H_2-O_2$ [49] it intensifies the ignition and enhances the decomposition kinetic. The sections below illustrate the physical aspect and chemical reactivity of singlet oxygen,



various generation techniques, practical detection methods, and its implications relevant to the oxidation of hydrocarbons. A case study of coal spontaneous combustion is also discussed [50]

2.2.1.1 Physical aspect of singlet oxygen $O_2(^1\Delta_g)$

The electronic configuration of $O_2(^1\Delta_g)$ in its excited state is $(1\sigma_g)^2(1\sigma_u)^2(2\sigma_g)^2(2\sigma_u)^2(3\sigma_g)^2(3\sigma_u)^2(3\pi_g)^4(3\pi_u)^2$. The superscript “1” in $O_2(^1\Delta_g)$ indicates that it corresponds to a singlet state, the “ Δ ”, that its orbital angular momentum (M_L) equals 2 and the subscript “g”, that the symmetry of the molecule is pair (g from the German *gerade*, meaning together). In the last century, the physical and chemical properties of singlet oxygen $O_2(^1\Delta_g)$ have been the subject of broad investigations. Starting from 1925, when Robert Mulliken applied the modern quantum theory to explain the magnetic property of molecular oxygen. Where such magnetic behaviour rationalised by the two unpaired electrons located in the antibonding π^* orbitals (i.e., π^*_{2py} and π^*_{2pz}). The terms 'singlet oxygen' and 'triplet oxygen' appear from each form's number of electron spins. When the spin restrictions is overcome in triplet oxygen, these electrons join into one of these orbitals, forming “singlet oxygen delta” $O_2(^1\Delta_g)$, rare chemical species with high chemical reactivity [6,15]. The presence of an empty π^* orbital assigns strong acidic properties to $O_2(^1\Delta_g)$ (i.e., accepting a pair of electrons). Hence, singlet oxygen $O_2(^1\Delta_g)$, unlike triplet oxygen $O_2(^3\Sigma^-_g)$, acts as a strong electrophile agent and paramagnetic due to a net orbital (and not spin) electronic angular momentum, as shown by the observation of an electron paramagnetic resonance (EPR) spectrum.

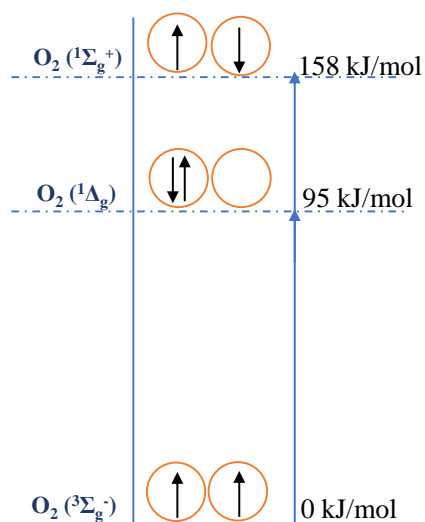
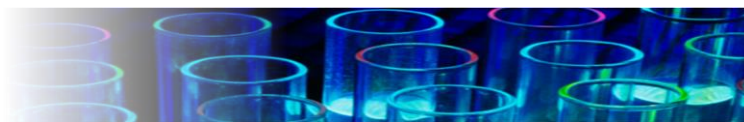


Figure 2.2. Energy levels of the three low-lying electronic state of oxygen with their orbital assignment.

Singlet oxygen $O_2(^1\Delta_g)$ and $O_2(^1\Sigma_g^+)$ exhibit energy levels of about 95 kJ mol^{-1} and 158 kJ mol^{-1} , respectively, above the ground state oxygen $O_2(^3\Sigma_g^-)$ as seen in Figure 2.2. Of these, only the former, i.e., $O_2(^1\Delta_g)$, plays a major role in reactions. The later deactivates rapidly with no chance of reaction [39,40]. Based on the energy levels of singlet oxygen $O_2(^1\Delta_g)$ and $O_2(^1\Sigma_g^+)$, luminescence decays are detected at 1270 nm ($^1O_2 \rightarrow ^3O_2 + h\nu$) and at 762 nm ($O_2(^1\Sigma_g^+) \rightarrow ^3O_2 + h\nu$). 1O_2 relaxes to 3O_2 by physical quenching (dissipation of energy as heat or charge transfer) or by chemical quenching (oxidation reaction) with other substances generating excited/radical complexes [51]. Unless mentioned otherwise, the term "singlet oxygen" or "singlet 1O_2 " refers to the first excited state of oxygen $O_2(^1\Delta_g)$ throughout this review chapter. Some other detailed physical aspects singlet oxygen have been documented by Schweitzer and Schmidt [52]

Singlet oxygen has a short lifetime in solution that limits its reactivity to the proximity of the site where the 1O_2 was formed, i.e., 3.1 μ sec in water. However, in vacuum, singlet oxygen have a relatively longer lifetime estimated to be 45 min, and this corresponds to a diffusion



distance of ~ 220 nm [51]. In general, the distance d that $^1\text{O}_2$ would move in a time t can be expressed by: $d = (6tD)^{1/2}$ (comprehended from Fick's law (i.e., three-dimensional molecule diffusion in a uniform concentration); where D is oxygen diffusion coefficient [53,54]). The lifetime of singlet oxygen changes dramatically in different solvents [55] depending on the energy-transfer efficiency from electronic to vibrational states. The closer the vibrational mode of the solvent to that of singlet oxygen, the higher the effectiveness of the deactivating process. For instance, O–D and O–H bonds vibrate at 2550 and 3500 cm^{-1} , respectively, whereas singlet oxygen vibrates at 3286 cm^{-1} ; hence, it quenches far faster in water than deuterium oxide (heavy water) [12]. Rodgers and T. Snowden [56] estimated the natural lifetime of singlet oxygen to be thirteen times higher in D_2O than in H_2O . Table 2.2 provides quenching rate constants k_q of delta and sigma singlet oxygen in different media or its reciprocal parameter, the $\text{O}_2(^1\Delta_g)$ lifetime (τ_Δ), in Table 2.3. Both Table 2.2 and 2.3 reveal that strong dependency of $\text{O}_2(^1\Delta_g)$ decay kinetics on the media of formation.

Table 2.2. Rate constant k_q for the deactivation of $\text{O}_2(^1\Delta_g)$ and $\text{O}_2(^1\Sigma^+_g)$ ($\text{M}^{-1} \text{s}^{-1}$) [52,57,58]

Medium	$\text{O}_2(^1\Delta_g)$	$\text{O}_2(^1\Sigma^+_g)$	Medium	$\text{O}_2(^1\Sigma^+_g)$
O_2	1.4×10^3 [57]	$2.7\text{-}9.0 \times 10^8$	CH_4	5.0×10^7
H_2O	9×10^3 [57]	$3.2\text{-}20 \times 10^8$	C_2H_6	2.3×10^8
CO_2	2.3×10^3	$2.3\text{-}26 \times 10^7$	C_3H_8	2.7×10^8
CO	NA	$1.5\text{-}2.6 \times 10^6$	C_4H_{10}	3.8×10^8
N_2	$< 6.0 \times 10$ [57]	$2.1\text{-}12 \times 10^5$	C_5H_{12}	4.5×10^8
Ar	$< 1.2 \times 10^2$ [57]	$1.9 \times 10^6\text{-} 3.5 \times 10^8$	C_6H_{14}	5.5×10^8
D_2O	NA	3.7×10^8	C_7H_{16}	6.0×10^8
NH_3	NA	8.3×10^8	C_6H_6	3.9×10^8
H_2S	NA	2.6×10^8	CS_2	1.7×10^6
NO_2	NA	1.5×10^7	CCl_4	2.7×10^5

**Table 2.3.** Lifetime of singlet oxygen in different solvents [52,59,60].

Solvent	Lifetime	Solvent	Lifetime	Solvent	Lifetime
H ₂ O	3.1 μs	CH ₂ Cl ₂	99.0 μs	CDCl ₃	7.0 ms
D ₂ O	68 μs	CH ₃ CN	77.1 μs	C ₆ F ₁₃ I	25 ms
C ₆ H ₁₄	23.4 μs	C ₅ H ₁₂	34.7 μs	CS ₂	45 ms
(CH ₃) ₂ CO	51.2 μs	CH ₃ OH	9.5 μs	CCl ₄	59 ms
(CD ₃) ₂ CO	992 μs	C ₂ HCl ₃	247 μs	C ₆ F ₁₄	68 ms
C ₆ H ₆	30.0 μs	CHCl ₃	229 μs	C ₁₀ F ₁₈	59 ms
C ₆ D ₆	681 μs	C ₆ F ₆	21 ms	C ₂ Cl ₃ F ₃	72 ms

2.2.1.2 Chemistry and reactivity of singlet oxygen

As earlier describes, singlet oxygen is an electrophilic reactant. Thus, unlike triplet oxygen, introducing singlet oxygen atoms into olefins, dienes or aromatic structures will take different reaction pathways such as Diels-Alder [4 + 2] and [2 + 2] cycloadditions, and ene reactions with isolated double bonds [40,61,62]. For instance, electron rich olefins and substances with inaccessible allylic hydrogens are the best candidates to undergo [2+2]-cycloaddition with singlet oxygen forming dioxetanes as the four-membered ring compounds, see Figure 2.3 (2) [63]. However, allylic hydrogens in the most congested side of olefins will undergo ene reaction by abstraction of the allylic proton yielding the allyl hydroperoxide, R–O–OH (R = alkyl), which can then be reduced to the corresponding allylic alcohol [64]. Nevertheless, a five- or six- membered hetero-rings will form through the 1,3 addition of singlet oxygen to dienes. Singlet oxygen reacts with 1,3-dienes in any structures: cyclic, non-cyclic or aromatic to produce endoperoxides [65]. In addition, singlet oxygen can react with sulphides and converts it to sulfoxides 4- Figure 2.3.

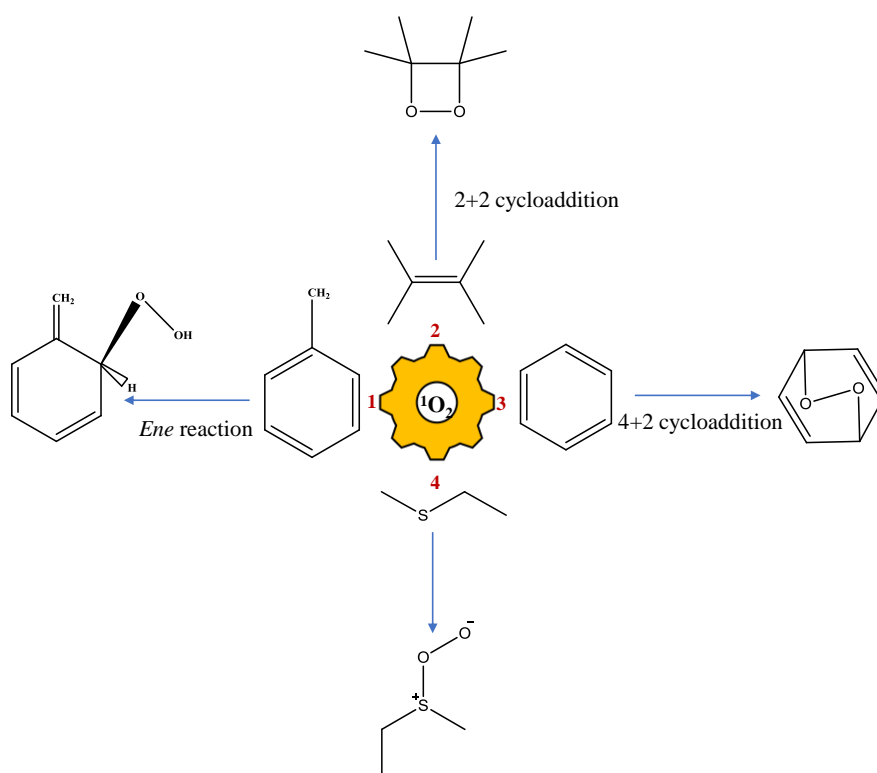
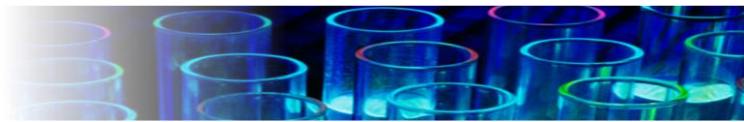


Figure 2.3. Singlet Oxygen reaction pathways; Ene reaction (1), 2+2 cycloaddition (2), 4+2 cycloaddition (3), and addition to sulphides (4).

Determination of dominant reaction rests on different factors. For example, the distance between C_1 and C_4 atoms, ionization potential of the 1,3 diene, spatial alignment of allylic hydrogens, and solvent [63,66], for instance, [4 + 2]-cycloaddition reaction is highly solvent-dependent [67].

The electrophilic nature of singlet oxygen engenders the rate constant for its reaction with substituted benzene ring to increase in the order of $H < C_6H_5 < CH_3 < OCH_3$ [68]. This means that, the electron density of a HC species dictates its reactivity towards singlet oxygen. Singlet oxygen reacts with electron-rich organic molecules such as polycyclic aromatic compounds, sulfides, or phenols in a high rates [69], almost at the same rate as the diffusion rate.



Consequently, singlet oxygen is one of the key reagents in the photo-oxygenation and thermal degradation processes.

The Diels–Alder reactions of singlet oxygen range from stepwise, proceeding through polarised diradical intermediates, to highly asynchronous concerted. When singlet oxygen reacts with electron rich molecules, the frontier orbital interactions are responsible of these highly asynchronous concerted or stepwise paths. These interactions also influence the properties of these intermediates, causing significant rotational barriers about single bonds of the polarised diradical. The frontier molecular orbitals of singlet oxygen (HOMO and LUMO) shown in Figure 2.4 are both π^* orbitals.

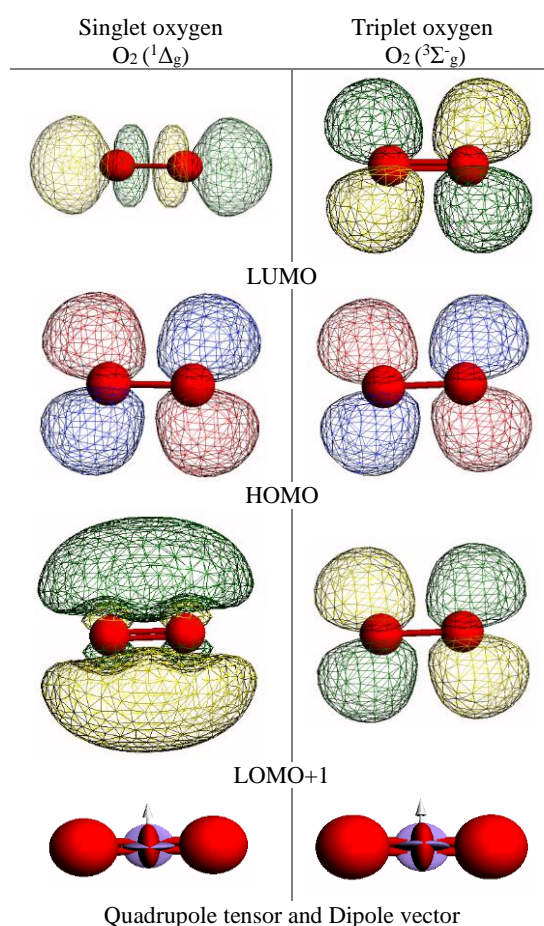


Figure 2.4. Singlet and triplet oxygen HOMO, LUMO, and LUMO+1 molecular orbital maps along with their respective quadrupole tensor and Dipole vector as obtained from ADF software applying M062X functional.

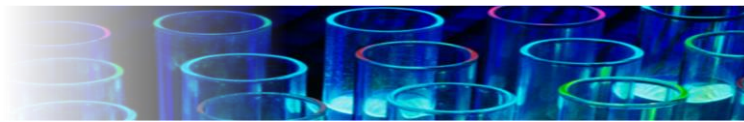


2.2.2 Generation of singlet oxygen $^1\text{O}_2$

Singlet oxygen can be generated via various techniques, ranging from chemical to biological means. Some practically applied techniques comprise photochemical method, chemical reactions, and thermo- and photo-catalytic based methods. While each method exhibits favourable advantages and disadvantages, the photochemical method (otherwise termed as dye-sensitised oxidation) has gained wide popularity in the (bio)chemical and health sectors [70–72].

2.2.2.1 Photosensitisation methods

Photosensitisation represent the response of a substance to visible and ultraviolet (UV) radiations [73,74]. This includes photolysis of colourless substances because of the exposure to UV. Conversely, coloured substance (dyes) absorbs visible light to initiate physical and/or chemical changes in the substrate. This is called the first law of photochemistry (i.e., Grotthus-Draper law). The second law of photochemistry by Stark-Einstein, however, indicates that the number of activated molecules for instance singlet oxygen is equivalent to the light absorbed (number of photons) [75]. A pioneering study by Kautsky [76] proposed that singlet oxygen might exist as a reaction intermediate in dye sensitised photo oxygenations. This was later confirmed in 1964 by comparing the physiochemical features of the ROS (i.e., singlet oxygen) generated by the photosensitisation method to that obtained from chemical alternatives [76] [77]. and radio-frequency [18]. Dye-sensitised photo-oxidation is known to be one of the most



common and most efficient techniques to produce singlet oxygen and is widely used in chemical [78], medical [79] and biological [80] systems.

In the production of singlet oxygen, based on the environmental conditions and the efficiency required, the light source can be either monochromatic (lamp) [81] or polychromatic (laser) [82]. For example, in biological system laser sources are used for illuminating living cells. Whereas, in large areas like in the treatment of wastewater; monochromatic (lamp) light such as UV radiation is implemented for the degradation of the organic matter dissolved in water [81]. There are different types of monochromatic lamp comes with different photons intensity and efficiency such as, LED, Xenon arc, and medium pressure Hg lamp. In photo-oxygenation LED lamp was the most efficient among all other lamps with efficiency around 70% of its emitted light being absorbed in the photoreaction [83].

Equations 2.4-2.8 describe the dye-photoreaction mechanism [84]. Starting from a sensitizer molecule in its ground state, 1S absorbs green photon to form a singlet excited state ($^1S^*$, Eq. 2.4) [85]. Subsequently, the $^1S^*$ spin-flips to the triplet state ($^3S^*$, reaction 2.6) through intersystem crossing (ISC) [86]. $^3S^*$ may deactivate by fluorescence or non-radiative processes [87] to 1S . While the photosensitizer molecule relaxes to its ground state, it transfers the excitation energy to a molecule of triplet oxygen 3O_2 , forming singlet state oxygen 1O_2 (Reaction 2.7). The vibronic coupling with the solvent (i.e., water) quenches singlet oxygen with a pseudo-first-order rate constant of $k_d = 5 \times 10^5 \text{ s}^{-1}$ [88]. In aqueous media, the radiative decay of singlet oxygen (k_p , Reaction 2.9) as this pathway makes negligible contribution to the decay process in solutions [52]. The product of $h\nu$ in Reaction 2.4 represents the light intensity absorbed by S, and 1S_b denotes the sensitizer bleaching product.



It is worth mentioning that, molecular oxygen can be excited into its singlet state by photosensitization directly without the need of the sensitizer by a microwave or radio frequency discharge generator where low pressure oxygen electrically discharged to produce singlet oxygen at efficiency around 10-20% [89]. However, the microwave or radio frequency discharge generator cannot produce singlet oxygen in pure form it will always be contaminated with other oxygen forms such as oxygen atoms and ozone that can quench singlet oxygen violently.

The selection of a good sensitizer is mandatory for an effectual singlet oxygen production. The properties of such photosensitizers should include a high light absorption at the wavelength of study (i.e., high extinction coefficient of light), a high quantum yield ϕ_Δ , and resistance to oxidation by singlet oxygen or other oxidants present in the system (i.e., long lifetime for the excited triplet state). Some typical dyes and their structure, Absorbance range, and quantum yield in different solution are illustrated in Table 2.4.


Table 2.4. Singlet oxygen generation from typical photosensitisers in various solvents [60,75,90–92]

Sensitisers	Structure	Absorbance Region	λ_{max} (absorption)	Quantum yield ϕ_{Δ}
Rose Bengal (RB)		490 - 575 nm	510 nm	ϕ_{Δ} (CH ₃ OH) = 0.80 ϕ_{Δ} (H ₂ O) = 0.76
Erythrosin B		470 - 530 nm	510 nm	ϕ_{Δ} (H ₂ O) = 71
Methylene Blue (MB)		550 - 700 nm	670 nm	ϕ_{Δ} (CH ₃ OH) = 0.51
Benzophenone		240 – 380 nm	250 nm	ϕ_{Δ} (C ₆ H ₆) = 0.36
2-Acetonaphthone		280 - 320 nm	293 nm	ϕ_{Δ} (C ₆ H ₆) = 0.71
Acridine		200 - 400 nm	250 nm	ϕ_{Δ} (C ₆ H ₆) = 0.83
Buckminsterfullerene (C ₆₀)		NA	NA	ϕ_{Δ} (CH ₃ OH) = 0.90
Tetraphenylporphine (TPP)		NA	NA	ϕ_{Δ} (C ₆ H ₆) = 0.66
9,10-Dicyanoanthracene (DCA)				ϕ_{Δ} (C ₆ H ₆) = 1.66 ϕ_{Δ} (CH ₃ CN) = 2.03
Eosin Y		200-560 nm	517 nm	ϕ_{Δ} (H ₂ O) = 0.61



2.2.2.2 Chemically derived sources

Half a century ago, Seliger [93] using a low-resolution photomultiplier photographed an unexplained red light emitting with low intensity after mixing hydrogen peroxide (H_2O_2) with sodium hypochlorite NaOCl . A decade later, Khan and Kasha [94] explained that such observation is associated to the decay of singlet oxygen generated at a single chemiluminescence band of 634.8 nm. Moreover, the authors successfully recorded the emission of singlet oxygen (in solution) at some other wavelength as shown in Equations 2.10 and 2.11 [94]. Ever since, several experimental and theoretical studies have investigated some other aspects involving the generation and detection of singlet oxygen, as well as pertinent products and reaction mechanisms in the dark (i.e., chemically-derived means without the involvement of light), Figure 2.4 [2,95,96].

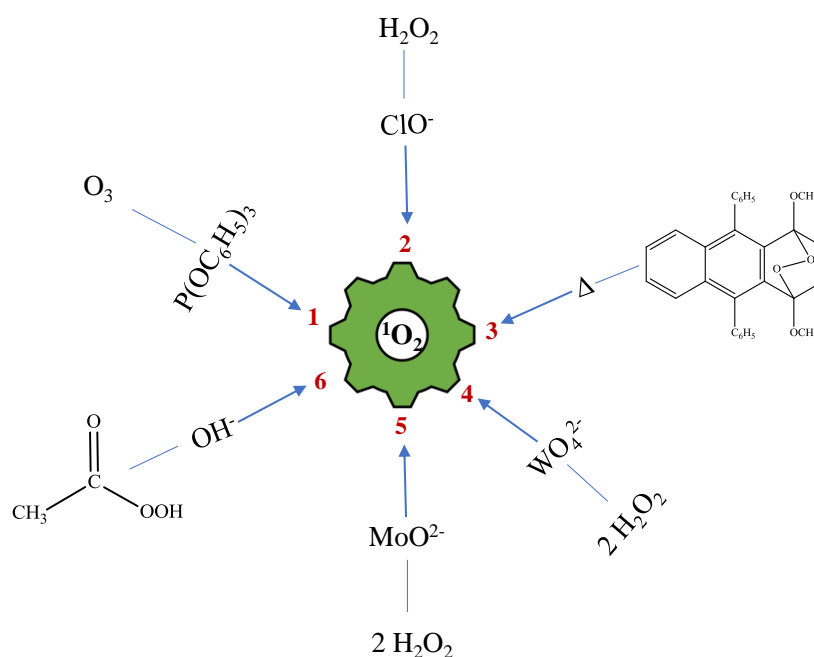


Figure 2.4. Most efficient chemical sources of singlet oxygen.



Singlet oxygen ${}^1\text{O}_2$ can also be generated chemically by the decomposition of ozonides [97], endoperoxides [98,99] and superoxide ion [20,100], see Figure 2.5. Among all, thermal decomposition of endoperoxides is the cleanest. However, the chlorination of an alkaline solution of hydrogen peroxide is the most widely used dark reaction. In general, at room temperature, hydrogen peroxide decomposes into water and singlet oxygen poorly, but in the presence of catalysts such as MoO_4^{2-} , $\text{Ca}(\text{OH})_2$ and NaOCl [101] the story is different. Equation 2.12 describes the decomposition of hydrogen peroxide, where M represent an atom of an alkali metal (K, Na, Li).

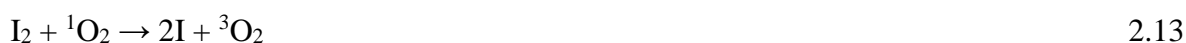


In the case of using molybdate ions (MoO_4^{2-}) as a catalyst, excess amount of hydrogen peroxide would not produce higher amount of ${}^1\text{O}_2$; due to the formation of the MoO_8^{2-} ion which gives a relatively lower ${}^1\text{O}_2$ yield [102]. Solvation effect plays a crucial role in both photosensitized and chemical generation of singlet oxygen. For instance, in methanol, a yield of 70% singlet oxygen (based on hypochlorite) could be achieved, while water results in 10 % yield [103]. This can be rationalised to the higher physical quenching ability of water as compared to methanol.



One of the practical uses for the chemically generated singlet oxygen is the “chemical generator of singlet oxygen”, hence the name. This kind of generators found primary application in the chemical oxygen-iodine lasers (COIL). The iodine atoms necessary for the COIL operations are as a result of the rapid chemical quenching of singlet oxygen with iodine as expressed in Equation 2.13. At least two singlet oxygen molecules are required to dissociate one iodine molecule, requiring a dissociation energy of $D_0(I_2) = 146 \text{ kJ mol}^{-1}$, as compared to the excitation power of singlet oxygen (95 kJ mol^{-1}). Advances in chemical singlet oxygen generators has led to the production of higher concentration of singlet oxygen in gas streams, suitable for the operation of COIL at output power up to 100 kilowatts.

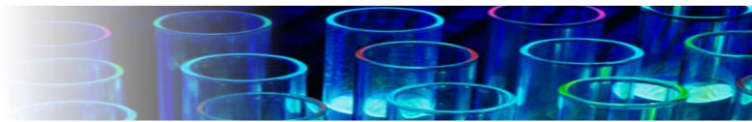
Chemical generators of singlet oxygen constitute several chain reactions that can be globalized in Equation 2.12. However, the most important step in Equation 2.14 represents the interaction between a gaseous chlorine and hydroperoxide ion. In order to retain the maximum concentration of 1O_2 , as well as to achieve higher degree of chlorine utilisation, the process must be adjusted for optimum conditions [95]. The degree of utilisation of chlorine $U(t)$ and the singlet-oxygen content $\eta(t)$ are described by Equations 2.14 – 2.17:



$$U(t) = 1 - \exp\left(-\frac{t}{\tau_{chl}}\right) \quad 2.15$$

$$\eta(t) = \frac{Y_{int}^\circ}{1 + Y_{int}^\circ U(t) \tau_{react} / \tau_{loss}} \quad 2.16$$

$$Y_{int}^\circ = \left[1 + \left(\frac{D_{Cl_2}^{liq}}{\tau_{A17} K_{17} [HO_2^-]_{int} D_{O_2}^{liq}} \right)^{1/2} \right]^{-1} \quad 2.17$$



where τ_{chl} denotes the characteristic chlorine utilisation time, τ_{loss} represents the characteristic time of loss of a singlet oxygen by energy pooling reaction, $\tau_{\text{react}} = (\tau_{\text{chl}} / U^2 [t / \tau_{\text{chl}} - U(1 + 0.5U)])$, and Y_{int}° signifies the yield of singlet oxygen at the gas - liquid interface, giving by the equation 2.17, wherein τ_{Δ} expresses the life time of singlet oxygen, D_{Cl_2} corresponds to the diffusion coefficient of Cl_2 , and D_{O_2} typifying the diffusion coefficient of oxygen [95].

Regardless of the complexity of Equations 2.15 – 2.17, the fundamental rule of thumb is to achieve a high degree of singlet oxygen utilisation $\eta(t)$ by chlorination of an alkaline solution of hydrogen peroxide, while adjusting for a higher Y_{int}° and a lower τ_{react} . The yield of singlet oxygen Y_{int}° can be unity (i.e., maximum) if the $[\text{HO}_2^-]_{\text{int}}$ is high enough – this can be achieved by employing excess amount of alkali in the solution and by preventing a higher chlorine pressure build up, i.e., higher mass transfer rates. τ_{react} is proportional to τ_{chl} and the later inversely proportional to the specific interface area. Thus, the larger the specific area of contact the higher the efficiency of the singlet oxygen generator [95].

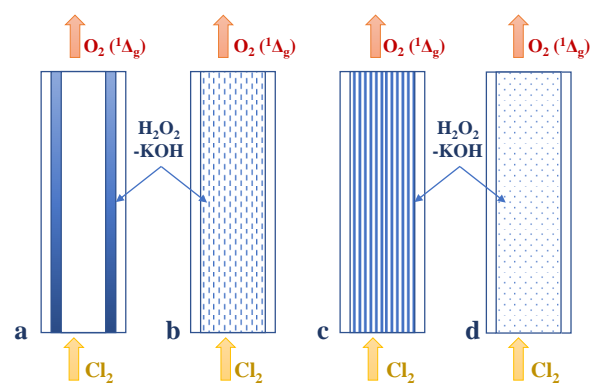


Figure 2.6. Methods used to achieve gas-liquid reaction in a singlet oxygen generator: a- wetted wall; b- aerosol; c-jet; d- sparger.



Figure 2.7 illustrates different types of singlet oxygen generators based on the methods shown in Figure 2.6, including wetted wall, aerosol, jet, and sparger.

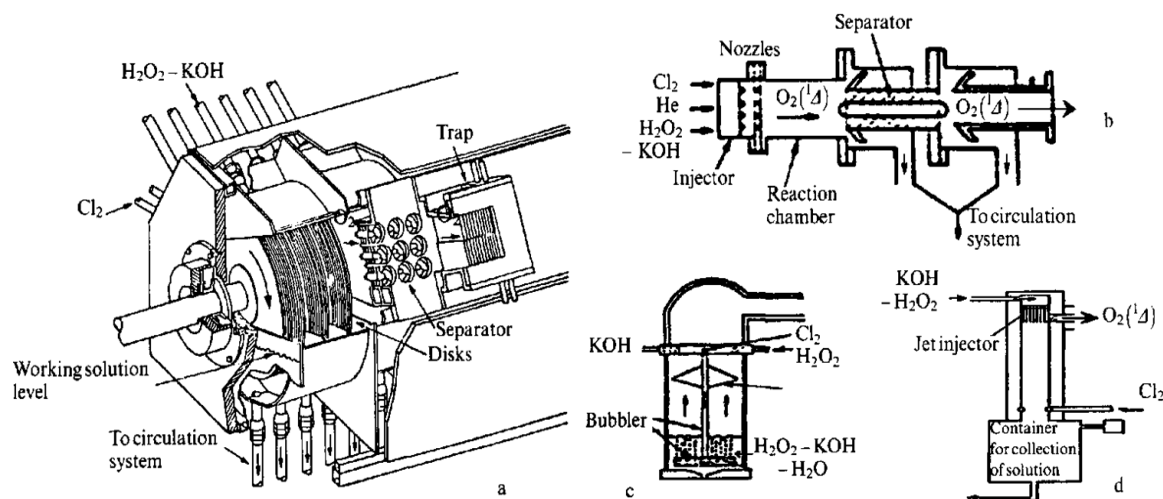


Figure 2.7. Different types of chemical singlet oxygen generator: a- wetted wall, with rotating disks; b- aerosol; c- sparger; d- jet [95].

In summary, chemical techniques appears unclean and uneconomical. The processes has low efficiency as it applies excess quantities of reagents, and in most of the cases, the strong oxidisers give rise to side products [104]. Therefore, chemical methods are only applied in situations where the use of light is prohibited or restricted [40].

2.2.2.3 Methods involving surface-reactions

Singlet oxygen forms via surface-mediated reactions on particles such as silicon dioxide, aluminium oxide, and transition metal oxides [16,17]. A recent review by Nosaka et. al. describes the photocatalytic method of generating ROS generation on TiO_2 , as well as the supplementary techniques [90]. The catalytic surfaces can be activated by heat (thermally) or during light exposure (photons). In the latter case, the induction of photos (on the surface of



the catalyst) generates electrons (e^-) and holes (h^+) responsible for the formation of ROS through oxidative and reductive reactions.

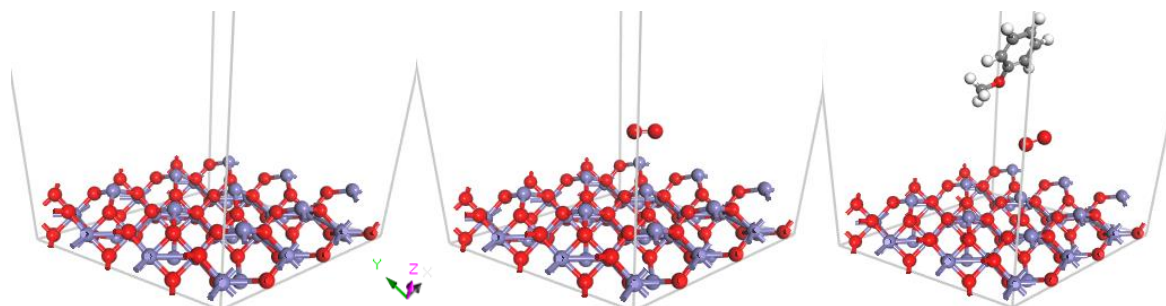


Figure 2.8. From left to right surface activated oxygen radical followed by hydrocarbon reaction.

As early as the mid-1960s, it was suggested that singlet oxygen might be behind the thermal oxidation of aromatic hydrocarbons on heterogeneous oxide catalysts, Figure 2.8. As was found that for activating the oxidative transformations of hydrocarbons such as naphthalene, toluene, and benzene around 121 kJ mol^{-1} were necessary. This was linked later to the energy consumed in the triplet–singlet transition (96 kJ mol^{-1}) of adsorbed oxygen molecules. However, the methods that allowed singlet oxygen to be detected qualitatively and quantitatively on heterogeneous systems appeared later on [105–108].

2.2.3 Detection of singlet oxygen

Detection of singlet oxygen can be classified as direct or indirect methods. Direct detection of singlet oxygen applies two major techniques, i.e., the electron paramagnetic resonance (EPR) [109], and germanium photodiode (or photomultipliers), requiring a singlet oxygen lifetime of a sub-millisecond timescale. On the other hand, indirect methods singlet oxygen



reacts with probe molecules (i.e., chemical or spin traps) to yield a more stable, long-lived analyte. Therefore, the detection timescale of indirect methods can scale up hours. Technically, the two classes of techniques require thorough consideration sensitivity, selectivity, and sufficiently fast time resolution [2], otherwise termed as the triple S.

2.2.3.1 Time-resolved EPR technique

In view of the fact that dioxygen exists as a paramagnetic species that has unpaired electrons in its electronic structures, EPR spectrometer remains the most reliable technique for detecting singlet oxygen (as well as other radicals and paramagnetic compounds) in any phase [110]. EPR technique accurately predicts the structures of radicals, and can further be applied for quantification via standard calibration. The major drawback is the short life time of radicals. Hence, EPR detector should be used in situ, with adequate consideration of the pressure (vacuum) and temperature (cryogenic condition) in order to increase the lifetime and achieve a strong EPR signals [111].

As a result, Kearns et al. [112] placed their reactor inside the EPR cavity and irradiated an oxygen stream saturated with sensitiser (Naphthalene) inside it using a mercury lamp. Wasserman et al. [62] also applied the same idea but extended it to study the other derivatives of Naphthalene as photosensitisers such as octafluronaphthalene and perdeuterated naphthalene vapours at low pressures in the range of 0.1 to 1 Torr. Where 70 % of triplet oxygen excited to singlet oxygen. Snelling [113] reported that at about the same pressure limit (1 Torr) the photochemical generation of $^1\text{O}_2$ will reach its maximum. Even though, the use of EPR has a pivotal role in the direct detection of singlet oxygen. Up to now, little attention has been paid



to its application, resulting in limited amount of published data. Generally, the EPR can be sub-grouped into the *direct* and *indirect* (using spin trap) methods.

Indirect detection of singlet oxygen using chemical traps: Spin trap or chemical trap is defined as the use of high reactive chemical agents in solution to capture singlet oxygen by forming a stable compounds (endoperoxide) making the detection of the short-lived singlet oxygen easier and more accurate. To choose a chemical trap specified for singlet oxygen, it must react rapidly and selectively with $^1\text{O}_2$ to produce a distinct and stable endoperoxide without any side products. It must also be highly solubility in solvent of interest, and transparent in the range of excitation wavelength [114,115] . One of the most common singlet oxygen spin traps, 2,2,6,6-tetramethyl-4-piperidone (TEMP) reacts with singlet oxygen to form 2,2,6,6-tetramethyl-4-piperidone-N-oxyl (TEMPO) that is easily detectable by EPR spectroscopy [116], polycyclic aromatic compounds such as tetrapotassium rubrene-2,3,8,9-tetracarboxylate (RTC) and disodium 9,10-anthracenedipropanoate (ADP) are also considered popular chemical traps even though they lack the transparency criteria [117]. Moreover, probes such as 9,10-Anthracenedipropionic acid (ADPA), 2,2,6,6-Tetramethylpiperidine (TEMP), Furfuryl alcohol (FFA) and 1,3-Diphenylisobenzofuran (DPBF) are also widely used for indirect detection of $^1\text{O}_2$ [118].

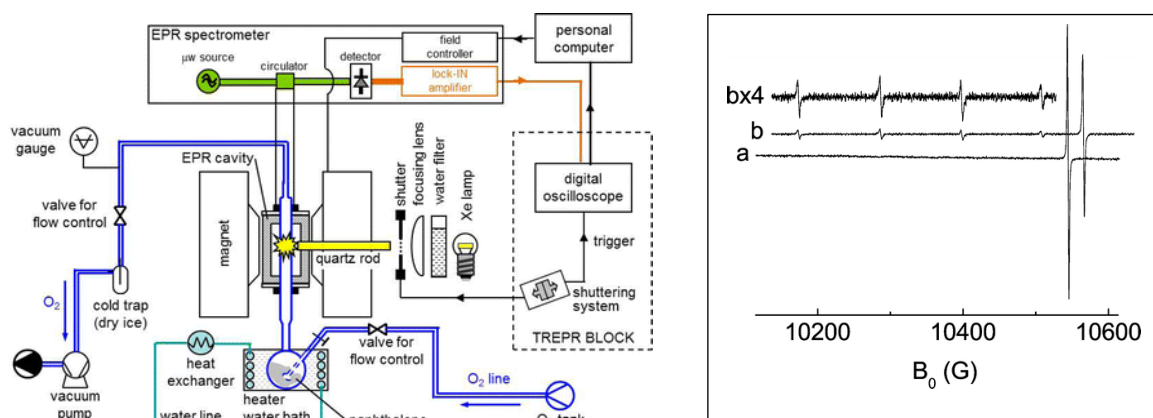


Figure 2.9. An example of *direct* EPR sampling of singlet oxygen, generated by photosensitisation (naphthalene) of pure triplet oxygen. The right figure compares the spectrum of triplet oxygen (a) to singlet oxygen (b) [109].

Up to date, no body reported a validated concentration course of trapped singlet oxygen in solution using EPR. Therefore, such work remains a gap in the literature. There by the kinetic of trapped singlet oxygen against a theoretical model has been provided in Chapter 7.

2.2.3.2 Photodiode techniques

Photodiodes are semiconductors typically made from materials such as silicon and germanium that turn light into electrical current. When $^1\text{O}_2$ decays it emits light that can be detected by the photodiode, its energy will be transferred to surface electrons that pass through a depletion layer. Leaving behind a charge difference between electrodes proportional to the amount of light received. On the other hand, photomultipliers are vacuum tubes with high photosensitivity in ultraviolet, visible, and near-infrared regions, it can detect weak emissions because for each dynode electron double photoelectrons are released at the surface by that the signal is magnified by 100 % with a faster response and lower noise [119,120]. For instance,



the chemiluminescence method measure the light that emitted through transition of $^1\text{O}_2$ to its ground state (dimol light emission and monomol light emission) [9]. Such emission in solutions can be detected also by a liquid nitrogen cooled germanium photodiode detector [98] or by using photomultiplier tubes (PMTs) where the later more efficient and can identify both forms of singlet oxygen ($^1\Delta_g$ and $^1\Sigma_g^+$) separately [9]. However, in solutions, the detection is more challenging due to the short lifetime of $^1\text{O}_2$ and the low emission (quantum yields $< 10^{-8}$) so photomultiplier tubes (PMTs) is applied if the concentration of singlet oxygen is quite big [112,113,121].

2.2.4 Role of singlet oxygen in initiation of hydrocarbon reactions

One promising area of research is concerned with studying the influence of singlet oxygen O_2 $^1\Delta_g$ on combustion and spontaneous ignition of hydrocarbon fuels [122,123]. As earlier discussed singlet oxygen O_2 $^1\Delta_g$ resides 95 kJ mol^{-1} ($\Delta_G H_{298}^0$) above the ground state triplet oxygen molecule O_2 $^3\Sigma_g^-$ [39,40]. Therefore, even when injected in minuscule quantities, singlet oxygen O_2 $^1\Delta_g$ accelerates the chain-branching mechanism, decreasing the ignition temperature as well as the induction time [42,47,49,122,124–127].

Applying the excitation power of singlet oxygen, emerged as one of the most attractive approaches in combustion enhancement in internal combustion (IC) engines [122,128–132]. This implies that, when singlet oxygen is presented in combustion systems, such as $\text{H}_2\text{--O}_2$ [42–45], $\text{CH}_4\text{--O}_2$ [46–48], and $\text{CO--H}_2\text{--O}_2$ [49] it intensifies the ignition and enhances the decomposition kinetic. For example, in the $\text{CO--H}_2\text{--O}_2$ system, singlet oxygen showed an ability to convert selectively and rapidly CO into CO_2 at 900 K [49]. Likewise, linear

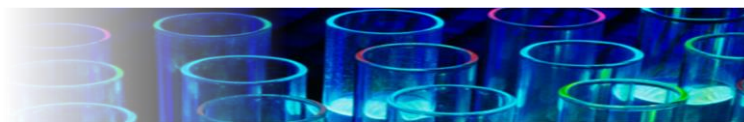


hydrocarbons (HCs) such as ethene (C_2H_4) and propane (C_3H_8) [133–135], and alkyl benzenes display notable improvements in combustion parameters with the addition of singlet O_2 [17,136,137]. The latter group constitutes a major additive fraction in transportation fuels, e.g., gasoline and diesel [138,139]. To date, many experimental results and computational simulations proved the significant impact of singlet oxygen on accelerating the chain-branching mechanism, decreasing the ignition temperature as well as the induction time [42,47,49,122,124–127]. Starik and Titova [131,140] in their computational studies projected substantial reduction in the induction length of ignition followed the excitation of oxygen to singlet oxygen. This enhanced the formation of O, HO, H radicals. Whereas, Smirnov et al. [132] used a plasma discharge to excite the oxygen stream right before merging it with hydrogen. They reported a reduction in the induction length and attributed it to the generated singlet oxygen molecules. However, the plasma discharge suffers from contamination of other radicals. Therefore, Ombrello et al. [132,135] in their following research adopted a lifted flame configuration to study the isolated effect of singlet oxygen. Where they found that singlet oxygen solely is behind the increment of the flame speed. Lebedev et al. [141] modelled the reaction of singlet oxygen with methane applying ab initio functional. Table 2.5 expresses the role of singlet oxygen on reactions of hydrocarbons in term of governing rate parameters.



Table 2.5. Documented reactions of singlet of with hydrocarbons

Singlet oxygen + HC	Medium	Rate parameters			Notes	Ref.
		A ($\text{cm}^3 \text{ s}$)	n	Ea (kJ mol^{-1})		
Hydrogen abstraction						
CH ₄ -air mixture CH ₄ + ¹ O ₂ = CH ₃ + HO ₂	Gaseous	7.59×10 ¹³	0	18.3	Numerically, the presence of 10% ¹ O ₂ in molecular oxygen increase the speed of flame propagation by a factor of 1.7 in a fuel-lean ($\phi = 0.45$)	[142]
H + ¹ O ₂ = OH + H	Gaseous	1.10×10 ¹⁴	0	3.2	Evidence that the reaction occurs principally via abstraction, H + ¹ O ₂ → OH + O, rather than via physical quenching, H + ¹ O ₂ → H + ³ O ₂ .	[143]
N + ¹ O ₂ = NO + O	Gaseous	6.46×10 ⁹	1	2.1	NO _x formation in the reaction of atomic nitrogen and NO with ¹ O ₂	[110]
¹ O ₂ + NO = O + NO ₂	Gaseous	1.00×10 ¹²	0	12.5		
C ₂ H ₆ -air mixture C ₂ H ₆ + ¹ O ₂ = C ₂ H ₄ + H ₂ O ₂	Gaseous	5.47×10 ⁻¹	3.66	5.1	At low temperatures ($T_0 < 850 \text{ K}$) and high pressure ($P_0 = 10 \text{ atm}$), the photodissociation of O ₂ by laser photons with $\lambda_l = 193.3 \text{ nm}$ was effective in accelerating the ignition.	[144]
CO-H ₂ mixture CO + ¹ O ₂ = CO ₂ + O	Gaseous	6.77×10 ⁷	1.6	13.7	Modelling studies showed that the abundance of singlet delta oxygen in the CO-O ₂ , CO-H ₂ O-O ₂ and CO-H ₂ -O ₂ mixtures results in the acceleration of oxidation process and allows to shorten the induction time and decrease the ignition temperature even at a small content of ¹ O ₂	[145–147]
CO-H ₂ O mixture H ₂ O + ¹ O ₂ = OH + HO ₂	Gaseous	2.05×10 ¹⁵	0	25.0		
³ O ₂ + ¹ O ₂ = O ₃ + O	Gaseous	1.20×10 ¹³	0	39.7	The presence of vibrationally and electronically excited ¹ O ₂ molecules in the discharge-activated oxygen flow allows to intensify the chain mechanism and to shorten significantly the induction zone length at shock-induced combustion.	[148]
O ₃ + ¹ O ₂ = 2·O ₂ + O	Gaseous	3.13×10 ¹³	0	2.8		
H ₂ S + ¹ O ₂ = HSO + OH	Gaseous	2.85×10 ⁸	0.97	11.5	The abundance of ¹ O ₂ molecules at only 1% in total oxygen intensify the chain-branching in the H ₂ S-air mixture.	[149]



					At $\phi = 0.6$, the presence of 5 % $^1\text{O}_2$ molecules in total oxygen increases the flame speed by 25 %.
$\text{CH}_2=\text{CHCH}_3 + ^1\text{O}_2 = \text{CH}_2=\text{CHCH}_2 + \text{HO}_2$	Gaseous	8.38×10^0	3.11	19.1	Elimination of a labile hydrogen atom from a linear or cyclic hydrocarbon. [150]
$\text{CH}_2=\text{C}(\text{CH}_3)_2 + ^1\text{O}_2 = \text{CH}_2=\text{C}(\text{CH}_3)\text{CH}_2 + \text{HO}_2$	Gaseous	1.08×10^2	2.98	13.5	
$\text{C}_7\text{H}_8 + ^1\text{O}_2 = \text{C}_7\text{H}_7 + \text{HO}_2$	Gaseous	7.42×10^{-2}	3.77	53.3	
Cycloaddition via Diels-Alder					
Isoprene + $^1\text{O}_2$	Solution	2.6×10^{-12}	0	55	Cycloaddition via [2 + 2] route [151]
Isoprene + $^1\text{O}_2$	Solution	1.6×10^{-12}	0	105	
Benzene + $^1\text{O}_2$	Solid	--	-	-	Cycloaddition via [2 + 2] route/ V_2O_5 [136,137]
Pyrrole + $^1\text{O}_2$	Solution	5.40×10^{-13}	0	111	<i>Ene</i> reaction [151]
Pyrrole + $^1\text{O}_2$	Solution	1.87×10^{-13}	0	48	Cycloaddition via [4 + 2] route
Pyrrole + $^1\text{O}_2$	Solution	2.48×10^{-1}	0	158	Cycloaddition via [2 + 2] route

As listed in Table 2.5, the major pathways of singlet oxygen reaction with hydrocarbon features:

- Hydrogen abstraction, i.e., elimination of a labile hydrogen atom from a linear or cyclic hydrocarbon.
- Cycloaddition via Diels-Alder [4 + 2] channel. Refer to Section 2.2.1.2 for details.
- Cycloaddition via [2 + 2] route. Refer to Section 2.2.1.2 for details.
- Concerted (and non-concerted) to hydrocarbon backbone, i.e., typically known as the *ene* reactions with isolated double bonds, and hydrogen abstraction [40,61,62].



However, the catalytic effect of metal-oxide surfaces, e.g., on oxidation of hydrocarbons (HC), materialises in different channels. Metal-oxides serve as excellent generators of singlet oxygen [16,17,106,108], catalysing the oxidation of HC via surface oxidation mechanisms such as Eley-Rideal (E-R), Langmuir-Hinshelwood (L-H) and Mars-van Krevelen (M-vK) or via the gas-phase oxidation of HC with $O_2\ ^3\Sigma_g^-$ desorbed from the catalytic surface. The literature still lacks the effects of functional groups and the preferential feasibilities of the above-mentioned pathways. Hence, the subsequent chapter of this thesis include the detailed mechanisms for the reaction of singlet oxygen with benzene as well as functionalised benzene species, i.e., aniline, phenol and toluene, assembling the associated rate functions.

2.3 Research Gaps and Outlooks

The ability of singlet oxygen to open up new reaction channels with hydrocarbons have been established in many fields including biological stress, drug formulation, photodynamic therapy, environmental studies, and combustion enhancement. However, limited information exists regarding the broader class of hydrocarbons and newly immersing applications. Likewise, few is known regarding the effect of singlet oxygen generated through dissolved organic matter on organic constituents in aqueous media. The considerable steady-state concentration and lifetime of photochemically-produced singlet 1O_2 further emphasises its importance in the environment. Hence, it is of interest to illustrate, both experimentally and computationally, the attributes, benefits and application of singlet oxygen (and some other ROS) in industrial processes involving wastewater and biological environments. In addition, it will be highly instrumental to assemble (and compare) the enthalpic requirements of initiation reactions comprising singlet oxygen and various groups of hydrocarbons, i.e., testing the effect of



functional groups. This constitutes an interesting and important challenge in developing efficient internal combustion (IC) engines based on the electrophilic properties of singlet oxygen. The chapters of this thesis do not only develop methods to study the detection and generation of ROS in various media, but also focuses on the thermal generation and evolution of ROS on catalytic surfaces. The latter aims at elucidating the influence of ROS generated on the surface of nano-particles on spontaneous fires organic materials, e.g., coal.

Contrary to non-spontaneous fires of coal that emerges in the presence of combustible gases and ignition sources, spontaneous fires in coal mines depends solely on the self-heating oxidation reactions [152]. In Australian coal mines, hundreds of spontaneous combustions of coal incidents have been reported. For instance, in Queensland alone, 51 spontaneous combustion incidents have been identified, three of which ended up in closures of the mines and 37 fatality [153]. The persistence occurrence of spontaneous fires across the globe necessitates the need for further investigations of the initiation cause [154]. These initiation reactions have two major criterions; operate at room temperature and maintain an adequate heat rate enough to generate the first or main long-living radical. Herein the hypothesis is that, the so-called singlet oxygen ($^1\text{O}_2$) or other surface-generated ROS maybe the initiator of the self-heating chain reactions. Electronically-excited species of oxygen can be formed spontaneously at room temperature by photosensitisation [82,113], “dark” reaction [83,95], and thermo-generation on surfaces of silica, alumina and transition metals surfaces present in coal [16]. Therefore, this thesis explores such the role of ROS generated on the surface of nano-particles in initiating the room-temperature combustion of organic fuel surrogates.



2.4 References

- [1] Gerschman R, Gilbert D, Nye SW, Dwyer P, Fenn WO. Oxygen poisoning and X-irradiation: a mechanism in common. 1954. *Nutr Burbank Los Angel Cty Calif* 2001;17:162.
- [2] Burns JM, Cooper WJ, Ferry JL, King DW, DiMento BP, McNeill K, et al. Methods for reactive oxygen species (ROS) detection in aqueous environments. *Aquat Sci* 2012;74:683–734.
- [3] Bartosz G. Use of spectroscopic probes for detection of reactive oxygen species. *Clin Chim Acta* 2006;368:53–76.
- [4] Kieber DJ, Peake BM, Scully NM. Reactive oxygen species in aquatic ecosystems. *UV Eff Aquat Org Ecosyst* 2003:251–288.
- [5] Johnson DR, Decker EA. The Role of Oxygen in Lipid Oxidation Reactions: A Review. *Annu Rev Food Sci Technol* 2015;6:171–90. doi:10.1146/annurev-food-022814-015532.
- [6] Petrou AL, Petrou PL, Ntanos T, Liapis A. A Possible Role for Singlet Oxygen in the Degradation of Various Antioxidants. A Meta-Analysis and Review of Literature Data. *Antioxidants* 2018;7:35. doi:10.3390/antiox7030035.
- [7] Edge R, Truscott TG. Singlet Oxygen and Free Radical Reactions of Retinoids and Carotenoids—A Review. *Antioxidants* 2018;7:5. doi:10.3390/antiox7010005.
- [8] Ghogare AA, Greer A. Using Singlet Oxygen to Synthesize Natural Products and Drugs. *Chem Rev* 2016;116:9994–10034. doi:10.1021/acs.chemrev.5b00726.
- [9] Lu C, Song G, Lin J-M. Reactive oxygen species and their chemiluminescence-detection methods. *TrAC Trends Anal Chem* 2006;25:985–995.
- [10] Klán P, Wirz J. *Photochemistry of Organic Compounds: From Concepts to Practice*. John Wiley & Sons; 2009.
- [11] Al-Nu'airat J, Altarawneh MK, Gao X, Westmoreland PR, Dlugogorski BZ. Reaction of Aniline with Singlet Oxygen ($O_2\ 1\Delta_g$). *J Phys Chem A* 2017.
- [12] Boix-Garriga E, Rodríguez-Amigo B, Planas O, Nonell S. Chapter 2: Properties of Singlet Oxygen, 2016, p. 23–46.



- [13] Gorman AA, Rodgers M a. J. Singlet molecular oxygen. *Chem Soc Rev* 1981;10:205–31. doi:10.1039/CS9811000205.
- [14] DeRosa MC, Crutchley RJ. Photosensitized singlet oxygen and its applications. *Coord Chem Rev* 2002;233:351–371.
- [15] Kearns DR. Physical and chemical properties of singlet molecular oxygen. *Chem Rev* 1971;71:395–427.
- [16] Shcherbakov NV, Emel'yanov AN, Khaula EV, Il'ichev AN, Vishnetskaya MV, Rufov YN. Photo-and thermogeneration of singlet oxygen by the metal ions deposited on Al₂O₃ and SiO₂. *Russ J Phys Chem* 2006;80:799–802. doi:10.1134/S0036024406050232.
- [17] Vishnetskaya M, Tomskiy I. Role of Singlet Oxygen in the Oxidation of Toluene on Vanadium Molybdenum Catalytic Systems, *Russ J Phys Chem*, 2010.
- [18] Corey EJ, Mehrotra MM, Khan AU. Generation of Delta oxygen from triethylsilane and ozone. *J Am Chem Soc* 1986;108:2472–2473.
- [19] Saito I, Matsuura T, Inoue K. Formation of superoxide ion via one-electron transfer from electron donors to singlet oxygen. *J Am Chem Soc* 1983;105:3200–6. doi:10.1021/ja00348a040.
- [20] Corey EJ, Mehrotra MM, Khan AU. Water induced dismutation of superoxide anion generates singlet molecular oxygen. *Biochem Biophys Res Commun* 1987;145:842–846.
- [21] Ganjali MR, Gupta VK, Faridbod F, Norouzi P. Lanthanides Series Determination by Various Analytical Methods. Elsevier; 2016.
- [22] Valko M, Leibfritz D, Moncol J, Cronin MT, Mazur M, Telser J. Free radicals and antioxidants in normal physiological functions and human disease. *Int J Biochem Cell Biol* 2007;39:44–84.
- [23] Muller FL, Lustgarten MS, Jang Y, Richardson A, Van Remmen H. Trends in oxidative aging theories. *Free Radic Biol Med* 2007;43:477–503.
- [24] Hayyan M, Hashim MA, AlNashef IM. Superoxide ion: generation and chemical implications. *Chem Rev* 2016; 116:3029–3085.



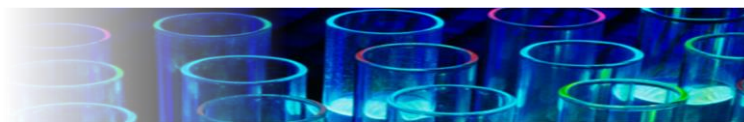
- [25] Makino K, Mossoba MM, Riesz P. Chemical effects of ultrasound on aqueous solutions. Evidence for hydroxyl and hydrogen free radicals (OH and H) by spin trapping. *J Am Chem Soc* 1982; 104:3537–3539.
- [26] Moorhouse CP, Halliwell B, Grootveld M, Gutteridge JM. Cobalt (II) ion as a promoter of hydroxyl radical and possible ‘crypto-hydroxyl’ radical formation under physiological conditions. Differential effects of hydroxyl radical scavengers. *Biochim Biophys Acta BBA-Gen Subj* 1985;843:261–268.
- [27] Zhang Y, Klammerth N, Chelme-Ayala P, El-Din MG. Comparison of classical fenton, nitrilotriacetic acid (NTA)-Fenton, UV-Fenton, UV photolysis of Fe-NTA, UV-NTA-Fenton, and UV-H₂O₂ for the degradation of cyclohexanoic acid. *Chemosphere* 2017;175:178–185.
- [28] Greenwald RA. *Handbook Methods For Oxygen Radical Research*. CRC press; 2018.
- [29] Vissers MC, Hampton M, Kettle AJ. *Hydrogen Peroxide Metabolism in Health and Disease*. CRC Press; 2017.
- [30] Phillips CA. *Microfluidic Study of Hydrogen Peroxide (H₂O₂) Transport Modeled on the MSN-DA Neuron Pathway* 2018.
- [31] Campos-Martin JM, Blanco-Brieva G, Fierro JL. Hydrogen peroxide synthesis: an outlook beyond the anthraquinone process. *Angew Chem Int Ed* 2006;45:6962–6984.
- [32] Offermanns H, Dittrich G, Steiner N. Wasserstoffperoxid in Umweltschutz und Synthese. *Chem Unserer Zeit* 2000;34:150–159.
- [33] Hage R, Lienke A. Applications of Transition-Metal Catalysts to Textile and Wood-Pulp Bleaching. *Angew Chem Int Ed* 2006;45:206–222.
- [34] Bertini I, Gray HB, Lippard SJ, Valentine JS. *Bioinorganic chemistry*. University Science Books; 1994.
- [35] Lippard SJ, Berg JM. *Principles of bioinorganic chemistry*. University Science Books; 1994.
- [36] Robinett NG, Peterson RL, Culotta VC. Eukaryotic copper-only superoxide dismutases (SODs): A new class of SOD enzymes and SOD-like protein domains. *J Biol Chem* 2018;293:4636–4643.



- [37] Rosso JA, Astorga MA, Mártire DO, Gonzalez MC. Alloxan-dialuric acid cycling: A complex redox mechanism. *Free Radic Res* 2009;43:93–99.
- [38] Halliwell B, Gutteridge JM. *Free radicals in biology and medicine*. Oxford University Press, USA; 2015.
- [39] Wilkinson F, Helman WP, Ross AB. Rate constants for the decay and reactions of the lowest electronically excited singlet state of molecular oxygen in solution. An expanded and revised compilation. *J Phys Chem Ref Data* 1995;24:663–677.
- [40] Foote CS. *Active oxygen in chemistry*. Springer Science & Business Media; 1995.
- [41] Girotti AW, Korytowski W. Reactions of singlet oxygen with membrane lipids: lipid hydroperoxide generation, translocation, reductive turnover, and signaling activity. *Singlet Oxyg Appl Biosci Nanosci* 2016;1:409.
- [42] Starik AM, Titova NS, Sharipov AS. Kinetic mechanism of H₂-O₂ ignition promoted by singlet oxygen O₂. *Deflagrative Detonative Combust Torus Press Mosc* 2010:19–42.
- [43] Gerasimov GY, Shatalov OP. Numerical Modeling of the Ignition of Hydrogen–Oxygen Mixtures Under Nonequilibrium Conditions. *J Eng Phys Thermophys* 2014;87:1063–1070.
- [44] Chukalovsky AA, Rakhimova TV, Klopovsky KS, Popov NA, Mankelevich YA, Proshina OV. Specific features of the kinetics of H₂-O₂-O₂ mixtures: I. formation and quenching of electronically and vibrationally excited (A') molecules in H₂-O₂-O₂ mixtures at a temperature of 300 K. *Plasma Phys Rep* 2014;40:34–51.
- [45] Chukalovsky AA, Klopovsky KS, Liberman MA, Mankelevich YA, Popov NA, Proshina OV, et al. Study of singlet delta oxygen O₂ impact on H₂-O₂ mixture ignition in flow reactor: 2D modeling. *Combust Sci Technol* 2012;184:1768–1786.
- [46] Starik AM, Kuleshov PS, Sharipov AS, Titova NS. Kinetics of Ignition and Combustion in the Al-CH₄-O₂ System. *Energy Fuels* 2014;28:6579–6588.
- [47] Starik AM, Titova NS. Possibility of Initiation of Combustion of CH₄-O₂ (Air) Mixtures with Laser-Induced Excitation of O₂ Molecules. *Combust Explos Shock Waves* 2004;40:499–510.



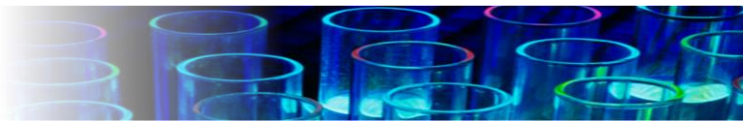
- [48] Shi R, Wang CH, Chang YN. The Influence of Singlet Oxygen and Ozone on the Combustion in Methane-Air Mixture. *Adv. Mater. Res.*, vol. 699, Trans Tech Publ; 2013, p. 111–118.
- [49] Sharipov AS, Starik AM. Kinetic mechanism of CO–H₂ system oxidation promoted by excited singlet oxygen molecules. *Combust Flame* 2012;159:16–29.
- [50] Li J, Li Z, Yang Y, Kong B, Wang C. Laboratory study on the inhibitory effect of free radical scavenger on coal spontaneous combustion. *Fuel Process Technol* 2018;171:350–60. doi:10.1016/j.fuproc.2017.09.027.
- [51] Redmond RW, Kochevar IE. Spatially resolved cellular responses to singlet oxygen. *Photochem Photobiol* 2006;82:1178–1186.
- [52] Schweitzer C, Schmidt R. Physical mechanisms of generation and deactivation of singlet oxygen. *Chem Rev* 2003;103:1685–1758.
- [53] Pimenta FM, Jensen RL, Holmegaard L, Esipova TV, Westberg M, Breitenbach T, et al. Singlet-oxygen-mediated cell death using spatially-localized two-photon excitation of an extracellular sensitizer. *J Phys Chem B* 2012;116:10234–10246.
- [54] Atkins P, De Paula J. *Atkins' physical chemistry*. N Y 2006:77.
- [55] Minaev BF. Spin-orbit coupling mechanism of singlet oxygen quenching by solvent vibrations. *Chem Phys* 2017;483:84–95.
- [56] Rodgers, T. Snowden. Lifetime of ¹O₂ in Liquid Water As Determined by Time-Resolved Infrared Luminescence Measurements 1982.
- [57] Clark ID, Wayne RP. The reaction of O₂ with atomic nitrogen and with atomic oxygen. *Chem Phys Lett* 1969;3:405–407.
- [58] Izod TPJ, Wayne RP. The Formation, Reaction and Deactivation of ¹O₂. *Proc. R. Soc. Lond. Math. Phys. Eng. Sci.*, vol. 308, The Royal Society; 1968, p. 81–94.
- [59] Clennan EL, Pace A. Advances in singlet oxygen chemistry. *Tetrahedron* November 7;61:6665–91. doi:10.1016/j.tet.2005.04.017.
- [60] Nonell S, Flors C. *Singlet Oxygen: Applications in Biosciences and Nanosciences*. Royal Society of Chemistry; 2016.



- [61] Albin A, Fagnoni M. Handbook of synthetic photochemistry. John Wiley & Sons; 2009.
- [62] Wasserman E, Kuck VJ, Delavan WM, Yager WA. Electron paramagnetic resonance of DELTA oxygen produced by gas-phase photosensitization with naphthalene derivatives. *J Am Chem Soc* 1969;91:1040–1041.
- [63] Clennan EL. Synthetic and mechanistic aspects of 1, 3-diene photooxidation. *Tetrahedron* 1991;47:1343–1382.
- [64] Bartlett PD, Mendenhall GD, Schaap AP. Competitive Modes Of Reaction Of Singlet Oxygen*. *Ann N Y Acad Sci* 1970;171:79–88.
- [65] Gollnick K, Griesbeck A. Interactions of singlet oxygen with 2, 5-dimethyl-2, 4-hexadiene in polar and non-polar solvents evidence for a vinyllog ene-reaction. *Tetrahedron* 1984;40:3235–3250.
- [66] Griesbeck AG, Oelgemöller M, Ghetti F. *CRC Handbook of Organic Photochemistry and Photobiology*. vol. 1. CRC Press; 2012.
- [67] Aubry J-M, Mandard-Cazin B, Rougee M, Bensasson RV. Kinetic studies of singlet oxygen [4+ 2]-cycloadditions with cyclic 1, 3-dienes in 28 solvents. *J Am Chem Soc* 1995;117:9159–9164.
- [68] Aubry J-M, Pierlot C, Rigaudy J, Schmidt R. Reversible binding of oxygen to aromatic compounds. *Acc Chem Res* 2003;36:668–675.
- [69] Packer L, Sies H. *Singlet Oxygen, UV-A, and Ozone*. Academic Press; 2000.
- [70] Pyryaeva AP, Goldort VG, Kochubei SA, Baklanov AV. Singlet oxygen O₂ formation via UV-excitation of isoprene-oxygen C₅ H₈-O₂ encounter complexes in gas phase. *Chem Phys Lett* 2014;610:8–13.
- [71] Eisenberg WC, Snelson A, Butler R, Veltman J, Murray RU. Gas phase generation of singlet oxygen at atmospheric pressure. *Tetrahedron Lett* 1981;22:377–380.
- [72] Bartusik D, Aebischer D, Ghafari B, Lyons AM, Greer A. Generating singlet oxygen bubbles: A new mechanism for gas-liquid oxidations in water. *Langmuir* 2012;28:3053–3060.



- [73] Wainwright M. Photosensitisers and Photosensitisation. *Photosensit Biomed*, 2009, 27–41.
- [74] Wainwright M. *Photosensitisers in biomedicine*. John Wiley & Sons; 2009.
- [75] DeRosa MC, Crutchley RJ. Photosensitized singlet oxygen and its applications. *Coord Chem Rev* 2002;233:351–371.
- [76] Foote CS, Wexler S. Singlet oxygen. A probable intermediate in photosensitized autoxidations. *J Am Chem Soc* 1964;86:3880–3881.
- [77] Foote CS. Photosensitized oxygenations and the role of singlet oxygen. *Acc Chem Res* 1968;1:104–110.
- [78] Takizawa S, Aboshi R, Murata S. Photooxidation of 1, 5-dihydroxynaphthalene with iridium complexes as singlet oxygen sensitizers. *Photochem Photobiol Sci* 2011;10:895–903.
- [79] Bhatnagar S, Kumar A, Ameta SC. Photooxidation of Some Pharmaceutical Drugs by Singlet Molecular Oxygen. *Asian J Pharm Biol Res* 2011;1:210–217.
- [80] Weishaupt KR, Gomer CJ, Dougherty TJ. Identification of singlet oxygen as the cytotoxic agent in photo-inactivation of a murine tumor. *Cancer Res* 1976;36:2326–2329.
- [81] De la Cruz N, Giménez J, Esplugas S, Grandjean D, De Alencastro LF, Pulgarin C. Degradation of 32 emergent contaminants by UV and neutral photo-fenton in domestic wastewater effluent previously treated by activated sludge. *Water Res* 2012;46:1947–1957.
- [82] Kochevar IE, Redmond RW. [2] Photosensitized production of singlet oxygen. *Methods Enzymol* 2000;319:20–28.
- [83] Loponov KN, Lopes J, Barlog M, Astrova EV, Malkov AV, Lapkin AA. Optimization of a scalable photochemical reactor for reactions with singlet oxygen. *Org Process Res Dev* 2014;18:1443–1454.
- [84] Gollnick K. Type II photooxygenation reactions in solution. *Adv Photochem* 1968;6.
- [85] Ludvíková L, Friš P, Heger D, Šebej P, Wirz J, Klán P. Photochemistry of rose bengal in water and acetonitrile: a comprehensive kinetic analysis. *Phys Chem Chem Phys* 2016;18:16266–16273.



- [86] Chesneau E, Neckers DC. Electron transfer sensitized photobleaching of rose bengal induced by triplet benzophenones. *J Photochem Photobiol Chem* 1988;42:269–281.
- [87] Zhang X-F, Zhang I, Liu L. Photophysics of halogenated fluoresceins: involvement of both intramolecular electron transfer and heavy atom effect in the deactivation of excited states. *Photochem Photobiol* 2010;86:492–498.
- [88] Hasty N, Merkel PB, Radlick P, Kearns DR. Role of azide in singlet oxygen reactions: Reaction of azide with singlet oxygen. *Tetrahedron Lett* 1972;13:49–52.
- [89] Wayne RP. Singlet molecular oxygen. *Adv Photochem* 1969;7:1.
- [90] Nosaka Y, Nosaka AY. Generation and Detection of Reactive Oxygen Species in Photocatalysis. *Chem Rev* 2017;117:11302–36. doi:10.1021/acs.chemrev.7b00161.
- [91] Noimark S, Salvadori E, Gómez-Bombarelli R, J. MacRobert A, P. Parkin I, M. Kay CW. Comparative study of singlet oxygen production by photosensitiser dyes encapsulated in silicone: towards rational design of anti-microbial surfaces. *Phys Chem Chem Phys* 2016;18:28101–9. doi:10.1039/C6CP02529C.
- [92] Lambert C, Sarna T, Truscott TG. Rose bengal radicals and their reactivity. *J Chem Soc Faraday Trans* 1990;86:3879–3882.
- [93] Seliger HH. A photoelectric method for the measurement of spectra of light sources of rapidly varying intensities. *Anal Biochem* 1960;1:60–65.
- [94] Khan AU, Kasha M. Chemiluminescence arising from simultaneous transitions in pairs of singlet oxygen molecules. *J Am Chem Soc* 1970;92:3293–3300.
- [95] Yuryshev NN. Chemically pumped oxygen—iodine laser. *Quantum Electron* 1996;26:567–84. doi:10.1070/QE1996v026n07ABEH000730.
- [96] Kanofsky JR. Singlet oxygen production by biological systems. *Chem Biol Interact* 1989;70:1–28.
- [97] Murray RW, Lumma Jr WC, Lin JWP. Singlet oxygen sources in ozone chemistry. Decomposition of oxygen-rich intermediates. *J Am Chem Soc* 1970;92:3205–3207.
- [98] Di Mascio P, Sies H. Quantification of singlet oxygen generated by thermolysis of 3,3'-(1,4-naphthylene)dipropionate endoperoxide. Monomol and dimol photoemission and the



effects of 1,4-diazabicyclo[2.2.2]octane. *J Am Chem Soc* 1989;111:2909–14. doi:10.1021/ja00190a027.

[99] Pierlot C, Aubry J-M, Briviba K, Sies H, Di Mascio P. [1] Naphthalene endoperoxides as generators of singlet oxygen in biological media. *Methods Enzymol* 2000;319:3–20.

[100] Khan AU. Singlet molecular oxygen from superoxide anion and sensitized fluorescence of organic molecules. *Science* 1970;168:476–477.

[101] Aubry JM. Search for singlet oxygen in the decomposition of hydrogen peroxide by mineral compounds in aqueous solutions. *J Am Chem Soc* 1985;107:5844–9. doi:10.1021/ja00307a002.

[102] Böhme K, Brauer HD. Generation of singlet oxygen from hydrogen peroxide disproportionation catalyzed by molybdate ions. *Inorg Chem* 1992;31:3468–3471.

[103] Foote CS, Wexler S, Ando W, Higgins R. Chemistry of singlet oxygen. IV. Oxygenations with hypochlorite-hydrogen peroxide. *J Am Chem Soc* 1968;90:975–981.

[104] Foote CS, Clennan EL. Properties and reactions of singlet dioxygen. *Act. Oxyg. Chem.*, Springer; 1995, p. 105–140.

[105] Boikov EV, Vishnetskaya MV, Emel'yanov AN, Rufov YN, Shcherbakov NV, Tomskii IS. Singlet oxygen in the heterogeneous catalytic oxidation of benzene. *Russ J Phys Chem A* 2007;81:861–5. doi:10.1134/S0036024407060052.

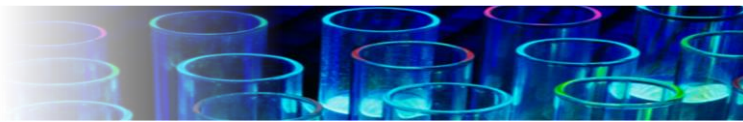
[106] Boikov EV, Vishnetskaya MV, Emel'yanov AN, Tomskii IS, Shcherbakov NV. The selective catalytic oxidation of toluene. *Russ J Phys Chem Focus Chem* 2008;82:2233–2237.

[107] Tomskii IS, Vishnetskaya MV, Kokorin AI. The partial catalytic oxidation of toluene on vanadium and molybdenum oxides. *Russ J Phys Chem B Focus Phys* 2008;2:562–567.

[108] Tomskii IS, Vishnetskaya MV, Rufov YN. The oxidation of toluene on transition metal oxides. *Russ J Phys Chem A* 2009;83:1868–1872.

[109] Ruzzi M, Sartori E, Moscatelli A, Khudyakov IV, Turro NJ. Time-resolved EPR study of singlet oxygen in the gas phase. *J Phys Chem A* 2013;117:5232–5240.

[110] Moscatelli A. Part I. Interactions between singlet (Δ) oxygen and nitroxides as seen by electron paramagnetic resonance methods: Quenching, chemically induced electron spin



polarization, and applications in oximetry. Part II. Photolysis of dibenzylketones sorbed in MFI zeolite in the presence of spectator molecules: Cage effect, kinetics and external surface sites characterization. COLUMBIA UNIVERSITY, 2008.

[111] Hunger M, Weitkamp J. In situ IR, NMR, EPR, and UV/Vis spectroscopy: Tools for new insight into the mechanisms of heterogeneous catalysis. *Angew Chem Int Ed* 2001;40:2954–2971.

[112] Kearns DR, Khan AU, Duncan CK, Maki AH. Detection of the naphthalene-photosensitized generation of singlet (DELTA) oxygen by paramagnetic resonance spectroscopy. *J Am Chem Soc* 1969;91:1039–1040.

[113] Snelling DR. Production of singlet oxygen in the benzene oxygen photochemical system. *Chem Phys Lett* 1968;2:346–348.

[114] Qi H, Dong X, Zhao Y, Li N, Fu H, Feng D, et al. ROS production in homogenate from the body wall of sea cucumber *Stichopus japonicus* under UVA irradiation: ESR spin-trapping study. *Food Chem* 2016;192:358–362.

[115] Yaghini E, Pirker KF, Kay CW, Seifalian AM, MacRobert AJ. Quantification of Reactive Oxygen Species Generation by Photoexcitation of PEGylated Quantum Dots. *Small* 2014;10:5106–5115.

[116] Han SK, Hwang T-M, Yoon Y, Kang J-W. Evidence of singlet oxygen and hydroxyl radical formation in aqueous goethite suspension using spin-trapping electron paramagnetic resonance (EPR). *Chemosphere* 2011;84:1095–1101.

[117] Nardello V, Brault D, Chavalle P, Aubry J-M. Measurement of photogenerated singlet oxygen ($^1\text{O}_2$ ($^1\Delta_g$)) in aqueous solution by specific chemical trapping with sodium 1, 3-cyclohexadiene-1, 4-diethanoate. *J Photochem Photobiol B* 1997;39:146–155.

[118] Burns JM, Cooper WJ, Ferry JL, King DW, DiMento BP, McNeill K, et al. Methods for reactive oxygen species (ROS) detection in aqueous environments. *Aquat Sci* 2012;74:683–734.

[119] Healey P. Instrumentation principles for optical time domain reflectometry. *J Phys [E]* 1986;19:334.



- [120] Lakowicz JR. Principles of fluorescence spectroscopy. Springer Science & Business Media; 2013.
- [121] Kummler RH, Bortner MH. Production of O₂ (DELTA) by energy transfer from excited benzaldehyde. *Environ Sci Technol* 1969;3:944–946.
- [122] Starik AM, Kozlov VE, Titova NS. On the influence of singlet oxygen molecules on the speed of flame propagation in methane–air mixture. *Combust Flame* 2010;157:313–27. doi:10.1016/j.combustflame.2009.11.008.
- [123] Starik AM, Kozlov VE, Titova NS. On mechanisms of a flame velocity increase upon activation of O₂ molecules in electrical discharge. *J Phys Appl Phys* 2008;41:125206.
- [124] Ó Conaire M, Curran HJ, Simmie JM, Pitz WJ, Westbrook CK. A comprehensive modeling study of hydrogen oxidation. *Int J Chem Kinet* 2004;36:603–622.
- [125] Bourig A, Thévenin D, Martin J-P, Janiga G, Zähringer K. Numerical modeling of H₂–O₂ flames involving electronically-excited species O₂ (¹Δ_g), O (¹D) and OH (²Σ⁺). *Proc Combust Inst* 2009;32:3171–3179.
- [126] Starikovskiy A, Aleksandrov N. Plasma-assisted ignition and combustion. *Prog Energy Combust Sci* 2013;39:61–110.
- [127] Washington DA, Shapiro HN. A Phenomenological Analysis of Exergy Destruction During Hydrogen Combustion With Electronically Excited Oxygen. ASME 2013 Power Conf., American Society of Mechanical Engineers; 2013, p. V001T01A024–V001T01A024.
- [128] Starik AM, Kozlov VE, Titova NS. On the influence of singlet oxygen molecules on characteristics of HCCI combustion: A numerical study. *Combust Theory Model* 2013;17:579–609. doi:10.1080/13647830.2013.783238.
- [129] Wu Z, Kang Z, Deng J, Hu Z, Li L. Effect of oxygen content on n-heptane auto-ignition characteristics in a HCCI engine. *Appl Energy* 2016;184:594–604. doi:10.1016/j.apenergy.2016.10.050.
- [130] Starik AM, Titova NS. On a possibility to reduce the ignition threshold for combustible mixtures by selective excitation of molecular vibrations in initial reagents. *Dokl. Phys.*, vol. 45, Springer; 2000, p. 5–10.



- [131] Starik AM, Titova NS. Kinetics of detonation initiation in the supersonic flow of the $\text{H}_2 + \text{O}_2$ (air) mixture in O_2 molecule excitation by resonance laser radiation. *Kinet Catal* 2003;44:28–39.
- [132] Smirnov VV, Stelmakh OM, Fabelinsky VI, Kozlov DN, Starik AM, Titova NS. On the influence of electronically excited oxygen molecules on combustion of hydrogen–oxygen mixture. *J Phys Appl Phys* 2008;41:192001.
- [133] Won TOSH, Ju Y, Williams S. Lifted flame speed enhancement by plasma excitation of oxygen 2009.
- [134] Ombrello T, Sun W, Won SH, Ju Y, Williams S, Carter C. Mechanisms of Kinetic Combustion Enhancement by O_2 ($^1\Delta_g$). 48th AIAA Aerosp. Sci. Meet. New Horiz. Forum Aerosp. Expo., 2010, p. 1586.
- [135] Ombrello T, Won SH, Ju Y, Williams S. Flame propagation enhancement by plasma excitation of oxygen. Part II: Effects of O_2 ($^1\Delta_g$). *Combust Flame* 2010;157:1916–1928.
- [136] Cheikh F, Boucekkine A, Cartier A. Computational study of the addition of molecular oxygen to benzene. *J Mol Struct THEOCHEM* 1997;397:13–20.
- [137] Bobrowski M, Liwo A, Oldziej S, Jeziorek D, Ossowski T. CAS MCSCF/CAS MCQDPT2 study of the mechanism of singlet oxygen addition to 1, 3-butadiene and benzene. *J Am Chem Soc* 2000;122:8112–8119.
- [138] Wang J, Yang B, Li Y, Tian Z, Zhang T, Qi F, et al. The tunable VUV single-photon ionization mass spectrometry for the analysis of individual components in gasoline. *Int J Mass Spectrom* 2007;263:30–37.
- [139] Battin-Leclerc F. Detailed chemical kinetic models for the low-temperature combustion of hydrocarbons with application to gasoline and diesel fuel surrogates. *Prog Energy Combust Sci* 2008;34:440–498.
- [140] Starik AM, Titova NS. Low-temperature initiation of the detonation combustion of gas mixtures in a supersonic flow under excitation of the O_2 ($^1\Delta_g$) state of molecular oxygen. *Dokl. Phys.*, vol. 46, Springer; 2001, p. 627–632.
- [141] Lebedev AV, Deminsky MA, Zaitzevsky AV, Potapkin BV. Effect of O_2 ($^1\Delta_g$) on the low-temperature mechanism of CH_4 oxidation. *Combust Flame* 2013;160:530–538.

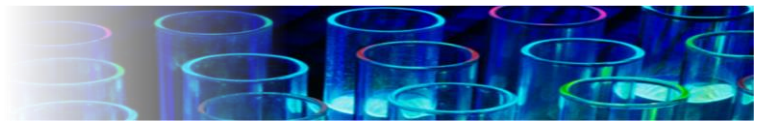


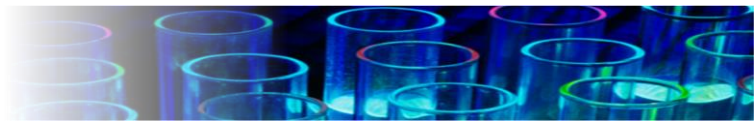
- [142] Starik AM, Kozlov VE, Titova NS. On the influence of singlet oxygen molecules on the speed of flame propagation in methane–air mixture. *Combust Flame* 2010;157:313–327.
- [143] Schmidt C, Schiff HI. Reactions of $O_2 (^1\Delta_g)$ with atomic nitrogen and hydrogen. *Chem Phys Lett* 1973;23:339–42. doi:10.1016/0009-2614(73)85092-4.
- [144] Starik AM, Pelevkin AV, Titova NS. Modeling study of the acceleration of ignition in ethane–air and natural gas–air mixtures via photochemical excitation of oxygen molecules. *Combust Flame* 2017;176:81–93. doi:10.1016/j.combustflame.2016.10.005.
- [145] Sharipov AS, Starik AM. Kinetic mechanism of $CO-H_2$ system oxidation promoted by excited singlet oxygen molecules. *Combust Flame* 2012;159:16–29. doi:10.1016/j.combustflame.2011.06.015.
- [146] Sayós R, Oliva C, González M. Ab initio CASPT2//CASSCF study of the $O(^1D)+H_2O$ reaction. *J Chem Phys* 2001;115:8828–37. doi:10.1063/1.1408298.
- [147] Gonzalez C, Theisen J, Zhu L, Schlegel HB, Hase WL, Kaiser EW. Kinetics of the reaction between hydroxyl and hydroperoxyl on the singlet potential energy surface. *J Phys Chem* 1991;95:6784–92. doi:10.1021/j100171a010.
- [148] Starik AM, Loukhovitski BI, Sharipov AS, Titova NS. Intensification of shock-induced combustion by electric-discharge-excited oxygen molecules: Numerical study. *Combust Theory Model* 2010;14:653–79. doi:10.1080/13647830.2010.499966.
- [149] Starik AM, Savelieva VA, Sharipov AS, Titova NS. Enhancement of hydrogen sulfide oxidation via excitation of oxygen molecules to the singlet delta state. *Combust Flame* 2016;170:124–34. doi:10.1016/j.combustflame.2016.05.014.
- [150] Zhou C-W, Simmie JM, Somers KP, Goldsmith CF, Curran HJ. Chemical Kinetics of Hydrogen Atom Abstraction from Allylic Sites by 3O_2 ; Implications for Combustion Modeling and Simulation. *J Phys Chem A* 2017;121:1890–9. doi:10.1021/acs.jpca.6b12144.
- [151] Zeinali N, Altarawneh M, Li D, Al-Nu'airat J, Dlugogorski BZ. New Mechanistic Insights: Why Do Plants Produce Isoprene? *ACS Omega* 2016;1:220–225.
- [152] Stracher GB, Taylor TP. Coal fires burning out of control around the world: thermodynamic recipe for environmental catastrophe. *Int J Coal Geol* 2004;59:7–17.
- [153] Ham B. A review of spontaneous combustion incidents 2005.



[154] Cliff D, Brady D, Watkinson M. Developments in the Management of Spontaneous Combustion in Australian Underground Coal Mines 2014.

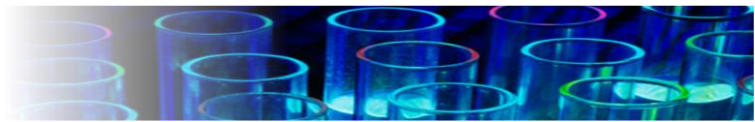
Jomana Al-Nu'airat





Chapter 3

Methodology





3.1 Experimental Configurations

3.1.1 Overview of experimental techniques

The experimental work of this thesis illustrates two main research investigations. The first investigation explores the effect of iron (III) oxide nanoparticles, a mediating surface for the formation of ROS (singlet oxygen $O_2(^1\Delta_g)$, superoxide anion ($O_2^{\cdot-}$), and hydroxyl ($HO\cdot$)), on the combustion of coal surrogate, i.e., anisole, identifying the changes in ignition features as well as the occurrence of persistent organic pollutants in the initiation channels. The method applies packed-bed reactor coupled with Fourier transform infrared spectroscopy (FTIR) to quantitate the ignition temperatures under typical fuel-rich conditions, in-situ electron paramagnetic resonance (EPR) to elucidate the formation of environmentally-persistent free radicals (EPFR), diffuse reflectance infrared Fourier transform spectroscopy (DRIFTS) to monitor the chemisorption of organic substrates on the nanoparticles, as well as X-ray diffraction for particles characterisation.

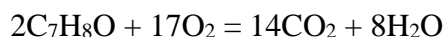
The second investigation studies the reaction mechanisms governing the ROS (singlet oxygen $O_2(^1\Delta_g)$ and superoxide anion ($O_2^{\cdot-}$)) with important hydrocarbons, i.e., phenol and alloxan, respectively, in aqueous media. Phenol represents a biodegradable-resistant species persisting in waste water, while alloxan remains a heterocyclic derivative of pyrimidine with relevant application in biological systems. The phenol-experiments combine customised LED-photoreactors with known initial concentration of phenol and $O_2(^1\Delta_g)$ produced continuously in situ from bubbled triplet oxygen $O_2(^3\Sigma_g^-)$ employing rose bengal as a sensitiser. We identify and quantitate the intermediate and product species as a function of time from UV-Vis and high-performance liquid chromatography (HPLC) analyses. The electron paramagnetic



resonance (EPR) measurements confirmed the appearance of radical species. Nonetheless, combined in situ EPR imaging and broad-scan UV-Vis spectroscopy illuminate the mechanistic pathways governing the alloxan–GSH redox cycle by identifying major products as well as main intermediate radicals of the reaction. The sections below provide concise description of each of the experimental settings. However, subsequent chapters present relatively more detailed accounts.

3.1.2 Tubular packed-bed reactor setup

Figure 3.1a illustrates the bench-scale packed-bed reactor in which a digital syringe pump released the fuel surrogate (anisole; purity > 99.0%, $1.32 - 0.45 \mu\text{L min}^{-1}$) into the preheated combined stream of N_2 and synthetic air (SA) flowing through the system at between 102 and 295 mL min^{-1} (at STP, NIST). Anisole concentration in the diluted stream amounted to 1000 ppm on molar basis. We centred a bed consisting of 200 mg hematite nanoparticles ($\alpha\text{-Fe}_2\text{O}_3$, Sigma-Aldrich, 99.98 %, < 50 nm) inside the quartz reactor tube and placed the tube into an electrically heated three-zone horizontal furnace with the bed located in a well-defined isothermal reaction zone (cf. Figure 3.1a, zone 2, 300 mm). To maintain an exact residence time, the volume (estimated from mass and density) of the Fe_2O_3 nanoparticle was controlled by adjusting the inner rods (9.5 mm OD) of the reactor. We metered the flow of N_2 and SA corresponding to oxygen-fuel equivalent ratio λ of 0.8 (i.e., moderately fuel rich condition, also expressed as the fuel-oxygen equivalence ratio Φ of 1.25) based on the stoichiometry of Equation 3.1.



The premixed charge of the fuel and oxidiser entered the reaction zone under ambient pressure, amounting to a constant residence time of 2.0 s. Charles' temperature-volume relationship served to adjust the gas flow rates metered by the mass flow controllers (MFC, operated at the room temperature) with the gases preheated just before the reactor entry. Similarly, we employed a mass balance to convert the flow rate of the fuel needed for the predefined concentration at isothermal reaction temperature, into the corresponding set-values at room temperature.

An online Fourier transform infrared (FTIR) spectroscopy monitored the gaseous product species exiting the tubular reactor. The reactor was linked via an electrically heated transfer line (3.175 mm ID×300 mm) to a small volume (100 mL) 2.4 m path-length online gas-sampling cell (Pike) placed inside an FTIR compartment. Both the sample line and the sampling cell remained at 170 °C, to eliminate condensation of volatile products prior and during the analysis, and adequate to vaporise the reactant (anisole) which boils at 154°C. The spectrometer averaged 64 accumulated scans per spectrum at 1 cm⁻¹ resolution. The nanoparticle residues, as well as the neat control sample, were tested using X-ray powder diffraction (PXRD) technique on GBC eMMA instrument. The PXRD method operated within the scanning angle (2θ) range of 10 ° - 70 °, at a regular step size of 0.010 ° and speed of 1° min⁻¹, using a Ni filtered Cu Kα1 radiation (λ = 1.5406 Å). The voltage and current settings corresponded to 35 kV and 28 mA, respectively.



3.1.3 Electron paramagnetic resonance

EPR (Bruker EMX Plus 10/2.7) coupled to a high-temperature cavity (ER4114HT) equipped with cooling-side plates facilitated the in-situ detection of the formation of phenoxy radicals on α -Fe₂O₃ surface during its reaction with anisole. The EPR spectra represent the average of 5 scans at a resonant frequency of 9.76 GHz. The spectrometer operated at the following settings: microwave power of 20 mW, modulation frequency of 100 kHz, modulation amplitude of 3 G, sweep width of 3000 G, time constant of 0.01 ms, conversion time of 50 ms, sweep time of 100 s, receiver gain of 2×10^5 , 10000 number of data points, and a centre field of 3000.0 G. As shown in Figure 3.1, we applied a custom vacuum exposure system to allow anisole vapour to enter the critically-coupled cavity chamber at a pre-set temperature.

3.1.4 Diffuse reflectance infrared Fourier transform spectroscopy

Agilent Cary 670 FTIR spectrometer combined with a gas-purged PIKE Technologies DiffusIR accessory with gold-coated optical components served to study the surface reaction of anisole on α -Fe₂O₃ nanoparticles. We conducted the experiments under steady conditions and temperature-based total gas flow rate of 100 mL min⁻¹, adjusting the pump rate of anisole, synthetic air and N₂ to oxygen-fuel equivalent ratio $\lambda=0.8$ based on Equation 3.1. The sample preparation step applied potassium bromide (KBr) powder as a spectroscopically-pure matrix to dilute the α -Fe₂O₃ nanoparticles to 2 % (w/w). We employed vortex mixing to enhance the particle size consistency. Portions of 50 mg of the resulting samples were placed inside the environment chamber, sealed with zinc selenide (ZnSe) window, heated up to the desired



temperature, before pumping anisole into the preheated stream of the carrier gases. The spectrometer operated at 4 cm^{-1} , averaged 24 accumulated scans per spectrum, resulting in temporal resolution of 55 s on mercury cadmium telluride (MCT) detector.

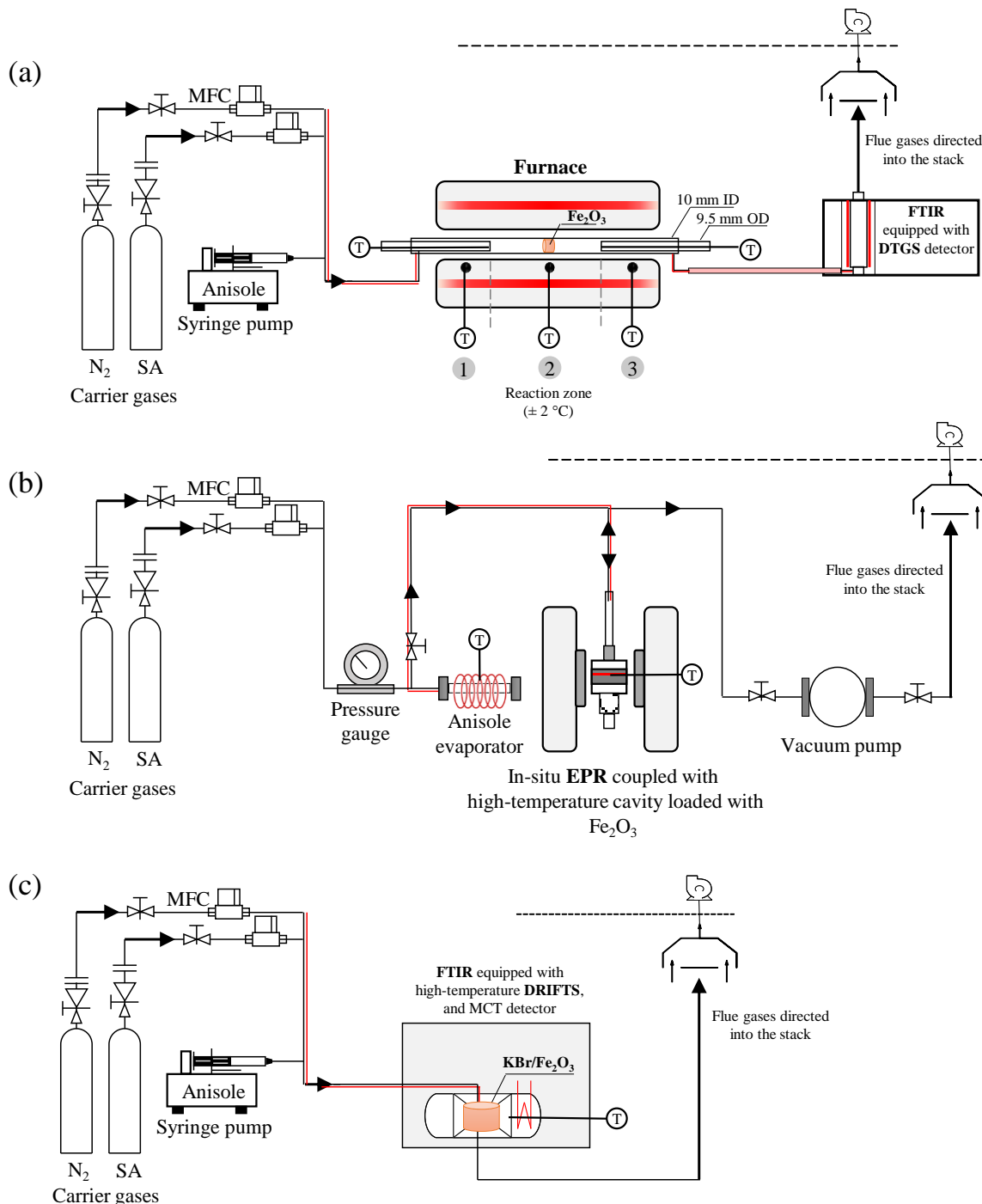


Figure 3.1. Schematic of experimental packed-bed reactor (a), EPR (b), and DRIFTS (c) setups. All data are logged automatically via computer systems.



3.1.5 Photo-reactors

The relevant chapters record the identity, purity and sources of chemicals used in the reaction of ROS with hydrocarbons in aqueous systems. This study deployed LEDs as a light source because LED lamps exhibit the most effective operation, with the efficiency of photo-oxygenated system attaining 70 % of the emitted light.[1] Figure 3.2 illustrates the photo-reactor, employing 24 green LEDs ($4.5 \times 10 \times 500$ mm) operated between 7 and 24 V. The LEDs form 0.1 m long illuminating zone, assembled from 8 strips, each consisting of 3 units. We uniformly mounted the strips onto the inside of a white PVC tube casing that surrounds the reactor. The dead-zone thickness between the LED units in a single strip amounted to 0.68 cm, based on a 120° beam angle, prompting us to centre the quartz reactor 1 cm away from the PVC holder.

Again, EPR spectrometer served to quantitate the concentration of spin-trapped singlet oxygen, as well as to monitor in situ the appearance of radical species. Chemical spin traps represent highly reactive species that capture singlet oxygen by forming a stable compound (endoperoxide), detectable by the EPR spectrometry. We placed the samples in a 10.5 mm flat cell (WG-812-Q), and bubbled the oxygen, in He carrier gas, for a least 20 min. Figure 3.3 illustrates a LED light fixed on a wooden holder, to prevent metallic interference with the magnetic field, that irradiated the sample in situ; i.e., inside the EPR resonator cavity. The spectrometer functioned at the same parameter settings as mentioned in Section 3.1.3.

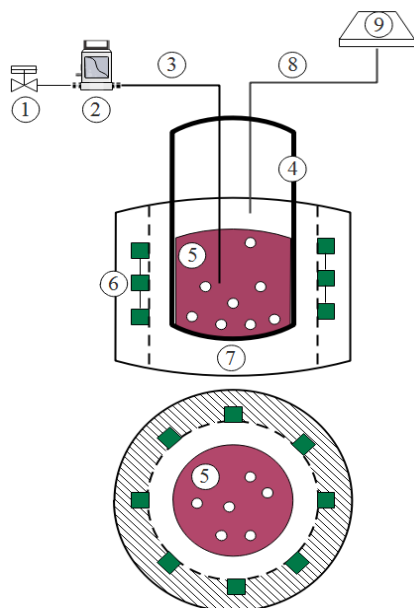


Figure 3.2. Schematic diagram of photochemical reactor shown in side and cross-sections. 1: O₂/He (3 %) valve, 2: mass flow controller, 3: inlet gas, 4: Pyrex reactor, 5: phenol dyed solution (pH = 6), 6: LED strip (7 V), 7: PVC holder, 8: off-gas outlet, 9: exhaust.

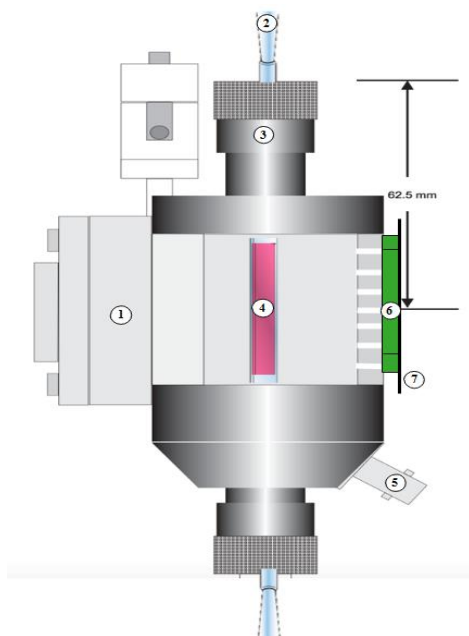


Figure 3.3. In-situ EPR photoreactor schematic; 1: EPR resonator, 2: WG-812-Q quartz flat cell, 3: collet nut, 4: dyed sample, 5: modulation cable, 6: green LED (24 V), 7: wooden support.



3.1.6 Analytical HPLC and UV-Vis techniques

Shimadzu HPLC equipped with a C18 analytical column (4.6 mm diameter and 150 mm length) and controlled by the data acquisition software served to quantitate the conversion of phenol and the yields of the reaction products from the LED photo-reactor. The analytical method involved an injection of samples of 10 μL in volume and maintaining the oven temperature 30 $^{\circ}\text{C}$. The mobile phase comprised solution of 0.01 mol L^{-1} phosphate buffer (pH 4.5), methanol and tetrahydrofuran (THF) in the ratio of 90:5:5, v/v, flowing at a rate of 1 mL min^{-1} , under low-pressure condition. The analyte eluted into a UV-Vis detector operating at 254 nm using a reversed phase elution mode. Furthermore, we obtained the absorption spectra of RB, phenol, hydroquinone, benzoquinone, and 1,10-phenanthroline (actinometry experiment) in a quartz cell (1 cm pathlength) using Agilent Carry 5000 UV-Vis-NIR spectrophotometer operated at a resolution of 1 nm.

In addition to EPR, broad-scan UV-Vis spectroscopy also served to identify the major products, as well as the main intermediate radicals of alloxan – glutathione redox cycle. We obtained the glutathione and alloxan UV-Vis spectra using an Agilent Carry 5000 UV-Vis-NIR spectrophotometer operated at a resolution of 1 nm. For alloxan-glutathione solutions, phosphate buffers served to obtain the biological pH of 7.4 along with a pH of 6.4. We obtained the absorption profiles in situ by scanning the samples for time intervals of 0–10 h and corrected the baseline by subtracting the spectra of the corresponding blank buffer solutions. Sigma Aldrich supplied glutathione and alloxan with the highest commercial purity available of more than > 98%. For each experiment, we prepared fresh solutions containing alloxan or glutathione prior to analysis in a 25 $^{\circ}\text{C}$ temperature-controlled laboratory. We prepared all aqueous solutions for EPR, UV-Vis, and HPLC standards and mobile phases using ultrapure



water (resistivity $>18 \text{ M}\Omega \text{ cm}$), tapped from a Sartorius Arium Pro UV/DI water purification system.

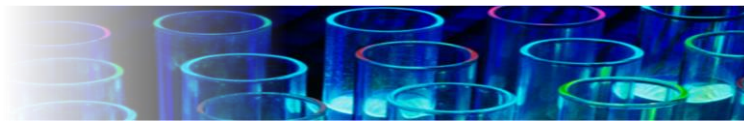
3.2 Computational Details

3.2.1 Overview of computational method

Some of the most fascinating techniques in all fields of science include the computational ab initio methods. The ab initio techniques predict the energy and optimum conformational structure of a molecule by solving the Schrödinger equation (Equation (3.2)), where Ψ represents the wavefunction, and m , h , and V denote the mass of particle, Planck's constant and the potential energy, respectively.

$$\left\{ -\frac{\hbar^2}{8\pi^2m} \nabla^2 + V \right\} \Psi(r, t) = \frac{i\hbar}{2\pi} \frac{\partial \Psi(r, t)}{\partial t} \quad (3.2)$$

Even with the most powerful computational tools at hand, the accuracy of the final molecular energy and configuration relies on the chosen level of theory. This dissertation applies the density functional theory (DFT) to map all essential reaction routes within the framework of DMol³ package [2] and the Gaussian 09 [3] suite of programs as enumerated below:



- i. DMol³ package [2] afforded all structural optimisations and energy calculations for the thermo-catalytic reaction of anisole over iron (III) oxide nanoparticles. The theoretical approach involved the generalised gradient approximation (GGA) of the Perdew–Burke–Ernzerhof (PBE) functional,[4] with the total energy convergence tolerance of 1×10^{-6} Ha. The electronic core treatment included all electrons and deployed a double numerical plus polarisation (DNP) basis set [5] and a global cut-off of 4.1 Å. The calculated energies were modified by the Tkatchenko and Scheffler [6] dispersion correction term so as to account for any non-bonding interactions in the investigated systems. All energetic values are reported at 298.15 K. The calculations involved a modelled dehydrated cluster of stoichiometric neutrally-charged α -Fe₆O₉, i.e., (Fe₂O₃)_{n=3} obtained from bulk α -Fe₂O₃. A recent ab initio atomistic thermodynamic study [7] illustrated that, the most stable termination of hematite surface, i.e. α -Fe₂O₃(0001), contains surface Fe-O bonds, which are also present in the considered cluster. Finally, the DMol³ code [8] facilitated the calculations of the Hirshfeld atomic charges [9] and the Fukui (f^1) indices [10]. The Fukui indices indicate the tendency of a molecular site to undergo an electrophilic addition. The choice of the Hirshfeld scheme stems from its superior performance in estimating atomic charges in reference to other approaches, such as the commonly deployed Mulliken population analysis[11] that often displays severe sensitivity to the implemented basis set.

- ii. The Gaussian 09 [3] suite of programs affords all structural optimisations and energy calculations ($\Delta^{\#}H^{\circ}_{298}$, $\Delta_r H^{\circ}_{298}$, $\Delta^{\#}G^{\circ}_{298}$, and $\Delta_r G^{\circ}_{298}$) for gaseous and aqueous reactions as covered in Chapters 4, 6, 7, and 8. The theoretical methodology comprises the gradient-corrected density functional theory (DFT) functionals B3LYP [12,13] and the



meta-hybrid M06 [14] functional, both, supplemented with the polarised basis set of 6-311+G(d,p).[15] For hydrogen abstraction reactions, mostly illustrated in chapter 8, the complex chemistry model of CBS-QB3 provides the most accurate estimates of geometries and enthalpies [16–19]. We model reactions in the aqueous phase by deploying the polarisable continuum model (PCM) with the dielectric constant (ϵ) equal to 78.39 at 298.15 K [20]. Furthermore, we perform intrinsic reaction coordinate (IRC) calculations, confirming the identity of each transition structure found and reported. Evaluation of rate constants and Arrhenius parameters is carried out by the KiSThelP code [21] within the temperature range of each study, based on the conventional transition state theory with the inclusion of a one dimensional Eckart barrier that accounts for contribution of the quantum-tunnelling effect.

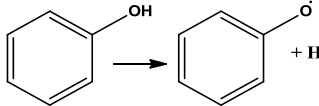
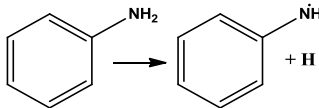
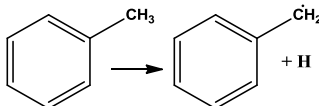
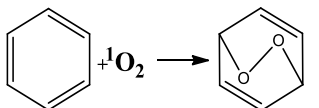
3.2.1 Error estimation of M062X, B3LYP, and CBS-QB3 approaches

In view of the biradical character that might mark the benzene, toluene, aniline, or phenol - O₂ (¹ Δ_g) systems, one must determine the spin state of intermediate and transition structures along the entire potential energy surface. Severe spin contamination necessitates energy refinements based on the approximate spin-projection scheme (AP) pioneered by Yamagushi's group.[22,23] Located transition structures and intermediates converge on a pure low-spin solution with zero-spin densities. Structural optimisations that involve fixing the frontier molecular orbitals, i.e., the broken symmetry solution allows assessing a plausible spin contamination by examining a value of the total spin angular momentum operator S^2 [24]. A value of this operator of near unity for high spin (HS) configuration indicates a significant spin contamination by the triplet state. We found the expected values of spin contamination



operator of all intermediates and transition structures to cluster close to zero. This means that, the benzene, toluene, aniline, or phenol - O₂(¹Δ_g) system exists in a genuine singlet ground LS state, eliminating the need for further energy refinement. However, the energy of the O₂(¹Δ_g) suffers from contamination by the group triplet state as evident from the value of the spin contamination operator S² (HS) of approximately 1. As such, we applied the AP approach to refine the energy O₂ (¹Δ_g).

Table 3.1. M062X energy error estimate in comparison with the experimental values of selected reactions

Species	Reaction	Calculated M062X (kJ mol ⁻¹)	Experimental [25,26] and theoretical (kJ mol ⁻¹) [27]	Absolute error (kJ mol ⁻¹)
Oxygen	$^3\text{O}_2 \longrightarrow ^1\text{O}_2$	103.2	94.6	8.5
Phenol		376.9	378.2±4.2 in solution	1.3
		365.7	368.2±6.3 in gas	2.5
Aniline		381.3	385.8 in solution	4.5
		377.1	375.3 in gas	2.2
Toluene		374.5	370.3±6.3	4.2
Benzene		116.6	116.5	0.1
Mean unsigned error (MUE) = 3.33				

We first assess the performance of several DFT methods at 298.15 K in calculating the enthalpy gap between singlet and triplet states ($\Delta_G H_{298}$) for selected diradical species, namely O, O₂, NH, NF, C, and Si. In the case of the oxygen molecule, M06 significantly overestimates the $\Delta_G H_{298}^{S-T}$ value by 37.7 kJ/mol, while B3LYP shows an excellent performance with only 8.5



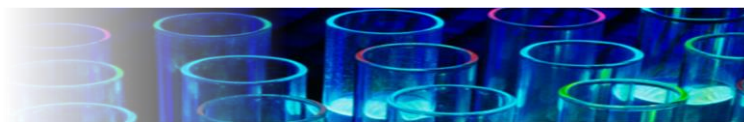
kJ/mol offset from the experimental value (94.6 kJ/mol) [25]. The noticeable difference in the $\Delta_G H_{298}^{S-T}$ value between the two methods confirms the relative accuracy of B3LYP in determining thermochemical values for oxygen. However, except for O_2 , M06 yields $\Delta_G H_{298}^{S-T}$ values that are closer to experimental measurements than those computed with B3LYP. B3LYP does, however, have some limitations in computing reaction barriers, with the M06 family of functionals delivering more satisfactory performance, well documented in literature [14,28]. Thus, in this investigation, we report reaction and activation energies for all considered reactions using the two methods but mainly M062X. Table 3.1 shows the energy error estimate based on the M062X level of theory of selected reaction illustrating a mean unsigned error of 3.33 kJ mol⁻¹. On the other hand, Table 3.2 presents the validation of the computational method for Chapter 8 (Alloxan – Glutathione Redox Cycle). We compared the values of both lengths and bond angles for the alloxan molecule, as computed from M062X, CBS-QB3 and CBS-QB3 (solvation) models with the results of experimental measurements. We selected the CBS-QB3 (solvation) model based on a mean unsigned errors (MUE) of 0.007 Å for bond length and 0.68° for bond angles.

**Table 3.2.** Validation of computational methods

	Distances (Å)	M06-2X	CBS-QB3		Experimental [29–32]	
		Gas	Gas	Solvation (PCM)		
	C(5)-O(5)	1.187	1.195	1.197	[1.198]	
	C(5)-C(4)	1.543	1.546	1.542	[1.529]; 1.537	
	C(4)-O(4)	1.194	1.201	1.206	[1.212]	
	C(4)-N(3)	1.384	1.388	1.378	[1.365]; 1.371	
	N(3)-C(2)	1.392	1.395	1.393	1.374	
	N(3)-H(3)	1.014	1.014	1.015	[1.021]	
	MUE	0.012	0.011	0.007		
	Angles (°)					
	C(4)-C(5)-O(5)	120.79	120.78	120.73	[120.7]	
	C(4)-C(5)-C(6)	118.42	118.44	118.55	[118.7]; 113.8	
	C(5)-C(4)-N(3)	114.61	114.56	114.69	[115.3]; 117.4	
	C(5)-C(4)-O(4)	122.10	122.36	121.64	[120.8]; 121.7	
	N(3)-C(4)-O(4)	123.29	123.08	123.67	[123.9]	
	C(4)-N(3)-C(2)	128.43	128.63	128.14	[126.5]; 126.7	
	C(4)-N(3)-H(3)	116.87	116.71	117.08	[117.9]; 118.0	
C(4)-N(3)-H(3)	114.70	114.65	114.79	[115.5]		
N(3)-C(2)-O(2)	122.25	122.41	122.09	[121.1]; 121.4		
N(3)-C(2)-N(1)	115.49	115.18	115.81	[117.8]		
MUE	0.89	1.03	0.68			

3.3 Data Analyses

Unless otherwise stated, Microsoft Excel and Origin software packages served as the main numerical analysis tools for data presented in this thesis. The results from analytical instruments were processed in the respective software provided by the vendors. Regarding the FTIR spectra, QASoft database enabled the semi-quantitation of product species by their characteristic IR bands. POLYMATH [33] software solved the system of ordinary differential equations (ODEs) for the chemical reaction models. Subsequent chapters provide further details.

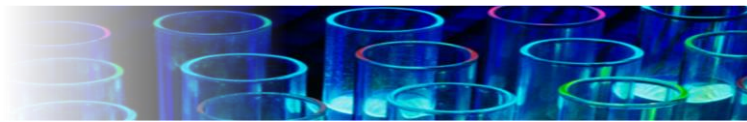


3.4 References

- [1] Loponov KN, Lopes J, Barlog M, Astrova EV, Malkov AV, Lapkin AA. Optimization of a scalable photochemical reactor for reactions with singlet oxygen. *Org Process Res Dev* 2014;18:1443–1454.
- [2] Delley B. From molecules to solids with the DMol 3 approach. *J Chem Phys* 2000;113:7756–7764.
- [3] Frisch M, Trucks GW, Schlegel HB, Scuseria GE, Robb MA, Cheeseman JR, et al. Gaussian 09, Revision A. 02, Gaussian. Inc Wallingford CT 2009;200.
- [4] Perdew JP, Burke K, Ernzerhof M. Generalized gradient approximation made simple. *Phys Rev Lett* 1996;77:3865.
- [5] Delley B. An all-electron numerical method for solving the local density functional for polyatomic molecules. *J Chem Phys* 1990;92:508–517.
- [6] Tkatchenko A, Scheffler M. Accurate molecular van der Waals interactions from ground-state electron density and free-atom reference data. *Phys Rev Lett* 2009;102:073005.
- [7] Huang X, Ramadugu SK, Mason SE. Surface-Specific DFT+ U Approach Applied to α -Fe₂O₃ (0001). *J Phys Chem C* 2016;120:4919–4930.
- [8] Delley B. From molecules to solids with the DMol3 approach. *J Chem Phys* 2000;113:7756–7764.
- [9] Hirshfeld FL. Bonded-atom fragments for describing molecular charge densities. *Theor Chim Acta* 1977;44:129–138.
- [10] Fukui K. The role of frontier orbitals in chemical reactions (Nobel Lecture). *Angew Chem Int Ed Engl* 1982;21:801–809.
- [11] Fonseca Guerra C, Handgraaf J-W, Baerends EJ, Bickelhaupt FM. Voronoi deformation density (VDD) charges: Assessment of the Mulliken, Bader, Hirshfeld, Weinhold, and VDD methods for charge analysis. *J Comput Chem* 2004;25:189–210.
- [12] Becke AD. Density-functional exchange-energy approximation with correct asymptotic behavior. *Phys Rev A* 1988;38:3098.

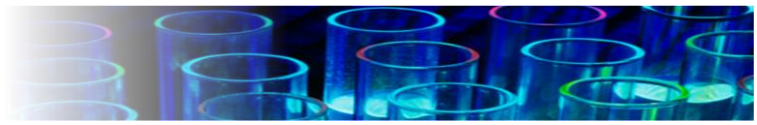


- [13] Lee C, Yang W, Parr RG. Development of the Colle-Salvetti correlation-energy formula into a functional of the electron density. *Phys Rev B* 1988;37:785.
- [14] Zhao Y, Truhlar DG. The M06 suite of density functionals for main group thermochemistry, thermochemical kinetics, noncovalent interactions, excited states, and transition elements: two new functionals and systematic testing of four M06-class functionals and 12 other functionals. *Theor Chem Acc* 2008;120:215–241.
- [15] Montgomery Jr JA, Ochterski JW, Petersson GA. A complete basis set model chemistry. IV. An improved atomic pair natural orbital method. *J Chem Phys* 1994;101:5900–5909.
- [16] Vandeputte AG, Reyniers M-F, Marin GB. A theoretical study of the thermodynamics and kinetics of small organosulfur compounds. *Theor Chem Acc* 2009;123:391–412.
- [17] Vandeputte AG, Sabbe MK, Reyniers M-F, Van Speybroeck V, Waroquier M, Marin GB. Theoretical study of the thermodynamics and kinetics of hydrogen abstractions from hydrocarbons. *J Phys Chem A* 2007;111:11771–11786.
- [18] Casanovas R, Frau J, Ortega-Castro J, Salvà A, Donoso J, Muñoz F. Simplification of the CBS-QB3 method for predicting gas-phase deprotonation free energies. *Int J Quantum Chem* 2010;110:323–330.
- [19] Zeng Z, Altarawneh M, Oluwoye I, Glarborg P, Dlugogorski BZ. Inhibition and Promotion of Pyrolysis by Hydrogen Sulfide (H₂S) and Sulfanyl Radical (SH). *J Phys Chem A* 2016;120:8941–8. doi:10.1021/acs.jpca.6b09357.
- [20] Mennucci B. Polarizable continuum model. *Wiley Interdiscip Rev Comput Mol Sci* 2012;2:386–404.
- [21] Canneaux S, Bohr F, Henon E. KiSThelP: A program to predict thermodynamic properties and rate constants from quantum chemistry results†. *J Comput Chem* 2014;35:82–93.
- [22] Saito T, Nishihara S, Kataoka Y, Nakanishi Y, Matsui T, Kitagawa Y, et al. Transition state optimization based on approximate spin-projection (AP) method. *Chem Phys Lett* 2009;483:168–171.



- [23] Yamanaka S, Kawakami T, Nagao H, Yamaguchi K. Effective exchange integrals for open-shell species by density functional methods. *Chem Phys Lett* 1994;231:25–33.
- [24] Abe M. Diradicals. *Chem Rev* 2013;113:7011–7088.
- [25] Slipchenko LV, Krylov AI. Singlet-triplet gaps in diradicals by the spin-flip approach: A benchmark study. *J Chem Phys* 2002;117:4694–4708.
- [26] Luo Y-R. Handbook of bond dissociation energies in organic compounds. CRC press; 2002.
- [27] Bobrowski M, Liwo A, Oldziej S, Jeziorek D, Ossowski T. CAS MCSCF/CAS MCQDPT2 study of the mechanism of singlet oxygen addition to 1, 3-butadiene and benzene. *J Am Chem Soc* 2000;122:8112–8119.
- [28] Zhao Y, Truhlar DG. Exploring the Limit of Accuracy of the Global Hybrid Meta Density Functional for Main-Group Thermochemistry, Kinetics, and Noncovalent Interactions. *J Chem Theory Comput* 2008;4:1849–68. doi:10.1021/ct800246v.
- [29] Bolton W. The crystal structure of alloxan. *Acta Crystallogr* 1964;17:147–152.
- [30] Harrowfield JM, Skelton BW, Soudi AA, White AH. Crystal Structure of Alloxan Monohydrate: A Redetermination. *Aust J Chem* 1989;42:1795–1798.
- [31] Singh C. The structure of the pyrimidines and purines. VIII. The crystal structure of alloxan $C_4H_4N_2O_5$. *Acta Crystallogr* 1965;19:759–767.
- [32] Bolton W. The crystal structure of triketoindane (anhydrous ninhydrin). A structure showing close CO- C interactions. *Acta Crystallogr* 1965;18:5–10.
- [33] POLYMATH is copyrighted by M. Shacham, M.B. Cutlip and M. Elly <http://www.polymath-software.com/>.

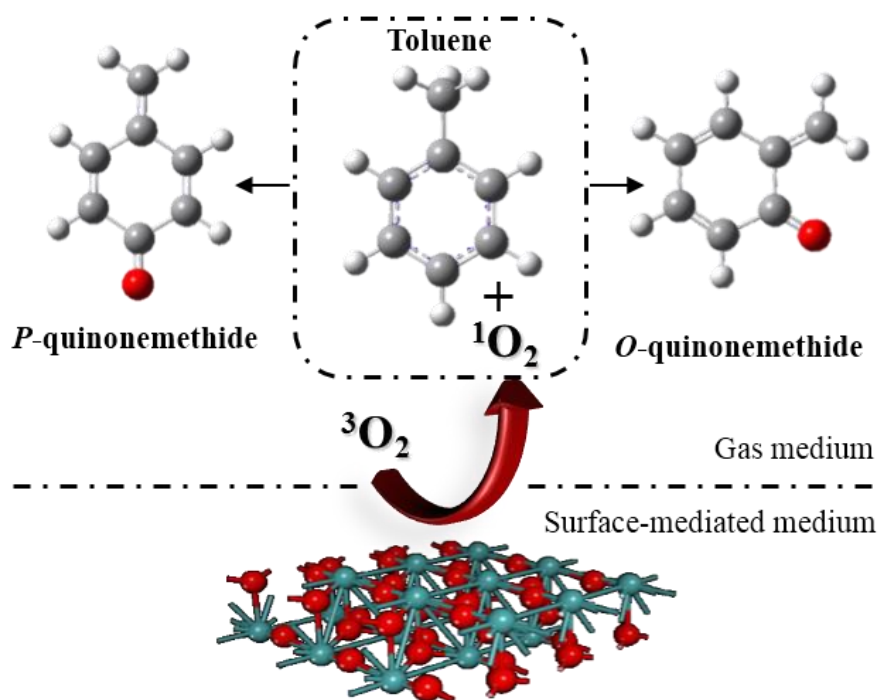
Jomana Al-Nu'airat

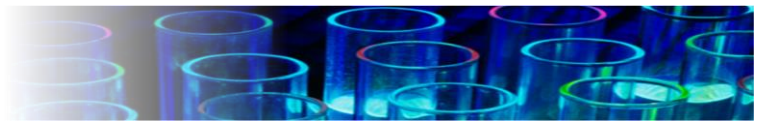


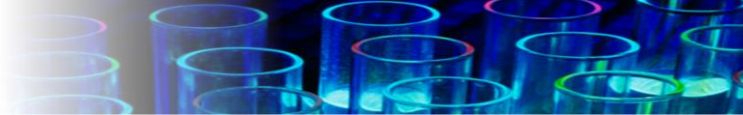


Chapter 4

Role of Singlet Oxygen in Combustion Initiation of Aromatic Fuels

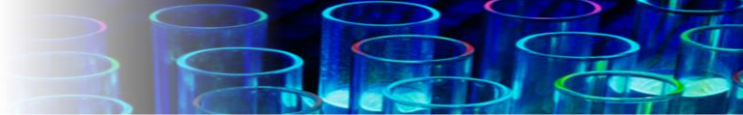






Abstract

Application of singlet oxygen in oxy-fuel systems reduces the activation energy of the initiation reactions, accelerating the chain-branching mechanism and decreasing the overall ignition temperature. However, the underlining reaction mechanism of the surface-generated singlet oxygen $O_2\ ^1\Delta_g$ that reacts with fuel surrogates (i.e. toluene) in the gas media remains poorly explored. Herein, comprehensive mechanistic and thermo-kinetic accounts underpinning the reaction of the simplest alkylbenzene, namely toluene, with singlet oxygen in the gas phase are reported. In analogy to reaction of singlet oxygen with benzene, the titled reaction branches into several opening channels. The 1,4 cycloaddition and *ene* type reactions of toluene with singlet oxygen affords *p*-quinonemethide (4-methylenecyclohexa-2,5-dienone) and *o*-quinonemethide (6-methylenecyclohexa-2,4-dienone), respectively (i.e., very reactive intermediates). The initiation of the *para* channel follows a concerted mechanism through an enthalpic barrier of 34.5 kJ mol⁻¹ with a fitted reaction rate coefficient of $k(T) = 1.51 \times 10^{-15} \exp(-34\ 500/(RT))$ cm³ molecule⁻¹ s⁻¹. A corresponding value for the formation of *o*-quinonemethide amounts to 47.6 kJ mol⁻¹ and $k(T) = 8.31 \times 10^{-14} \exp(-42\ 600/RT)$ cm³ molecule⁻¹ s⁻¹. Moreover, the relative reactivity of singlet oxygen, based on the reaction rate constants, follows the order of OH > H > CH₃ > ¹O₂ > HO₂ > ³O₂. These indicate that the presence of singlet oxygen considerably lowers the activation energy of the initiation channels, resulting in an energetically improved combustion process. In addition, the result illustrates that, the reported *meta* route (2+2 cyclo addition) in the catalytic reaction of toluene with metal oxides occur when the metal oxide promotes triplet to singlet oxygen and positions the adsorbed molecule of ¹O₂ parallel to one of the sides of the aromatic ring of benzene molecule.

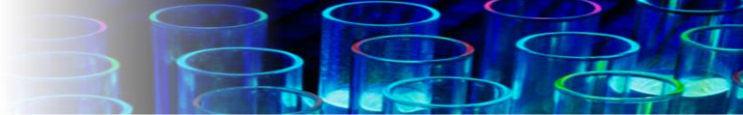


4.1 Introduction

Enhancing the efficiency of fuel combustion constitutes a mainstream strategy in the pursuit of meeting the ever-increasing energy demand. In this regard, oxy-fuel systems present an attractive approach toward efficient energy conversion, reducing the fuel consumption and minimising the ignition delay time. One promising area of research is concerned with studying the influence of singlet oxygen $O_2\ ^1\Delta_g$ on combustion and spontaneous ignition of hydrocarbon fuels [1,2]. Singlet oxygen $O_2\ ^1\Delta_g$ resides 95 kJ mol^{-1} ($\Delta_G H^{\circ}_{298}$) above the ground state triplet oxygen molecule $O_2\ ^3\Sigma_g^-$ [3,4]. Therefore, even when injected in minuscule quantities, singlet oxygen $O_2\ ^1\Delta_g$ accelerates the chain-branching mechanism, decreasing the ignition temperature as well as the induction time [1,5–8].

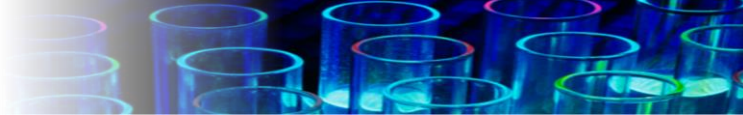
The open literature presents reacting systems of singlet oxygen with simple species, such as H_2-O_2 [9], CH_4-O_2 [10], and $CO-H_2-O_2$ [5]. In all these processes, remarkable upgrades, i.e., enhanced decomposition kinetic, have been reported. For example, in the $CO-H_2-O_2$ system, singlet oxygen showed an ability to convert selectively and rapidly CO into CO_2 at 900 K [5]. Likewise, linear hydrocarbons (HCs) such as ethene (C_2H_4) and propane (C_3H_8) [11], and alkyl benzenes display notable improvements in combustion parameters with the addition of singlet O_2 [12,13]. The latter group constitutes a major additive fraction in transportation fuels, e.g., gasoline and diesel [14].

Singlet oxygen forms either spontaneously by photosensitisation [15] and electrical discharge [16] or thermally via surface-mediated reactions on particles such as silicon dioxide, aluminium oxide, and transition metal oxides [17]. Metal-oxide surfaces, which are well known for their catalytic effect on HC oxidation, serve as excellent generators of singlet oxygen [18],



catalysing the oxidation of HC via surface oxidation mechanisms such as Eley-Rideal (E-R), Langmuir-Hinshelwood (L-H) and Mars-van Krevelen (M-vK) or via the gas-phase oxidation of HC with $O_2 \ ^3\Sigma_g^-$ desorbed from the catalytic surface. The L-H route commences with physical and chemical adsorption of both HC and triplet oxygen $O_2 \ ^3\Sigma_g^-$ on the metal oxide surface, followed by in situ excitation of triplet oxygen $O_2 \ ^3\Sigma_g^-$ to the singlet form. Singlet oxygen $O_2 \ ^1\Delta_g$ then reacts with the surface-adsorbed HC in the subsequent steps. In the E-R process, metal oxides only excite the adsorbed triplet oxygen $O_2 \ ^3\Sigma_g^-$ to singlet oxygen $O_2 \ ^1\Delta_g$ without adsorbing the HC on the surface. The oxygen occupying crystal sites at surfaces of metal oxides represents an active part in the M-vK reaction process. In M-vK, HCs form a thin metal-reactant layer by chemisorbing on the surface. When the reaction product desorbs, an oxygen vacancy forms in the surface layer of the catalyst, subsequently filled with a fresh oxygen atom, following the adsorption and dissociation of a new molecule of triplet oxygen. The final mechanism (i.e., the surface induced oxidation) involves excitation of triplet to singlet by the catalyst, desorption of $O_2 \ ^1\Delta_g$ into the gas phase and ensuing reaction between HC and singlet oxygen in the gas phase.

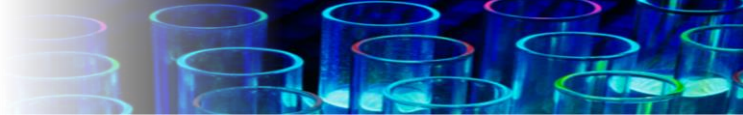
Boikov et al. [19] and Tomskii et al. [18] attempted to distinguish between the surface-induced oxidation and the three surface oxidation routes of vanadium-molybdenum oxide systems in the oxidation of toluene (i.e. fuel surrogate). They found that vanadium (V) oxide (V_2O_5) and molybdenum (VI) oxide (MoO_3) oxidise toluene to different products even though both metal oxides generate $O_2 \ ^1\Delta_g$. These researchers suggested a reaction mechanism initiated by the attack of $O_2 \ ^3\Sigma_g^-$ or $O_2 \ ^1\Delta_g$ on the *meta* and *para* carbons of the ring, and proposed deploying quantum chemical calculations to gain insights into the elementary steps [20]. Along this line of enquiry, a decade earlier, a computational study by Cheikh et al. [12], on a similar system (benzene ring), demonstrated that, in the presence of V_2O_5 - MoO_3 , oxygen $O_2 \ ^3\Sigma_g^-$ first attaches



itself onto the para carbon of the benzene ring and subsequently forms hydroquinone. However, adsorption ability of V_2O_5 - MoO_3 significantly affects the overall reaction mechanism. To examine the reaction of $O_2\ ^1\Delta_g$ with toluene, a detailed computational study should resolve the isolated interactions of singlet oxygen with toluene in the absence of metal oxides (and their adsorption ability).

Experimenting with such systems represents a challenging and laborious task, especially, with short-lived singlet oxygen that exhibits a lifetime of $4\ \mu s$ [21]. This is not surprising since each fuel is unique and displays a distinct blend of various HCs. Moreover, the physical and chemical interactions of HC with metal-oxide surfaces make it even harder to elucidate the (surface-induced) gas-phase pathways, driven by the desorbed singlet oxygen $O_2\ ^1\Delta_g$. To simplify this problem, in this contribution, this paper focus on the oxidation of the most reactive aromatic HC, namely toluene (methylbenzene). Toluene occurs naturally at low levels in crude oil and forms during the industrial production of gasoline, coal-coke transformation, as well as during the oxidation of spark-ignition (SI) engine fuels [22,23]. Toluene often serves as a surrogate for the alkyl benzene fraction in transportation fuels.

By implementing the quantum chemical framework of density functional theory (DFT), this work aims at (i) differentiating the surface-induced oxidation apart from the surface oxidation (E-R, L-H, and M-vK) processes, (ii) providing detailed mechanistic and thermo-kinetic parameters for the paths encountered in the oxidative transformation of oxy-fuel by singlet oxygen, and (iii) justifying the reduction of activation energies of the initiation reactions and the chain-branching mechanism acceleration. This paper maps all the reaction routes, assessing their relative feasibility based on computed reaction rate constants, and describing the enhanced conversion of aromatic HCs.



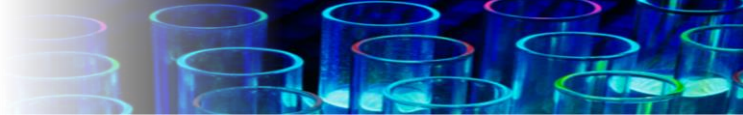
4.2 Computational Methodology

The Gaussian 09 [24] suite of programs executed all structural optimisation and energy calculation for toluene, singlet oxygen as well as all other targeted intermediate species using the B3LYP and M06 DFT functionals along with the 6-311+G(d,p) basis set [25]. B3LYP performs effectively in energy calculations of singlet diradicals [26]. The accuracy of ten DFT functionals for calculating the enthalpy gap between singlet and triplet states ($\Delta_G H_{298}$) for selected diradical species, namely O, O₂, NH, NF, C, and Si have been tested previously in the literature [27], revealing that, B3LYP accurately predicts the enthalpy gap for singlet oxygen with only 8.5 kJ mol⁻¹ offset from the experimental value (94.6 kJ mol⁻¹) [28]; i.e., exhibiting performance similar to that of multi-reference wave function methods, such as CASSAF and CASSTP2 [13,29]. On the other hand, due to the limitation of B3LYP in computing kinetic parameters in general, the computational scheme of this work relies on the M06 functional, known for its excellent performance in estimating different kinetics parameters [30]. The intrinsic reaction coordinate (IRC) calculations have been performed on selected transition structures to confirm their respective identity. Table 4.1 indicates the accuracy threshold of the M062X functional for some pertinent reactions; the error analysis reveals an unsigned error of 3.33 kJ mol⁻¹ on the reported energy values in the result section. For further accuracy benchmarking, the applied M062X method was employed to compute the rate of reaction of benzenamine with singlet oxygen, at 313 K; $k = 1.85 \times 10^9$ (M⁻¹ s⁻¹), concurring well with the experimental measurement [27] of $k = 2.0 \times 10^9$ (M⁻¹ s⁻¹) within a 7 % ceiling. Likewise, some recent studies [31,32] have reported a similar level of accuracy for the adapted DFT methodologies for hydroxylated aromatics and H-transfer reactions.

**Table 4.1.** Error analysis of M062X energy for selected reactions

Species	Reaction	Calculated M062X (kJ mol ⁻¹)	Experimental [3,28] and theoretical (kJ mol ⁻¹) [13]	Absolute error (kJ mol ⁻¹)
Oxygen	$^3\text{O}_2 \longrightarrow ^1\text{O}_2$	103.2	94.6	8.5
Phenol		376.9	378.2±4.2 in solution	1.3
		365.7	368.2±6.3 in gas	2.5
Aniline		381.3	385.8 in solution	4.5
		377.1	375.3 in gas	2.2
Toluene		374.5	370.3±6.3	4.2
Benzene		116.6	116.5	0.1
Mean unsigned error (MUE) = 3.33 kJ mol⁻¹				

Evaluation of rate constants and Arrhenius parameters was carried out by the KiSTheIP code [33] within the temperature range of 300-1200 K, based on the conventional transition state theory with the inclusion of a one dimensional Eckart barrier that accounts for contribution of the quantum-tunnelling effect. The internal rotation in toluene and transition structures is treated as hindered rotors with a barrier of 8.2 kJ mol⁻¹ [34]. Furthermore, as singlet oxygen functions as an electrophilic reagent, the Hirshfeld atomic charges and the Fukui (f^1) [35] indices identify the preferred substitution sites on the benzene ring; i.e., *ipso*, *ortho*, *meta* and *para* positions. Material studio DMol³ software [36] afforded the estimation of the Hirshfeld atomic charges and Fukui (f^1) indices of nucleophilic attack. Finally, in view of the biradical character that might mark the toluene + O₂ (¹Δ_g) system, one must determine the spin state of intermediate and transition structures along the entire potential energy surface. Severe spin

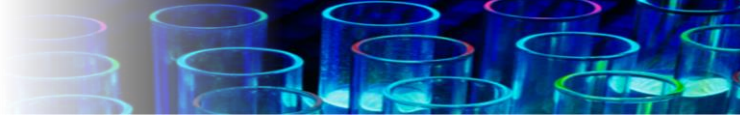


contamination necessitates energy refinements based on the approximate spin-projection scheme (AP) pioneered by Yamagushi's group [37,38]. The located transition structures and intermediates converge on a pure low-spin (LS) solution with zero spin densities. Performing structural optimisations with mixed frontier molecular orbitals (i.e., the broken symmetry (BS) solution [29]) assesses plausible spin contamination. Spin contamination value of the BS state (S_2 (HS)) of near unity indicates a significant spin contamination by the triplet state. All the estimated values for intermediates and transition structures fall very close to zero. It follows that, the toluene + O₂ ($^1\Delta_g$) system displays a genuine LS ground state, eliminating the need for a further energy-refinement procedure. However, the energy of the O₂ ($^1\Delta_g$) suffers from contamination by the ground triplet state as evidenced by an estimate of the spin contamination operator S_2 (HS)~ 1. As such, the applied the AP approach is applied to refine the energy O₂ ($^1\Delta_g$).

4.3 Results and Discussion

4.3.1 Preliminary assessment of gas-phase reaction of benzene with singlet oxygen

Singlet oxygen reacts with olefins, dienes or aromatic structures via distinct channels, namely, the Diels-Alder [4+2] and [2+2] cycloadditions, as well as the *ene* type reactions [4,39,40]. Based on orbital correlations, a stepwise process characterises the formation of the [4+2] cycloadduct [41]. However in benzene, this reaction follows a concerted pathway [13] that constitutes the principal mechanism for the attack of singlet oxygen against the unsubstituted benzene ring [12,13,42–44]. Figure 4.1 depicts the initiation reaction of benzene and O₂ $^1\Delta_g$, via the mechanism of 1,4 cycloaddition. Firstly, singlet oxygen O₂ $^1\Delta_g$ binds with the benzene



ring diagonally from above (or below) its ring plane through **TS₁₋₄**. The saddle point **TS₁₋₄** displays a C_{2v} symmetry with diagonal *supra-supra* oxygen conformation with the length of O–O bond of 1.32 Å (B3LYP). Subsequently, the O–O bond stretches to 1.46 Å (B3LYP), forming a “boat like” bicyclic configuration of **M₁₋₄**. This intermediate incurs an enthalpic barrier of 116.6 kJ mol⁻¹, in agreement with the comparable value reported by Bobrowski et al. obtained at the MCQDPT2/BSSE level of theory [13]. For comparison, the experimental value of the enthalpy of activation required for the thermolysis of **M₁₋₄** amounts to 74.4 kJ mol⁻¹ [45]. Finally, the O–O bond in this complex elongates enough to form *p*-hydroquinone as previously described by Witko et al. [46,47].

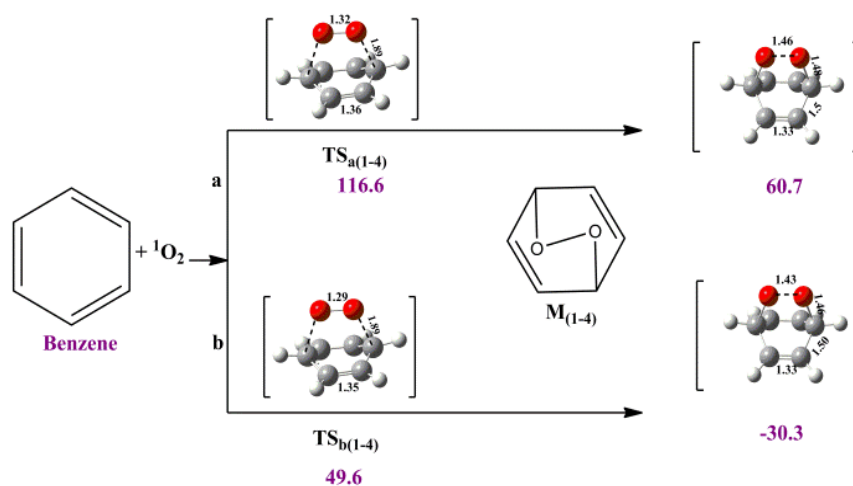
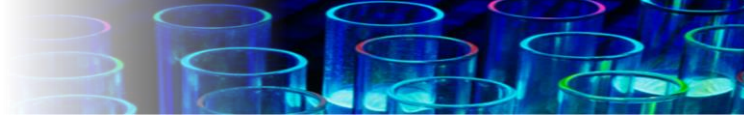
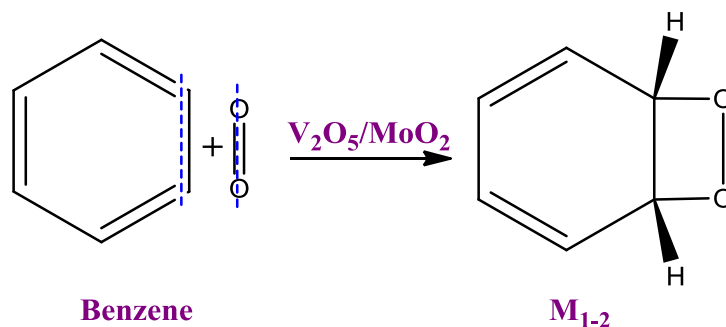


Figure 4.1. Optimised structures of the transition states and intermediates of benzene oxidation by singlet oxygen (distances are in Å), activation enthalpies calculated at 298.15 K, a: M06 and b: B3LYP. All values are in kJ mol⁻¹.

Cheikh et al. [12] conducted an analogous reaction on V_2O_5 – MoO_3 surfaces, reporting the energy map of all stationary points. The authors observed the repeated hydrogen transfer to oxygen atoms producing *p*-hydroquinone. Moreover, they also reported a 2+2 cycloaddition reaction, made possible by the metal-oxide surface (MOS) positioning the oxygen parallel to one of the sides of the benzene ring. As shown in Scheme 4.1, singlet oxygen approaches the



benzene ring from the side, repositioning a hydrogen atom to be perpendicular to the plane defined by the reacting species. M_{1-2} , the precursor of the *o*-dihydroxybenzene [47] adduct, successively forms when another H atom moves out of the plane.



Scheme 4.1. 2+2 Cycloaddition of O_2 $^1\Delta_g$ to Benzene on V_2O_3/MoO_2 Surface

4.3.2 Initial steps of gaseous reaction of toluene with singlet oxygen

The electrophilic nature of singlet oxygen engenders the rate constant for its reaction with substituted benzene ring to increase in the order of $H < C_6H_5 < CH_3 < OCH_3$ [45]. This means that, the electron density of a particular HC species dictates its reactivity towards singlet oxygen. From this perspective, it is interesting to query the effect of replacing a hydrogen atom in benzene ring with a single methyl group (CH_3) on the reaction pathways and product species. By examining the 1H -NMR data, core-electron binding energy (CEBE) shifts, and Hammett constants assembled in Table 4.2, one can easily conclude that, the CH_3 group (as an electron donating group, EDG) displays a *para*-directory character. Thus, the group induces a reaction to occur preferentially at the *para* and *ortho* positions compared to the *meta* carbon (< 2 %) [48].

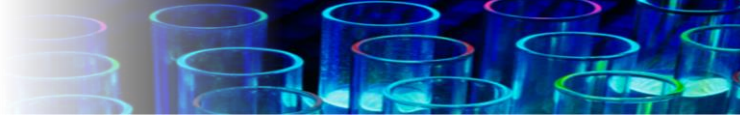
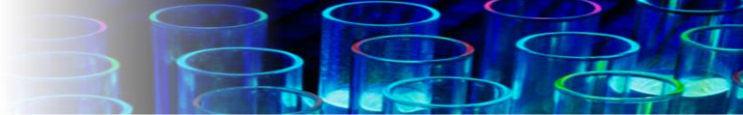


Table 4.2. *Ortho*, *meta*, and *para* directory effect of methyl substituent on the benzene ring in toluene. Values in brackets refer to an unsubstituted benzene ring

Method	Methyl (CH ₃)			Reference
	<i>o</i>	<i>m</i>	<i>p</i>	
Chemical shift, ppm	7.10 (7.27)	7.18 (7.27)	7.09 (7.27)	Amzel et al. [48]
Core-electron binding energy (CEBE) shifts, eV	-0.22	-0.05	-0.27	Takahata and Chong [55]
Hammett σ constants	-0.170	-0.069	-0.170	Hammett [54]
Hirshfeld atomic charges	-0.0374 (-0.041)	-0.0341 (-0.041)	-0.0349 (-0.041)	Present work
Fukui indices	0.083 (0.110)	0.088 (0.110)	0.090 (0.110)	Present work

The [4+2] cycloaddition dominates in the presence of one electron donating group (EDG), such as methyl group in toluene. Whereas, the 2+2 cycloaddition pathway necessities at least two EDGs. Thus, the probability of 4+2 cycloaddition with singlet oxygen exceeds that of the 2+2 cycloaddition. Furthermore, the *ene* reaction, forming allylic hydroperoxides, favours the allylic hydrogen in the alkyl substituents [49,50]. The reaction of toluene with singlet oxygen demonstrates a process controlled by frontier molecular orbitals, with the LUMOs of singlet oxygen interacting with the HOMOs of toluene. The methyl group present on the benzene ring increases the energy gap between the HOMO (-6.461 eV) and LUMO (-0.218 eV) orbitals in comparison with that of the HOMO (-5.388 eV) and LUMO (-0.168 eV) of benzene [51,52]. This difference explains the elevated reactivity of the ring with singlet oxygen, induced by the presence of a methyl substituent. Table 4.2 presents the Fukui indices and Hirshfeld electronic charges in toluene with respect to benzene. Higher f^1 values at the *para*, *ortho*, and *meta* carbon atoms of toluene with respect to the indistinguishable sites in benzene imply higher rate of addition of singlet delta oxygen to toluene, compared with the analogous process involving



benzene. The higher f^1 associated with the *para* carbon further highlights the *para* position as a more preferred site for the electrophilic O_2 $^1\Delta_g$ addition in reference to *ortho* and *meta* sites.

Figure 4.2 illustrate five initiation channels (representing three pathways) for the oxidation of toluene with singlet oxygen; 4+2 cycloaddition, *ene* reaction, and direct abstraction of methyl hydrogen. The first two concur with the results of the published experimental investigations on photo-oxidation of methyl-substituted benzene [52,53]. The 4+2 cycloaddition affords 1,4-peroxides **M1** and **M2** akin to **M1-4** in benzene. Formation of **M1** exhibits a slightly lower enthalpic barrier (**TS1** = 32.6 kJ mol⁻¹, M06) as compared to **M2** (**TS2** = 44.1 kJ mol⁻¹, M06). The *para* regioselectivity of toluene explains this difference. Indeed, the Hammett σ constants for toluene of -0.17, the same for both *para* and *ortho*, and a contrasting value of -0.07 for *meta* (Table 2), indicated the *para-ortho* director [54]. The results of the DFT calculations corroborate this directing character from the calculated core-electron binding energy (CEBE) that shifts by -0.27, -0.22 and -0.05 for *para*, *ortho*, and *meta*, respectively revealing preference of the *para* over the *ortho* site [55]. The *ene* hydroperoxide adducts of singlet oxygen (**M3** and **M4**) arise when one of the atoms of the molecular oxygen approaches a *para* or *ortho* ring position while the other oxygen atom simultaneously abstracts one of the hydrogens attached to the methyl group. Intermediate **M4** holds the highest enthalpic barrier of **TS4** = 183.3 kJ mol⁻¹ (M06). Figure 4.3 illustrates the optimised geometries of the located transition structures, for the B3LYP and M06 functionals.

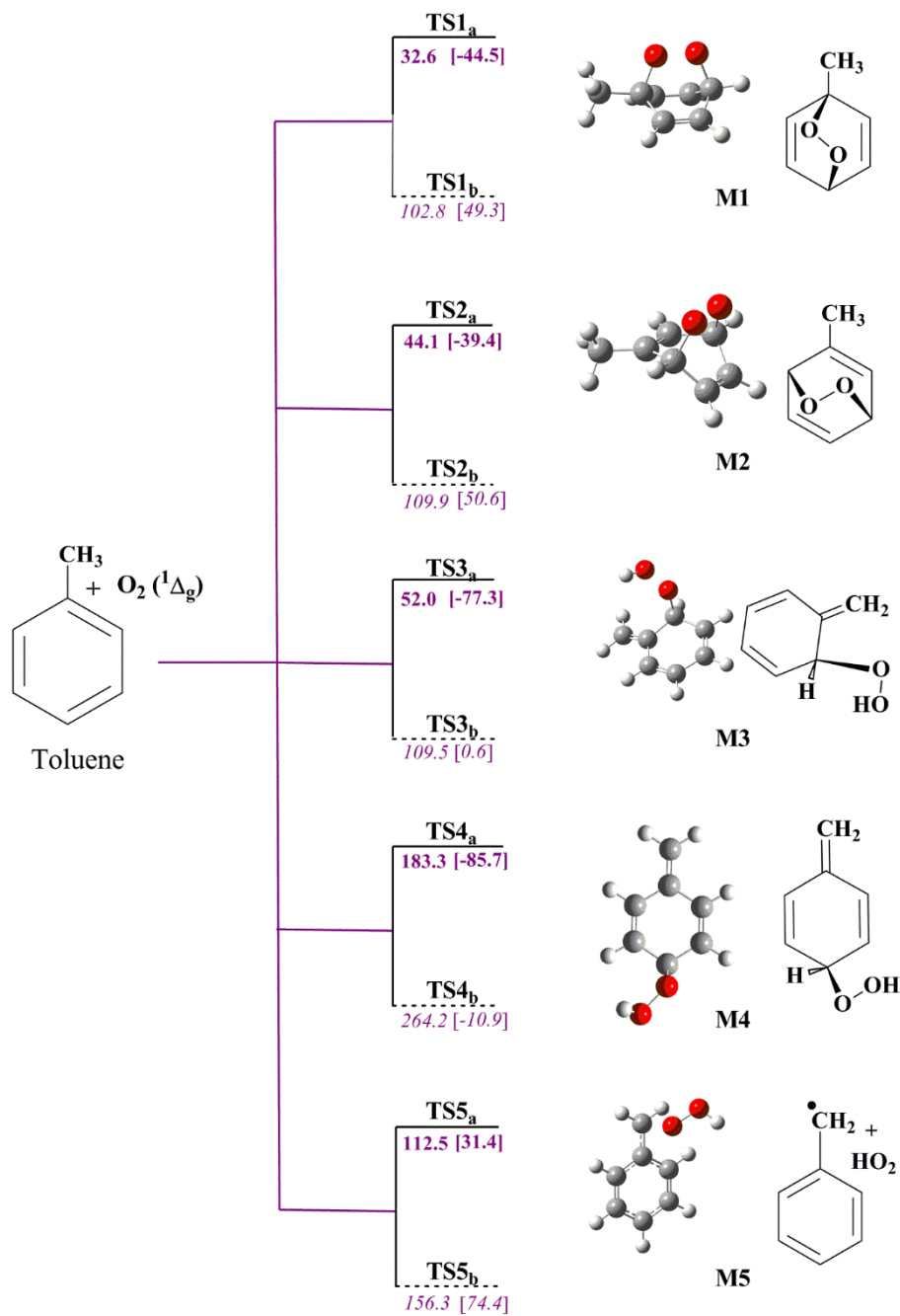


Figure 4.2. Initiation channels in the reaction of $\text{O}_2 (^1\Delta_g)$ with toluene, with their activation $\Delta^\ddagger H^\circ_{298}$ and reaction $\Delta_r H^\circ_{298}$ (in brackets) enthalpies, calculated using the M06/6-311+G(d,p) (represented by solid line and bold values), and B3LYP/6-311+G(d,p) (dotted line and italicised values). All values are in kJ mol^{-1} at 298.15 K.

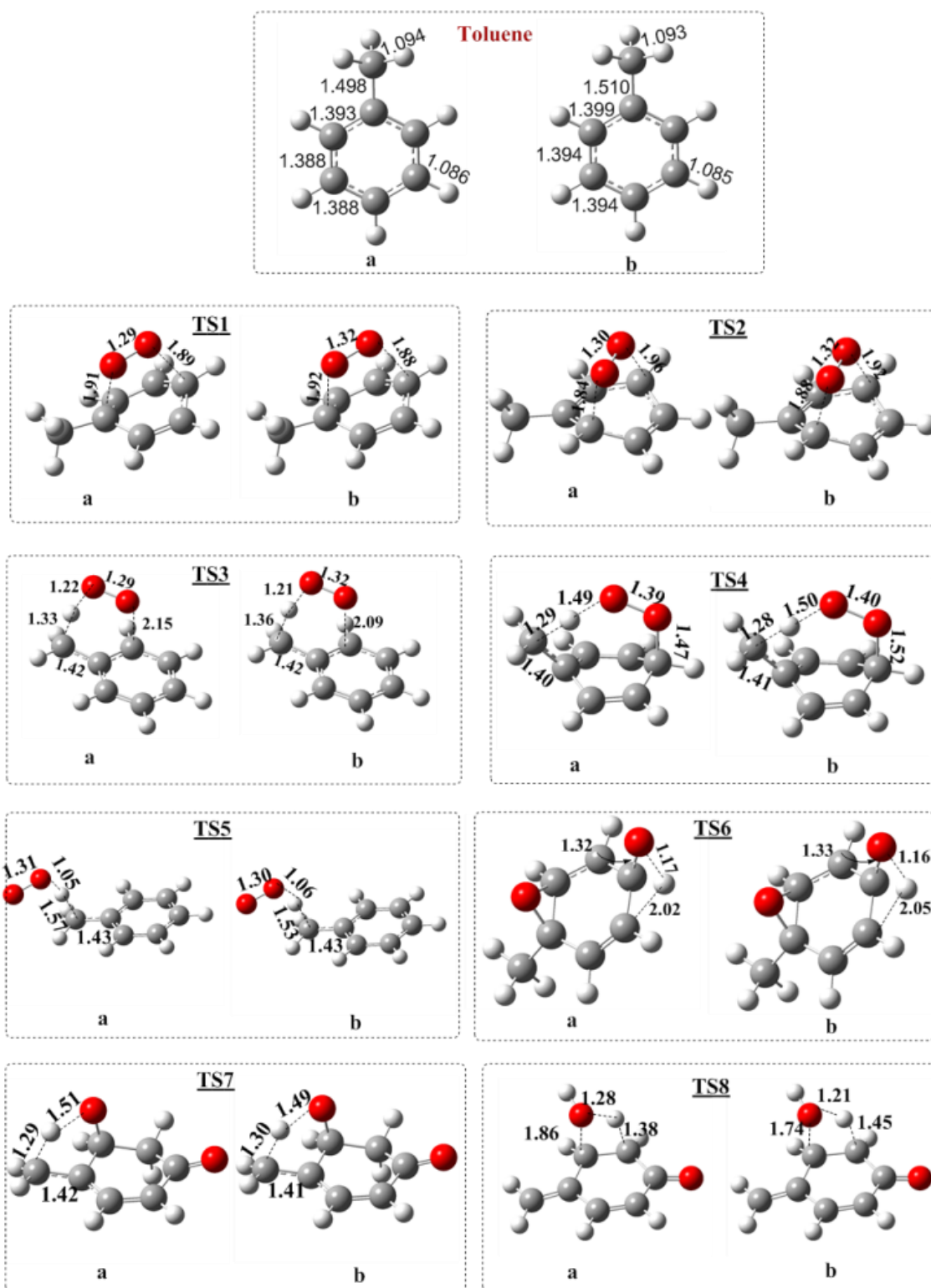
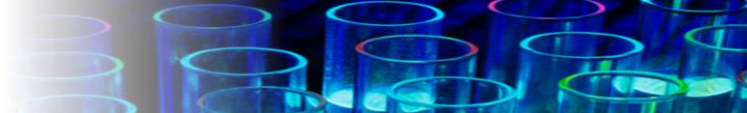
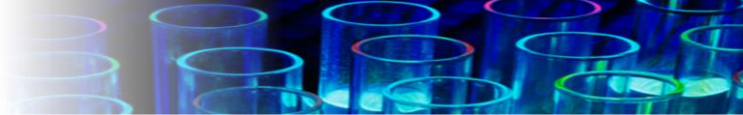


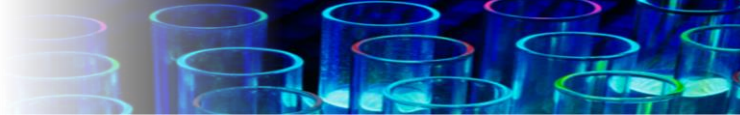
Figure 4.3. Optimised structures of transition states of toluene oxidised by singlet oxygen (distances are in Å), a: M06/6-311+G(d,p) and b: B3LYP/6-311+G(d,p). All values are calculated at 298.15 K.



4.3.3 Routes for formation of primary products

Intermediates **M1** and **M3** that form at the *ipso-para* and the *ortho-meta* positions, respectively, seem to favour the generation of the *o* and *p*-quinonemethides. The **M1** channel involves the appearance of four complex transition states and four intermediates (Figure 4.4 and Table 4.3) to produce *p*-quinonemethide. Intermediate **M1** that resides 49.3 kJ mol⁻¹ above the entrance channel rearranges to the **M6** tricyclic intermediate, in which two of the rings possess a three-membered ring structure. A 1,2 hydrogen transfer forms **M7** with an enthalpic barrier of 231.2 kJ mol⁻¹ that represents the highest hurdle in Figure 4.4. Therefore, the appearance of **M7** represents a “bottleneck” for the *p*-methylquinone mechanism. Furthermore, with respect to the *p*-hydroquinone route, Cheikh et al. reported that, the same step also holds the highest activation enthalpy of 287.6 kJ mol⁻¹, based on their B3LYP/6-311G(d,p) calculations [12]. The activation of the benzene ring by the presence of the methyl substituent explains the 56 kJ mol⁻¹ reduction. In the subsequent isomerisation step, hydrogen transfers intramolecularly from the methyl group to the neighbouring oxygen atom through **TS7** to generate **M8**, which subsequently affords the exothermic formation of *p*-quinonemethide by elimination of a water molecule.

Generally, quinonemethides are chemically more reactive and polar than the corresponding quinones [56,57]. Therefore, the quinonemethides will be short-lived, rapidly disappearing in reactions with other reactive intermediates, especially nucleophiles. For example, *o*-quinonemethide represents a critical intermediate in the combustion of transportation fuels as well as in the pyrolysis of wood and low-rank coals [58]. Interestingly, da Silva et al. [59] stated that, the *o*-quinonemethide decomposes further to benzene during combustion with the rate constant of $k(T) \text{ (s}^{-1}\text{)} = 2.64 \times 10^{14} \exp(-35\,900/T \text{ (K)})$ [60]. Quinonemethides are also



common constituents of biological systems, participating directly in the process of lignification in plants [58,61]. The suggested mechanism for *o*-quinonemethide (Figure 4.4) reveals hydroxyl elimination as the rate-determining step, through an open shell mechanism into **M10**, the enthalpic barrier of which amounts to $192.2 \text{ kJ mol}^{-1}$, with **M11** (*o*-quinonemethide) located $299.7 \text{ kJ mol}^{-1}$ below the entrance channel. Moreover, the result illustrates that, the reported *meta* route (2+2 cyclo addition) in the catalytic reaction of toluene with metal oxides occur when the metal oxide promotes triplet to singlet oxygen and positions the adsorbed molecule of $^1\text{O}_2$ parallel to one of the sides of the aromatic ring of benzene molecule.

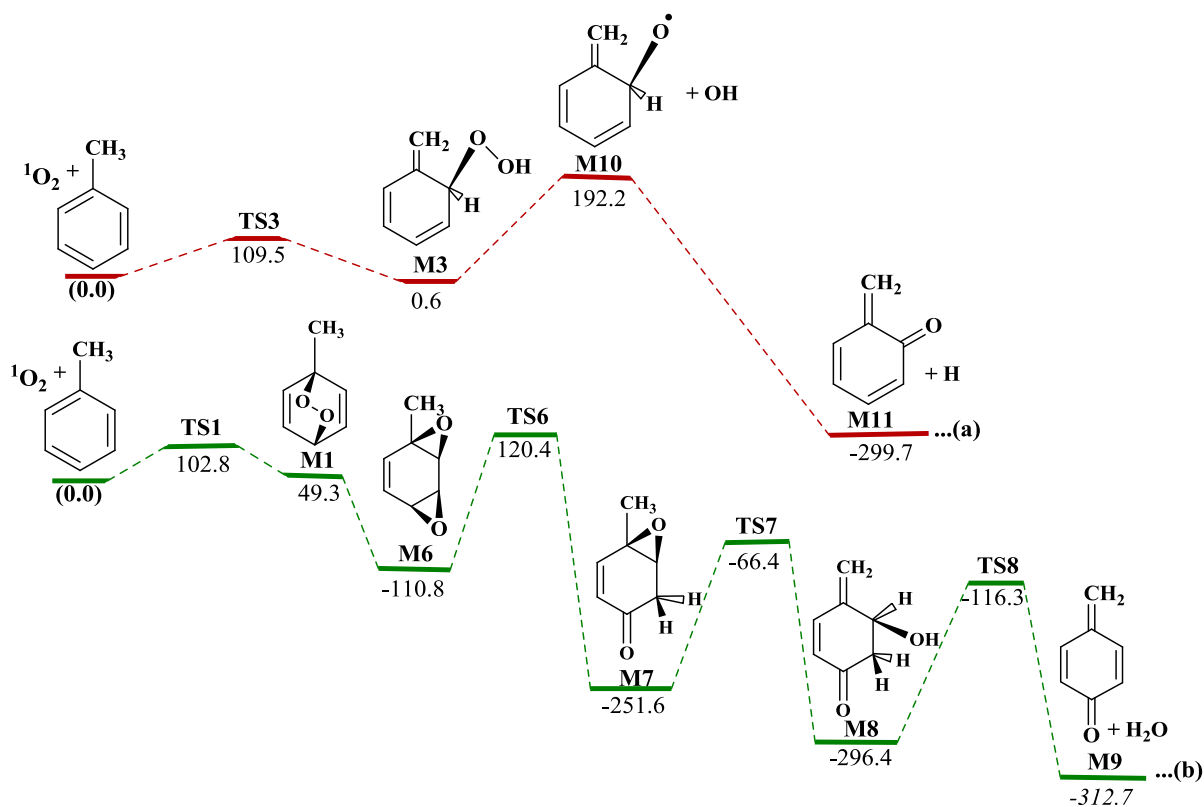


Figure 4.4. Enthalpy map for the formation of (a): *o*-quinonemethide (6-methylenecyclohexa-2,4-dienone) and (b): *p*-quinonemethide (4-methylenecyclohexa-2,5-dienone) from the reaction of singlet oxygen with toluene, B3LYP/6-

311+G(d,p). All values are in kJ mol^{-1} at 298.15 K.

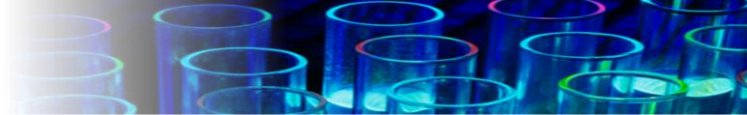


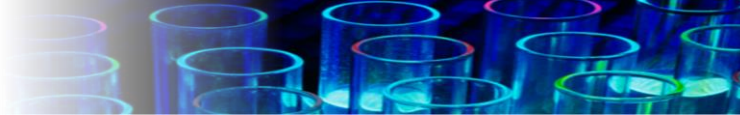
Table 4.3. Arrhenius rate parameters A ($\text{cm}^3 \text{ molecule}^{-1} \text{ s}^{-1}$) and E_a in (kJ mol^{-1}) fitted in the temperature range of 298-1200 K and for pressure of 1 bar for the initiation channels involved in the reaction of toluene with singlet O_2

Reaction	B3LYP		M062X	
	A	E_a	A	E_a
Toluene + $^1\text{O}_2 \rightarrow \text{M1}$	5.92×10^{-15}	112.9	1.51×10^{-15}	34.5
Toluene + $^1\text{O}_2 \rightarrow \text{M2}$	2.34×10^{-14}	120.0	3.97×10^{-14}	48.2
Toluene + $^1\text{O}_2 \rightarrow \text{M3}$	1.53×10^{-14}	109.0	8.31×10^{-14}	47.6
Toluene + $^1\text{O}_2 \rightarrow \text{M4}$	4.35×10^{-15}	260.6	2.17×10^{-14}	175.2
Toluene + $^1\text{O}_2 \rightarrow \text{M5}$	3.17×10^{-12}	156.4	7.23×10^{-12}	108.8

4.3.4 Thermodynamic and kinetic considerations

Figure 4.5 presents the change in the standard Gibbs free energy of all reactions, as function of temperature. Over the considered temperature range, the change in this thermodynamic potential indicates the less spontaneous nature of the initiation channels as temperature increases. However, the relatively low values of $\Delta_r G^\circ$ for reactions leading to **M6** – **M11** (except for **M10**) indicate irreversibility of the forward processes. The Supplementary Material assembles the thermochemical data in the NASA polynomial format as determined from the ChemRate software, for the temperature range of between 300 and 5000 K.

With the aid of the KiSTheIP code, Tables 4.3 and 4.4 itemise the Arrhenius rate constants for the five initiation channels and the subsequent reaction steps, respectively. Figure 4.6 (M06) plots the branching ratios for the competing initiation channels based on the reaction rate constants illustrated in Table 4.4. At 300 K, the formation of the **M1** adduct represents the



main channel with noticeable contributions from the channels generating **M2** and **M3**. The importance of the M3 channel notably increases with temperature; however, the **M1** route remains the leading channel over the entire temperature range.

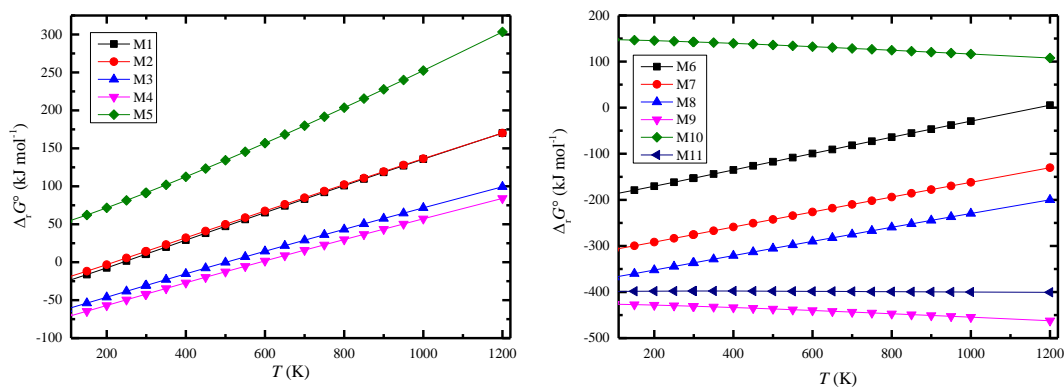
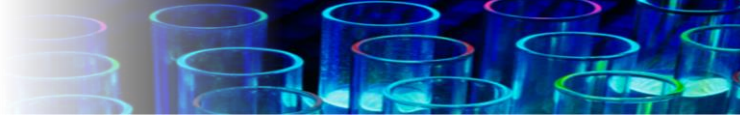


Figure 4.5. Variation of the standard Gibbs free energy change of reaction with temperatures, for all reactions leading to the stationary points illustrated in Figure 4.4.

Table 4. Arrhenius rate parameters A ($\text{cm}^3 \text{molecule}^{-1} \text{s}^{-1}$) and E_a in (kJ mol^{-1}) fitted in the temperature range of 298-1200 K for the formation of *p*-quinonemethide (4-methylenecyclohexa-2,5-dienone), M1, and M6-M9 adducts

Reaction	B3LYP		M062X	
	A	E_a	A	E_a
Toluene + $^1\text{O}_2 \rightarrow \text{M1}$	5.92×10^{-15}	112.9	1.51×10^{-15}	34.5
M6 \rightarrow M7	1.05×10^{14}	217.7	1.63×10^{14}	77.8
M7 \rightarrow M8	4.08×10^{13}	196.6	1.05×10^{14}	481.3
M8 \rightarrow M9	5.79×10^{13}	190.6	7.76×10^{13}	479.4



Figures 4.7a and 4.7b contrast the rate of initiation reactions involving singlet oxygen with those of molecular $^3\text{O}_2$ [62] and important reactive radical species [63,64], respectively. The reactivity of these compounds, solely based on the reaction rate constants, follows the order of $\text{OH} > \text{H} > \text{CH}_3 > ^1\text{O}_2 > \text{HO}_2 > ^3\text{O}_2$. However, the most significant contribution to the initiation of oxidation depends on the concentration of the oxidisers themselves. Prior to the establishment of the H/O radical pool at higher temperatures, the reactions involving singlet and triplet oxygen govern the oxidation rates. Establishing the relative contribution of singlet and triplet oxygen necessitates deploying accurately measured concentration of singlet oxygen in typical combustion environments. In this regard, Boikov et al. [65] reported the formation of singlet oxygen $^1\text{O}_2$ below 773.15 K on surfaces of solid and Si-supported V_2O_5 and MoO_3 catalysts at rates of 10^{15} - 10^{17} molecules $(\text{g catalyst})^{-1} \text{h}^{-1}$. A robust comparison between combustion initiations by triplet and singlet oxygen (formed over transitional metal oxides) will be carried out in a subsequent contribution.

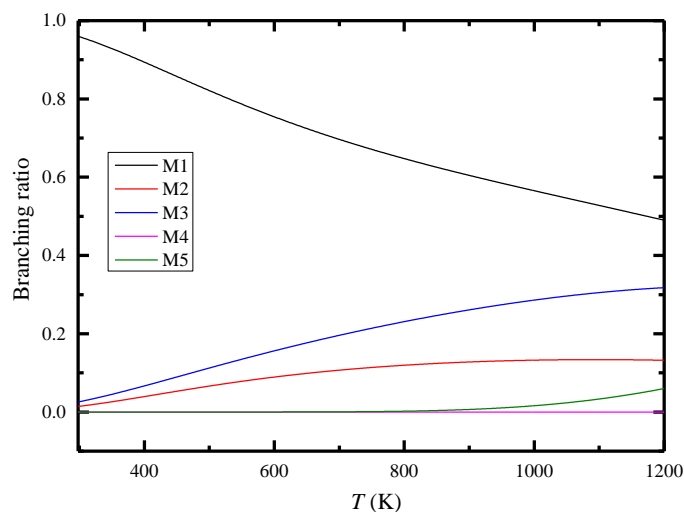


Figure 4.6. Relative branching ratios of the five initiation channels in the reaction of toluene with singlet oxygen, M06/6-311+G(d,p).

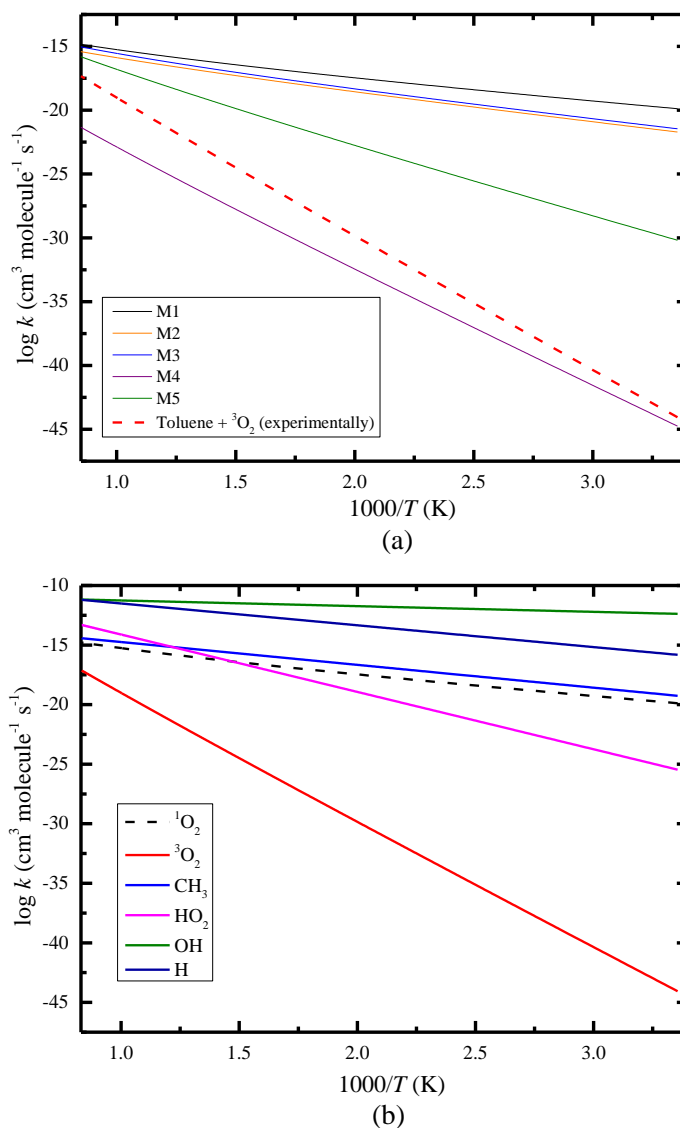
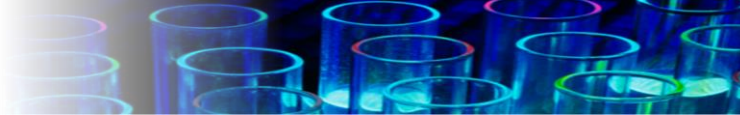


Figure 4.7. Arrhenius plots for initiation of gaseous reaction of toluene with singlet oxygen; (a) contrasts initiation by singlet oxygen (present work) with the experimentally reported triplet $^3\text{O}_2$ [62], and (b) compares the most preferred pathway (M1, present study) with the corridors induced by the presence of other reactive radical species [63,64].



This paragraph illustrates an approximate comparison of the relative importance of singlet and triplet channels on the equilibrium concentration of singlet oxygen. By considering the energy gap between triplet and singlet oxygen molecules of 95 kJ mol^{-1} , the equilibrium concentration of singlet oxygen falls below that of triplet oxygen by a factor of 1.18×10^{-10} . The rate constant for the oxidation of toluene with triplet oxygen, $\text{toluene} + {}^3\text{O}_2 \rightarrow \text{benzyl} + \text{HO}_2$, amounts to $5.55 \times 10^{-11} T^{2.5} \exp(23\,200/T) \text{ cm}^3 \text{ molecule}^{-1} \text{ s}^{-1}$ [66]. Table S4.1 in Supplementary Material lists rates of the initiation reactions (in s^{-1}) for the two oxidisers. Here, the rate of the M06-calculated rate constant for the channel of $\text{toluene} + {}^1\text{O}_2 \rightarrow \text{M1}$ is adopted to account for the consumption of toluene by singlet oxygen. It is evident that, the initiation of combustion by singlet oxygen dominates the analogous reaction due to triplet oxygen up to 550 K.

4.4 Concluding Remarks and Practical Implications

This study presents substantial mechanistic and kinetic information on the interaction of singlet oxygen with toluene in the absence of metal oxides (and their adsorption ability). The gaseous reaction pathways obtained from the application of the B3LYP and M06 functionals predict the formation of *para* and *ortho*-quinonemethides, reactive intermediate species. The results of kinetic modelling indicate that, the formation of intermediates **M1** and **M3** initiates the oxidation of toluene by singlet oxygen.

From an application point of view, the present results elucidate the heightened performance of oxy-fuel engines via singlet oxygen surcharge. Singlet oxygen, in comparison to triplet molecular oxygen, noticeably boost the conversion of aromatic hydrocarbons. The innovative



concept of this study resolves the relative reactivity of singlet oxygen with aromatic hydrocarbons, following the order of $\text{OH} > \text{H} > \text{CH}_3 > {}^1\text{O}_2 > \text{HO}_2 > {}^3\text{O}_2$. These indicate that the systematic addition of singlet oxygen into combustion engine can enhance the ignition, reduce the enthalpic requirements and result in an energetically improved combustion process. As demonstrated in Table S1, the rate of combustion initiation can be significantly accelerated by singlet oxygen at temperatures up to 550 K, i.e., the representative bulk gas temperatures of compression combustion engines. This phenomenon, for instance, can provide insight into practical scenario [67] in which the addition of 1 % singlet oxygen in the total oxygen intake of HCCI engine increases the power output value by 7–14 %. Overall, increasing the combustion efficiency of these engines will also make up for simultaneous reduction in nitric oxide (NO), carbon monoxide (CO) and particulate carbon emissions.

Supplementary material

The Supporting Information is included in Chapter 10 (Appendix I) of the thesis. Table S4.1 comparing oxidation rates involving singlet and triplet oxygen; Thermochemical data in the NASA database format; Atomic coordinates, rotational constants and vibrational wave numbers for species appearing in this article



4.5 References

- [1] Starik AM, Kozlov VE, Titova NS. On the influence of singlet oxygen molecules on the speed of flame propagation in methane–air mixture. *Combust Flame* 2010;157:313–27. doi:10.1016/j.combustflame.2009.11.008.
- [2] Starik AM, Kozlov VE, Titova NS. On mechanisms of a flame velocity increase upon activation of O₂ molecules in electrical discharge. *J Phys Appl Phys* 2008;41:125206.
- [3] Luo Y-R. *Handbook of bond dissociation energies in organic compounds*. CRC press; 2002.
- [4] Foote CS. *Active oxygen in chemistry*. Springer Science & Business Media; 1995.
- [5] Sharipov AS, Starik AM. Kinetic mechanism of CO–H₂ system oxidation promoted by excited singlet oxygen molecules. *Combust Flame* 2012;159:16–29.
- [6] Starik AM, Titova NS. Possibility of Initiation of Combustion of CH₄–O₂ (Air) Mixtures with Laser-Induced Excitation of O₂ Molecules. *Combust Explos Shock Waves* 2004;40:499–510.
- [7] Bourig A, Thévenin D, Martin J-P, Janiga G, Zähringer K. Numerical modeling of H₂–O₂ flames involving electronically-excited species O₂ (¹Δ_g), O (¹D) and OH (²Σ⁺). *Proc Combust Inst* 2009;32:3171–3179.
- [8] Washington DA, Shapiro HN. A Phenomenological Analysis of Exergy Destruction During Hydrogen Combustion with Electronically Excited Oxygen. *ASME 2013 Power Conf., American Society of Mechanical Engineers*; 2013, p. V001T01A024–V001T01A024.
- [9] Chukalovsky AA, Klopovsky KS, Liberman MA, Mankelevich YA, Popov NA, Proshina OV, et al. Study of singlet delta oxygen O₂ (¹Δ_g) impact on H₂–O₂ mixture ignition in flow reactor: 2D modeling. *Combust Sci Technol* 2012;184:1768–1786.
- [10] Shi R, Wang CH, Chang YN. The Influence of Singlet Oxygen and Ozone on the Combustion in Methane-Air Mixture. *Adv. Mater. Res.*, vol. 699, Trans Tech Publ; 2013, p. 111–118.



- [11] Starik AM, Pelevkin AV, Titova NS. Modeling study of the acceleration of ignition in ethane–air and natural gas–air mixtures via photochemical excitation of oxygen molecules. *Combust Flame* 2017;176:81–93. doi:10.1016/j.combustflame.2016.10.005.
- [12] Cheikh F, Boucekkine A, Cartier A. Computational study of the addition of molecular oxygen to benzene. *J Mol Struct THEOCHEM* 1997;397:13–20.
- [13] Bobrowski M, Liwo A, Oldziej S, Jeziorek D, Ossowski T. CAS MCSCF/CAS MCQDPT2 study of the mechanism of singlet oxygen addition to 1, 3-butadiene and benzene. *J Am Chem Soc* 2000;122:8112–8119.
- [14] Battin-Leclerc F. Detailed chemical kinetic models for the low-temperature combustion of hydrocarbons with application to gasoline and diesel fuel surrogates. *Prog Energy Combust Sci* 2008;34:440–498.
- [15] DeRosa MC, Crutchley RJ. Photosensitized singlet oxygen and its applications. *Coord Chem Rev* 2002;233:351–371.
- [16] Kearns DR. Physical and chemical properties of singlet molecular oxygen. *Chem Rev* 1971;71:395–427.
- [17] Shcherbakov NV, Emel'yanov AN, Khaula EV, Il'ichev AN, Vishnetskaya MV, Rufov YN. Photo- and thermogeneration of singlet oxygen by the metal ions deposited on Al₂O₃ and SiO₂. *Russ J Phys Chem* 2006;80:799–802. doi:10.1134/S0036024406050232.
- [18] Tomskii IS, Vishnetskaya MV, Rufov YN. The oxidation of toluene on transition metal oxides. *Russ J Phys Chem A* 2009;83:1868–1872.
- [19] Boikov EV, Vishnetskaya MV, Emel'yanov AN, Tomskii IS, Shcherbakov NV. The selective catalytic oxidation of toluene. *Russ J Phys Chem Focus Chem* 2008;82:2233–2237.
- [20] Vishnetskaya M, Tomskiy I. Role of singlet oxygen in the oxidation of toluene on vanadium molybdenum catalytic systems. *Chem Sustainable Dev* 2011; 19: 321-325.
- [21] Clennan EL, Pace A. Advances in singlet oxygen chemistry. *Tetrahedron* 2005;61:6665–6691.
- [22] Dagaut P, Pengloan G, Ristori A. Oxidation, ignition and combustion of toluene: Experimental and detailed chemical kinetic modelling Arrhenius parameters for reactions. *Phys Chem Chem Phys* 2002;4:1846–54. doi:10.1039/b110282f.



- [23] Palminteri MC. Toluene: Chemical Properties, Applications, and Toxicology. Nova Science Publishers, Incorporated; 2013.
- [24] Frisch M, Trucks GW, Schlegel HB, Scuseria GE, Robb MA, Cheeseman JR, et al. Gaussian 09, Revision A. 02, Gaussian. Inc Wallingford CT 2009;200.
- [25] Montgomery Jr JA, Ochterski JW, Petersson GA. A complete basis set model chemistry. IV. An improved atomic pair natural orbital method. *J Chem Phys* 1994;101:5900–5909.
- [26] Cramer CJ, Thompson J. Quantum chemical characterization of singlet and triplet didehydroindenes. *J Phys Chem A* 2001;105:2091–2098.
- [27] Al-Nu'airat J, Altarawneh MK, Gao X, Westmoreland PR, Dlugogorski BZ. Reaction of Aniline with Singlet Oxygen ($O_2^1\Delta_g$). *J Phys Chem A* 2017.
- [28] Slipchenko LV, Krylov AI. Singlet-triplet gaps in diradicals by the spin-flip approach: A benchmark study. *J Chem Phys* 2002;117:4694–4708.
- [29] Abe M. Diradicals. *Chem Rev* 2013;113:7011–7088.
- [30] Zhao Y, Truhlar DG. The M06 suite of density functionals for main group thermochemistry, thermochemical kinetics, noncovalent interactions, excited states, and transition elements: two new functionals and systematic testing of four M06-class functionals and 12 other functionals. *Theor Chem Acc* 2008;120:215–241.
- [31] Altarawneh M, Dlugogorski BZ. Formation of dibenzofuran, dibenzo-p-dioxin and their hydroxylated derivatives from catechol. *Phys Chem Chem Phys* 2015;17:1822–1830.
- [32] Ahubelem N, Altarawneh M, Dlugogorski BZ. Dehydrohalogenation of ethyl halides. *Tetrahedron Lett* 2014;55:4860–4868.
- [33] Canneaux S, Bohr F, Henon E. KiSThelP: A program to predict thermodynamic properties and rate constants from quantum chemistry results†. *J Comput Chem* 2014;35:82–93.
- [34] Zanganeh J, Altarawneh M, Saraireh I, Namazi S, Zanganeh J. Theoretical study on thermochemical parameters and pKa values for fluorinated isomers of toluene. *Comput Theor Chem* 2013;1011:21–29.



- [35] Fukui K. The role of frontier orbitals in chemical reactions (Nobel Lecture). *Angew Chem Int Ed Engl* 1982;21:801–809.
- [36] Delley B. From molecules to solids with the DMol3 approach. *J Chem Phys* 2000;113:7756–7764.
- [37] Saito T, Nishihara S, Kataoka Y, Nakanishi Y, Matsui T, Kitagawa Y, et al. Transition state optimization based on approximate spin-projection (AP) method. *Chem Phys Lett* 2009;483:168–171.
- [38] Yamanaka S, Kawakami T, Nagao H, Yamaguchi K. Effective exchange integrals for open-shell species by density functional methods. *Chem Phys Lett* 1994;231:25–33.
- [39] Albini A, Fagnoni M. *Handbook of synthetic photochemistry*. John Wiley & Sons; 2009.
- [40] Wasserman E, Kuck VJ, Delavan WM, Yager WA. Electron paramagnetic resonance of 1. DELTA. oxygen produced by gas-phase photosensitization with naphthalene derivatives. *J Am Chem Soc* 1969;91:1040–1041.
- [41] McCarrick MA, Wu YD, Houk KN. Hetero-Diels-Alder reaction transition structures: reactivity, stereoselectivity, catalysis, solvent effects, and the exo-lone-pair effect. *J Org Chem* 1993;58:3330–3343.
- [42] Clar E, Schoental R. *Polycyclic hydrocarbons*. vol. 2. Springer; 1964.
- [43] Chien S-H, Cheng M-F, Lau K-C, Li W-K. Theoretical study of the Diels-Alder reactions between singlet ($^1\Delta_g$) oxygen and acenes. *J Phys Chem A* 2005;109:7509–7518.
- [44] Reddy AR, Bendikov M. Diels–Alder reaction of acenes with singlet and triplet oxygen—theoretical study of two-state reactivity. *Chem Commun* 2006:1179–1181.
- [45] Aubry J-M, Pierlot C, Rigaudy J, Schmidt R. Reversible binding of oxygen to aromatic compounds. *Acc Chem Res* 2003;36:668–675.
- [46] Broclawik E, Haber J, Witko M. Quantum-chemical description of the catalytic oxidation of benzene. *J Mol Catal* 1984;26:249–258.
- [47] Witko M, Broclawik E, Haber J. Stereochemistry of the catalytic oxidation of benzene as revealed by quantum chemical calculations. *J Mol Catal* 1986;35:179–189.

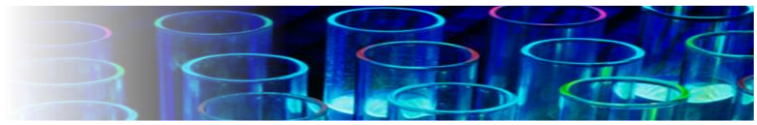


- [48] Amzel LM, Covey DF, Fenselau C, Nickon A, Robinson CH. Organic structural analysis. JB Lambert, HF Shurvell, L. Berbit, RG Cooks, GH Stout, Macmillan Publishing Co. Inc., New York, NY, 1976. 596 pp.
- [49] Bartlett PD, Mendenhall GD, Schaap AP. Competitive modes of reaction of singlet oxygen*. *Ann N Y Acad Sci* 1970;171:79–88.
- [50] Gollnick K, Griesbeck A. Interactions of singlet oxygen with 2, 5-dimethyl-2, 4-hexadiene in polar and non-polar solvents evidence for a vinylogous ene-reaction. *Tetrahedron* 1984;40:3235–3250.
- [51] Klopman G, others. *Chemical reactivity and reaction paths* 1974.
- [52] Van den Heuvel CJM, Hofland A, Steinberg H, de Boer TJ. The photo-oxidation of hexamethylbenzene and pentamethylbenzene by singlet oxygen. *Recl Trav Chim Pays-Bas* 1980;99:275–278.
- [53] Van den Heuvel CJM, Steinberg H, de Boer TJ. The photooxidation of mono- and dimethylnaphthalenes by singlet oxygen. *Recl Trav Chim Pays-Bas* 1980;99:109–113.
- [54] Hammett LP. The effect of structure upon the reactions of organic compounds. Benzene derivatives. *J Am Chem Soc* 1937;59:96–103.
- [54] Takahata Y, Chong DP. Estimation of Hammett sigma constants of substituted benzenes through accurate density-functional calculation of core-electron binding energy shifts. *Int J Quantum Chem* 2005;103:509–515.
- [55] Turner AB. Quinone methides. *Q Rev Chem Soc* 1964;18:347–360.
- [56] Rokita SE. Quinone methides. vol. 4. John Wiley & Sons; 2009.
- [57] Singh MS, Nagaraju A, Anand N, Chowdhury S. ortho-Quinone methide (o-QM): a highly reactive, ephemeral and versatile intermediate in organic synthesis. *RSC Adv* 2014;4:55924–59. doi:10.1039/C4RA11444B.
- [59] da Silva G, Chen C-C, Bozzelli JW. Toluene combustion: reaction paths, thermochemical properties, and kinetic analysis for the methylphenyl radical + O₂ reaction. *J Phys Chem A* 2007;111:8663–8676.



- [60] da Silva G, Bozzelli JW. Quantum chemical study of the thermal decomposition of o-quinone methide (6-methylene-2, 4-cyclohexadien-1-one). *J Phys Chem A* 2007;111:7987–7994.
- [61] Thompson DC, Thompson JA, Sugumaran M, Moldéus P. Biological and toxicological consequences of quinone methide formation. *Chem Biol Interact* 1993;86:129–62. doi:10.1016/0009-2797(93)90117-H.
- [62] Oehlschlaeger MA, Davidson DF, Hanson RK. Investigation of the reaction of toluene with molecular oxygen in shock-heated gases. *Combust Flame* 2006;147:195–208.
- [63] Braun-Unkloff M, Frank P, Just T. High temperature reactions of benzyl radicals. *Berichte Bunsenges Für Phys Chem* 1990;94:1417–1425.
- [64] Mirokhin Y, Mallard G, Westley F, Herron J, Frizzell D, Hampson R. NIST Standard Reference Database 17-2Q98 (Chemical Kinetics Database). Natl Inst Stand Technol Gaithersburg MD 1998.
- [65] Tomskii IS, Vishnetskaya MV, Kokorin AI. The partial catalytic oxidation of toluene on vanadium and molybdenum oxides. *Russ J Phys Chem B Focus Phys* 2008;2:562–567.
- [66] Oehlschlaeger MA, Davidson DF, Hanson RK. Investigation of the reaction of toluene with molecular oxygen in shock-heated gases. *Combust Flame* 2006;147:195–208.
- [67] Starik AM, Korobov AN, Titova NS. Combustion improvement in HCCI engine operating on synthesis gas via addition of ozone or excited oxygen molecules to the charge: Modeling study. *Int J Hydrog Energy* 2017;42:10475–84. doi:10.1016/j.ijhydene.2017.01.179.

Jomana Al-Nu'airat





Chapter 5

Effect of Fe₂O₃ Nanoparticles on Combustion of Coal Surrogate (Anisole): Enhanced Ignition and Formation of Persistent Free Radicals





Abstract

This contribution explores the effect of iron (III) oxide nanoparticles on the combustion of coal surrogate, i.e., anisole, identifying the changes in ignition features as well as the occurrence of persistent organic pollutants in the initiation channels. The method applies packed-bed reactor coupled with Fourier transform infrared spectroscopy (FTIR) to quantitate the ignition temperature under typical fuel-rich conditions, in-situ electron paramagnetic resonance (EPR) to elucidate the formation of environmentally-persistent free radicals (EPFR), diffuse reflectance infrared Fourier transform spectroscopy (DRIFTS) to monitor the chemisorption of organic substrates on the nanoparticles, as well as X-ray diffraction for particles characterisation. We employ cluster-based quantum mechanical calculation to map the reaction pathway within the scope of the density functional theory. The results of Fe₂O₃-mediated combustion of anisole depict an excessive reduction in ignition temperature from 500 °C to below 200 °C at $\lambda = 0.8$. Chemisorption of anisole on α -Fe₂O₃ surfaces follows direct dissociation of the O–CH₃ (and OCH₂–H), leading to the formation of surface-bound phenoxy radicals and gaseous species at temperatures as low as 25 °C, confirmed both from EPR and DRIFTS measurements, incurring an estimated energy barrier of $E_a = 18 \text{ kJ mol}^{-1}$ and a preexponential factor of $A = 2.7 \times 10^{12} \text{ M}^{-1} \text{ s}^{-1}$. This insight applies to free-radical chain reactions that induce spontaneous fires of coal, as coal comprises ferric oxide nanoparticles, and equally to coexistence of aromatic fuels with thermodynamically reactive Fe₂O₃ surface, e.g., in fly ash, at the cooled-down tail of combustion stacks.



5.1 Introduction

Factors responsible for spontaneous fires of coal comprise the reactions between coal, oxygen and aggressive (reactive) contaminants. Spontaneous fires of coal (i.e., fires of mined coal and coal seams) and cleaning rejects from coal processing, that have been observed globally for decades, result in diverse safety and economic drawbacks [1–12]. Adsorption of molecular O_2 onto the surface of coal pores induces the formation of free radicals that further react with oxygen at low temperature, yielding the transient intermediates, reactive oxygen species (ROS) and gaseous products. The generated heat activates subsequent chain reactions that induce thermal runaway prompting spontaneous fires [13–18].

Despite the progress made in understanding the spontaneous combustion of coal, the mechanism underlying the emergence of the first surface radicals remains obscure. One hypothesis posits that, the presence of reactive O_2 species (e.g., superoxide anion, hydroxy radical, and singlet oxygen) opens up initiation pathways with lower activation energy. Moreover, metal-oxides such as Fe_2O_3 can easily facilitate this condition, as Fe_2O_3 fixes oxygen exothermically on its iron-centred sites [19,20], changing its electronic configurations. This surface-mediated reactions catalyse the oxidation of hydrocarbons via mechanisms such as that of Mars-van Krevelen (M-vK) [21]. Iron exists in coal at about 2.6 % to 4.2 % (weight percent), majority of which appears in the reduced pyrite form [22,23]. Although previous work [24] identified pyrite in accelerating the process of spontaneous combustion, the role of other Fe-carriers remains poorly investigated. Bulk analyses (e.g., X-ray powder diffraction, XRD) often hide the presence of other iron species. The particle nano-characterisation techniques have revealed the occurrence of nano- Fe_2O_3 in coal [25–28] as well as in overburden [28] of coal deposits.



Similarly, the geochemistry and nano-mineralogy of coal seams that ignite spontaneously, as well as burning of coal cleaning rejects (BCCR), revealed considerable amount of Fe-oxide nanoparticles [1,11,29,30]. Fe_2O_3 serves as a burn rate modifier, i.e., it enhances the burning rate of composite solid propellants [31]. The nanoparticles of Fe_2O_3 often find applications as structural, catalytic, magnetic, electronic, and optical materials [32,33]. In fact, Ghorishi et al. [34] suggested that, the iron level of fly ash can predict its catalytic activity.

Coal incorporates condensed aromatic units characterised by various degree of substitution on their periphery, linked by methylenic, etheric and hydroaromatic bridges. The cleavage of these bridges sustains thermal processes such as high-temperature and high-pressure liquefaction of coal. In comparison to higher-ranked coals, peats and low-rank coals (i.e., lignite) contain relatively more oxygen, in the form of methoxyl groups, making them quite susceptible to spontaneous ignition [35,36]. Phenyl ethers often serve as surrogate for low-rank coal and biomass lignin [36]. Anisole (methoxybenzene, $\text{C}_7\text{H}_8\text{O}$) represents the simplest monocyclic aromatic hydrocarbon with a methyl ether functional group. The alkoxy-aryl linkage in anisole plays a crucial role in the low-temperature oxidation of coal.

Accordingly, this investigation seeks understanding of the mechanistic aspects of oxidative interactions between coal and Fe_2O_3 [37]. The study has been designed to provide insights into the changes in ignition characteristics of a coal surrogate (anisole) on Fe_2O_3 nanoparticles. In addition, we study the initiation reactions that form the environmentally-persistent free radicals (EPFR). We juxtapose the results of experimental measurements with theoretical calculations based on the density functional theory. The results explain the role of iron (III) oxide, as an inorganic component of coal that initiates its self-ignition. As most of the iron in coal converts



in combustion into Fe_2O_3 that partitions into the fly ash [22], our findings also elucidate the formation of pollutants in the cooling-down zones of industrial combustion processes.

5.2 Experimental and Computational Methodology

5.2.1 Tubular packed-bed reactor setup

Figure 5.1a illustrates the bench-scale packed-bed reactor in which a digital syringe pump released the fuel surrogate (anisole; purity > 99.0%, $1.32 - 0.45 \mu\text{L min}^{-1}$) into the preheated combined stream of N_2 and synthetic air (SA) flowing through the system at combined rates of between 295 and 102 mL min^{-1} (at STP, IUPAC). Anisole concentration in the diluted stream amounted to 1000 ppm on molar basis. We centred a bed consisting of 200 mg hematite nanoparticles ($\alpha\text{-Fe}_2\text{O}_3$, used as received from Sigma-Aldrich, 99.98 %, BET surface area of $39.02 \text{ m}^2/\text{g}$, pore volume of $0.1035 \text{ cm}^3/\text{g}$, < 50 nm) inside the quartz reactor tube and placed the tube into an electrically heated three-zone horizontal furnace with the bed located in a well-defined isothermal reaction zone (cf. Figure 5.1a, zone 2, 300 mm). To maintain an exact residence time, we increased the length of the reaction zone by adjusting the inner (9.5 mm OD) rods. This helped accommodate the bed volume of Fe_2O_3 nanoparticles (estimated from mass and density) without altering the overall volume of the reaction zone. We metered the flow of N_2 and SA corresponding to oxygen-fuel equivalent ratio λ of 0.8 (i.e., moderately fuel rich condition, also expressed as the fuel-oxygen equivalence ratio Φ of 1.25) based on the stoichiometry of Equation 5.1.



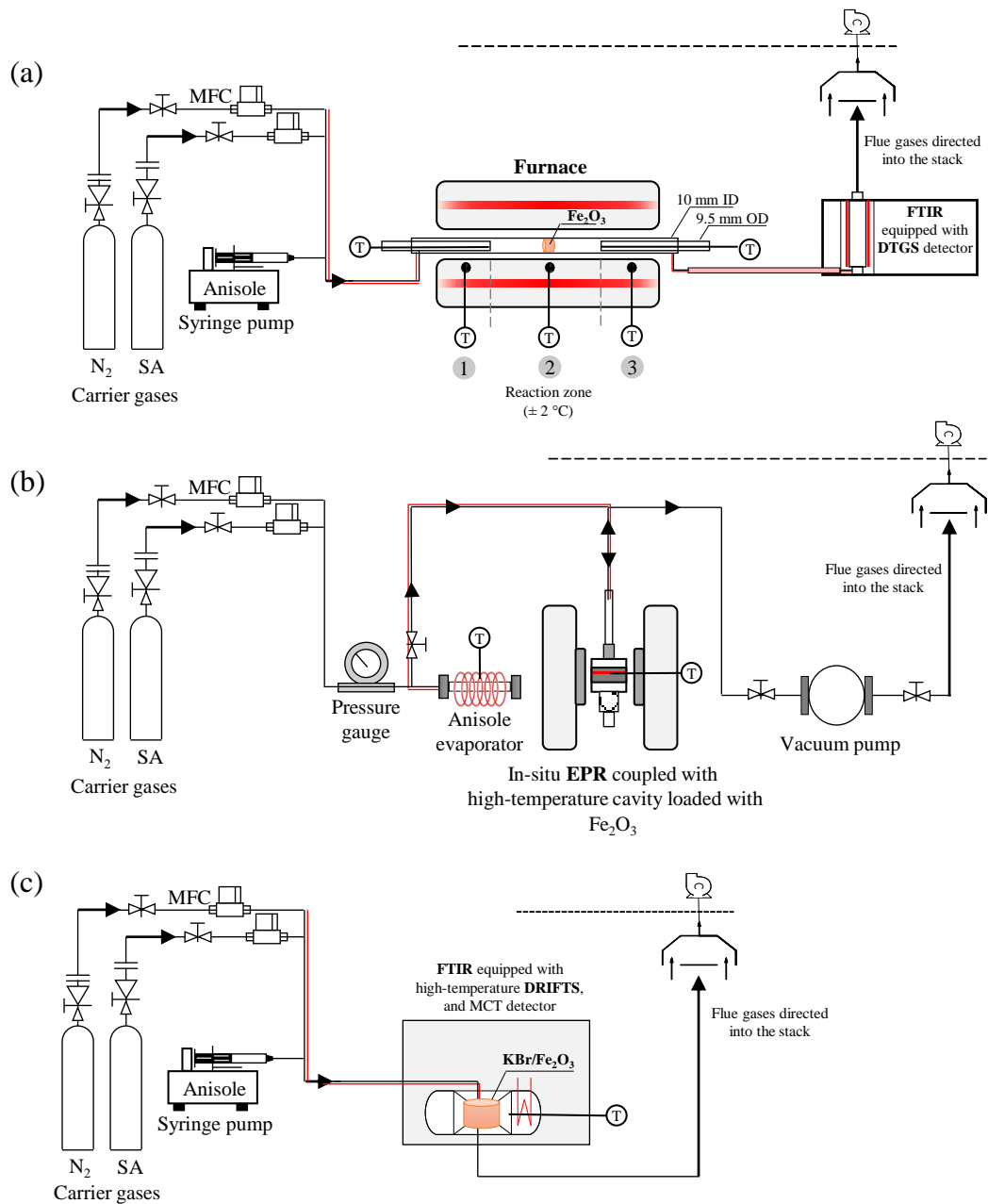
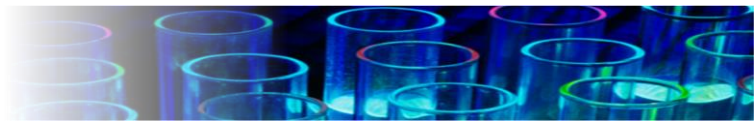


Figure 5.1. Schematic of experimental packed-bed reactor (a), EPR (b), and DRIFTS (c) setups. All data are logged automatically via computer systems.

The premixed charge of the fuel and oxidiser entered the reaction zone under ambient pressure, amounting to a constant residence time of 2.0 s. Charles' temperature-volume relationship served to adjust the gas flow rates metered by the mass flow controllers (MFC, operated at the room temperature) with the gases preheated just before the reactor entry. Similarly, we



employed a mass balance to convert the flow rate of the fuel needed for the predefined concentration at isothermal reaction temperature, into the corresponding set-values at room temperature.

An online Fourier transform infrared (FTIR) spectroscopy monitored the gaseous product species exiting the tubular reactor. The reactor was linked via an electrically heated transfer line (3.175 mm ID×300 mm) to a small volume (100 mL) 2.4 m path-length online gas-sampling cell (Pike) placed inside an FTIR compartment. Both the sample line and the sampling cell remained at 170 °C, to eliminate condensation of volatile products prior and during the analysis. The spectrometer averaged 64 accumulated scans per spectrum at 1 cm⁻¹ resolution within 7.5 min. Therefore, the duration of the experiment at each temperature amounts to approximately 7.5 min. The experimental error was estimated based on the standard deviation of four repeated runs. The nanoparticle residues, as well as the neat control sample, were tested using X-ray powder diffraction (PXRD) technique on GBC eMMA instrument. The PXRD method operated within the scanning angle (2θ) range of 10 ° - 70 °, at a regular step size of 0.010 ° and speed of 1° min⁻¹, using a Ni filtered Cu Kα1 radiation (λ = 1.5406 Å). The voltage and current settings corresponded to 35 mV and 28 mA, respectively. Crystal Impact Match! Software served to identify the diffraction patterns (phases) of iron oxides nanoparticles.

5.2.2 Electron paramagnetic resonance

EPR (Bruker EMX Plus 10/2.7) coupled to a high-temperature cavity (ER4114HT) equipped with cooling-side plates facilitated the in-situ detection of the formation of phenoxy radicals



on α -Fe₂O₃ surface during its reaction with anisole. The EPR spectra represent the average of 5 scans at a resonant frequency of 9.76 GHz. The spectrometer operated at the following settings: microwave power of 20 mW, modulation frequency of 100 kHz, modulation amplitude of 3 G, sweep width of 3000 G, time constant of 0.01 ms, conversion time of 50 ms, sweep time of 100 s, receiver gain of 2×10^5 , 10000 number of data points, and a centre field of 3000.0 G. The standard deviation in the relative EPR intensity amounted to ± 10 %. As shown in Figure S1b, we applied a custom vacuum exposure system to allow anisole vapour to enter the critically-coupled cavity chamber at a pre-set temperature.

5.2.3 Diffuse reflectance infrared Fourier transform spectroscopy

Agilent Cary 670 FTIR spectrometer combined with a gas-purged PIKE Technologies DiffusIR accessory with gold-coated optical components served to study the surface reaction of anisole on α -Fe₂O₃ nanoparticles. We conducted the experiments under steady conditions and temperature-based total gas flow rate of 100 mL min⁻¹, adjusting the pump rate of anisole, synthetic air and N₂ to oxygen-fuel equivalent ratio $\lambda=0.8$ based on Equation 5.1. The sample preparation step applied potassium bromide (KBr) powder as a spectroscopically-pure matrix to dilute the α -Fe₂O₃ nanoparticles to 2 % (w/w). We employed vortex mixing to enhance the particle size consistency. Portions of 50 mg of the resulting samples were placed inside the environment chamber, sealed with zinc selenide (ZnSe) window, heated up to the desired temperature, before pumping anisole into the preheated stream of the carrier gases. The spectrometer operated at 4 cm⁻¹, averaged 24 accumulated scans per spectrum, resulting in temporal resolution of 55 s on mercury cadmium telluride (MCT) detector.



5.2.4 Computational details

DMol³ package [38] afforded all structural optimisations and energy calculations. The theoretical approach involved the generalised gradient approximation (GGA) of the Perdew–Burke–Ernzerhof (PBE) functional [39], with the total energy convergence tolerance of 1×10^{-6} Ha. The electronic core treatment included all electrons and deployed a double numerical plus polarisation (DNP) basis set [40] and a global cut-off of 4.1 Å. The calculated energies were modified by the Tkatchenko and Scheffler [41] dispersion correction term so as to account for any non-bonding interactions in the investigated systems. All energetic values are reported at 298.15 K.

The calculations involved a modelled dehydrated cluster of stoichiometric neutrally-charged α -Fe₆O₉, i.e., (Fe₂O₃)_{n=3} obtained from bulk α -Fe₂O₃. A recent ab initio atomistic thermodynamic study [19] illustrated that, the most stable termination of hematite surface, i.e. α -Fe₂O₃(0001), contains surface Fe-O bonds, which are also present in the considered cluster. All Fe-O bonds are electronically equivalent, as follows from the inspection of the Hirshfeld charges and the Mayer bond orders listed in our previous study [42]. Furthermore, interatomic Fe-O and Fe-Fe distances in the Fe₂O₃ cluster reasonably match the corresponding distances in bulk α -Fe₂O₃, 1.92/2.13 Å and 2.86 Å, respectively [43]. As demonstrated in the article, the decomposition of C-OCH₃ or OCH₂-H bonds take place on the exposed Fe-O linkages in the cluster. Reaction rate constants were estimated based on the conventional transition state theory (TST), We fit reaction rate constants to the two-parameters Arrhenius formula, $k(T) = A \exp(-E_a/RT)$, over the temperature range of 300 K to 1000 K, according to:



$$k(T) = \frac{k_B T}{\sigma_e h} \exp\left(\frac{\Delta S^\ddagger}{R}\right) \exp\left(\frac{-\Delta H^\ddagger}{RT}\right) \quad 5.2$$

Where: k_B is Boltzmann's constant, h signifies Plank's constant, R is the universal gas constant. ΔS^\ddagger and ΔH^\ddagger stand for temperature-dependented entropy and enthalpy of activation, correspondingly. σ_e represents the reaction degeneracy number. Dmol3 compute the vibrational frequencies to calculate the entropy of each of the reactants and transition states. The enthalpy (at the desired temperature) has been competed relatively to the zero-point energy at 0 K.

5.3 Results and Discussion

5.3.1 Assessment of thermal decomposition of anisole in presence of Fe_2O_3

Table S5.1 assembles the detailed vibrational modes of vaporised anisole. Previous studies on pyrolysis and oxidation of the fuel [44–46] showed that the thermal decomposition pathway begins by dissociation of the most labile, i.e., O–CH₃, bond in the molecule, with phenol, cresols and toluene appearing as the major cyclic intermediate species. Figure 5.2 depicts the infrared spectra of species exiting the reactor operated under various temperature and carrier-gas conditions. The black-coloured spectra represent detectable changes to original spectrum (grey spectra) of anisole. As the reaction temperature increases, anisole converts into cresols, toluene, carbon monoxide (CO), and carbon dioxide (CO₂), depending on the composition of the inlet gas mixture. The conversion of anisole plotted in Figure 5.3 follows from the height of the O–CH₃ stretch (wavenumber = 1046 cm⁻¹), as measured by FTIR at the reactor outlet



and from application of Equation 5.3. Abs_i denotes the initial concentration (proportional to absorbance value at 1046 cm^{-1}) at the reactor inlet, and Abs_T stands for the concentration of the fuel at the reactor outlet.

$$X = \left(\frac{Abs_i - Abs_T}{Abs_i} \right)_{i=1046\text{ cm}^{-1}} \times 100\% \quad 5.3$$

In accordance with previous work [44], the onset temperature for neat decomposition (Figure 5.2a and 5.2b) of anisole remains approximately the same at $500\text{ }^\circ\text{C}$ and $520\text{ }^\circ\text{C}$ with or without O_2 , respectively. This is because under both pyrolytic and oxidative conditions, the relatively weak bond between the oxygen and the methyl group, $\sim 272\text{ kJ mol}^{-1}$ [47] governs the unimolecular decomposition of anisole to phenoxy and methyl radicals. However, oxygen rapidly oxidises the hydrocarbon fragments of anisole into CO , CO_2 and H_2O , as temperature increases (Figure 2b). Similarly, under N_2 (Figure 5.2c), the estimated onset temperature of the decomposition process appears approximately the same, noting that at high temperature, the hydrocarbons rapidly consume the O-content of Fe_2O_3 in a fashion that changes the product selectivity. This process is similar to that of chemical-looping combustion of coal utilising metal oxides as oxygen carriers [48,49] and typically applied to the carbothermic processing of iron ore in blast furnaces to produce metallic iron [50].

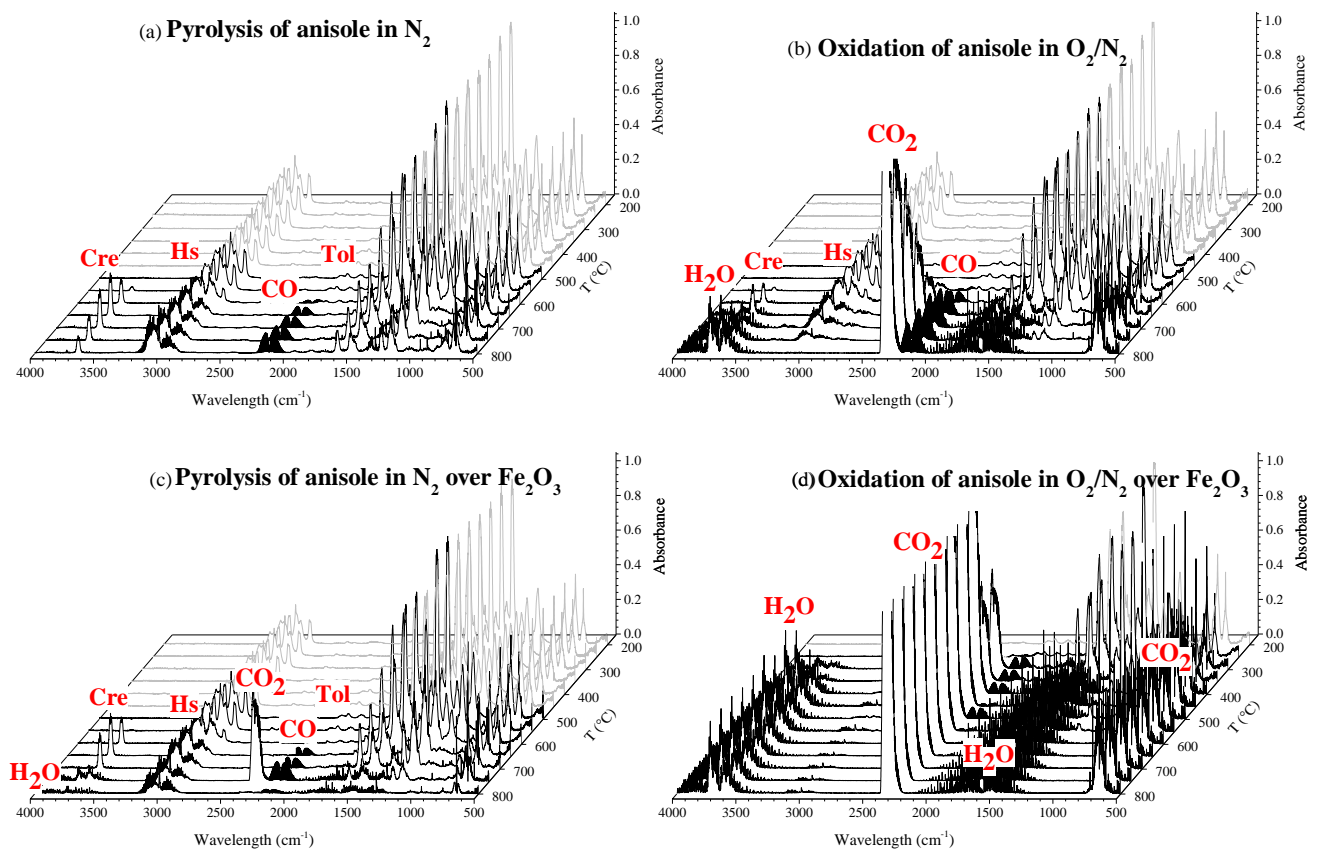
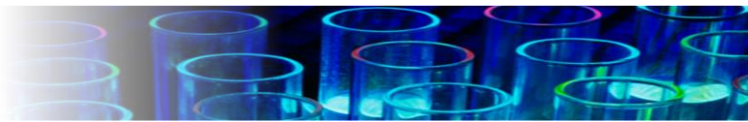


Figure 5.2. Recorded FTIR spectra of pyrolysis of anisole in N_2 (a), oxidation of anisole in O_2/N_2 (b), pyrolysis of anisole in N_2 over Fe_2O_3 (c), and oxidation of anisole in O_2/N_2 over Fe_2O_3 (d). Dark-coloured spectra denote detectable changes to the original (grey-coloured) anisole spectrum. Cre, Tol and Hs represent cresol, toluene and other hydrocarbons, respectively.

Enlarged versions of individual charts are provided in the SMM.

As expected, the case of anisole- $(Fe_2O_3-O_2/N_2)$ displays an interesting conversion profile. The extrapolated ignition temperature, estimated based on extrapolated onset temperature, reduces to around $220\text{ }^\circ\text{C}$, as a result of initial radical channels that comprise surface-mediated reactions based on our model, later described in Section 5.3.3. Moreover, from geochemical and mineralogical evidence, those reactions can sustain rapid thermal decomposition, releasing volatile compounds that feed the energy loop in coal-seam fires [1]. The formation routes as well as the enthalpic provisions of these reactions are reported in the following sections.



The PXRD patterns in Figure 5.4 characterise the nanoparticles recovered after each experiment. As revealed by Crystal Impact Match! Software, the clean (as-received) nanoparticles display lattice configurations matching α -Fe₂O₃ [51,52], with no detectable impurity. Under the combustion (and pyrolysis) scenarios, the nature of the α -Fe₂O₃ nanoparticles depends on the thermodynamic stability of crystal surfaces at a given chemical potential of oxygen. Based on the phase diagram of iron oxides [53], α -Fe₂O₃, Fe₃O₄ and FeO constitute the expected oxidation states at temperatures above 570 °C and for lean oxygen concentration. The spent solid residues obtained after pyrolysis indicate thermal reduction of Fe₂O₃ at 800 °C, with a hump in the diffractogram, centred around 22°, reflecting the formation of amorphous carbon. This agrees with the FTIR scan of product species in Figure 2c wherein the hydrocarbons converted selectively and rapidly into CO₂ at 750 °C, with CO₂ formation terminated at 800 °C after consumption of the entire oxygen present in α -Fe₂O₃. A practical example of such reactions is the carbothermic processing of Fe₂O₃ with carbon and/or hydrocarbons during the production of metallic iron [50], exhibiting an almost-complete reduction of Fe₂O₃ into Fe [54,55] with the appearance of char residue on the surface. Oxidative conditions preserve the lattice oxygens, as it is shown in Section 3.3. The reactions have been facilitated by oxygen absorbed on the ferryl iron [56]. PXRD diffractograms reveal the appearance of magnetite (Fe₃O₄) and FeO phases [57].

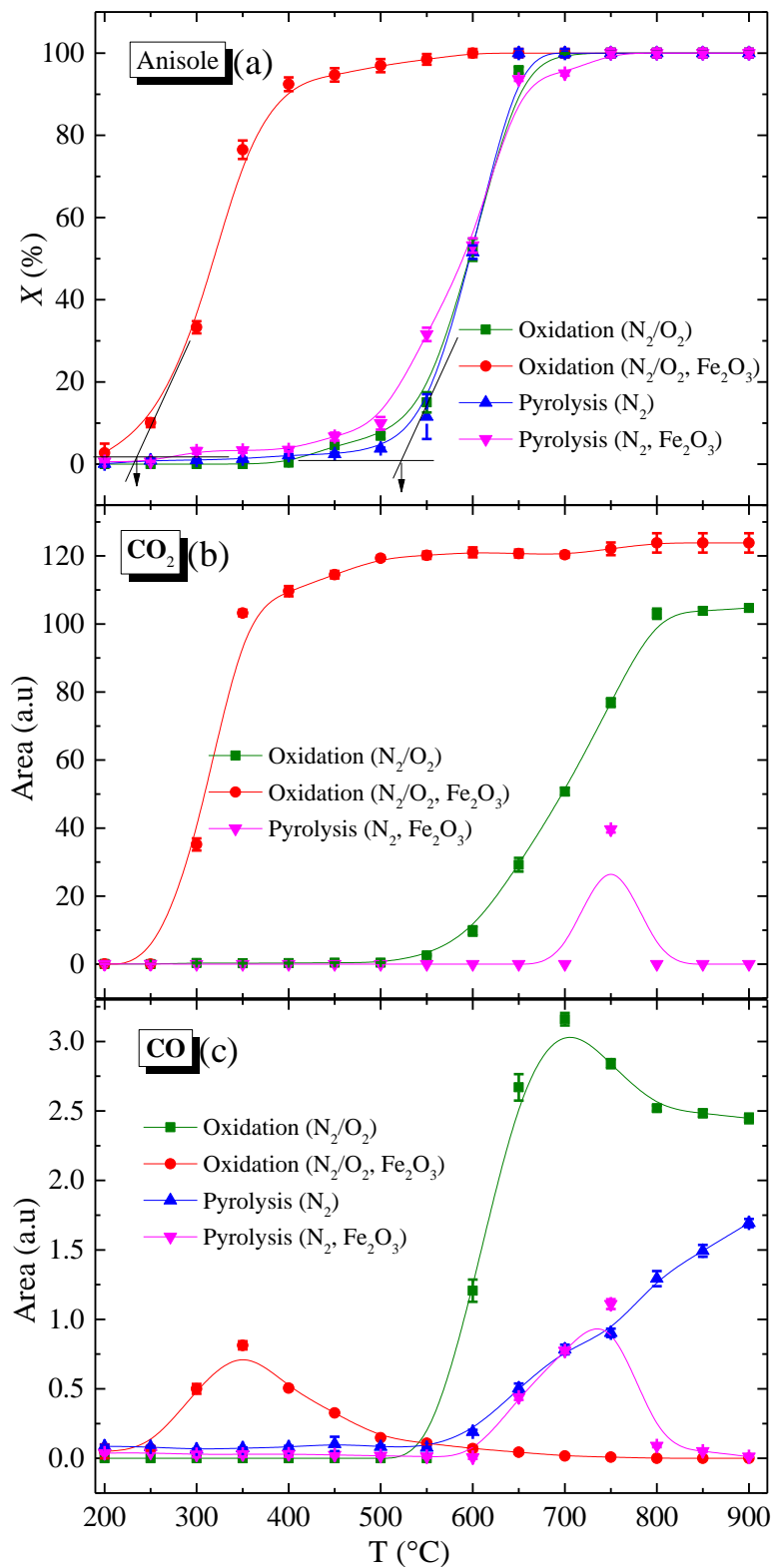


Figure 5.3. Percent conversion (X , %) of anisole under various experimental conditions and relative formation of CO and CO_2 . Points are connected by basis-spline function, as guide to the eye, and extrapolated in (a) for determination of the onset ignition temperatures.

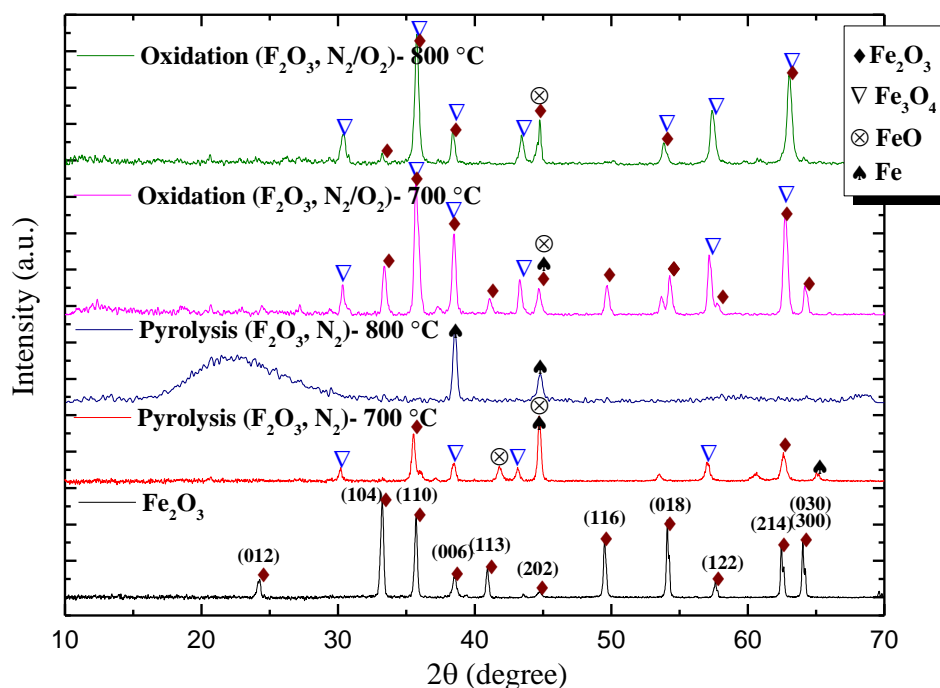
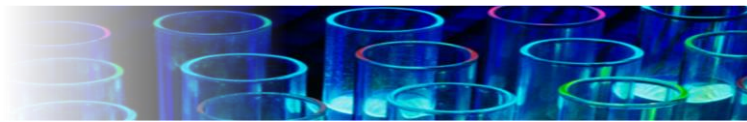


Figure 5.4. XRD pattern of Fe_2O_3 nanoparticle before and after thermal reactions.

5.3.2 Low-temperature formation of environmentally-persistent free radicals (EPFR)

EPFR represent a class of combustion pollutants arising through a series of surface-mediated reactions between transition metals and organic precursors [58]. EPFR display prolonged life span in an ambient environment, leading to diverse environmental and health implications. The present context describes the formation of these species via the interaction of anisole with Fe_2O_3 as it occurs (i) on the fly ash in the cooling-down zones of combustion systems [58–60], (ii) in iron-rich soils contaminated with polycyclic aromatic hydrocarbons (PAHs) [61,62], and (iii) during the low-temperature oxidation of coal proceeding via free-radical chain reactions. Thermodynamically, the formation of surface-bound radicals favours successive propagation reactions as it usually incurs high reaction exothermicity.



The electron paramagnetic resonance study elucidated the nature of the free radicals formed during the low-temperature interaction of Fe_2O_3 with anisole. Figure 5.5 depicts the formation of EPFR at low temperatures (i.e., below 200 °C). The EPR spectrum of bulk $\alpha\text{-Fe}_2\text{O}_3$ nanoparticles exhibits two resonance signals, i.e., $g \approx 4.61$ and $g \approx 2.32$ at 100 °C (cf. Figure 5.5a, also identical to spectrum recorded at 25 °C but not shown in the figure). The Fe^{3+} ions in Fe_2O_3 have a d^5 configuration with 6S exemplifying free ions in the ground state with no spin-orbit interaction [63]. At 100 °C, a line broadening appears as reported by Piazzesi et al. [64] with iron samples in the nanometre range. The second g value shows the transition of isolated Fe^{3+} sites in strong rhombic or axial distortion, typically known as Kramers doublets $|\pm 1/2, |\pm 3/2\rangle$ and $|\pm 5/2\rangle$ when the free ions in the 6S state split up [65].

The quenching of the signal recorded in Figure 5.5b (relatively to Figure 5.5a) after the contact of anisole represents the partial interaction of phenoxy radical with Fe (II) centres, signifying the antiferromagnetic coupling. Furthermore, according to Vajerano et al. [66], the radical signal originates from the electronic interaction between the chemisorbed species and the metal-ion centres. This interaction emerges because of a one-electron transfer from the adsorbed molecule towards the metal centre and the formation of radical species. Depending on the relative concentration of this radical, one observes an overall shift of the EPR signal. We note that, vacuuming the products at 100 °C smoothens the spike-like features of the signal; hence, such features may refer to physisorbed radicals on the surface of $\alpha\text{-Fe}_2\text{O}_3$. Figure 5.5c demonstrates the absence of low-temperature radicals in pyrolytic reactions of anisole with Fe_2O_3 , supporting the previously explained results collected in the experiments performed with the packed-bed reactor.

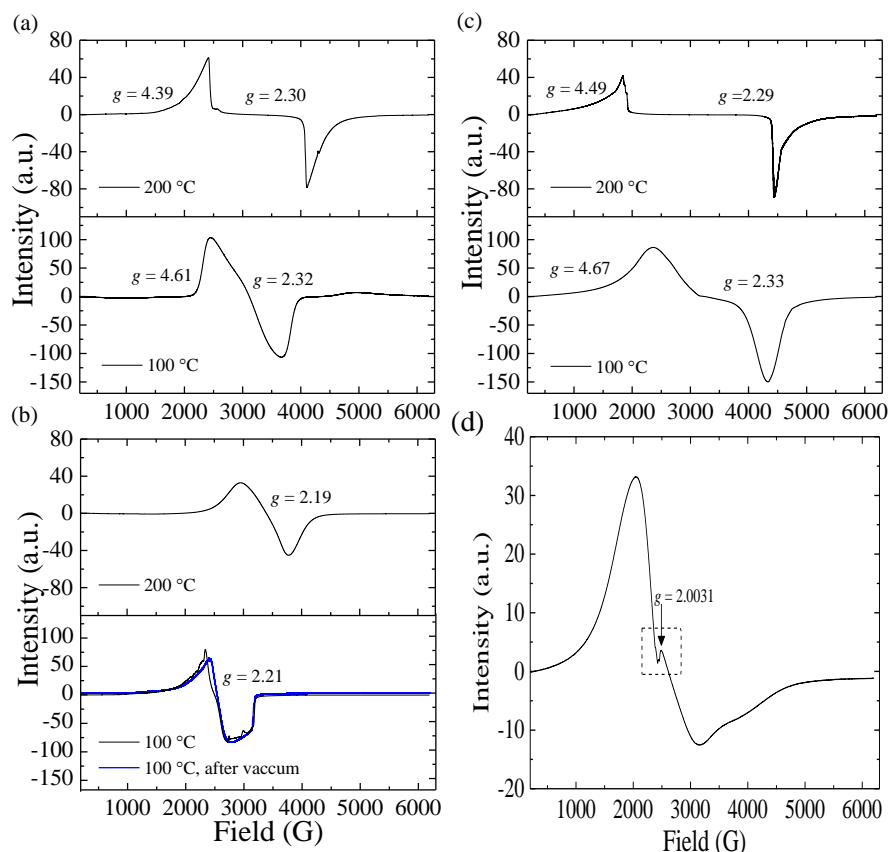


Figure 5.5. EPR spectrum of α - Fe_2O_3 nanoparticles (a), α - Fe_2O_3 nanoparticles exposed to anisole under oxidation atmosphere (b), and α - Fe_2O_3 nanoparticles exposed to anisole under pyrolytic condition. The pane (d) represents the EPR spectrum of Fe_2O_3 – anisole suspension, recorded after 24 h at 25 °C.

Furthermore, to evaluate the tendency of these reactions to induce autoxidation under atmospheric conditions, we obtained another spectrum at room temperature. We suspended α - Fe_2O_3 nanoparticles in anisole, sonicated the suspension for 2 min, and left it under ambient condition for 24 h. The resulting spectrum, shown in Figure 5d is typical of EPFR displaying a measured g factor that amounts to 2.0031, i.e., the characteristic value of phenoxy radical [59]. The adsorbate signal centred at ~ 3000 Gauss with a line-width (ΔH_{p-p}) of ~ 7 to 12 Gauss further confirms the appearance of an aromatic radical species.

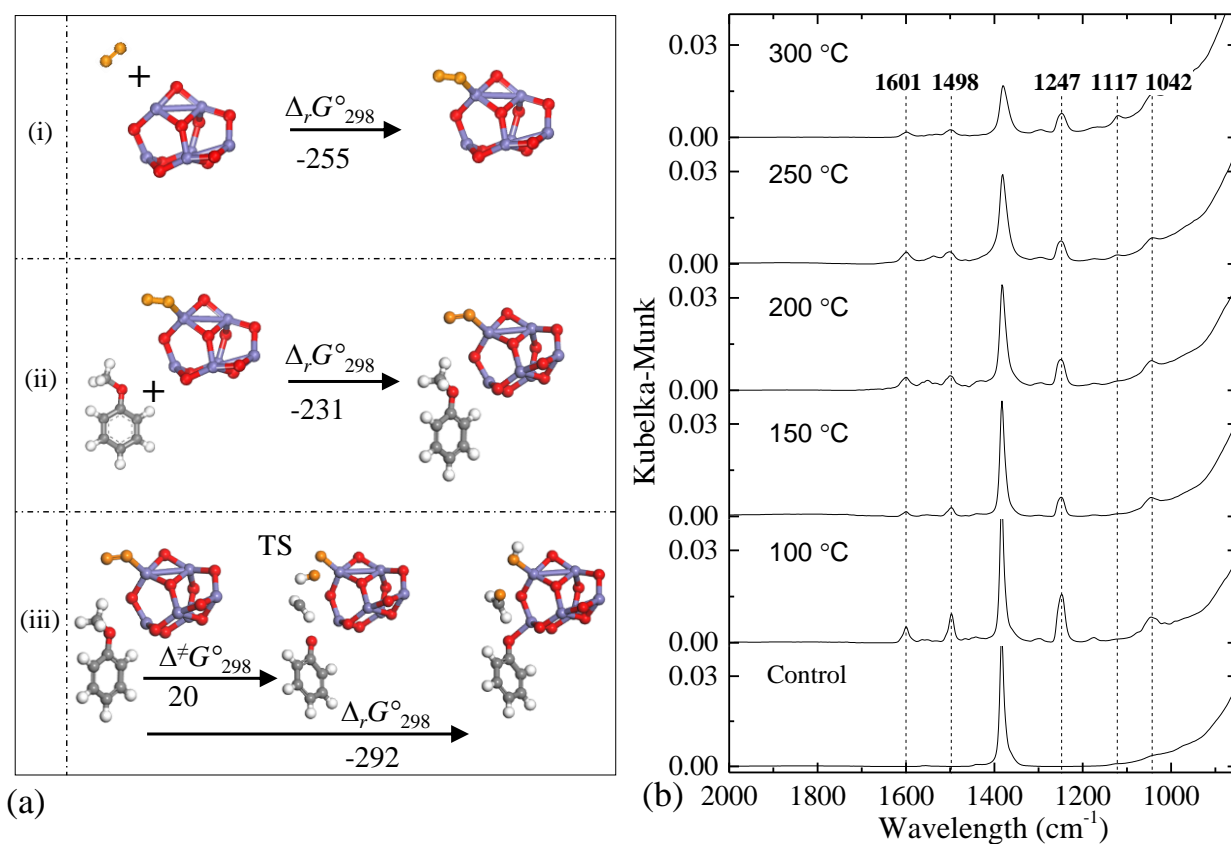
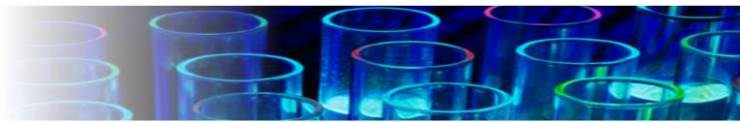


Figure 5.6. Modelling of the dissociative addition of anisole on the oxygenated Fe₂O₃ cluster (a); oxygenation of the Fe₂O₃ cluster (i), physisorption of anisole on the oxygenated cluster (ii), followed by chemisorption (iii), and DRIFTS adsorption spectra of anisole on Fe₂O₃ surface (control) after 3 h at different temperature (b). Values are in kJ mol⁻¹ with respect to the initial reactant at 298.15 K. Atmospheric oxygen atoms are denoted by an orange colour. Estimated rate parameters for (iii) correspond to E_a of 18 kJ mol⁻¹ and A of 2.7×10^{12} M⁻¹ s⁻¹. Note that CH₂O physisorbs, rather than chemisorps, onto the surfaces. A very weak signal appears for the wave number in excess of 3000 cm⁻¹, due to stretches in the hydroxyl group; see Supplemental Material for details.

5.3.3 Chemisorption of anisole on oxygenated Fe₂O₃ cluster

Our DFT calculations illustrate the mechanism governing the formation of the surface radicals. Figure 5.6a depicts an optimised structure of the dehydrated cluster that contains threefold



coordinated iron atoms and twofold coordinated oxygen atoms, as well as molecular adsorbates. Chemisorption of oxygen on α -Fe₂O₃ cluster constitutes a highly exothermic reaction releasing about 294 kJ (mol Fe₂O₃)⁻¹ ($\Delta_r H_{298}^0$), in agreement with the [0001] terminations reported in the literature [19,20]. Anisole, a weak Lewis base adsorbs on the acidic centre of α -Fe₂O₃ becoming vulnerable towards any nucleophilic attack. The O₂ primarily bonded to ferryl ion represents the only reactive nucleophile. This O atom attacks the methyl group of the nearest physisorbed anisole molecule. This step results in the formation of hydroxy and phenoxy radicals bound to the neighbouring ferryl ion with Arrhenius parameters (fitted from 25 °C to 727 °C based on DFT calculation) of E_a of 18 kJ mol⁻¹ and a preexponential A factor of $2.7 \times 10^{12} \text{ M}^{-1}\text{s}^{-1}$. In-situ surface vibrational analysis (DRIFTS) support the mechanism as the spectra in Figure 5.6b show two bands appearing at 1601 and 1498 that result from the strong interaction of anisole methoxy oxygen with Fe ion (Lewis acid site) [67], and the bands at 1247 and 1042 are for C-O and O-CH₂ stretches, respectively. Refer to Supplemental Material for the full-range spectra.

5.4 Conclusions

In this contribution, we addressed the effect of α -Fe₂O₃ on the ignition features of coal surrogate (anisole) as well as the formation of a phenoxy radical, an environmentally persistent free radical, that forms in the initiation channels. The main conclusions are as follows: (i) α -Fe₂O₃ particles reduced the ignition temperature of anisole by more than 300 °C, (ii) EPFR formed at low temperatures (i.e., 25 °C) with a measured g factor amounting to 2.0031, i.e., the characteristic value of phenoxy radical, and (iii) oxygen bonded to the α -Fe₂O₃ surface attacks the methyl group of the nearest physisorbed anisole molecule resulting in the formation of



hydroxy and phenoxy with rate constant of $k(T)$ ($M^{-1}s^{-1}$) = $2.7 \times 10^{12} \exp(-2114/T$ (K)). Our results have demonstrated that, the oxidation of aryl-alkyl ethers present in coal matrix, in reactions catalysed by particles of α -Fe₂O₃, may indeed be responsible for the initiation of spontaneous fires of coal seams, mined coal and cleaning rejects from coal processing. We recommend further work on coal residues, as well as the identification of other factors that may contribute to the low-temperature ignition phenomenon in mine sites.

Supplemental material

The Supporting Information is included in Chapter 10 (Appendix I) of the thesis. Details of experimental and computational methodologies. Table S5.1. IR bands of vaporised anisole, 1000 ppm in 2.4 m path-length gas cell, and Figures S5.2-S5.5. Full range DRIFTS spectra of Fe₂O₃ (control, dashed line) under various experimental conditions.

5.5 References

- [1] Sehn JL, de Leão FB, da Boit K, Oliveira MLS, Hidalgo GE, Sampaio CH, et al. Nanomineralogy in the real world: A perspective on nanoparticles in the environmental impacts of coal fire. *Chemosphere* 2016;147:439–43. doi:10.1016/j.chemosphere.2015.12.065.
- [2] Engle MA, Radke LF, Heffern EL, O’Keefe JMK, Hower JC, Smeltzer CD, et al. Gas emissions, minerals, and tars associated with three coal fires, Powder River Basin, USA. *Science of The Total Environment* 2012;420:146–59. doi:10.1016/j.scitotenv.2012.01.037.
- [3] Rein G. Smouldering Fires and Natural Fuels. 2013. doi:https://dx.doi.org/10.1002/9781118529539.ch2.
- [4] Stracher GB, Prakash A, Rein G. Coal and Peat Fires: A Global Perspective: Volume 4: Peat–Geology, Combustion, and Case Studies. Elsevier; 2015.



- [5] Carras JN, Day SJ, Saghafi A, Williams DJ. Greenhouse gas emissions from low-temperature oxidation and spontaneous combustion at open-cut coal mines in Australia. *International Journal of Coal Geology* 2009;78:161–8. doi:10.1016/j.coal.2008.12.001.
- [6] Finkelman RB. Potential health impacts of burning coal beds and waste banks. *International Journal of Coal Geology* 2004;59:19–24. doi:10.1016/j.coal.2003.11.002.
- [7] Querol X, Izquierdo M, Monfort E, Alvarez E, Font O, Moreno T, et al. Environmental characterization of burnt coal gangue banks at Yangquan, Shanxi Province, China. *International Journal of Coal Geology* 2008;75:93–104. doi:10.1016/j.coal.2008.04.003.
- [8] Ribeiro J, Flores D, Ward CR, Silva LFO. Identification of nanominerals and nanoparticles in burning coal waste piles from Portugal. *Science of The Total Environment* 2010;408:6032–41. doi:10.1016/j.scitotenv.2010.08.046.
- [9] O’Keefe JMK, Neace ER, Lemley EW, Hower JC, Henke KR, Copley G, et al. Old Smokey coal fire, Floyd County, Kentucky: Estimates of gaseous emission rates. *International Journal of Coal Geology* 2011;87:150–6. doi:10.1016/j.coal.2011.06.005.
- [10] Stracher GB, Prakash A, Sokol EV. *Coal and Peat Fires: A Global Perspective*. Photographs and multimedia tours. Newnes; 2012.
- [11] UNESCO. *Spontaneous Coal Seam Fires: Mitigating a Global Disaster*. Beijing, China: United Nations Education, Scientific, and Cultural Organization; 2008.
- [12] Rein G. *Smouldering combustion phenomena in science and technology* 2009.
- [13] Wang H, Dlugogorski BZ, Kennedy EM. Coal oxidation at low temperatures: oxygen consumption, oxidation products, reaction mechanism and kinetic modelling. *Progress in Energy and Combustion Science* 2003;29:487–513.
- [14] Wang D, Xin H, Qi X, Dou G, Qi G, Ma L. Reaction pathway of coal oxidation at low temperatures: a model of cyclic chain reactions and kinetic characteristics. *Combustion and Flame* 2016;163:447–60. doi:10.1016/j.combustflame.2015.10.019.
- [15] Hadden RM, Rein G, Belcher CM. Study of the competing chemical reactions in the initiation and spread of smouldering combustion in peat. *Proceedings of the Combustion Institute* 2013;34:2547–2553.



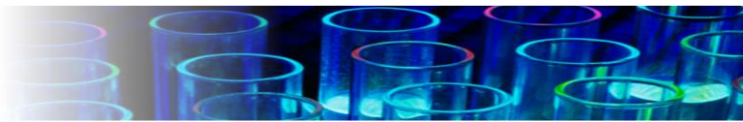
- [16] Wang H, Dlugogorski BZ, Kennedy EM. Analysis of the mechanism of the low-temperature oxidation of coal. *Combustion and Flame* 2003;134:107–117.
- [17] Singh RVK. Spontaneous heating and fire in coal mines. *Procedia Engineering* 2013;62:78–90.
- [18] Xin-hai NHZ. Research on the Coal Self-ignition and Prevention Techniques Classification [J]. *Industrial Safety and Environmental Protection* 2007;10:018.
- [19] Huang X, Ramadugu SK, Mason SE. Surface-Specific DFT+ U Approach Applied to α -Fe₂O₃ (0001). *The Journal of Physical Chemistry C* 2016;120:4919–4930.
- [20] Tang J-J, Liu B. Reactivity of the Fe₂O₃ (0001) Surface for Methane Oxidation: A GGA+ U Study. *The Journal of Physical Chemistry C* 2016;120:6642–6650.
- [21] Wagloehner S, Kureti S. Study on the mechanism of the oxidation of soot on Fe₂O₃ catalyst. *Applied Catalysis B: Environmental* 2012;125:158–165.
- [22] Yu D, Zhao L, Zhang Z, Wen C, Xu M, Yao H. Iron transformation and ash fusibility during coal combustion in air and O₂/CO₂ medium. *Energy & Fuels* 2012;26:3150–3155.
- [23] Goodarzi F. Mineralogy, elemental composition and modes of occurrence of elements in Canadian feed-coals. *Fuel* 2002;81:1199–213. doi:10.1016/S0016-2361(02)00023-6.
- [24] Deng J, Ma X, Zhang Y, Li Y, Zhu W. Effects of pyrite on the spontaneous combustion of coal. *International Journal of Coal Science & Technology* 2015;2:306–311.
- [25] Silva LF, Kátia M. Nanominerals and nanoparticles in feed coal and bottom ash: implications for human health effects. *Environmental Monitoring and Assessment* 2011;174:187–197.
- [26] Cutruneo CM, Oliveira ML, Ward CR, Hower JC, de Brum IA, Sampaio CH, et al. A mineralogical and geochemical study of three Brazilian coal cleaning rejects: demonstration of electron beam applications. *International Journal of Coal Geology* 2014;130:33–52.
- [27] Dias CL, Oliveira MLS, Hower JC, Taffarel SR, Kautzmann RM, Silva LFO. Nanominerals and ultrafine particles from coal fires from Santa Catarina, South Brazil. *International Journal of Coal Geology* 2014;122:50–60. doi:10.1016/j.coal.2013.12.011.



- [28] Saikia BK, Ward CR, Oliveira ML, Hower JC, De Leao F, Johnston MN, et al. Geochemistry and nano-mineralogy of feed coals, mine overburden, and coal-derived fly ashes from Assam (North-east India): a multi-faceted analytical approach. *International Journal of Coal Geology* 2015;137:19–37.
- [29] Silva LFO, Moreno T, Querol X. An introductory TEM study of Fe-nanominerals within coal fly ash. *Science of The Total Environment* 2009;407:4972–4. doi:10.1016/j.scitotenv.2009.05.044.
- [30] Silva LFO, Macias F, Oliveira MLS, Boit MK da, Waanders F. Coal cleaning residues and Fe-minerals implications. *Environ Monit Assess* 2011;172:367–78. doi:10.1007/s10661-010-1340-8.
- [31] Ishitha K, Ramakrishna PA. Studies on the role of iron oxide and copper chromite in solid propellant combustion. *Combustion and Flame* 2014;161:2717–28. doi:10.1016/j.combustflame.2014.03.015.
- [32] Yang S, Song X, Zhang P, Gao L. Heating-rate-induced porous α -Fe₂O₃ with controllable pore size and crystallinity grown on graphene for supercapacitors. *ACS Applied Materials & Interfaces* 2014;7:75–79.
- [33] Yu W-J, Hou P-X, Zhang L-L, Li F, Liu C, Cheng H-M. Preparation and electrochemical property of Fe₂O₃ nanoparticles-filled carbon nanotubes. *Chemical Communications* 2010;46:8576–8578.
- [34] Ghorishi SB, Lee CW, Jozewicz WS, Kilgroe JD. Effects of fly ash transition metal content and flue gas HCl/SO₂ ratio on mercury speciation in waste combustion. *Environmental Engineering Science* 2005;22:221–231.
- [35] Küçük A, Kadioğlu Y, Gülaboğlu MŞ. A study of spontaneous combustion characteristics of a turkish lignite: particle size, moisture of coal, humidity of air. *Combustion and Flame* 2003;133:255–61. doi:10.1016/S0010-2180(02)00553-9.
- [36] Li G, Li L, Shi L, Jin L, Tang Z, Fan H, et al. Experimental and theoretical study on the pyrolysis mechanism of three coal-based model compounds. *Energy & Fuels* 2014;28:980–986.



- [37] Wang H, Dlugogorski BZ, Kennedy EM. Tests for spontaneous ignition of solid materials, Woodhead Publishing Limited; 2006.
- [38] Delley B. From molecules to solids with the DMol³ approach. *The Journal of Chemical Physics* 2000;113:7756–7764.
- [39] Perdew JP, Burke K, Ernzerhof M. Generalized gradient approximation made simple. *Physical Review Letters* 1996;77:3865.
- [40] Delley B. An all-electron numerical method for solving the local density functional for polyatomic molecules. *The Journal of Chemical Physics* 1990;92:508–517.
- [41] Tkatchenko A, Scheffler M. Accurate molecular van der Waals interactions from ground-state electron density and free-atom reference data. *Physical Review Letters* 2009;102:073005.
- [42] Altarawneh M, Ahmed OH, Jiang Z-T, Dlugogorski BZ. Thermal Recycling of Brominated Flame Retardants with Fe₂O₃. *J Phys Chem A* 2016;120:6039–47. doi:10.1021/acs.jpca.6b04910.
- [43] Rozenberg GK, Dubrovinsky LS, Pasternak MP, Naaman O, Le Bihan T, Ahuja R. High-pressure structural studies of hematite Fe₂O₃. *Physical Review B* 2002;65:064112.
- [44] Nowakowska M, Herbinet O, Dufour A, Glaude P-A. Detailed kinetic study of anisole pyrolysis and oxidation to understand tar formation during biomass combustion and gasification. *Combustion and Flame* 2014;161:1474–1488.
- [45] Hemings EB, Bozzano G, Dente M, Ranzi E. Detailed kinetics of the pyrolysis and oxidation of anisole. *Chem Eng Trans* 2011;24:61–66.
- [46] Pecullan M, Brezinsky K, Glassman I. Pyrolysis and Oxidation of Anisole near 1000 K. *J Phys Chem A* 1997;101:3305–16. doi:10.1021/jp963203b.
- [47] Wagnon SW, Thion S, Nilsson EK, Mehl M, Serinyel Z, Zhang K, et al. The Development and Validation of a Chemical Kinetic Model for Anisole, a Compound to Represent Biomass Pyrolysis Fuels. Lawrence Livermore National Laboratory (LLNL), Livermore, CA; 2017.

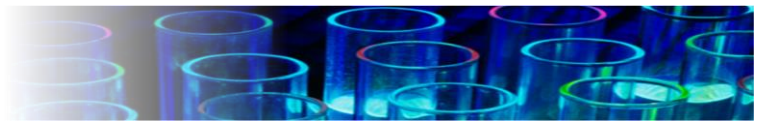


- [48] Zhang S, Saha C, Yang Y, Bhattacharya S, Xiao R. Use of Fe₂O₃-containing industrial wastes as the oxygen carrier for chemical-looping combustion of coal: effects of pressure and cycles. *Energy & Fuels* 2011;25:4357–4366.
- [49] Shi S, Dong C, Qin W, Wang L, Li W, Yang Y. Experimental and theoretical study of Fe₂O₃/coal ash oxygen carrier in CLC system. *CIESC Journal* 2012;12:045.
- [50] Biswas AK. *Principles of Blast Furnace Ironmaking: theory and practice*. Cootha; 1981.
- [51] Xu S, Habib A, Gee S-H, K. Hong Y, McHenry M. Spin orientation, structure, morphology, and magnetic properties of hematite nanoparticles. *Journal of Applied Physics* 2015;117:17A315. doi:10.1063/1.4914059.
- [52] Jahagirdar AA, Dhananjaya N, Monika DL, Kesavulu CR, Nagabhushana H, Sharma SC, et al. Structural, EPR, optical and magnetic properties of α - Fe₂O₃ nanoparticles. *Spectrochimica Acta Part A: Molecular and Biomolecular Spectroscopy* 2013;104:512–8. doi:10.1016/j.saa.2012.09.069.
- [53] (Ken) Ostrikov K, Levchenko I, Cvelbar U, Sunkara M, Mozetic M. From nucleation to nanowires: a single-step process in reactive plasmas. *Nanoscale* 2010;2:2012–27. doi:10.1039/C0NR00366B.
- [54] Lak A, Kraken M, Ludwig F, Kornowski A, Eberbeck D, Sievers S, et al. Size dependent structural and magnetic properties of FeO–Fe₃O₄ nanoparticles. *Nanoscale* 2013;5:12286–95. doi:10.1039/C3NR04562E.
- [55] Chekli L, Bayatsarmadi B, Sekine R, Sarkar B, Shen AM, Scheckel K, et al. Analytical characterisation of nanoscale zero-valent iron: An illustrated methodological review. *Analytica Chimica Acta* 2015;903. doi:10.1016/j.aca.2015.10.040.
- [56] Grosvenor AP, Kobe BA, McIntyre NS. Examination of the oxidation of iron by oxygen using X-ray photoelectron spectroscopy and QUASES TM. *Surface Science* 2004;565:151–162.
- [57] Simeonidis K, Martinez-Boubeta C, Balcells L, Monty C, Stavropoulos G, Mitrakas M, et al. Fe-based nanoparticles as tunable magnetic particle hyperthermia agents. *Journal of Applied Physics* 2013;114:103904.



- [58] Feld-Cook EE, Bovenkamp-Langlois L, Lomnicki SM. Effect of Particulate Matter Mineral Composition on Environmentally Persistent Free Radical (EPFR) Formation. *Environ Sci Technol* 2017;51:10396–402. doi:10.1021/acs.est.7b01521.
- [59] D'Arienzo M, Gamba L, Morazzoni F, Cosentino U, Greco C, Lasagni M, et al. Experimental and Theoretical Investigation on the Catalytic Generation of Environmentally Persistent Free Radicals from Benzene. *J Phys Chem C* 2017;121:9381–93. doi:10.1021/acs.jpcc.7b01449.
- [60] Assaf NW, Altarawneh M, Oluwoye I, Radny M, Lomnicki SM, Dlugogorski BZ. Formation of environmentally persistent free radicals on α -Al₂O₃. *Environmental Science & Technology* 2016;50:11094–11102.
- [61] Jia H, Nulaji G, Gao H, Wang F, Zhu Y, Wang C. Formation and Stabilization of Environmentally Persistent Free Radicals Induced by the Interaction of Anthracene with Fe(III)-Modified Clays. *Environ Sci Technol* 2016;50:6310–9. doi:10.1021/acs.est.6b00527.
- [62] Jia H, Zhao S, Nulaji G, Tao K, Wang F, Sharma VK, et al. Environmentally Persistent Free Radicals in Soils of Past Coking Sites: Distribution and Stabilization. *Environ Sci Technol* 2017;51:6000–8. doi:10.1021/acs.est.7b00599.
- [63] Loveridge D, Parke S. Electron spin resonance of Fe³⁺, Mn²⁺, and Cr³⁺ in glasses. *Physics and Chemistry of Glasses* 1971;12:19–+.
- [64] Piazzesi G, Nicosia D, Devadas M, Kröcher O, Elsener M, Wokaun A. Investigation of HNCO adsorption and hydrolysis on Fe-ZSM5. *Catalysis Letters* 2007;115:33–39.
- [65] Goldfarb D, Bernardo M, Strohmaier KG, Vaughan DEW, Thomann H. Characterization of iron in zeolites by X-band and Q-band ESR, pulsed ESR, and UV-visible spectroscopies. *Journal of the American Chemical Society* 1994;116:6344–6353.
- [66] Vejerano E, Lomnicki S, Dellinger B. Formation and Stabilization of Combustion-Generated Environmentally Persistent Free Radicals on an Fe(III)₂O₃/Silica Surface. *Environ Sci Technol* 2011;45:589–94. doi:10.1021/es102841s.
- [67] Trunschke A, Deutsch J, Müller D, Lieske H, Quaschnig V, Kemnitz E. Nature of surface deposits on sulfated zirconia used as catalyst in the benzoylation of anisole. *Catalysis Letters* 2002;83:271–279.

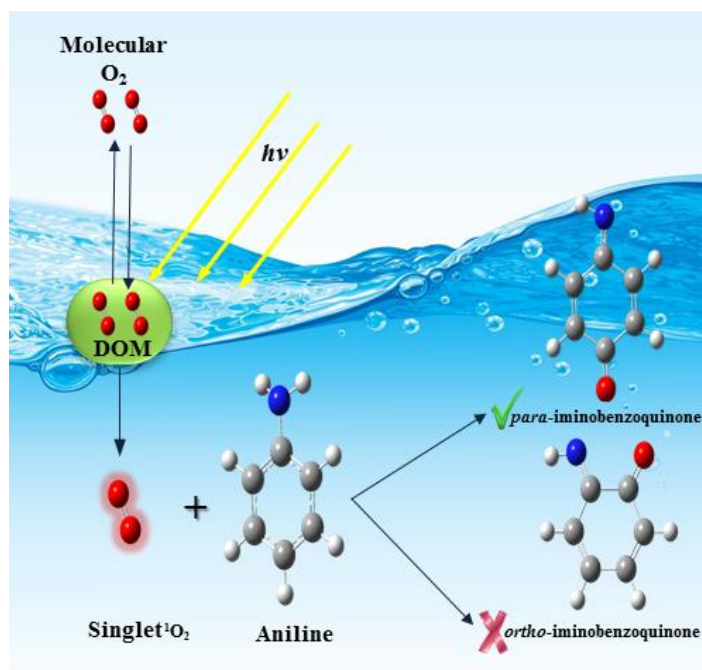
Jomana Al-Nu'airat

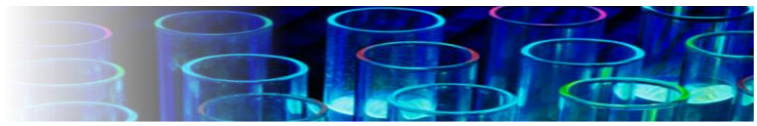


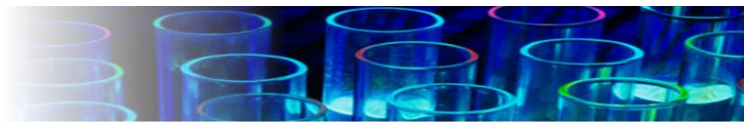


Chapter 6

Reaction of Aniline with Singlet Oxygen ($O_2^1\Delta_g$)







Abstract

Dissolved organic matter (DOM) acts as an effective photochemical sensitiser that produces the singlet delta state of molecular oxygen ($O_2\ ^1\Delta_g$), a powerful oxidiser that removes aniline from aqueous solutions. However, the exact mode of this reaction, the *para* to *ortho*-iminobenzoquinone ratio, and the selectivity of one over the other remain largely speculative. This contribution resolves these uncertainties. We report, for the first time, a comprehensive mechanistic and kinetic account of the oxidation of aniline with the singlet delta oxygen using B3LYP and M06 functionals in both gas and aqueous phases. Reaction mechanisms have been mapped out at *E*, *H* and *G* scales. The 1,4-cycloaddition of $O_2\ ^1\Delta_g$ to aniline forms a 1,4-peroxide intermediate (**M1**), which isomerises via a closed-shell mechanism to generate a *para*-iminobenzoquinone molecule. On the other hand, the $O_2\ ^1\Delta_g$ ene-type reaction forms an *ortho*-iminobenzoquinone product when the hydroperoxyl bond breaks, splitting hydroxyl from the 1,2-hydroperoxide (**M3**) moiety. The gas-phase model predicts the formation of both *para* and *ortho* iminobenzoquinones. In the latter model, the **M1** adduct displays the selectivity of up to 96 %. A water-solvation model predicts that **M1** decomposes further, forming only *para*-iminobenzoquinone with a rate constant of $k = 1.85 \times 10^9$ (L/(mol s)) at $T = 313$ K. These results corroborate the recent experimental findings of product concentration profile in which *para*-iminobenzoquinone represents the only detected product.



6.1 Introduction

Aniline (phenylamine, $C_6H_5NH_2$) acts as an important precursor or intermediate in manufacturing of isocyanates, polymers, dyes, rubbers, pesticides, pharmaceuticals and explosives [1,2]. However, its hazardous properties, once aniline enters the environment, overshadow its industrial merits, especially in aquatic media [3,4]. Concentrations of aniline, as low as a few ppb in water, induce severe effects on ecosystems and on human health [3,5,6]. Industrial discharges, forest fires, tobacco smoking, and automobile exhaust fumes represent the primary routes for aniline pollution [1,7]. Aniline constitutes a hazardous organic compound according to US Environmental Protection Agency [8] because of its high toxicity and its chemical and biochemical stability [9] that renders the traditional water treatment technologies [10–12] ineffective, such as ozone oxidation and biological treatments. This stability makes it necessary to deploy other techniques, such as photodegradation [2,13,14] that relies on reactive oxygen species (ROS) to remove aniline from water.

In aquatic systems, dissolved organic matter (DOM) [15–18] functions as a photoreaction and photodegradation agent capable of removing free aniline even at temperatures close to a freezing point [15–22]. DOM consists of humic materials derived from the dead cells of plants, bacteria, and algae that facilitate the generation of ROS, most notably singlet delta oxygen ($O_2^1\Delta_g$), hydroxyl radical (OH), superoxide anion ($O_2^{\cdot-}$), and hydrogen peroxide (H_2O_2) [23], among which the singlet delta oxygen is the most reactive [24,25]. The formation of ROS involves light excitation of complex molecules, such as DOM or rose bengal dye, which decay to their ground state in processes that generate ROS. Singlet delta oxygen resides 94.0 kJ/mol ($\Delta_G H^0_{298}$) above the ground-state triplet oxygen ($O_2^3\Sigma_g^-$). Literature documents well the

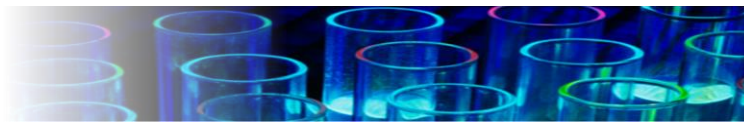


appearance of singlet oxygen in natural water containing high loading of humic substances, with a quantum yield varying from 1 to 3 % [26–28].

Prior experimental studies have demonstrated the efficient decomposition of aniline by singlet delta oxygen [29–31]. For example, the photo-induced oxidation of aniline with singlet delta oxygen [29,32,33] yields *para* and *ortho* iminobenzoquinones (C_6H_5NO), as detected in experiments. However, conflicting findings exist concerning the final product ratio and the selectivity of one over the other, as well as the presence of other competing pathways that might involve superoxide radical anion ($O_2^{\cdot-}$).

Briviba et al. [29] have suggested *para*-iminobenzoquinone as a key product of the reaction of aniline with singlet delta oxygen in water, apparently consistent with the findings of Karunakaran and Karuthapandian who have also reported *para*-iminobenzoquinone as the sole product of the oxidation of diphenylamine [34] with the superoxide radical-anion ($O_2^{\cdot-}$). This, however, raises the question of validity of the Briviba et al. conclusion [29] of the formation of the *para*-iminobenzoquinone via a singlet delta oxygen rather than the superoxide radical-anion pathway.

Regarding products variety and selectivity, Booth and Boyland [32] and Parke [35] have detected both the *ortho* and *para*-aminophenol isomers arising by photoreaction of aniline with singlet delta oxygen in rat and cat liver microsomes. However, Parke [35] published inconsistencies in the *para* to *ortho*-aminophenol product ratio varying from 2:5 in a cat to 15:1 in gerbil. Given that, the studies of Booth and Boyland as well as of Parke were carried out in



a biological framework, catalytic reactions of enzymes might have influenced the product distribution.

The highly transient nature of singlet oxygen, especially its lifetime of 4 μs , makes the experimental determination of the precise mode of the reaction between aniline and singlet oxygen a challenging task [36]. The involvement of other ROS and emergence of parallel reactions render it even harder to elucidate precise pathways driven solely by singlet oxygen. This motivates the present *in silico* study, in which we report a comprehensive mechanistic and kinetic account of pathways encountered in the oxidative transformation of aniline by singlet oxygen. We map out reaction routes and assess their relative feasibility based on computed reaction rate constants. The experimental profiles of product species reported in literature [29] show very good agreement with the results of the present calculations.

6.2 Methodology

The Gaussian 09 [37] suite of programs affords all structural optimisations and energy calculations ($\Delta^{\#}H^{\circ}_{298}$, $\Delta_{\text{r}}H^{\circ}_{298}$, $\Delta^{\#}G^{\circ}_{298}$, and $\Delta_{\text{r}}G^{\circ}_{298}$). The theoretical methodology comprises the gradient-corrected density functional theory (DFT) functionals B3LYP [38,39] and the meta-hybrid M06 [40] functional, both, supplemented with the polarised basis set of 6-311+G(d,p) [41]. Furthermore, we have performed intrinsic reaction coordinate (IRC) calculations, confirming the identity of each transition structure.

While the B3LYP function retains a relatively cost-effective accuracy in predicting thermochemistry for organic species, even in systems encompassing diradicals [42], it often



suffers fundamental shortcomings in predicting accurate kinetic parameters[43]. For this reason, we have also adopted the M06 method to obtain barriers of enthalpy and Gibbs free energy. We simulate reactions in the aqueous media by deploying the polarisable continuum model (PCM) [44]. Simulating aqueous-phase reactions based on gas phase models proves to represent an adequate and representative model for reactions occurring in aqueous media [42]. Albeit, we expect the energetic profiles representing water-phase reactions to fall below those associated with their gas-phase analogues [45].

The approximate spin-projection (AP) method pioneered by the Yamaguchi group [46,47] serves to refine the enthalpies and Gibbs free energies of activation and reaction ($\Delta^{\#}H^{\circ}_{298}$, $\Delta_{\text{r}}H^{\circ}_{298}$, $\Delta^{\#}G^{\circ}_{298}$ and $\Delta_{\text{r}}G^{\circ}_{298}$) of all singlet species that suffer from contamination by their lower-energy triplet state. As expected, a significant difference between energies on G and H scales for some reactions (especially for bimolecular channels) indicates entropy effects. We eliminate the spin contamination error of singlet delta oxygen based on the broken symmetry (BS) solution by performing structural optimisation with mixing the frontier molecular orbitals (HOMO and LUMO). Adapting this approach yields satisfactory performance in comparison with the more computationally expensive multi-reference wave-function methods such as CASSCF and CASSTP2 [48,49].

The KiSThelP package provides a means to estimate reaction rate constants fitted in the temperature range of 300 to 600 K [50]. The kinetic parameters are estimated based on the conventional transition state theory with the inclusion of one dimensional Eckart barrier, accounting for quantum tunnelling effect contribution. We treat the internal rotations in aniline and all derived species that involve the amine group as hindered rotors with the overall enthalpy barrier of 23.2 kJ/mol. The rotation enthalpy of the NH_2 group is derived from a recent estimate

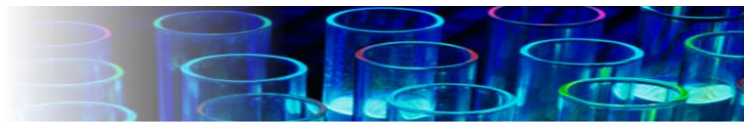


of Zanganeh et al. [51] Finally, the DMol³ code [52] facilitates the calculations of the Hirshfeld atomic charges [53] and the Fukui (f^1) indices [54]. The Fukui indices indicate the tendency of a molecular site to undergo an electrophilic addition. The choice of the Hirshfeld scheme stems from its superior performance in estimating atomic charges in reference to other approaches, such as the commonly deployed Mulliken population analysis [55] that often displays severe sensitivity to the implemented basis set.

6.3 Results and Discussions

6.3.1 Preliminary Analysis of Results from M06 and B3LYP Approaches

We first assess the performance of several DFT methods at 298.15 K in calculating the enthalpy gap between singlet and triplet states ($\Delta_G H_{298}$) for selected diradical species, namely O, O₂, NH, NF, C, and Si. Table S6.2 in Supporting Information (SI) lists ($\Delta_G H_{298}$) and the corrected calculated gap based on the broken symmetry solution ($\Delta_G H_{298}^{S-T}$) values for the chosen diradicals. Table S6.2 indicates that $\Delta_G H_{298}^{S-T}$ estimates obtained from the M06 calculations fall below those provided by the B3LYP computations. In the case of the oxygen molecule, M06 significantly overestimates the $\Delta_G H_{298}^{S-T}$ value by 37.7 kJ/mol, while B3LYP shows an excellent performance with only 8.5 kJ/mol offset from the experimental value (94.6 kJ/mol) [56]. The noticeable difference in the $\Delta_G H_{298}^{S-T}$ value between the two methods confirms the relative accuracy of B3LYP in determining thermochemical values for oxygen. However, except for O₂, M06 yields $\Delta_G H_{298}^{S-T}$ values that are closer to experimental measurements than those computed with B3LYP. Ess and Cook [57] reported similar results for diradicals, with a mean unsigned error (MUS) of 12.6 and 41.4 kJ/mol for M06 and B3LYP, respectively.

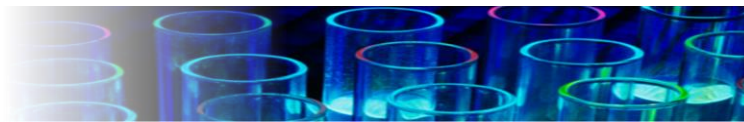


B3LYP does, however, have some limitations in computing reaction barriers, with the M06 family of functionals delivering more satisfactory performance, well documented in literature [40,58]. Thus, in this contribution, we report reaction and activation energies for all considered reactions using both the two methods.

6.3.2 Characterisation of Singlet Oxygen and Aniline

Singlet oxygen is an electrophilic agent. Thus, unlike triplet oxygen, introducing singlet oxygen atoms into olefins, dienes, or aromatic structures, such as aniline, proceeds through distinct routes of Diels-Alder [4+2] and [2+2] cycloadditions, and ene reactions with isolated double bonds.[59–61] Olefins and substances with inaccessible allylic hydrogens represent the primary candidates to undergo [2+2]-cycloaddition with singlet oxygen, forming dioxetanes [62]. In contrast, allylic hydrogen in the more congested side of olefins experiences the so-called ene reaction, forming allylic hydroperoxides [63]. Singlet oxygen reacts with structural entities of 1,3-dienes (cyclic, noncyclic or aromatic) to produce endoperoxides [64]. Determination of the dominant reaction rests on different electronic and structural factors, including the distance between C₁ and C₄ atoms in dienes, ionisation potential of the 1,3-diene, spatial alignment of allylic hydrogens, and the type of the solvent deployed [62,65].

Aniline reaction with singlet oxygen exemplifies a process controlled by frontier molecular orbitals, with singlet delta oxygen LUMOs interacting with aniline HOMOs. When the amine group is added to the benzene ring, it decreases the energy gap of the HOMO (-5.084 eV) and LUMO (-1.055 eV) orbitals in comparison with that of the HOMO (-5.388 eV) and LUMO (-0.168 eV) of benzene [66,67]. This change means that the ring becomes more reactive with



singlet oxygen in the presence of an amine substituent. Figure 6.1 indicates the Fukui indices and Hirshfeld electronic charges of aniline with respect to benzene. Higher f^1 values at the *para*, *ortho*, and *meta* carbon atoms of aniline with respect to the indistinguishable sites in benzene signify the addition of singlet delta oxygen to aniline proceeding at a higher rate when compared with the analogous process in benzene. The higher f^1 associated with the *para* carbon further highlights the *para* position as a more preferred site for the electrophilic $O_2\ ^1\Delta_g$ addition in reference to *ortho* and *meta* sites. This appears to agree with the HOMO map of aniline that shows the HOMO orbitals localised mainly on the *para* and *ortho* carbon atoms; see Figure S 6.1 in SI.

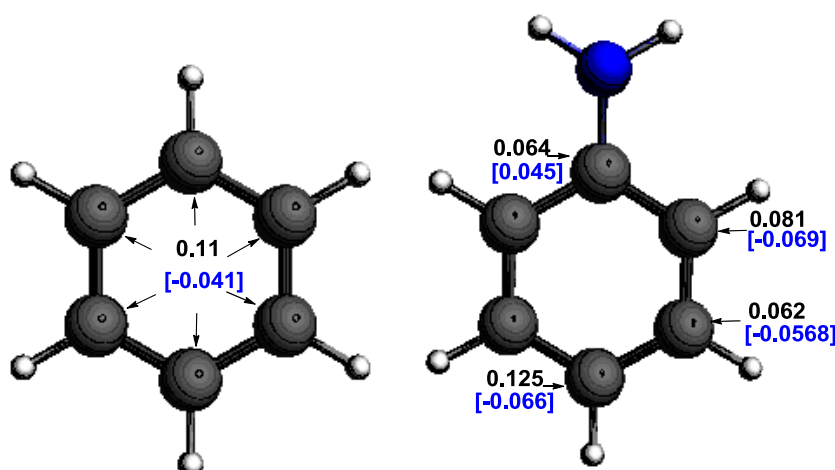
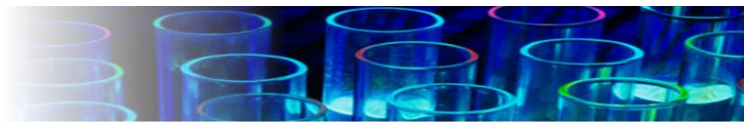


Figure 6.1. Fukui f^1 indices (in bold) and Hirshfeld charges (blue in brackets) on benzene (left) and aniline (right).

6.3.3 Reaction Mechanism

Figure 6.2 depicts the initial corridors in the aniline + $O_2\ ^1\Delta_g$ mechanism which branches into five channels via three routes, namely [4 + 2] cycloaddition reactions affording **M1** and **M2** 1,4 peroxides, ene-type reactions producing **M3** and **M4** 1,2/1,4 hydroperoxides, and direct



H-abstraction from the amine group generating the **M5** anilino radical. Table S6.3 assembles estimated reaction and activation enthalpies and Gibbs free energies based on the gas-phase (B3LYP and M06) and solvation (M06) models. The [2+2] reaction was not observed, as expected in aromatic rings holding only one electron-donating group such as an amine substitute. Figures S6.2 and S6.3 compare geometries of the located transition structures for the three theoretical approaches considered in this article.

The attack of the singlet oxygen at *para-ipso* and *ortho-meta* positions yields the two peroxides structures **M1** and **M2**, respectively. The enthalpy barrier in **M1**, characterised by the transition state **TS1**, is considerably lower than that embedded in **TS2** to form **M2**; i.e., 79 kJ/mol versus 101 kJ/mol, from the B3LYP calculations. By applying the Curtin-Hammond principle [33], the *para-meta* product ratio ($[P_{para}]/[P_{meta}]$) is dictated by the free energy gap (ΔG°_{298}) between the *para* and *meta* transition states (**TS1** and **TS2**) rather than the stabilities of the two intermediates (**M1** and **M2**); i.e., $\Delta_G G^{\circ}_{298}{}^{P-M} = 22$ kJ/mol, B3LYP, see Figure 2 and Table S3. Our ratios of $[P_{para}]/[P_{meta}]$ at 298.15 K correspond to 9160:1 and 215:1, for the B3LYP and M06 functionals, respectively. This finding indicates an expected dominance of the *para* isomer and a negligible abundance of the *meta* isomer. This excludes the *meta*-channel from further mechanistic analysis.

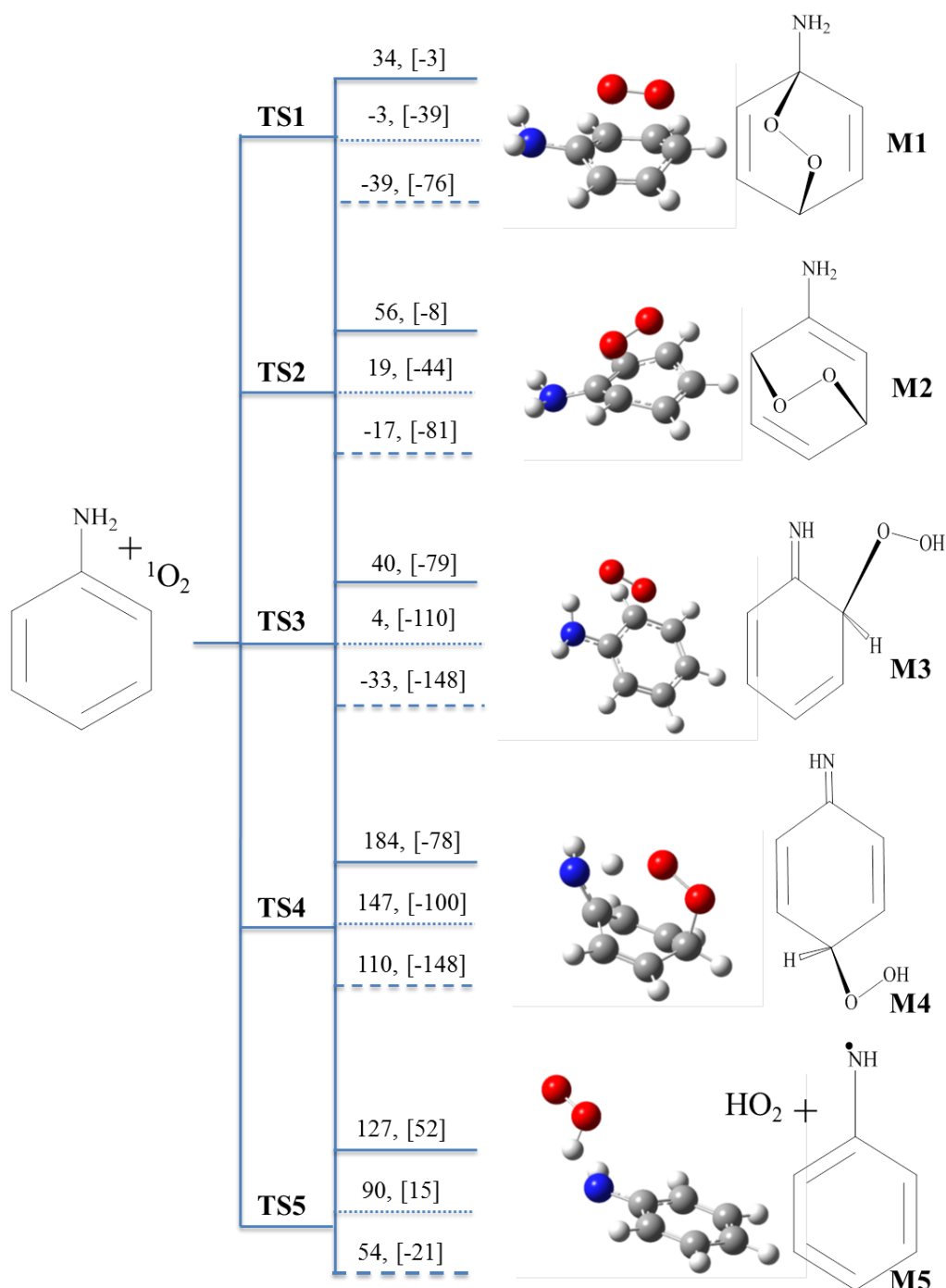


Figure 6.2. Initial channels in the reaction of $O_2\ ^1\Delta_g$ with aniline assigned with Gibbs free energies of activation $\Delta^\ddagger G^\circ_{298}$ and reaction $\Delta_r G^\circ_{298}$ (in brackets) calculated based on gas-phase B3LYP/6-311+G(d,p) represented by solid line, M062X/6-311+G(d,p) (gas phase, in dotted line), and M062X/6-311+G(d,p) (solvation, in dashed line). All values are in kJ/mol at 298.15 K.



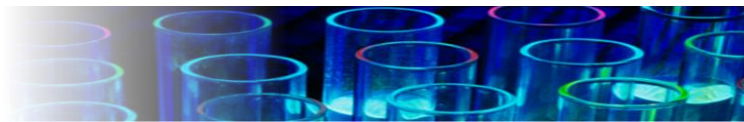
Hydroperoxides **M3** and **M4** originate from the ene-type reactions involving abstraction of one of the amine hydrogens and simultaneous addition of the singlet oxygen at *ortho* and *para* sites, respectively. The free energy of **TS3** leading to the formation of the **M3** adduct holds an intermediate barrier (4 kJ/mol, M06) comparing with the *para* and *meta* initial reaction channels. Unexpectedly, B3LYP *ortho*-**TS3** assumes a slightly lower enthalpy barrier than its *para* analogue (**TS1**), see Table S6.3. To examine the performance of the B3LYP further, we map out the HOMO and LUMO of reactants and transition states in Figures S6.1 and S6.4 in SI. Interestingly, the amine group visibly interacts with HOMO and LUMO of **TS3**, lowering its enthalpy barrier. Conversely, the HOMO and LUMO of *para* (**TS1**) are mainly located between the benzene ring and singlet delta oxygen, with no apparent contribution from the amine substituent. **TS4** requires a sizable activation barrier of 147 kJ/mol (M06) rendering this route inaccessible. Direct abstraction of an H atom from the amine group to form an anilino radical occurs through a barrier of 147 kJ/mol (M06), via **TS5**. In general, both of the methods M06 and B3LYP provide us with the same reaction pathways. However, the reaction enthalpies and free energies of reaction for the formation of the **M1-M5** intermediates in the gas phase, from B3LYP and M06 computations, differ by 17-80 kJ/mol ($\Delta_r H^\circ_{298}$, Table S6.3 and Figure 6.2). This difference accounts for the lower enthalpy barrier estimated for singlet oxygen by the M06 functional. Thus, even though both of the functionals yield the same trends, M06 enthalpy barriers fall below those calculated with the B3LYP functional.



Table 6.1. Arrhenius rate parameters fitted in the temperature range of 300-600 K at 1 M for the initial five channels as well as the formation of 4-iminocyclohexa-2,5-dienone (M9); A and $A_{\text{solvation}}$ are $\text{cm}^3 \text{ molecule}^{-1} \text{ s}^{-1}$ and E_a and $E_{a\text{-solvation}}$ in kJ/mol

Reaction	M06				B3LYP	
	A	$A_{\text{solvation}}$	E_a	$E_{a\text{-solvation}}$	A	E_a
Aniline + $^1\text{O}_2 \rightarrow \text{M1}$	3.40×10^{-14}	4.70×10^{-14}	11.2	-11.0	1.97×10^{-14}	89.8
Aniline + $^1\text{O}_2 \rightarrow \text{M2}$	1.56×10^{-14}	1.10×10^{-14}	31.7	8.59	1.46×10^{-14}	111.7
Aniline + $^1\text{O}_2 \rightarrow \text{M3}$	2.06×10^{-14}	5.07×10^{-14}	16.7	2.09	1.76×10^{-14}	84.3
Aniline + $^1\text{O}_2 \rightarrow \text{M4}$	4.98×10^{-14}	1.41×10^{-14}	142.3	116.1	6.70×10^{-20}	235.6
Aniline + $^1\text{O}_2 \rightarrow \text{M5}$	1.75×10^{-12}	3.75×10^{-12}	107.3	99.2	1.05×10^{-12}	160.4
M6 \rightarrow M7	7.66×10^{14}	1.83×10^{14}	136.8	125.8	1.53×10^{14}	115.6
M7 \rightarrow M8	2.13×10^{13}	4.10×10^{13}	108.1	61.8	2.19×10^{13}	92.8
M8 \rightarrow M9	3.88×10^{13}	1.73×10^{13}	209.1	198.3	3.42×10^{10}	197.1

Table 6.1 lists fitted modified Arrhenius parameters for the five entrance channels, and Figure 6.3 depicts branching ratios of these reactions. For the M06 functional, the formation of adduct **M1** dominates the fate of the reactants (aniline and singlet delta oxygen) in both gaseous (Figure 6.3a) and aqueous (Figure 6.3b) media. The trend based on the M06 calculations accords with the findings of Briviba et al. [29] in which the *para*-channel assumes chief importance; i.e., singlet delta oxygen selectively oxidises aniline to form *para*-iminobenzoquinone. Despite the discrepancy in pinning down the major initial channel from the two media, we are now in the position to limit the most critical operating pathways to the formation of **M1** and **M3**. Consequently, we mapped out the free energy surfaces for the further decompositions of **M1** and **M3** adducts in Figures 6.4 and 6.5, respectively, with their fitted



Arrhenius parameters listed in Table 6.1. Moreover, we mapped the IRC coordinates leading to the formation of **M1** and **M2** in Figure S6.5 and Figure S6.6 (SI) assigned with the corresponding structures.

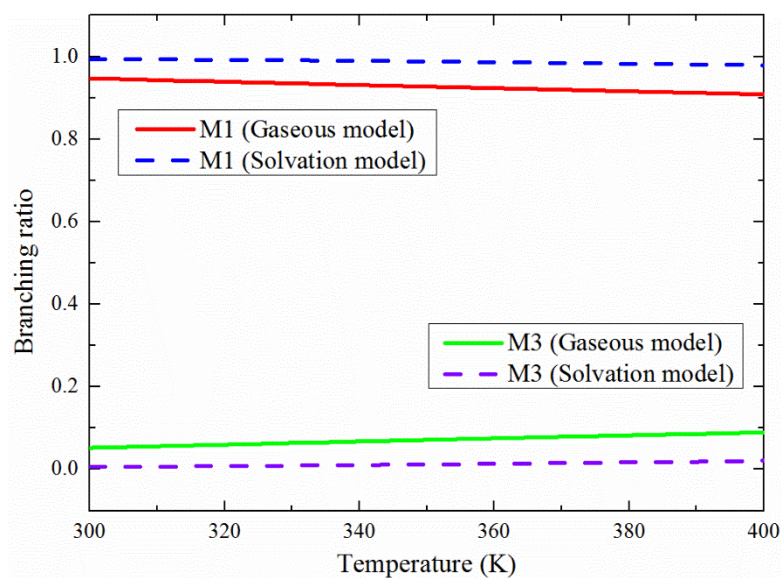


Figure 6.3. Relative branching rates for the formation of **M1** and **M3**; a: M06/6-311+G(d,p) (gas phase), and b: M06/6-311+G(d,p) (Solvation model) represented in dashed line.

As Figure 6.4 illustrates, the unimolecular isomerisation of the **M1** moiety proceeds via a closed-shell mechanism to generate the 4-iminobenzoquinone molecule. The final products along this route (**M06**) fall 471 kJ/mol below the entrance channel, and the overall enthalpy barrier of 10 kJ/mol (**M06**) corresponds to the initial 1,4-cycloaddition step. The elementary reactions comprise the formation of two epoxy intermediates (**M6** and **M7**) and water elimination from the **M8** adduct. **M1** stabilises into **M6** in one step without encountering an intrinsic reaction barrier. Inspection of the mechanism in Figure 4 reveals that, the water elimination step demands a significant enthalpy barrier of 219 kJ/mol (**M06**) through **TS8** over the highly stabilised adduct **M8**. Nonetheless, **TS8** remains submerged by 191 kJ/mol (**M06**) with respect to the initial reactants.

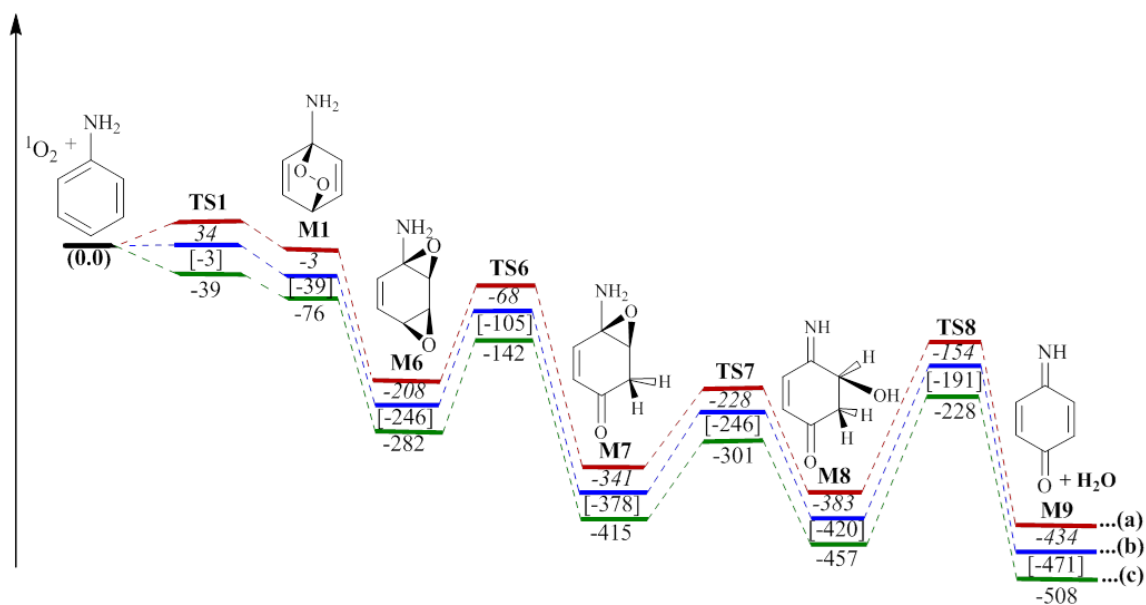


Figure 6.4. Gibbs free energy potential map for the formation of 4-iminocyclohexa-2,5-dienone (*para*-iminobenzoquinone) from the reaction of singlet oxygen with aniline. a: B3LYP/6-311+G(d,p) (gas phase, in italic), b: M06/6-311+G(d,p) (gas phase, in brackets), and c: M06/6-311+G(d,p) (solvation). All values are in kJ/mol at 298.15 K.

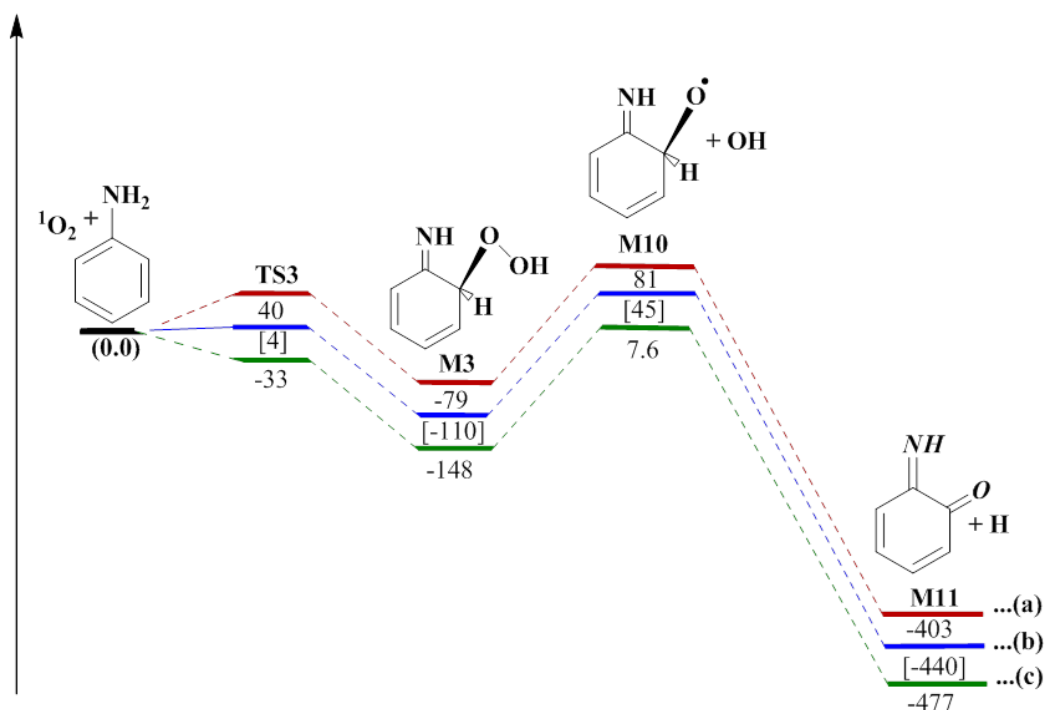
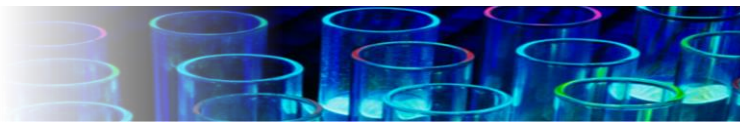


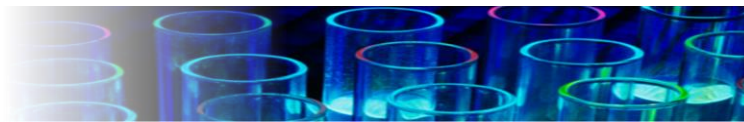
Figure 6.5. Gibbs free energy potential map for the formation of 6-iminocyclohexa-2,4-dienone (*ortho*-iminobenzoquinone) product from the reaction of singlet oxygen with aniline, a: B3LYP/6-311+G(d,p) (gas phase, in italic), b: M06/6-311+G(d,p) (gas phase, in brackets), and c: M06/6-311+G(d,p) (solvation). All values in kJ/mol at 298.15 K.



The formation of the *ortho*-iminobenzoquinone follows the fission of the hydroperoxyl bond in the **M3** intermediate (Figure 6.5). Endothermicity of this process amounts to 120 kJ/mol (solvation) and produces the **M10** radical. Direct elimination of the out-of-plane H atom from **M10** forms the *ortho*-iminobenzoquinone through a considerable exothermic reaction of 403 kJ/mol (solvation). In microorganisms, should the metabolism of aniline lead to *ortho*-aminophenol in the detoxification process, it would cause more harm than good, owing to the fact that *ortho*-aminophenol incurs more toxicity than the parent aniline.[35] Dennis et al.[68] attempted to explain the *ortho*-product formation from a biological point of view based on the presence of hydroxylation enzyme, saturation of the detoxification pathways, or DNA repair system.

In Figure S6.7, we compared the enthalpies with Gibbs free energies of activation and reaction for the formation of *para*-iminobenzoquinone in solution. A negative value of $\Delta_r G^{\circ}_{298}$ associated with a reaction reveals that this reaction may occur spontaneously at 298 K. Higher values of barriers of Gibbs free energy in comparison to enthalpies for **TS6** and **TS7** point to positive changes in entropy, and hence to tight transition structures. The remaining transition structures display loose transition structures.

Applying the values of the kinetic parameters for solution from the first row in Table 6.2, and converting the units to L and mol, our calculated rate constant of photooxidation of aniline with singlet delta oxygen, at 313 K, of $k = 1.85 \times 10^9$ (L/(mol s)) concurs with the experimental measurement of $k = 2.0 \times 10^9$ (L/(mol s)), in methanol solution [69]. With the aid of PolyMath [70] software, we solved a system of ordinary differential equations (ODEs) for our solvation model, assuming a batch reactor with a steady state approximation for singlet oxygen formation and a sensitiser quantum yield of 0.52, see Table S6.4 and Figure S6.8 in the SI. The initial



concentrations corresponded to 35 $\mu\text{mol/L}$ and 1 mmol/L for methylene blue sensitizer and aniline, respectively. In Figure 6.6, we compared the results of our solvation model with the experimental measurements of Briviba et al. [29], demonstrating close agreement with an overall reaction rate of *para*-iminobenzoquinone formation amount to 3.54 ($\text{mol}/(\text{L s})$).

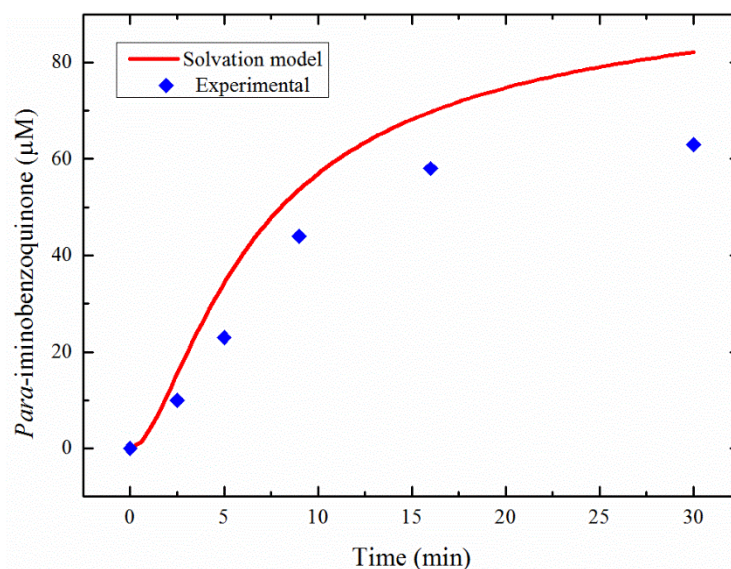
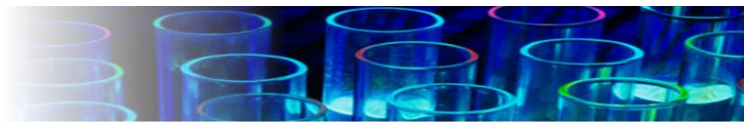


Figure 6.6. Concentration profiles for the formation of *para*-iminobenzoquinone via the water-solvation model (red line) and the published experimental measurements of Briviba et al. [29].

6.3.4 Conclusion

This contribution addressed the mechanistic and kinetic aspects pertinent of the photo-induced reaction of aniline with singlet oxygen. The gaseous reaction pathways obtained from the application of the B3LYP and M06 functionals predict the formation of *para* and *ortho*-iminobenzoquinones. A water solvation model reveals the formation of *para*-iminobenzoquinone as the predominant product. Moreover, our time-concentration history of



para-iminobenzoquinone matches the corresponding experimental profile of Briviba et al. [29] well. Our findings resolved the lack of consensus on literature on the expected products, their selectivity ratios and reaction mechanism of aniline reaction with O_2 $^1\Delta_g$.

Supporting Information

The Supporting Information is included in Chapter 10 (Appendix III) of the thesis. Table S6.1 (Singlet energy $H_{Singlet}$, triplet energy $H_{Triplet}$ and spin unrestricted $H(Singlet,Guess=Mix)$ energy calculated by B3LYP, HSEH1PBE, B3PW91, CAM-B3LYP, and M06 for O, O₂, NH, NF, C, and Si diradicals in addition to the spin contaminations $S^2_{Singlet}$ and $S^2_{Triplet}$ for singlet and triplet states, respectively), Table S6.2 Spin-projected (singlet-triplet) gap energy ($\Delta_G H_{298}^{S-T}$) for (O, O₂, NH, NF, C, and Si) diradicals and the (singlet-triplet) gap energy $\Delta_G H_{298}$ for spin unrestricted B3LYP, HSEH1PBE, B3PW91, CAM-B3LYP, and M06 functionals), Spin-projected (singlet-triplet) gap enthalpy ($\Delta_G H_{298}^{S-T}$) for O, O₂, NH, NF, C, and Si diradicals and the normal (singlet-triplet) gap energy $\Delta_G H_{298}$ for spin unrestricted B3LYP, HSEH1PBE, B3PW91, CAM-B3LYP, and M06 functionals. All energy values are in kJ/mol. Table S6.3 Enthalpies and Gibbs free energies of activation and reaction ($\Delta^\# H^\circ_{298}$, $\Delta_r H^\circ_{298}$, $\Delta^\# G^\circ_{298}$ and $\Delta_r G^\circ_{298}$) calculated based on gas-phase (B3LYP in italic and M06 in in brackets) and solvation (M06) models. Table S6.4 PolyMath [70] ordinary differential equations (ODEs) and parameters for the solvation model, Figure S6.1 HOMO of transition states, Figures S6.2 and S6.3 Optimised structures of transition states of aniline oxidation by singlet oxygen, and Figure S6.4 LUMO of transition states. Figure S6.5 IRC calculation (M06/6-311+G(d,p)) for the reaction pathway of aniline with singlet oxygen via TS1, Figure S6.6 IRC calculation (M06/6-311+G(d,p)) for the reaction pathway of aniline with singlet oxygen via TS3, Figure S6.7



Enthalpy map (blue) and Gibbs free energy map (red) for the formation of *para*-iminobenzoquinone from the reaction of singlet oxygen with aniline using M06 (solvation) model and Figure S6.8 Concentration profile for aniline photoreaction with singlet oxygen via the water-solvation model-M06 at 313 K.

6.3.5 References

- [1] Pinheiro HM, Touraud E, Thomas O. Aromatic amines from azo dye reduction: status review with emphasis on direct UV spectrophotometric detection in textile industry wastewaters. *Dyes and Pigments* 2004;61:121–139.
- [2] Gautam S, Kamble SP, Sawant SB, Pangarkar VG. Photocatalytic degradation of 4-nitroaniline using solar and artificial UV radiation. *Chemical Engineering Journal* 2005;110:129–37. doi:10.1016/j.cej.2005.03.021.
- [3] Buikema AL, McGinniss MJ, Cairns J. Phenolics in aquatic ecosystems: a selected review of recent literature. *Marine Environmental Research* 1979;2:87–181.
- [4] Shackelford WM, Cline DM, Faas L, Kurth G. An evaluation of automated spectrum matching for survey identification of wastewater components by gas chromatography—mass spectrometry. *Analytica Chimica Acta* 1983;146:15–27.
- [5] Garcia NA. New trends in photobiology: singlet-molecular-oxygen-mediated photodegradation of aquatic phenolic pollutants. A kinetic and mechanistic overview. *Journal of Photochemistry and Photobiology B: Biology* 1994;22:185–196.
- [6] Snyderwine EG, Sinha R, Felton JS, Ferguson LR. Highlights of the eighth international conference on carcinogenic/mutagenic N-substituted aryl compounds. *Mutat Res* 2002;506–507:1–8.
- [7] Stanley TW, Sawicki E, Johnson H, Pfaff JD. Comparison of methods for the spectrophotometric determination of phenols in automobile exhaust fumes. *Microchimica Acta* 1965;53:48–59.



- [8] US EPA O. Aniline | Technology Transfer Network Air Toxics Web site | US EPA, 2016.
- [9] Shahrezaei F, Mansouri Y, Zinatizadeh A a. L, Akhbari A, Shahrezaei F, Mansouri Y, et al. Photocatalytic Degradation of Aniline Using TiO₂ Nanoparticles in a Vertical Circulating Photocatalytic Reactor, Photocatalytic Degradation of Aniline Using TiO₂ Nanoparticles in a Vertical Circulating Photocatalytic Reactor. *International Journal of Photoenergy*, *International Journal of Photoenergy* 2012;2012, 2012:e430638. doi:10.1155/2012/430638, 10.1155/2012/430638.
- [10] Spain JC. Biodegradation of Nitroaromatic Compounds. *Annual Review of Microbiology* 1995;49:523–55. doi:10.1146/annurev.mi.49.100195.002515.
- [11] Lopez T, Gomez R, Sanchez E, Tzompantzi F, Vera L. Photocatalytic Activity in the 2,4-Dinitroaniline Decomposition Over TiO₂ Sol-Gel Derived Catalysts. *Journal of Sol-Gel Science and Technology* 2001;22:99–107. doi:10.1023/A:1011272521955.
- [12] Zhao G, Lu X, Zhou Y. Aniline degradation in aqueous solution by UV-aeration and UV-microO₃ processes: Efficiency, contribution of radicals and byproducts. *Chemical Engineering Journal* 2013;229:436–43. doi:10.1016/j.cej.2013.06.011.
- [13] Kamble SP, Sawant SB, Schouten JC, Pangarkar VG. Photocatalytic and photochemical degradation of aniline using concentrated solar radiation. *J Chem Technol Biotechnol* 2003;78:865–72. doi:10.1002/jctb.867.
- [14] Talebian N, Jafarinezhad F. Morphology-controlled synthesis of SnO₂ nanostructures using hydrothermal method and their photocatalytic applications. *Ceramics International* 2013;39:8311–7. doi:10.1016/j.ceramint.2013.03.101.
- [15] Canonica S, Hellrung B, Müller P, Wirz J. Aqueous oxidation of phenylurea herbicides by triplet aromatic ketones. *Environmental Science & Technology* 2006;40:6636–6641.
- [16] Canonica S. Oxidation of aquatic organic contaminants induced by excited triplet states. *Chimia International Journal for Chemistry* 2007;61:641–644.
- [17] Canonica S, Hellrung B, Wirz J. Oxidation of phenols by triplet aromatic ketones in aqueous solution. *The Journal of Physical Chemistry A* 2000;104:1226–1232.



- [18] Canonica S, Jans URS, Stemmler K, Hoigne J. Transformation kinetics of phenols in water: photosensitization by dissolved natural organic material and aromatic ketones. *Environmental Science & Technology* 1995;29:1822–1831.
- [19] Erickson PR, Walpen N, Guerard JJ, Eustis SN, Arey JS, McNeill K. Controlling Factors in the Rates of Oxidation of Anilines and Phenols by Triplet Methylene Blue in Aqueous Solution. *J Phys Chem A* 2015;119:3233–43. doi:10.1021/jp511408f.
- [20] Weber EJ, Spidle DL, Thorn KA. Covalent binding of aniline to humic substances. 1. Kinetic studies. *Environmental Science & Technology* 1996;30:2755–2763.
- [21] Eriksson J, Frankki S, Shchukarev A, Skyllberg U. Binding of 2, 4, 6-trinitrotoluene, aniline, and nitrobenzene to dissolved and particulate soil organic matter. *Environmental Science & Technology* 2004;38:3074–3080.
- [22] Fukushima M, Tatsumi K, Morimoto K. The fate of aniline after a photo-Fenton reaction in an aqueous system containing iron (III), humic acid, and hydrogen peroxide. *Environmental Science & Technology* 2000;34:2006–2013.
- [23] Appiani E, McNeill K. Photochemical Production of Singlet Oxygen from Particulate Organic Matter. *Environmental Science & Technology* 2015;49:3514–22. doi:10.1021/es505712e.
- [24] Sandvik SLH, Bilski P, Pakulski JD, Chignell CF, Coffin RB. Photogeneration of singlet oxygen and free radicals in dissolved organic matter isolated from the Mississippi and Atchafalaya River plumes. *Marine Chemistry* 2000;69:139–152.
- [25] Ray PZ, Tarr MA. Solar production of singlet oxygen from crude oil films on water. *Journal of Photochemistry and Photobiology A: Chemistry* 2014;286:22–28.
- [26] Zepp RG, Wolfe NL, Baughman GL, Hollis RC. Singlet oxygen in natural waters 1977.
- [27] Haag WR, Hoigne J. Singlet oxygen in surface waters. 3. Photochemical formation and steady-state concentrations in various types of waters. *Environmental Science & Technology* 1986;20:341–348.
- [28] Frimmel FH, Bauer H, Putzien J, Murasecco P, Braun AM. Laser flash photolysis of dissolved aquatic humic material and the sensitized production of singlet oxygen. *Environmental Science & Technology* 1987;21:541–545.



- [29] Briviba K, Devasagayam TPA, Sies H, Steenken S. Selective para-hydroxylation of phenol and aniline by singlet molecular oxygen. *Chem Res Toxicol* 1993;6:548–53. doi:10.1021/tx00034a025.
- [30] Ratti M, Canonica S, McNeill K, Bolotin J, Hofstetter TB. Isotope Fractionation Associated with the Indirect Photolysis of Substituted Anilines in Aqueous Solution. *Environ Sci Technol* 2015;49:12766–73. doi:10.1021/acs.est.5b03119.
- [31] Nilsson R, Merkel PB, Kearns DR. Unambiguous Evidence for The Participation Of Singlet Oxygen ($^1\delta$) In Photodynamic Oxidation Of Amino Acids. *Photochemistry and Photobiology* 1972;16:117–24. doi:10.1111/j.1751-1097.1972.tb07343.x.
- [32] Booth J, Boyland E. The biochemistry of aromatic amines. 3. Enzymic hydroxylation by rat-liver microsomes. *Biochem J* 1957;66:73–8.
- [33] Seeman JI. Effect of conformational change on reactivity in organic chemistry. Evaluations, applications, and extensions of Curtin-Hammett Winstein-Holness kinetics. *Chemical Reviews* 1983;83:83–134.
- [34] Karunakaran C, Karuthapandian S. Enhancement of TiO_2 -photocatalyzed organic transformation by ZnO and ZnS. Oxidation of diphenylamine. *Egyptian Journal of Basic and Applied Sciences* 2015;2:32–8. doi:10.1016/j.ejbas.2014.12.001.
- [35] Parke DV. Studies in detoxication. 84. The metabolism of [^{14}C] aniline in the rabbit and other animals. *Biochem J* 1960;77:493–503.
- [36] Clennan EL, Pace A. Advances in singlet oxygen chemistry. *Tetrahedron* 2005;61:6665–6691.
- [37] Frisch M, Trucks GW, Schlegel HB, Scuseria GE, Robb MA, Cheeseman JR, et al. *Gaussian 09, Revision A. 02*, Gaussian, Inc, Wallingford, CT 2009;200.
- [38] Becke AD. Density-functional exchange-energy approximation with correct asymptotic behavior. *Physical Review A* 1988;38:3098.
- [39] Lee C, Yang W, Parr RG. Development of the Colle-Salvetti correlation-energy formula into a functional of the electron density. *Physical Review B* 1988;37:785.
- [40] Zhao Y, Truhlar DG. The M06 suite of density functionals for main group thermochemistry, thermochemical kinetics, noncovalent interactions, excited states, and



transition elements: two new functionals and systematic testing of four M06-class functionals and 12 other functionals. *Theoretical Chemistry Accounts* 2008;120:215–241.

[41] Montgomery Jr JA, Ochterski JW, Petersson GA. A complete basis set model chemistry. IV. An improved atomic pair natural orbital method. *The Journal of Chemical Physics* 1994;101:5900–5909.

[42] Morales J, Günther G, Zanocco AL, Lemp E. Singlet Oxygen Reactions with Flavonoids. A Theoretical – Experimental Study. *PLOS ONE* 2012;7:e40548. doi:10.1371/journal.pone.0040548.

[42] Westmoreland, P.; Kollman, P. A.; Chaka, A. M.; Cummings, P. T.; Morokuma, K.; Neurock, M.; Stechel, E. B.; Vashishta, P. *Applying Molecular and Materials Modeling*; Springer Science & Business Media, 2013.

[44] Mennucci B. Polarizable continuum model. *Wiley Interdisciplinary Reviews: Computational Molecular Science* 2012;2:386–404.

[45] Rayson MS, Altarawneh M, Mackie JC, Kennedy EM, Dlugogorski BZ. Theoretical study of the ammonia- hypochlorous acid reaction mechanism. *The Journal of Physical Chemistry A* 2010;114:2597–2606.

[46] Saito T, Nishihara S, Kataoka Y, Nakanishi Y, Matsui T, Kitagawa Y, et al. Transition state optimization based on approximate spin-projection (AP) method. *Chemical Physics Letters* 2009;483:168–171.

[47] Yamanaka S, Kawakami T, Nagao H, Yamaguchi K. Effective exchange integrals for open-shell species by density functional methods. *Chemical Physics Letters* 1994;231:25–33.

[48] Bobrowski M, Liwo A, Oldziej S, Jeziorek D, Ossowski T. CAS MCSCF/CAS MCQDPT2 study of the mechanism of singlet oxygen addition to 1, 3-butadiene and benzene. *Journal of the American Chemical Society* 2000;122:8112–8119.

[49] Abe M. Diradicals. *Chemical Reviews* 2013;113:7011–7088.

[50] Canneaux S, Bohr F, Henon E. KiSThelP: A program to predict thermodynamic properties and rate constants from quantum chemistry results†. *Journal of Computational Chemistry* 2014;35:82–93.

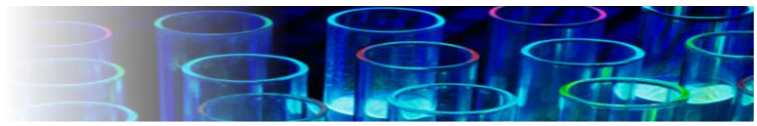


- [51] Zanganeh J, Altarawneh M, Saraireh I, Namazi S, Zanganeh J. Theoretical study on thermochemical parameters and pKa values for fluorinated isomers of toluene. *Computational and Theoretical Chemistry* 2013;1011:21–29.
- [52] Delley B. From molecules to solids with the DMol3 approach. *The Journal of Chemical Physics* 2000;113:7756–7764.
- [53] Hirshfeld FL. Bonded-atom fragments for describing molecular charge densities. *Theoretica Chimica Acta* 1977;44:129–138.
- [54] Fukui K. The role of frontier orbitals in chemical reactions (Nobel Lecture). *Angewandte Chemie International Edition in English* 1982;21:801–809.
- [55] Fonseca Guerra C, Handgraaf J-W, Baerends EJ, Bickelhaupt FM. Voronoi deformation density (VDD) charges: Assessment of the Mulliken, Bader, Hirshfeld, Weinhold, and VDD methods for charge analysis. *Journal of Computational Chemistry* 2004;25:189–210.
- [56] Slipchenko LV, Krylov AI. Singlet-triplet gaps in diradicals by the spin-flip approach: A benchmark study. *The Journal of Chemical Physics* 2002;117:4694–4708.
- [57] Ess DH, Cook TC. Unrestricted Prescriptions for Open-Shell Singlet Diradicals: Using Economical Ab Initio and Density Functional Theory to Calculate Singlet–Triplet Gaps and Bond Dissociation Curves. *The Journal of Physical Chemistry A* 2012;116:4922–4929.
- [58] Zhao Y, Truhlar DG. Exploring the Limit of Accuracy of the Global Hybrid Meta Density Functional for Main-Group Thermochemistry, Kinetics, and Noncovalent Interactions. *J Chem Theory Comput* 2008;4:1849–68. doi:10.1021/ct800246v.
- [58] Albini, A.; Fagnoni, M. *Handbook of Synthetic Photochemistry*; John Wiley & Sons, 2009.
- [60] Wasserman E, Kuck VJ, Delavan WM, Yager WA. Electron paramagnetic resonance of 1. DELTA. oxygen produced by gas-phase photosensitization with naphthalene derivatives. *Journal of the American Chemical Society* 1969;91:1040–1041.
- [60] Foote, C. S. *Active Oxygen in Chemistry*; Springer Science & Business Media, 1995.
- [62] Clennan EL. Synthetic and mechanistic aspects of 1, 3-diene photooxidation. *Tetrahedron* 1991;47:1343–1382.



- [63] Bartlett PD, Mendenhall GD, Schaap AP. Competitive Modes of Reaction of Singlet Oxygen*. *Annals of the New York Academy of Sciences* 1970;171:79–88.
- [64] Gollnick K, Griesbeck A. Interactions of singlet oxygen with 2, 5-dimethyl-2, 4-hexadiene in polar and non-polar solvents: evidence for a vinyllog ene-reaction. *Tetrahedron* 1984;40:3235–3250.
- [65] Griesbeck AG, Oelgemöller M, Ghetti F. *CRC Handbook of Organic Photochemistry and Photobiology*. vol. 1. CRC Press; 2012.
- [66] Klopman G, others. *Chemical reactivity and reaction paths* 1974.
- [67] Van den Heuvel CJM, Hofland A, Steinberg H, de Boer TJ. The photo-oxidation of hexamethylbenzene and pentamethylbenzene by singlet oxygen. *Recueil Des Travaux Chimiques Des Pays-Bas* 1980;99:275–278.
- [68] McCarthy DJ, Waud WR, Struck RF, Hill DL. Disposition and metabolism of aniline in Fischer 344 rats and C57BL C3H F1 mice. *Cancer Research* 1985;45:174–180.
- [69] Miyoshi, N.; Tomita, G. *Z. Naturforsch. B* 1980, 35 (1), 107.
- [70] POLYMATH is copyrighted by Shacham, M.; Cutlip, M. B; Elly M. POLYMATH, <http://www.polymath-software.com/>, (accessed Feb 23, 2016)

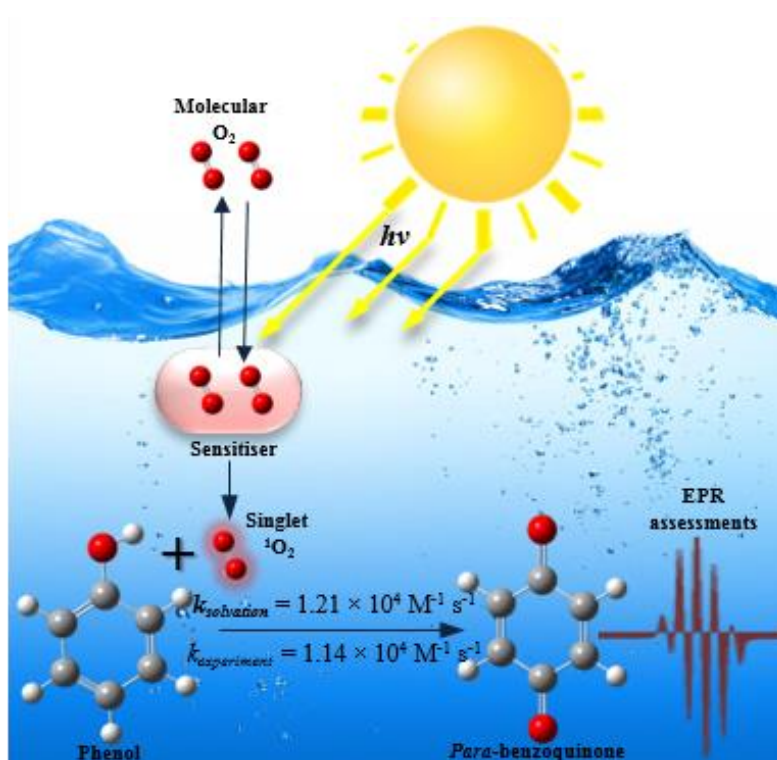
Jomana Al-Nu'airat

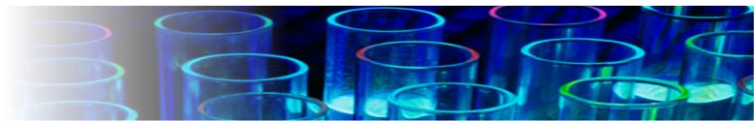




Chapter 7

Reaction of Phenol with Singlet Oxygen







Abstract

Photo-degradation of organic pollutants plays an important role in their removal from the environment. This study provides an experimental and theoretical account of the reaction of singlet oxygen $O_2(^1\Delta_g)$ with the biodegradable-resistant species of phenol in an aqueous medium. The experiments combine customised LED-photoreactors, high-performance liquid chromatography (HPLC), and electron paramagnetic resonance (EPR) imaging, employing rose bengal as a sensitiser. Guided by density functional theory (DFT) calculations at the M062X level, we report the mechanism of the reaction and its kinetic model. Addition of $O_2(^1\Delta_g)$ to the phenol molecule branches into two competitive 1,4-cycloaddition and *ortho ene*-type routes, yielding 2,3-dioxabicyclo[2.2.2]octa-5,7-dien-1-ol (i.e., 1,4-endoperoxide 1-hydroxy-2,5-cyclohexadiene) and 2-hydroperoxycyclohexa-3,5-dien-1-one, respectively. Unimolecular rearrangements of the 1,4-endoperoxide proceed in a facile exothermic reaction to form the only experimentally detected product, *para*-benzoquinone. EPR revealed the nature of the oxidation intermediates and corroborated the appearance of $O_2(^1\Delta_g)$ as the only active radical participating in the photosensitised reaction. Additional experiments excluded the formation of hydroxyl ($HO\cdot$), hydroperoxyl ($HO_2\cdot$), and phenoxy intermediates. We detected for the first time the *para*-semibenzoquinone anion (PSBQ) supporting the reaction pathway leading to the formation of *para*-benzoquinone. Our experiments and the water-solvation model result in the overall reaction rates of $k_{r-solvation} = 1.21 \times 10^4 \text{ M}^{-1} \text{ s}^{-1}$ and $k_r = 1.14 \times 10^4 \text{ M}^{-1} \text{ s}^{-1}$, respectively. These results have practical application to quantify the degradation of phenol in wastewater treatment.



7.1 Introduction

Even though light-induced reactions remain one of the less explored areas of green chemistry, many researchers have attempted to use sunlight in wastewater-detoxification processes, particularly in those involving biodegradation-resistant materials such as phenol [1]. An effective photosensitisation process relies on efficient light absorption. Unfortunately, the transparency of phenol mandates the use of an intermediate (dye) to absorb visible light in order to generate reactive oxygen species (ROS), mainly singlet oxygen $O_2(^1\Delta_g)$, to initiate the photo-degradation process [2–4].

Dye-sensitised photo systems generate singlet oxygen $O_2(^1\Delta_g)$ efficiently [5,6], resulting in a wide range of applications of such processes in chemical [7], medical [8], biological [9] and wastewater [10–12] treatments. Singlet oxygen $O_2(^1\Delta_g)$ represents one of the most reactive ROS, residing 94 kJ mol^{-1} ($\Delta_G H^{\circ}_{298}$) above the ground state triplet oxygen ($O_2(^3\Sigma_g^-)$) [13,14]. One of the prominent effects of singlet oxygen stems from its role in chain initiation and propagation [15–17] with aromatic organic compounds such as phenol. Reactions of $O_2(^1\Delta_g)$ include $[\pi_2 + \pi_2]$ 1,2-cycloaddition to isolated C=C bonds, $[\pi_2 + \pi_4]$ 1,4-cycloaddition to conjugated double bonds either in alkenes or aromatics, and the *ene* (Schenck) reaction normally involving the transfer of an allylic hydrogen from the carbon atom to the oxygen molecule [18,19].

Removing phenol and its derivatives, by reacting them with the ROS such as singlet oxygen, represents an attractive pathway for decreasing the toxicity of contaminated water. Phenols pollute surface water through industrial effluents in areas such as refineries ($6 - 500 \text{ mg L}^{-1}$) and coal processing ($9 - 6,800 \text{ mg L}^{-1}$) plants, severely affecting aquatic life, even at



concentrations as low as 1 ppb [4,20]. On the other hand, the steady-state concentration of singlet oxygen that exists in natural water varies within a range of $(6 - 28) \times 10^{-14}$ M [21]. In natural waters, singlet oxygen forms with a quantum yield of 1 to 3 % [22–24], indicating its likelihood to coexist with phenol.

Previous investigations on the photooxidation of phenol with singlet oxygen reported different products, such as *para*-benzoquinone, hydroquinone, and hydroxybiphenyls [10–12,25]. However, the underlining reaction mechanism remains poorly understood. Both the product distribution and photochemical efficiency strongly depend, in most cases, on the concentration of oxygen, a selected sensitiser and the pH of the reaction. For instance, alkaline conditions prompt phenol to deprotonate into phenoxide ion (aka phenolate, PhO^- , $\text{p}K_a = 9.8$) leading to the formation of 2-hydroxy-1,4-benzoquinone, 2-hydroxyhydroquinone, 2,5-dihydroxy-1,4-benzoquinone and others, rather than the usual *para*-benzoquinone [4]. Briviba et al. [12] and Pizzocaro et al. [25] demonstrated that reaction of $\text{O}_2(^1\Delta_g)$ with the phenol molecule leads selectively to the formation of *para*-benzoquinone. The absence of catechol and *ortho*-benzoquinone suggested the formation of a 1,4-endoperoxide (2,3-dioxabicyclo[2.2.2]octa-5,7-dien-1-ol) as an initial intermediate via a 1,4-cycloaddition mechanism, with subsequent steps proposed to involve unimolecular elimination of water. Other experimental studies attributed the formation of *para*-benzoquinone-type derivatives to the abstraction of phenolic hydrogen by $\text{O}_2(^1\Delta_g)$, followed by reactions with the ground-state triplet oxygen ($\text{O}_2(^3\Sigma_g^-)$) [26,27]. Hence, the overall oxidation pathways of phenol by singlet oxygen still remain largely speculative. Moreover, experiments appear insufficient for conclusive mechanistic and kinetic insights because of uncertainties relating to the very short lifetime of singlet molecular oxygen ($\sim 10^{-4}$ s) [14] and the possible parallel reactions involving triplet oxygen $\text{O}_2(^3\Sigma_g^-)$, and



hydroxyl radical ($\text{HO}\cdot$) [28]. Consequently, experimental investigation of the reaction of $\text{O}_2(^1\Delta_g)$ with phenol must be coupled with a sophisticated theoretical analysis.

To this end, the present contribution develops an experimental apparatus to react phenol with $\text{O}_2(^1\Delta_g)$ in a semi-batch reactor with known initial concentrations of phenol and $\text{O}_2(^1\Delta_g)$ produced continuously in situ from bubbled $\text{O}_2(^3\Sigma_g^-)$. We identify and quantify the intermediate and product species as a function of time using UV-Vis and high-performance liquid chromatography (HPLC). Reported findings map out the governing mechanism for the reaction of phenol with singlet oxygen, where the appearance of radical species is confirmed by electron paramagnetic resonance (EPR) measurements. These results, supplemented by the quantum chemical calculations, afford formulation of a kinetic model that offers practical applications to water treatment.

7.2 Materials and Methodology

7.2.1 Materials

We obtained all chemicals with the highest commercially available purity. The sensitiser (rose bengal, 85 %, Acros Organics), reactant (phenol, > 99 %, Sigma Aldrich) and expected products (1,4-benzoquinone, 99 %; hydroquinone, 98 %; catechol, > 99 %) were sourced from Sigma Aldrich, as were scavengers of the singlet oxygen (sodium azide, > 99.99 %; glutathione, > 98 %; DL-dithiothreitol, > 99 %; all Sigma Aldrich) and scavengers of hydroxyl radical (tert-butyl alcohol, > 99 %; sodium formate, 99.998 %). 2-Propanol (> 99 %) was from Ajax Finechem. TEMP (2,2,6,6-tetramethyl-4-piperidone 99.9 %), which functions as an EPR



spin trap for singlet O₂, and TEMPO (2,2,6,6-tetramethyl-4-piperidone-N-oxyl, 97 %), a standard product of the reaction of TEMP with singlet oxygen, were from Merck. Actinometry reagents (iron chloride, > 99 %; potassium oxalate monohydrate, 98.5 %; sodium acetate anhydrous, 99 %; and 1,10-phenanthroline monohydrate, 99.5 %) were from Chem Supply, and iron sulfate heptahydrate and sulfuric acid (98 %) were from Fisher Scientific. All aqueous solutions were prepared for EPR, UV-Vis, and HPLC standards and mobile phases using ultrapure water (resistivity >18 MΩ cm), tapped from a Sartorius Arium Pro UV/DI water purification system.

7.2.2 Photooxidation of phenol with singlet oxygen

Generally, polychromatic (lamp) [29] and monochromatic (laser) [30] lights generate the electromagnetic energy in the UV and visible range for photoreactions. The selection criteria depend on the environmental conditions and the required efficiency. For example, laser sources illuminate living cells in biological systems, while monochromatic light such as UV radiation covers larger areas; e.g., in wastewater treatment [29]. Examples of monochromatic lamps include light-emitting diodes (LEDs), xenon arcs, and medium-pressure Hg lamps selected by their relative photon intensity and efficiency. Among them, LEDs exhibit the most effective operation, with the lighting efficiency of photo-oxygenated system attaining 70 % [31]. Hence, the present study deployed LEDs as a light source. Figure 7.1 illustrates the photoreactor. We employed 24 green LEDs (4.5 × 10 × 500 mm), operated between 7 and 24 V. The LEDs form a 10-cm-long illuminating zone, assembled from eight strips, each consisting of three units. We uniformly mounted the strips onto the inside of a white PVC tube casing that surrounds the reactor. The dead-zone thickness between the LED units in a single



strip amounted to 0.68 cm, based on a 120° beam angle, prompting us to centre the quartz reactor 1 cm away from the PVC holder.

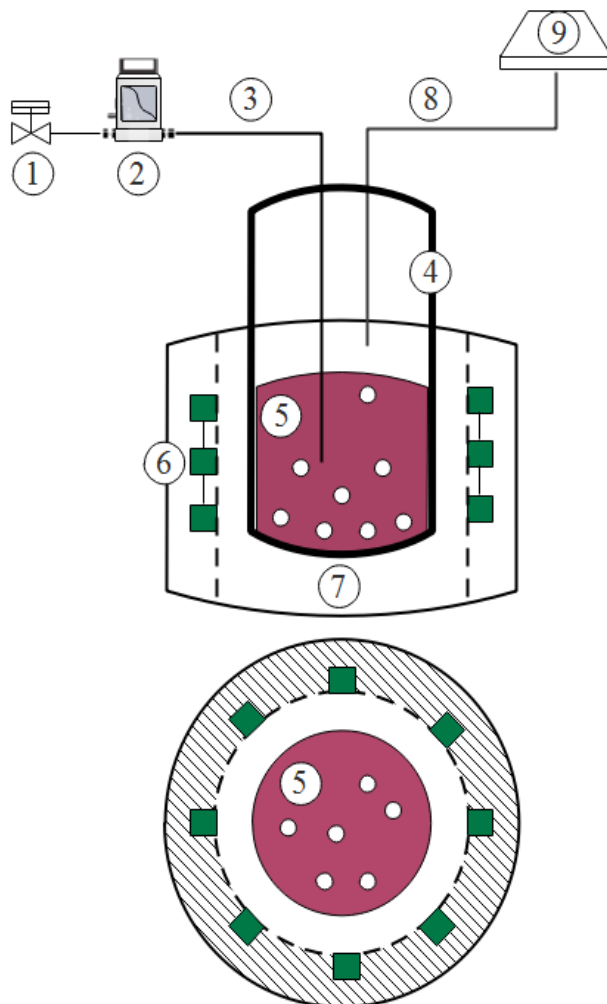


Figure 7.1. Schematic diagram of photochemical reactor shown in side and cross-sections. 1: O_2/He (3 %) valve, 2: mass flow controller, 3: inlet gas, 4: pyrex reactor, 5: phenol dyed solution (pH = 6), 6: LED strip (7 V), 7: PVC holder, 8: off-gas outlet, 9: exhaust.

Figure S7.1 in Supporting Information (SI) shows that rose bengal (RB) displays a strong absorption in the green band with a maximum around 510 nm and molar absorption coefficient as high as $10^5 \text{ M}^{-1} \text{ cm}^{-1}$ [32,33]. RB constitutes an efficient photosensitiser with a quantum yield of (0.76-0.85) [34]. To ensure a clean and pure source of singlet oxygen, the energy



difference between the sensitiser and its first triplet excited state should be equal or greater than the singlet oxygen energy level of about 94 kJ mol^{-1} (i.e. 0.98 eV) above the ground-state triplet oxygen [35]. The energy difference between RB singlet ground and its first triplet excited state corresponds to 166 kJ mol^{-1} (1.72 eV) [36]. Another reason for using RB lies in its stability over the time scale of our experiments (i.e., around 1 h). We conducted the bleaching test of RB by illuminating a $35 \mu\text{M}$ of the sensitiser-buffered solution for 0 – 24 h, followed by testing the absorbance (abs) in a range of 200 – 800 nm using a UV-Vis spectrophotometer. The bleaching rate of rose bengal (r_B), calculated from the rate of change of absorbance ($(\text{abs} - \text{abs}^\circ) \times t \text{ (s)}^{-1}$), amounts to $3.5 \times 10^{-15} \text{ M s}^{-1}$.

We prepared buffered solutions (pH = 6 or pD = 6.29, confirmed by a Hach pH-meter) of 1 mM phenol and $35 \mu\text{M}$ rose bengal (**5**, Figure 7.1) freshly in D_2O or H_2O in a temperature-controlled laboratory maintained at $25 \text{ }^\circ\text{C}$. The illumination experiments lasted 1 to 50 min and involved 5 mL aliquots, sourced from the stock solution and charged into the photoreactor. During the photo-induced reaction, a calibrated mass flow controller (Brooks 4800 series) fed a 3 % O_2 (in He balance) continuously at a constant rate of 500 mL min^{-1} . The helium carrier gas (instead of the generally applied N_2 medium) reduced the intermolecular interaction between the excited-state molecules and the inert gas. Okamoto et al. [37] reported no effect of superficial gas velocity (i.e., no mass transfer limitation) on the phenol reaction rate at above 0.35 cm s^{-1} , prompting us to adopt 0.44 cm s^{-1} as the superficial gas velocity in our experiments. We estimated the concentration of oxygen in the aqueous phase to reach $3.9 \times 10^{-5} \text{ M}$ based on Henry's law ($P_{\text{O}_2} = K_{\text{H}} [\text{O}_2]$, where $K_{\text{H}} = 769.23 \text{ atm M}^{-1}$) [38] and 3 % concentration of O_2 in He carrier gas ($P = 1 \text{ atm}$).



7.2.3 Analytical techniques

A Shimadzu HPLC instrument, equipped with a C18 analytical column (4.6 mm diameter and 150 mm length) and controlled by data acquisition software, served to quantify the conversion of phenol and the yields of the reaction products from the LED photoreactor. The analytical method involved injections of samples of 10 μL in volume and maintaining the oven temperature at 30 $^{\circ}\text{C}$. The mobile phase comprised a solution of 0.01 mol L^{-1} phosphate buffer (pH 4.5), methanol, and tetrahydrofuran (THF) in the ratio of 90:5:5, v/v, flowing at a rate of 1 mL min^{-1} , under low-pressure conditions. The analyte elutes into a UV-Vis detector operating at 254 nm using a reversed phase elution mode. Under these conditions, phenol eluted at 25.5 min and *para*-benzoquinone at 4 min (see Figure S7.2). Furthermore, we obtained the absorption spectra of RB, phenol, hydroquinone, *para*-benzoquinones, and 1,10-phenanthroline (actinometry experiment) in a quartz cell (1 cm pathlength) using Agilent Carry 5000 UV-Vis-NIR spectrophotometer operated at a resolution of 1 nm. Based on those spectra (Figure S3), we were able to confirm 254 nm as an optimum wavelength for HPLC analyses.

An electron paramagnetic resonance (EPR) spectrometer served to quantitate the concentration of spin-trapped singlet oxygen, as well as to monitor in situ the appearance of radical species. Chemical spin traps represent highly reactive species that capture singlet oxygen by forming a stable compound (endoperoxide), detectable by the EPR spectrometry. We used the most common singlet oxygen spin trap, 2,2,6,6-tetramethyl-4-piperidone (TEMP), because it reacts rapidly and selectively with $\text{O}_2(^1\Delta_g)$ to form 2,2,6,6-tetramethyl-4-piperidone-N-oxyl (TEMPO), a distinct and stable endoperoxide, with no side products. EPR spectroscopy readily detects TEMPO [39]. TEMP demonstrates high solubility in water and transparency to a range of excitation wavelengths [40,41]. We did not select other common spin traps (tetrapotassium



rubrene-2,3,8,9-tetracarboxylate (RTC) and disodium 9,10-anthracenedipropanoate (ADP) because of their reduced transparency [42].

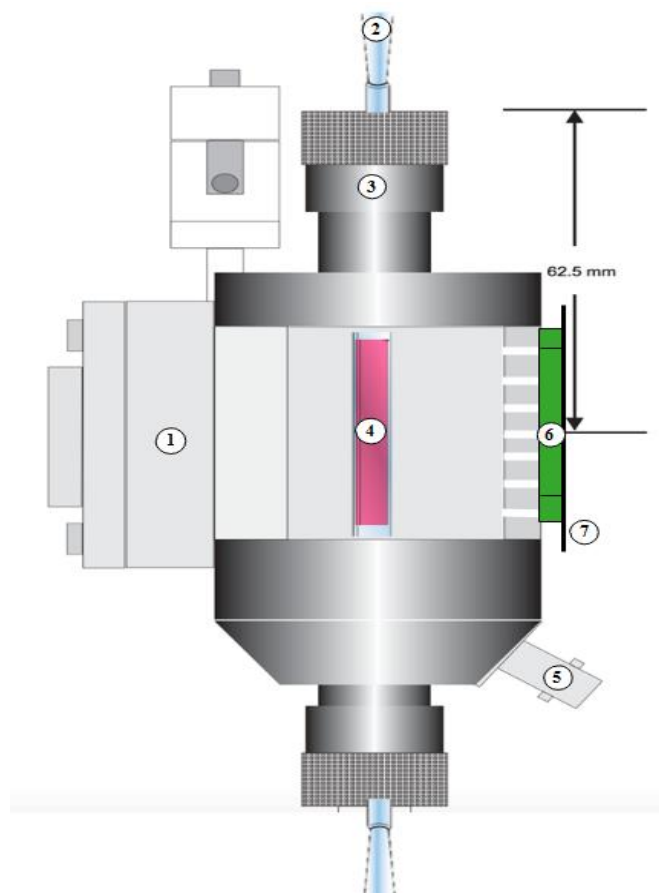


Figure 7.2. In-situ EPR photoreactor schematic; 1: EPR resonator, 2: WG-812-Q quartz flat cell, 3: collet nut, 4: dyed sample, 5: modulation cable, 6: green LED (24 V), 7: wooden support.

The EMXPlus 10/2.7 EPR spectrometer, fitted with an ER 4102ST general-purpose rectangular X-band cavity and cooling side plates, averaged 5 scans at a resonant frequency of 9.76 GHz. We placed the samples in a 10.5 mm flat cell (WG-812-Q), and bubbled a mixture of 3 % oxygen in He carrier gas for a least 20 min. Figure 7.2 illustrates an LED light, fixed on a wooden holder to prevent metallic interference with the magnetic field, that irradiated the sample in situ (i.e., inside the EPR resonator cavity). The spectrometer functioned at microwave power of 20 mW, modulation frequency of 100 kHz, modulation amplitude of 1 G,



sweep width of 100 G, and with the time constant set to 0.01 ms, conversion time to 50 ms, sweep time to 100 s, receiver gain to 2×10^5 , number of data points to 10000, and the centre field to 3487.00 G.

7.2.4 Estimated LED light intensity

A potassium ferrioxalate actinometer [43] was used to obtain light intensity based on the Hatchard–Parker approach for reactors in Figures 7.1 and 7.2 [44,45]. This method provides reliable results between 253 and 577 nm, based on established quantum yields for potassium ferrioxalate [43]. Supporting Information provides a more detailed description of the experimental procedure; Figure S7.4 (SI) illustrates the measurement of the absorbance of the ferrioxalate solution by UV-Vis spectroscopy.

Equations 7.1-7.3 yield the number of absorbed photons:

$$I\nu = \frac{\Delta n}{10^{-3} \cdot \Phi \cdot V_1 \cdot \Delta t} \quad 7.1$$

$$\Delta n = \frac{10^{-3} \cdot V_1 \cdot V_3 \cdot C_t}{V_2} \quad 7.2$$

$$C_t = \frac{abs.}{\varepsilon \cdot l} \quad 7.3$$

where Δn denotes change of the photo-generated ferrous iron (M), Φ the ferrioxalate quantum yield at the operated wavelength (0.86, 510 nm [43]), Δt irradiation time (s), V_1 irradiated volume (mL), and V_2 the volume taken from the irradiated samples (mL), V_3 the diluted volume (mL), C_t the concentration of ferrous iron after dilution (M), abs. the absorbance at 510 nm



which have been corrected by the background of a blank sample, l equals cm (the light path of the quartz cell) and ϵ represents the molar absorptivity in $\text{M}^{-1} \text{cm}^{-1}$ and the slope of the standard curve (11073, Figure S7.4). Our measurement of ϵ concurs well with the recently reported values of 11050 and 11100 $\text{M}^{-1} \text{cm}^{-1}$ [43].

After acquiring $\Delta n/\Delta t = 5.961 \times 10^{-8} \text{ mol min}^{-1}$ (the slope of the plot in Figure 7.3) for the photoreactor (Figure 1, LED operated at 7 V), the light intensity = $1.157 \times 10^{-9} \text{ E L}^{-1} \text{ s}^{-1}$. On the other hand, for the in situ EPR reactor (Figure 7.2), the light intensity amounts to $32.75 \times 10^{-5} \text{ E L}^{-1} \text{ s}^{-1}$ reflecting the higher voltage of 24 V of the LED light.

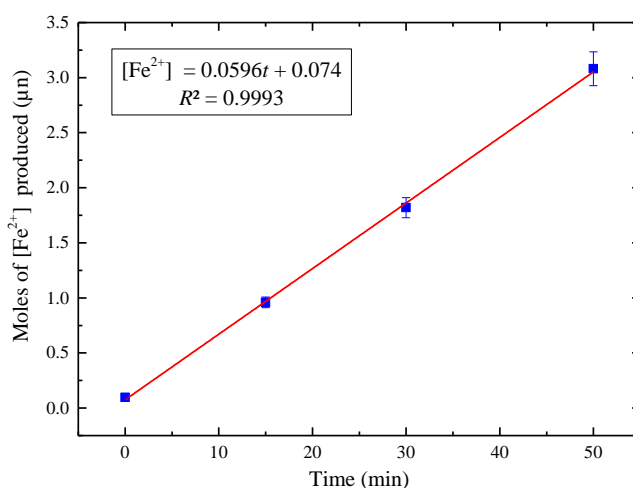


Figure 7.3. Photogenerated ferrous ions (Fe^{2+}) using 24 green LEDs at 0, 15, 30, and 50 min irradiation times.

7.2.5 Computational details

The Gaussian 09 suite of programs [46] was used for all energy calculations ($\Delta^\ddagger H^\circ_{298}$, $\Delta_r H^\circ_{298}$, $\Delta^\ddagger G^\circ_{298}$, and $\Delta_r G^\circ_{298}$) and structural optimisations. Possible biradical character of the phenol + $\text{O}_2(^1\Delta_g)$ system required determining the spin state of intermediate and transition structures



along the entire potential energy surface. Severe spin contaminations required energy refinements based on the approximated spin-projection scheme (AP) pioneered by the Yamaguchi group [47], in which the located transition structures and intermediates converge on a pure low-spin solution with zero-spin densities. Structural optimisations that involve fixing the frontier molecular orbitals (i.e., the broken symmetry solution) allow assessing a plausible spin contamination by examining a value of the total spin angular momentum operator S^2 [48]. A value of this operator of near unity for high spin configuration indicates a significant spin contamination. We found that expected values of the spin contamination operator of all of the present intermediates and transition structures clustered close to zero. This means that the phenol + O₂(¹Δ_g) system exists in a genuine singlet state, eliminating the need for further energy refinement. However, the energy of the O₂(¹Δ_g) suffers from contamination by the triplet state, as evident from the value of the spin contamination operator S^2 of approximately 1. As such, we applied the AP approach to refine the energy of the singlet oxygen molecule.

Cremer and co-workers [49] showed that unrestricted density functional methods (UDFT) perform well in comparison to multireference methods for deriving energies and geometries of singlet biradicals. Employing hybrid DFT functionals further enhances the accuracy of the UDFT in describing biradical systems [50]. Accordingly, we deployed the hybrid DFT functional of M062X [51] with the extended 6-311+G(3df,2p) [52] data set. The M062X functional has been parameterised to provide accurate and cost-effective performance for general application in organic chemistry [51,53]. In the next section, we quote changes in enthalpy and Gibbs energy calculated at 298.15 K. Finally, the KiSTheIP code [54] was used for computation of the reaction rate constants in the temperature range of 300-400 K, included in Table 7.1.



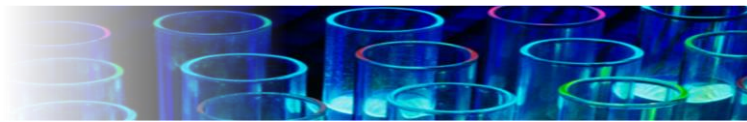
Table 7.1. Arrhenius rate parameters fitted in the temperature range of 300 – 400 K and 1 M for the phenol reaction channels with singlet oxygen; $A_{\text{solvation}}$ is $\text{cm}^3 \text{molecule}^{-1} \text{s}^{-1}$ or s^{-1} for unimolecular reaction and $E_{\text{a-solvation}}$ in kJ mol^{-1}

Reaction	$A_{\text{solvation}}$ (s^{-1} , $\text{cm}^3 \text{molecule}^{-1} \text{s}^{-1}$)	$E_{\text{a-solvation}}$ (kJ mol^{-1})	k ($\text{M}^{-1} \text{s}^{-1}$, s^{-1})
	300 – 400 K	300 – 400 K	298.15 K
Phenol + $\text{O}_2(^1\Delta_{\text{g}}) \rightarrow \text{M1}$	8.24×10^{-15}	15	1.21×10^4
Phenol + $\text{O}_2(^1\Delta_{\text{g}}) \rightarrow \text{M2}$	1.03×10^{-14}	41	4.07×10^{-1}
Phenol + $\text{O}_2(^1\Delta_{\text{g}}) \rightarrow \text{M3}$	9.75×10^{-15}	37	1.93×10^0
Phenol + $\text{O}_2(^1\Delta_{\text{g}}) \rightarrow \text{M4}$	1.76×10^{-15}	111	3.78×10^{-14}
Phenol + $\text{O}_2(^1\Delta_{\text{g}}) \rightarrow \text{M5}$	1.37×10^{-13}	116	3.91×10^{-13}
$\text{M6} \rightarrow \text{M7}$	1.57×10^8	57	1.62×10^{-2}
$\text{M7} \rightarrow \text{M8}$	1.31×10^{21}	134	2.91×10^{-3}
$\text{M8} \rightarrow \textit{para}\text{-BQ} + \text{H}_2\text{O}$	2.07×10^{21}	130	3.47×10^{-2}

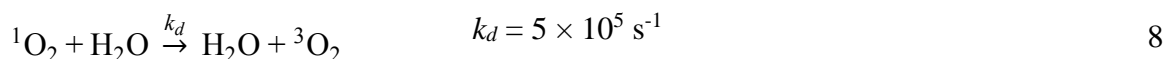
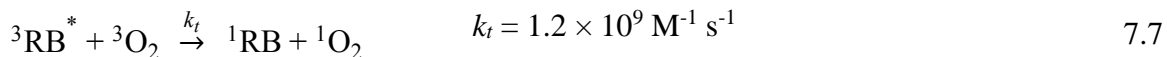
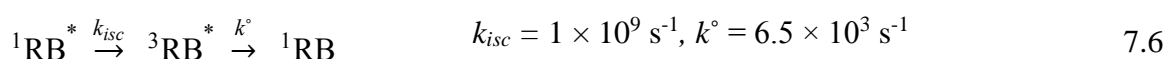
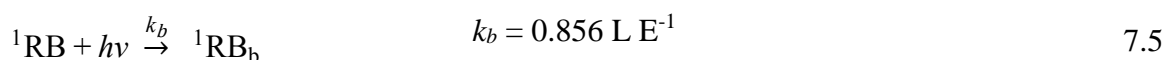
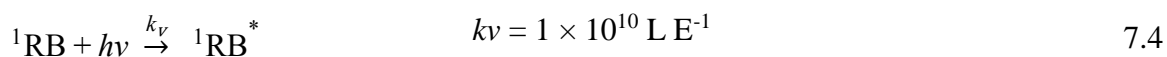
7.3 Results and Discussion

7.3.1 Generation of singlet oxygen

Equations 7.4-7.9 describe Type II dye-photoreaction mechanism for rose bengal [55]. Starting from a sensitizer molecule in its ground state, ^1RB absorbs green photon to form a singlet excited dianion ($^1\text{RB}^*$, Eq. 7.4) with singlet state energy of $E_S = 213 \text{ kJ mol}^{-1}$ [56]. Subsequently, the $^1\text{RB}^*$ spin-flips to the triplet state ($^3\text{RB}^*$, $E_T = 166 \text{ kJ mol}^{-1}$, Reaction 6) [57] through intersystem crossing (ISC). $^3\text{RB}^*$ may deactivate by fluorescence or non-radiative processes [58] to ^1RB with a rate constant of $k^\circ = 6.5 \times 10^3 \text{ s}^{-1}$ [55], and ^1RB bleaches with the



calculated rate of $r_B = 3.5 \times 10^{-15} \text{ M s}^{-1}$; see Section 7.2.2. While the photosensitiser molecule relaxes to its ground state, it transfers the excitation energy to a molecule of triplet oxygen $^3\text{O}_2$, forming singlet state oxygen $^1\text{O}_2$ (Reaction 7.7, $k_t = 1.2 \times 10^9 \text{ M}^{-1} \text{ s}^{-1}$ [55]). The vibronic coupling with water quenches singlet oxygen with a pseudo-first-order rate constant of $k_d = 5 \times 10^5 \text{ s}^{-1}$ [59]. We do not account for the radiative decay of singlet oxygen (k_p , Reaction 7.9) as this pathway makes negligible contribution to the decay process in solutions [60]. The product of $h\nu$ in Reaction 7.4 represents the light intensity absorbed by RB, calculated earlier using the actinometry technique, and $^1\text{RB}_b$ denotes the rose bengal bleaching product.



The lifetime of singlet oxygen changes dramatically in different solvents [61] depending on the energy-transfer efficiency from electronic to vibrational states. The closer the vibrational mode of the solvent to that of singlet oxygen, the higher the effectiveness of the deactivating process. For instance, O–D and O–H bonds vibrate at 2550 and 3500 cm^{-1} , respectively, whereas singlet oxygen vibrates at 3286 cm^{-1} ; hence, it quenches far faster in water than deuterium oxide (heavy water) [62]. Rodgers and T. Snowden [63] estimated the natural lifetime of singlet oxygen to be thirteen times higher in D_2O than in H_2O .



The strictly hindered amine (TEMP) reacts selectively with singlet oxygen to form nitroxide radical (TEMPO) that displays a characteristic EPR signal [64,65]. In Figure 7.4, we compare the TEMPO signals in 50 % (MeOH, D₂O) and in 50 % (MeOH, H₂O) by double-integrating the spectral areas. The yield of TEMPO is on average 8.45 times higher in D₂O than H₂O, corroborating a longer half-life of O₂(¹Δ_g) in D₂O. Figure 4b depicts the in situ spectral profiles of TEMPO after the reaction of TEMP with the photogenerated singlet oxygen, as recorded for the 35 μM RB sensitizer present in 50 % by volume solution of MeOH in D₂O. The signal increased steadily over the analysis time interval of 35 min. Figure 7.5 contrasts the experimental and modelled profiles of concentration of singlet oxygen in water, the former obtained from the EPR spin-trap technique and the latter from the solution of the coupled ordinary differential equations that describe the kinetics of the process, as coded in the POLYMATH software (Table S7.2). The measured trend correlates well with the kinetic approximation, indicating an expected concentration of singlet oxygen between $(3 - 4) \times 10^{-6}$ M in response to 3 h illumination by 24 V LED light.

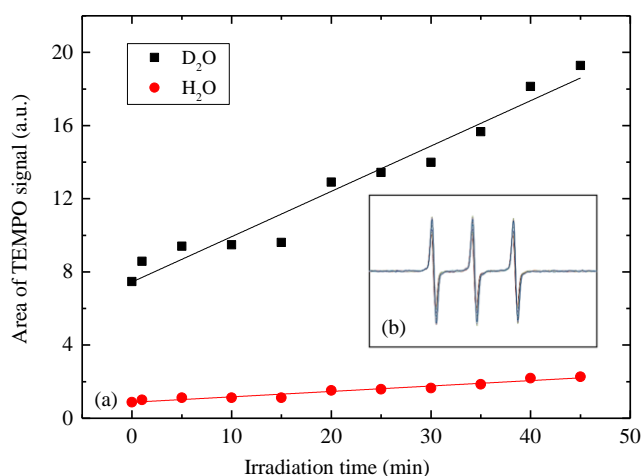


Figure 7.4. Double integrated area of the time course TEMPO signals in H₂O (red circles) and D₂O (black squares) (a), TEMPO spectra recorded in situ EPR after illuminating TEMP sample in dyed D₂O solution at pD = 6.35, g = 2.00062, and centre field = 3487.00 G (b).

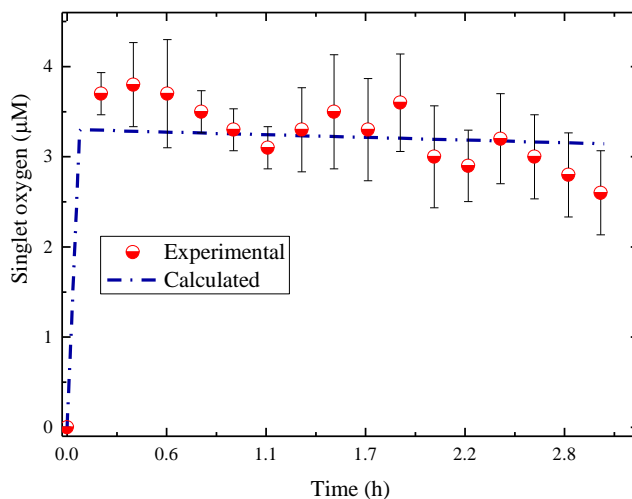


Figure 7.5. EPR concentration profile of singlet oxygen generated in H₂O using 24 V LED. The dash-dotted line represents the corresponding values obtained from POLYMATH kinetic solution detailed in Table S7.1.

7.3.2 Reaction of singlet oxygen with phenol

The photoreaction of phenol with singlet oxygen follows Eqs. 7.10 and 7.11. Equation 7.10 illustrates the physical quenching (spin orbital coupling), with no oxygen consumption ($k_q = 8 \times 10^6 \text{ M}^{-1} \text{ s}^{-1}$) [66], whereas, Eq. 7.11 describes the overall formation of *para*-benzoquinone (BQ), written here as a global step and broken down into elementary steps in the next section.





7.3.2.1 Mechanistic and kinetic analysis

As pictured in Figure 7.6, the reaction of phenol with $O_2(^1\Delta_g)$ branches into five initial channels with Gibbs free energies of activation spanning a relatively wide range between 59 kJ mol^{-1} and 168 kJ mol^{-1} (Figure S7.5 in Supporting Information depicts geometries of the located transition structures of all considered reactions). Figure 7.6 portrays two $[\pi_2 + \pi_4]$ 1,4-cycloaddition reactions producing intermediates **M1** and **M2** (1,4-peroxide structures). The concerted 1,4-cycloaddition of $O_2(^1\Delta_g)$ at *ipso* C(OH) and a *para* positions requires a $17 - 22 \text{ kJ mol}^{-1}$ lower energy barrier than corresponding addition at *ortho* and *meta* sites. This observation could easily be rationalised based on the charge distribution in the phenol molecule. The hydroxyl group donates charge to *ortho* and *para* carbon atoms, leaving C(OH) as an electron-deficient site. Calculated Mulliken charges at *para* C, *meta* (C), *ortho* (C) and *ipso* C sites amount to -0.194 eV , -0.133 eV , -0.143 eV , 0.354 eV , respectively. It follows that the *para* carbon appears relatively more susceptible to $O_2(^1\Delta_g)$ 1,4-cycloaddition than the *ortho* C atom, and consistently we find a lower energy barrier for the formation of **M1** in comparison to the emergence of **M2** (59 kJ mol^{-1} versus 81 kJ mol^{-1}).

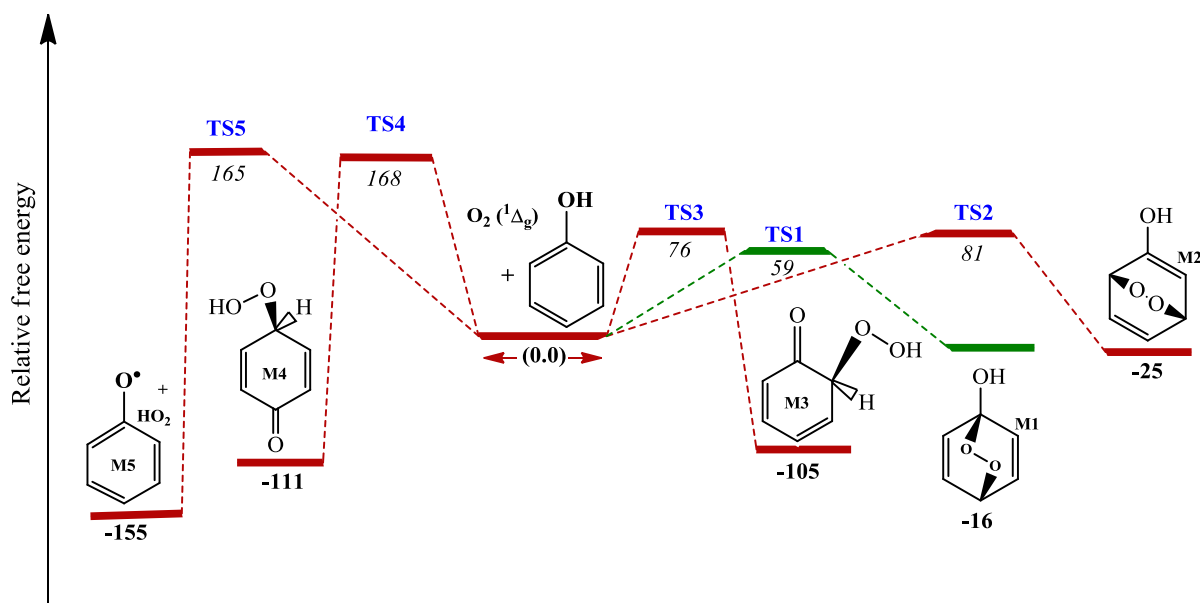


Figure 7.6. Potential energy map for the initial channels in the reaction of $\text{O}_2(^1\Delta_g)$ with phenol. Values in bold and italic denote Gibbs energy of reaction and activation ($\Delta^\ddagger G^\circ_{298}$ and $\Delta_r G^\circ_{298}$) calculated at 298.15 K, respectively in kJ mol^{-1} . The TS1 (green) line represents the preferred pathway, subsequently illustrated in Figure 7.7.

Two *ene*-type reactions lead to the formation of the two hydroperoxide ketones **M3** and **M4**. Transition structures TS3 and TS4 are concerted abstractions of the phenolic H simultaneously with the addition of the $\text{O}_2(^1\Delta_g)$ at an *ortho* or *para* positions, respectively. TS3 incurs a significantly lower energy barrier than TS4 (76 kJ mol^{-1} versus 168 kJ mol^{-1}) and contrasts with direct H-abstraction reaction, which is associated with a sizable barrier 165 kJ mol^{-1} . The high energy barrier of TS5 contradicts a previous mechanistic interpretation of dominance of the hydroxyl H-abstraction channel in the oxidation of phenolic moieties by $\text{O}_2(^1\Delta_g)$ (Heyne, 2003).

Table 7.1 lists the reaction rate constants for the five initial channels fitted in the low to intermediate temperature window of 300 – 400 K. Inspection of values in Table 7.1 reveals that, the formation of **M1** intermediate holds importance throughout the considered temperature range with a rather negligible contribution from the other four channels.



By applying the Curtin-Hammond principle [67], the ratio of *para-ipso* and *meta-ortho* products ($[P_{para}]/[P_{meta}]$) is dictated by the free energy gap ($\Delta_G G^{\circ}_{298}{}^{P-M}$) between the *para* and *meta* transition states (TS1 and TS2) rather than the stabilities of the two intermediates (**M1** and **M2**); i.e., $\Delta_G G^{\circ}_{298}{}^{P-M} = 21 \text{ kJ mol}^{-1}$. Our ratio of $[P_{para}]/[P_{meta}]$ at 298.15 K corresponds to $\sim 9000:1$. This finding indicates an expected dominance of the *para* isomer and a negligible abundance of the *meta* isomer, excluding the *meta*-channel from further mechanistic analysis. The prominence of the channel leading to the formation of **M1** concurs with the experimental detection of the 1,4-peroxide structures during UV radiation of several phenolic compounds. Consistently with the results of the present calculations, literature suggests no *ene*-type reaction at the *ortho* position as a main reaction channel in the system of phenol and $O_2(^1\Delta_g)$. In contrast, we predict that the commonly discussed route affording the **M4** intermediate constitutes a minor pathway.

The formation of phenoxy radical via direct abstraction could be ruled out in view of the high Gibbs free energy barrier embedded in TS5. Moreover, our in-situ EPR results revealed no formation of phenoxy radicals. This absence could potentially be explained easily through the ionisation of the hydroxyl group (i.e., deprotonation) as in Eq. 7.14, where K_a represents the acidity constant of the phenol group $-OH$. We calculated the deprotonation degree of the phenolic $-OH$ group at $pH = 6$ as $\alpha = 1.6 \times 10^{-4}$. Therefore, the ak_{PO} in Eq. 7.13 remains negligible with $ak_{PO} \approx 0$ [68].





$$k_r = (1-\alpha)k_{r-\text{POH}} + \alpha k_{\text{PO}^-} \quad 7.13$$

$$\alpha = \frac{1}{1+10^p K_{a-\text{pH}}} \quad 7.14$$

Next, we turn our attention to the selective formation of *para*-benzoquinone from reaction of phenol and $\text{O}_2({}^1\Delta_g)$. Any major product flux toward *para*-benzoquinone follows the two major initial pathways, producing **M1** and **M3** intermediates. Herein, we show that an unimolecular isomerisation of the **M1** moiety produces *para*-benzoquinone via a facile mechanism. Figure 7.7 depicts the potential energy surface for the formation of *para*-benzoquinone from oxidation of phenol by singlet oxygen. The **M1** intermediate incurs endothermicity of 25 kJ mol^{-1} (with exergicity of 16 kJ mol^{-1}) relative to the separated reactants, and it could further stabilise into the three-member-ring structure **M6** without passing through an intrinsic reaction barrier. A 1,2-hydrogen transfer via TS6 proceeds with an enthalpic barrier of 53 kJ mol^{-1} and yields the **M7** intermediate. In the subsequent step, intramolecular hydrogen transfer from the hydroxyl group through TS7 forms the significantly de-energised **M8** intermediate through an enthalpic barrier of 140 kJ mol^{-1} . Thus, the **M7** \rightarrow **M8** step represents one of the “bottlenecks” of the mechanism shown in Figure 7.7. Finally, elimination of water from intermediate **M8** yields *para*-benzoquinone. The enthalpy of the final products falls 360 kJ mol^{-1} below the separated reactants.

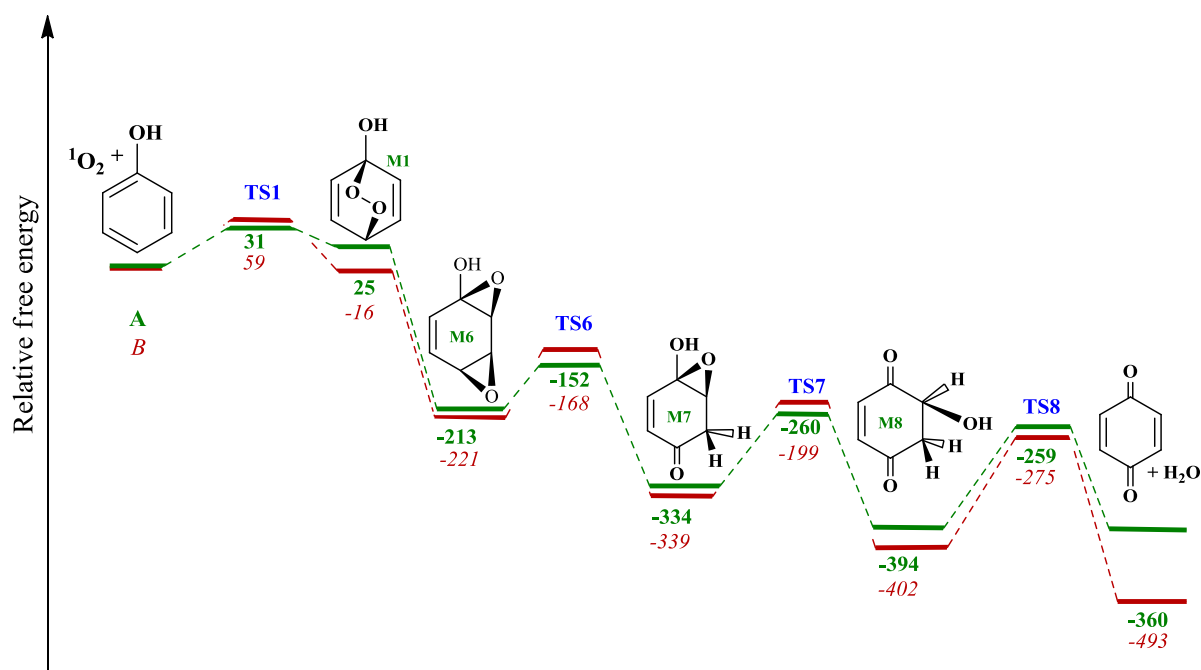


Figure 7.7. Enthalpy (bold non-italic green) and Gibbs free energy (italic red) map for the formation of *para*-BQ from the reaction of singlet oxygen with phenol using M062X (solvation) model. All values are in kJ mol⁻¹ at 298.15 K.

7.3.2.2 Formation of product species

HPLC data provides major insights into the $O_2(^1\Delta_g)$ interaction with phenol. The photolysis of phenol-RB buffered solution ultimately yielded *para*-benzoquinone with no other products detected (Figure 7.8). This high selectivity towards the formation of *para*-adduct product was also observed in the case of singlet-oxygen reaction with salicylic acid [69]. In Figure 7.9, singlet oxygen degrades phenol with a second-order rate constant of $k_r = 1.14 \times 10^4 \text{ M}^{-1} \text{ s}^{-1}$ in H_2O . In addition, in deuterium oxide, phenol reacts by approximately 7.5-fold faster than in water, supporting the involvement of singlet oxygen. We detected no trace of *para*-benzoquinone when executing the photoreaction of phenol in the absence of rose bengal or oxygen.

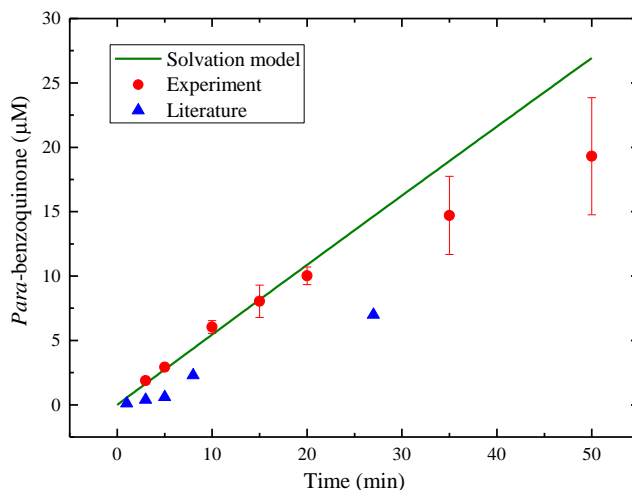


Figure 7.8. Concentration profiles for the formation of para-benzoquinone via the water-solvation model (green line) and the published experimental measurements of Briviba *et al.* (1993) (blue triangles, methylene blue) versus our present results (red circles, rose bengal).

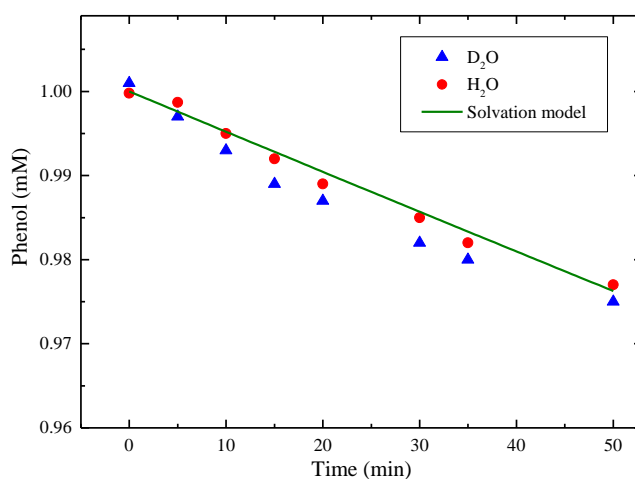


Figure 7.9. Concentration profiles for phenol depletion via our experimental results in H₂O (red circles) and D₂O (blue triangles), versus water-solvation model (green line). The overall mechanism for the water solvation model is discussed in Section 7.3.5.

Illumination of phenol in RB-buffered solution (50 % MOH, pH = 6.5) gives rise to the spectrum illustrated in Figure 7.10, showing a well-defined 1:4:6:4:1 stick configuration that represents the interaction of the radical with four identical protons. The five superhyperfine



lines in Figure 7.11 show splitting of *para*-semibenzoquinone anion (PSBQ) signal [70–72]. In addition to the PSBQ signal, we observed the appearance a semi-reduced anion spectrum of RB (i.e., the spectrum of an RB trianion radical), as shown in Figure 7.12, and described in Eqs. 7.15 and 7.16. The pattern of RB trianion radical illustrates an unpaired electron interacting with two equivalent protons (known as position 1 and 8 in the RB structure). Even though benzoquinone, as reported by Foote et al. [73] does not interact with singlet oxygen, it quenches the triplet state of rose bengal. Figure 7.13 graphs the spin counts profiles of both signals.

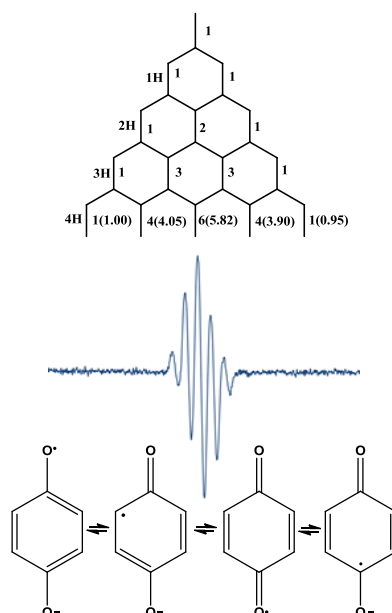


Figure 7.10. *In-situ* EPR spectrum of 0.5 mM *para*-benzoquinone and 35 μM RB in 50% buffered methanol solution (pH = 6.5) after illumination for 1 min.

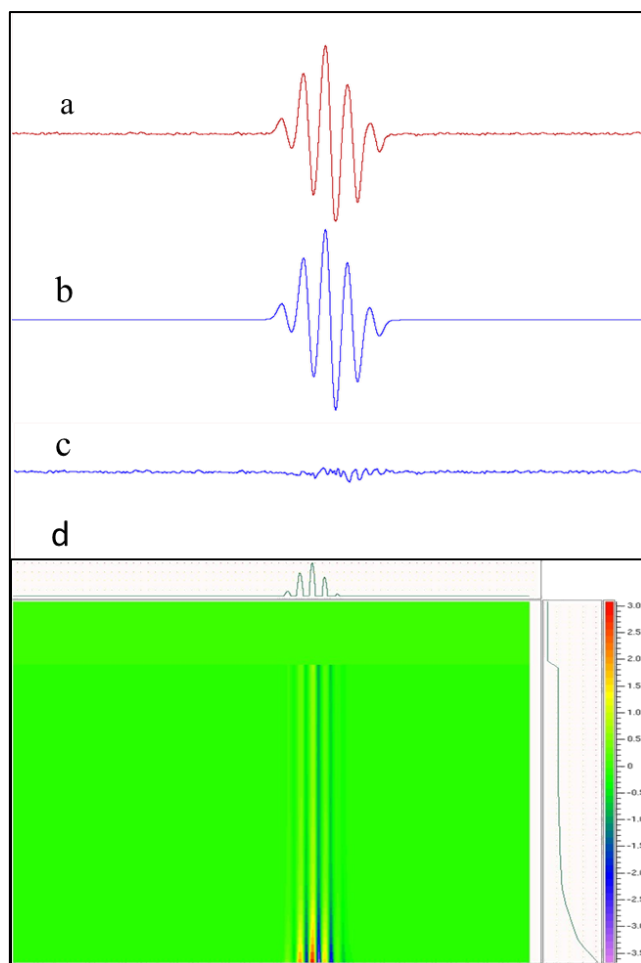


Figure 7.11. Experimental (a), simulated (b), residual (c) and time-course (d) EPR spectra obtained upon continuous in-situ irradiation of 35 μM RB and 1 mM phenol in 50 % buffered methanol solution (pH = 6.5) for 3 hr. Simulation parameters: RB trianion; $g = 2.00439$, hyperfine splitting HFS = 1.14224 ± 0.00005 , *para*-semibenzoquinone anion; $g = 2.00446$, HFS = 2.36955 ± 0.00005 .

In several mechanisms suggested for the photosensitised reaction of phenol, researchers argued the effect of hydroxyl radical ($\text{HO}\cdot$) on the product formation and selectivity. Reaction of phenol with hydroxyl radical proceeds via *ortho*, *meta*, and *para* routes [74]. Even though the *meta*-product was not detected in some scenarios, the *ortho* analogue was always present. For example, when $\text{HO}\cdot$ is generated using $\text{Fe(II)-EDTA/H}_2\text{O}_2$, hydroquinone (*para*) and catechol (*ortho*) are produced in equivalent quantities without appearance of the *meta*-product [75]. We tested the effect of radical scavengers for both singlet oxygen and hydroxyl radical ($\text{O}_2(^1\Delta_g)$),



HO \cdot) in order to verify their existence in our system. As noted in Table 7.2, the addition of the HO \cdot scavengers (tert-butyl alcohol, 2-propanol [76] , and sodium formate [77,78]) seemed to have no obvious effect on the benzoquinone production. In contrast, O $_2$ ($^1\Delta_g$) scavengers (sodium azide [79]; [59] dithiothreitol [80], and glutathione [81]) suppress the formation of *para*-benzoquinone (e.g., sodium azide <0.01, Table 7.2). The failure of the HO \cdot scavengers to block the formation of benzoquinone demonstrates the absence of HO \cdot radical in this reaction, whereas a significant effect of O $_2$ ($^1\Delta_g$) scavengers further supports the involvement of singlet oxygen O $_2$ ($^1\Delta_g$). Moreover, the presence of only the *para*-product in the reaction of phenol with O $_2$ ($^1\Delta_g$) indicates no involvement of HO \cdot in the oxidation process.

Applying the values of the kinetic parameters for solution from Table 7.1 and converting the units to L and mol, our calculated rate constant of photooxidation of phenol with singlet delta oxygen at 298.15 K is $k_{r-solvation} = 1.21 \times 10^4 \text{ M}^{-1} \text{ s}^{-1}$, which is consistent with the present experimental measurement of $k_r = 1.14 \times 10^4 \text{ M}^{-1} \text{ s}^{-1}$ as well as the literature value of $k_r = 2.4 \times 10^4 \text{ M}^{-1} \text{ s}^{-1}$ [12] in methanol solution [82]. We solved the system of ordinary differential equations (ODEs) for our solvation model (see Table S7.2 in SI) using POLYMATH software. The initial concentrations corresponded to 35 μM and 1 mM for rose-bengal sensitiser and phenol, respectively.

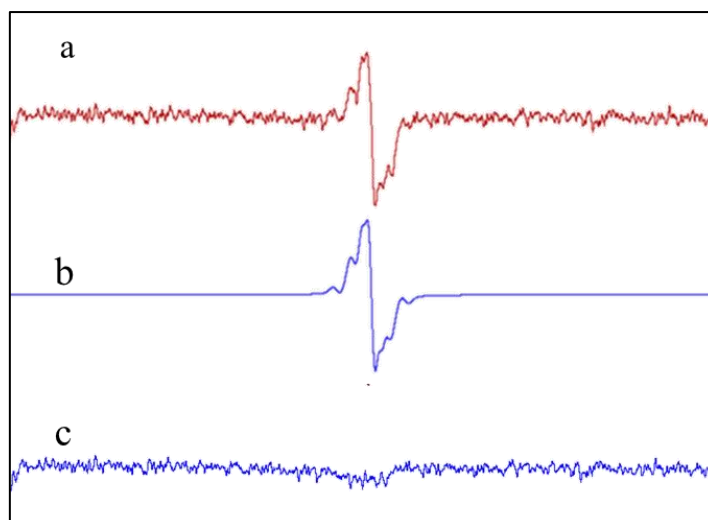


Figure 7.12. EPR signal of a: RB trianion radical formed after illuminating a sample containing 1 mM phenol, 35 μ M rose bengal in 50 % methanol solution, at pH = 6 for 1 min, b: simulated EPR spectrum and c: the subtract. Simulation parameters: $g = 2.00439$, $HFS = 1.14224 \pm 0.00005$.

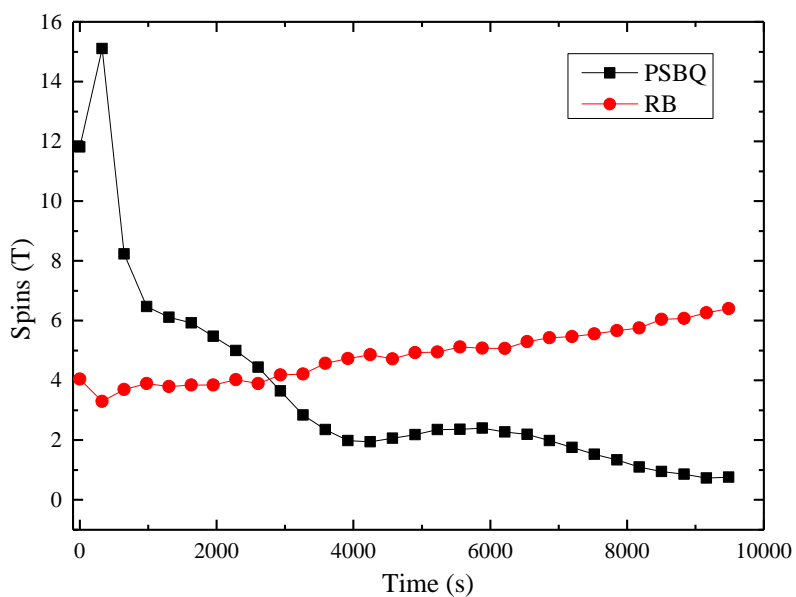


Figure 7.13. Spins-course EPR spectra obtained upon continuous irradiation *in-situ* of 35 μ M RB and 1 Mm phenol in 50 % buffered methanol solution (pH = 6.5) for 2.6 h. Simulation parameters: RB trianion (red circles); $g = 2.00439$, $HFS = 1.14224 \pm 0.00005$, *para*-semibenzoquinone anion (PSBQ, black squares); $g = 2.00446$, $HFS = 2.36955 \pm 0.00005$.



Table 7.2. Effect of $O_2(^1\Delta_g)$ and $HO\cdot$ scavengers on the formation of benzoquinone after 30 min of illumination (pH = 6, H_2O) at 298.15 K

Scavengers		Benzoquinone ($14\mu M$)
$O_2(^1\Delta_g)$ Scavengers	Sodium azide (10 mM)	<0.01
	Dithiothreitol (10 mM)	1.05 ± 0.05
	Glutathione (10 mM)	1.43 ± 0.17
$HO\cdot$ Scavengers	Sodium formate (10 mM)	13.55 ± 0.51
	Tert-butyl alcohol (100 mM)	13.02 ± 0.32
	2-propanol (100 mM)	14.30 ± 0.28

In the kinetic modelling, we apply a batch reactor model with a steady-state concentration of singlet oxygen and a sensitizer quantum yield of $26.6 \times 10^{-6} M^{-1}$ and 0.76, with the kinetic expressions derived from the solvation model. As illustrated in Figures 7.8 and 7.9, the results of the model compare well with the experimental measurements. In Figure 8, we also include the experimental measurements of Briviba et al. [12] demonstrating close agreement. The small difference reflects the lower quantum yield of methylene-blue dye used by Briviba et al. [12] The vibronic coupling of singlet oxygen with water or the physical quenching of singlet delta oxygen [60] with phenol may also explain the small discrepancy.



7.4 Conclusions

This contribution has addressed the mechanistic and kinetic aspects of the photo-induced reaction of phenol with singlet oxygen, coupling the experimental and theoretical results for the first time. Singlet oxygen reaction with phenol proved to have an extreme selectivity toward the *para* position. The suggested mechanism proceeds via the 1,4-endoperoxide species (**M1**) intermediate to yield *para*-benzoquinone, the only product detected. Herein, we show that the unimolecular isomerisation of the **M1** moiety produces *para*-benzoquinone via a facile mechanism. Our mechanistic maps are supported by the in-situ detection of *para*-semibenzoquinone anion (PSBQ) in the EPR resonator and by the results of singlet-oxygen spin trapping and experiments involving $O_2(^1\Delta_g)$ and $HO\cdot$ scavengers. The addition of the $HO\cdot$ scavengers has no obvious effect on the benzoquinone production. In contrast, $O_2(^1\Delta_g)$ scavengers suppress the formation of benzoquinone (e.g., sodium azide <0.01). Moreover, phenol disappears more rapidly in deuterium oxide compared to normal water (by approximately 7.5 times), supporting the involvement of singlet oxygen. Our experimental and modelling results should apply to decomposition of other biologically active phenolic entities, typically occurring in aqueous media.

Supporting Information

The Supporting Information is included in Chapter 10 (Appendix VI) of the thesis. Figures S7.1 Bleaching test of rose bengal in buffered solution (pH = 6), Figures S7.2 HPLC spectrum of (35 μ M RB, 1 mM phenol) illuminated sample in buffered solution, Figures S7.3 UV-Vis absorption spectra for benzoquinone and hydroquinone, Figures S7.4 Calibration curve for



ferrioxalate actinometer, Figures S7.5 Optimised structures of transition states of phenol oxidation by singlet oxygen, Table S7.1 POLYMATH ordinary differential equations (ODEs) and parameters for the estimated singlet oxygen concentration profile, Table S7.2 POLYMATH ordinary differential equations (ODEs) and parameters for the solvation model, and detailed description of the actinometry experiments.

7.5 References

- [1] Zhou Y, Jiang J, Gao Y, Pang S-Y, Yang Y, Ma J, et al. Activation of peroxymonosulfate by phenols: Important role of quinone intermediates and involvement of singlet oxygen. *Water Res* 2017;125:209–18. doi:10.1016/j.watres.2017.08.049.
- [2] Koehler B, Barsotti F, Minella M, Landelius T, Minero C, Tranvik LJ, et al. Simulation of photoreactive transients and of photochemical transformation of organic pollutants in sunlit boreal lakes across 14 degrees of latitude: A photochemical mapping of Sweden. *Water Res* 2018;129:94–104. doi:10.1016/j.watres.2017.10.064.
- [3] Vione D, Fabbri D, Minella M, Canonica S. Effects of the antioxidant moieties of dissolved organic matter on triplet-sensitized phototransformation processes: Implications for the photochemical modeling of sulfadiazine. *Water Res* 2018;128:38–48. doi:10.1016/j.watres.2017.10.020.
- [4] Garcia NA. New trends in photobiology: singlet-molecular-oxygen-mediated photodegradation of aquatic phenolic pollutants. A kinetic and mechanistic overview. *J Photochem Photobiol B* 1994;22:185–196.
- [5] Wainwright M. Photosensitisers and Photosensitisation. *Photosensit Biomed*, 2009:27–41.
- [6] Wainwright M. Photosensitisers in biomedicine. John Wiley & Sons; 2009.
- [7] Takizawa S, Aboshi R, Murata S. Photooxidation of 1, 5-dihydroxynaphthalene with iridium complexes as singlet oxygen sensitizers. *Photochem Photobiol Sci* 2011;10:895–903.



- [8] Bhatnagar S, Kumar A, Ameta SC. Photooxidation of Some Pharmaceutical Drugs by Singlet Molecular Oxygen. *Asian J Pharm Biol Res* 2011;1:210–217.
- [9] Weishaupt KR, Gomer CJ, Dougherty TJ. Identification of singlet oxygen as the cytotoxic agent in photo-inactivation of a murine tumor. *Cancer Res* 1976;36:2326–2329.
- [10] Li C, Hoffman MZ. Oxidation of Phenol by Singlet Oxygen Photosensitized by the Tris(2,2'-bipyridine)ruthenium(II) Ion. *J Phys Chem A* 2000;104:5998–6002. doi:10.1021/jp9937104.
- [11] Pizzocaro C, Bolte M, SUN H, Hoffman MZ. Metal complex sensitized photooxidation of phenol in aqueous solution. *New J Chem* 1994;18:737–743.
- [12] Briviba K, Devasagayam TPA, Sies H, Steenken S. Selective para-hydroxylation of phenol and aniline by singlet molecular oxygen. *Chem Res Toxicol* 1993;6:548–53. doi:10.1021/tx00034a025.
- [13] Khan AU. Singlet molecular oxygen from superoxide anion and sensitized fluorescence of organic molecules. *Science* 1970;168:476–477.
- [14] Clennan EL, Pace A. Advances in singlet oxygen chemistry. *Tetrahedron* 2005;61:6665–6691.
- [15] Starik AM, Titova NS. Possibility of Initiation of Combustion of CH₄-O₂ (Air) Mixtures with Laser-Induced Excitation of O₂ Molecules. *Combust Explos Shock Waves* 2004;40:499–510.
- [16] Starik AM, Kuleshov PS, Sharipov AS, Titova NS. Kinetics of Ignition and Combustion in the Al-CH₄-O₂ System. *Energy Fuels* 2014;28:6579–6588.
- [17] Starikovskiy A, Aleksandrov N. Plasma-assisted ignition and combustion. *Prog Energy Combust Sci* 2013;39:61–110.
- [18] Maranzana A, Canepa C, Ghigo G, Tonachini G. Theoretical Study on the Reactivity and Regioselectivity of the Ene Reaction of $1\Delta_g$ O₂ with α,β -Unsaturated Carbonyl Compounds. *Eur J Org Chem* 2005;2005:3643–9. doi:10.1002/ejoc.200500215.
- [19] Griesbeck AG, Oelgemöller M, Ghetti F. *CRC Handbook of Organic Photochemistry and Photobiology*. vol. 1. CRC Press; 2012.



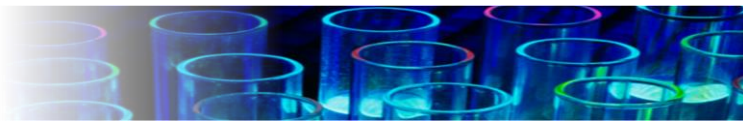
- [20] Mohammadi S, Kargari A, Sanaeepur H, Abbassian K, Najafi A, Mofarrah E. Phenol removal from industrial wastewaters: a short review. *Desalination Water Treat* 2015;53:2215–2234.
- [21] Tinsley IJ. *Chemical Concepts in Pollutant Behavior*. John Wiley & Sons; 2004.
- [22] Zepp RG, Wolfe NL, Baughman GL, Hollis RC. Singlet oxygen in natural waters 1977.
- [23] Haag WR, Hoigne J. Singlet oxygen in surface waters. 3. Photochemical formation and steady-state concentrations in various types of waters. *Environ Sci Technol* 1986;20:341–348.
- [24] Frimmel FH, Bauer H, Putzien J, Murasecco P, Braun AM. Laser flash photolysis of dissolved aquatic humic material and the sensitized production of singlet oxygen. *Environ Sci Technol* 1987;21:541–545.
- [25] Pizzocaro C, Bolte M, Hoffman MZ. Cr(bpy)₃³⁺-sensitized photo-oxidation of phenol in aqueous solution. *J Photochem Photobiol Chem* 1992;68:115–9. doi:10.1016/1010-6030(92)85023-N.
- [26] Heyne B, Kohnen S, Brault D, Mouithys-Mickalad A, Tfibel F, Hans P, et al. Investigation of singlet oxygen reactivity towards propofol. *Photochem Photobiol Sci* 2003;2:939–45. doi:10.1039/B302373G.
- [27] Heyne B, Brault D, Fontaine-Aupart M-P, Kohnen S, Tfibel F, Mouithys-Mickalad A, et al. Reactivity towards singlet oxygen of propofol inside liposomes and neuronal cells. *Biochim Biophys Acta BBA-Gen Subj* 2005;1724:100–107.
- [28] Burns JM, Cooper WJ, Ferry JL, King DW, DiMento BP, McNeill K, et al. Methods for reactive oxygen species (ROS) detection in aqueous environments. *Aquat Sci* 2012;74:683–734.
- [29] De la Cruz N, Giménez J, Esplugas S, Grandjean D, De Alencastro LF, Pulgarin C. Degradation of 32 emergent contaminants by UV and neutral photo-fenton in domestic wastewater effluent previously treated by activated sludge. *Water Res* 2012;46:1947–1957.
- [30] Kochevar IE, Redmond RW. [2] Photosensitized production of singlet oxygen. *Methods Enzymol* 2000;319:20–28.



- [31] Loponov KN, Lopes J, Barlog M, Astrova EV, Malkov AV, Lapkin AA. Optimization of a scalable photochemical reactor for reactions with singlet oxygen. *Org Process Res Dev* 2014;18:1443–1454.
- [32] Sarna T, Zajac J, Bowman MK, Truscott TG. Photoinduced electron transfer reactions of rose bengal and selected electron donors. *J Photochem Photobiol Chem* 1991;60:295–310.
- [33] Linden SM, Neckers DC. Type I and type II sensitizers based on rose bengal onium salts. *Photochem Photobiol* 1988;47:543–550.
- [34] Esser P, Pohlmann B, Scharf H-D. The photochemical synthesis of fine chemicals with sunlight. *Angew Chem Int Ed Engl* 1994;33:2009–2023.
- [35] Nifiatis F, C Athas J, Don Dasitha Gunaratne K, Gurung Y, Mae Monette K, Joseph Shivokevich P. Substituent effects of porphyrin on singlet oxygen generation quantum yields. *Open Spectrosc J* 2011;5.
- [36] Fukuzumi S, Fujita S, Suenobu T, Yamada H, Imahori H, Araki Y, et al. Electron transfer properties of singlet oxygen and promoting effects of scandium ion. *J Phys Chem A* 2002;106:1241–1247.
- [37] Okamoto K-I, Hondo F, Itaya A, Kusabayashi S. Kinetics of dye-sensitized photodegradation of aqueous phenol. *J Chem Eng Jpn* 1982;15:368–375.
- [38] Green D, Perry R. *Perry's Chemical Engineers' Handbook*, Eighth Edition. McGraw Hill Professional; 2007.
- [39] Han SK, Hwang T-M, Yoon Y, Kang J-W. Evidence of singlet oxygen and hydroxyl radical formation in aqueous goethite suspension using spin-trapping electron paramagnetic resonance (EPR). *Chemosphere* 2011;84:1095–1101.
- [40] Qi H, Dong X, Zhao Y, Li N, Fu H, Feng D, et al. ROS production in homogenate from the body wall of sea cucumber *Stichopus japonicus* under UVA irradiation: ESR spin-trapping study. *Food Chem* 2016;192:358–362.
- [41] Yaghini E, Pirker KF, Kay CW, Seifalian AM, MacRobert AJ. Quantification of Reactive Oxygen Species Generation by Photoexcitation of PEGylated Quantum Dots. *Small* 2014;10:5106–5115.



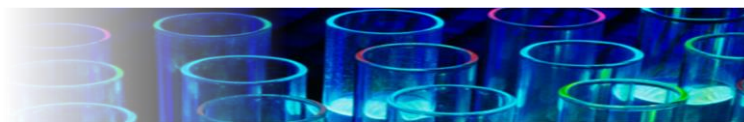
- [42] Nardello V, Brault D, Chavalle P, Aubry J-M. Measurement of photogenerated singlet oxygen (1O_2 ($^1\Delta_g$)) in aqueous solution by specific chemical trapping with sodium 1, 3-cyclohexadiene-1, 4-diethanoate. *J Photochem Photobiol B* 1997;39:146–155.
- [43] Klán P, Wirz J. *Photochemistry of Organic Compounds: From Concepts to Practice*. John Wiley & Sons; 2009.
- [44] Hatchard CG, Parker CA. A new sensitive chemical actinometer. II. Potassium ferrioxalate as a standard chemical actinometer. *Proc. R. Soc. Lond. Math. Phys. Eng. Sci.*, vol. 235, The Royal Society; 1956, p. 518–536.
- [45] Parker CA. A new sensitive chemical actinometer. I. Some trials with potassium ferrioxalate. *Proc. R. Soc. Lond. Math. Phys. Eng. Sci.*, vol. 220, The Royal Society; 1953, p. 104–116.
- [46] Frisch M, Trucks GW, Schlegel HB, Scuseria GE, Robb MA, Cheeseman JR, et al. *Gaussian 09, Revision A. 02*, Gaussian. Inc Wallingford CT 2009;200.
- [47] Yamanaka S, Kawakami T, Nagao H, Yamaguchi K. Effective exchange integrals for open-shell species by density functional methods. *Chem Phys Lett* 1994;231:25–33.
- [48] Abe M. Diradicals. *Chem Rev* 2013;113:7011–7088.
- [49] Gräfenstein J, Kraka E, Filatov M, Cremer D. Can unrestricted density-functional theory describe open shell singlet biradicals? *Int J Mol Sci* 2002;3:360–394.
- [50] Saito T, Nishihara S, Kataoka Y, Nakanishi Y, Matsui T, Kitagawa Y, et al. Transition state optimization based on approximate spin-projection (AP) method. *Chem Phys Lett* 2009;483:168–171.
- [51] Zhao Y, Truhlar DG. The M06 suite of density functionals for main group thermochemistry, thermochemical kinetics, noncovalent interactions, excited states, and transition elements: two new functionals and systematic testing of four M06-class functionals and 12 other functionals. *Theor Chem Acc* 2008;120:215–241.
- [52] Montgomery Jr JA, Ochterski JW, Petersson GA. A complete basis set model chemistry. IV. An improved atomic pair natural orbital method. *J Chem Phys* 1994;101:5900–5909.



- [53] Zhao Y, Truhlar DG. Exploring the Limit of Accuracy of the Global Hybrid Meta Density Functional for Main-Group Thermochemistry, Kinetics, and Noncovalent Interactions. *J Chem Theory Comput* 2008;4:1849–68. doi:10.1021/ct800246v.
- [54] Canneaux S, Bohr F, Henon E. KiSThelP: A program to predict thermodynamic properties and rate constants from quantum chemistry results†. *J Comput Chem* 2014;35:82–93.
- [55] Gollnick K. Type II photooxygenation reactions in solution. *Adv Photochem* 1968;6.
- [56] Ludvíková L, Friš P, Heger D, Šebej P, Wirz J, Klán P. Photochemistry of rose bengal in water and acetonitrile: a comprehensive kinetic analysis. *Phys Chem Chem Phys* 2016;18:16266–16273.
- [57] Chesneau E, Neckers DC. Electron transfer sensitized photobleaching of rose bengal induced by triplet benzophenones. *J Photochem Photobiol Chem* 1988;42:269–281.
- [58] Zhang X-F, Zhang I, Liu L. Photophysics of halogenated fluoresceins: involvement of both intramolecular electron transfer and heavy atom effect in the deactivation of excited states. *Photochem Photobiol* 2010;86:492–498.
- [59] Hasty N, Merkel PB, Radlick P, Kearns DR. Role of azide in singlet oxygen reactions: Reaction of azide with singlet oxygen. *Tetrahedron Lett* 1972;13:49–52.
- [60] Schweitzer C, Schmidt R. Physical mechanisms of generation and deactivation of singlet oxygen. *Chem Rev* 2003;103:1685–1758.
- [61] Minaev BF. Spin-orbit coupling mechanism of singlet oxygen $a^1\Delta_g$ quenching by solvent vibrations. *Chem Phys* 2017;483:84–95.
- [62] Boix-Garriga E, Rodríguez-Amigo B, Planas O, Nonell S. Chapter 2: Properties of Singlet Oxygen, 2016, p. 23–46.
- [63] Rodgers, T. Snowden. Lifetime of $O_2(1A_g)$ in Liquid Water As Determined by Time-Resolved Infrared Luminescence Measurements 1982.
- [64] Nardi G, Manet I, Monti S, Miranda MA, Lhiaubet-Vallet V. Scope and limitations of the TEMPO/EPR method for singlet oxygen detection: the misleading role of electron transfer. *Free Radic Biol Med* 2014;77:64–70.

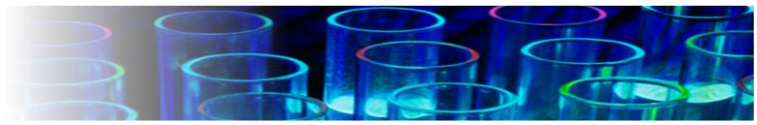


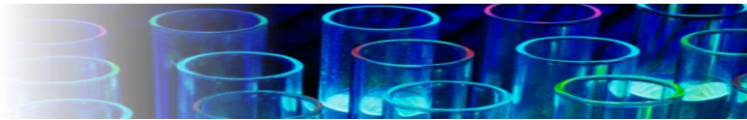
- [65] Zang L-Y, Zhang Z, Misra HP. EPR Studies of trapped singlet oxygen (1O_2) generated during photoirradiation of hypocrellin A. *Photochem Photobiol* 1990;52:677–683.
- [66] Erickson PR, Walpen N, Guerard JJ, Eustis SN, Arey JS, McNeill K. Controlling Factors in the Rates of Oxidation of Anilines and Phenols by Triplet Methylene Blue in Aqueous Solution. *J Phys Chem A* 2015;119:3233–43. doi:10.1021/jp511408f.
- [67] Seeman JJ. Effect of conformational change on reactivity in organic chemistry. Evaluations, applications, and extensions of Curtin-Hammett Winstein-Holness kinetics. *Chem Rev* 1983;83:83–134.
- [68] Scully FE, Hoigné J. Rate constants for reactions of singlet oxygen with phenols and other compounds in water. *Chemosphere* 1987;16:681–694.
- [69] Feix JB, Kalyanaraman B. Production of singlet oxygen-derived hydroxyl radical adducts during merocyanine-540-mediated photosensitization: analysis by ESR-spin trapping and HPLC with electrochemical detection. *Arch Biochem Biophys* 1991;291:43–51.
- [70] Leaver IH. Semiquinone radical intermediates in the eosin-sensitized photooxidation of phenols. *Aust J Chem* 1971;24:891–894.
- [71] Leaver IH. An ESR study of radical intermediates in the photoreduction of xanthene dyes. *Aust J Chem* 1971;24:753–763.
- [72] Lambert C, Sarna T, Truscott TG. Rose bengal radicals and their reactivity. *J Chem Soc Faraday Trans* 1990;86:3879–3882.
- [73] Foote CS, Denny RW, Weaver L, Chang Y, Peters J. Quenching of singlet oxygen. *Ann N Y Acad Sci* 1970;171:139–148.
- [74] Raghavan NV, Steenken S. Electrophilic reaction of the hydroxyl radical with phenol. Determination of the distribution of isomeric dihydroxycyclohexadienyl radicals. *J Am Chem Soc* 1980;102:3495–3499.
- [75] Moorhouse CP, Halliwell B, Grootveld M, Gutteridge JM. Cobalt (II) ion as a promoter of hydroxyl radical and possible ‘crypto-hydroxyl’ radical formation under physiological conditions. Differential effects of hydroxyl radical scavengers. *Biochim Biophys Acta BBA-Gen Subj* 1985;843:261–268.



- [76] Khopde SM, Priyadarsini KI, Venkatesan P, Rao MNA. Free radical scavenging ability and antioxidant efficiency of curcumin and its substituted analogue. *Biophys Chem* 1999;80:85–91.
- [77] Henglein A, Kormann C. Scavenging of OH radicals produced in the sonolysis of water. *Int J Radiat Biol Relat Stud Phys Chem Med* 1985;48:251–258.
- [78] Makino K, Mossoba MM, Riesz P. Chemical effects of ultrasound on aqueous solutions. Evidence for hydroxyl and hydrogen free radicals ($\cdot\text{OH}$ and $\cdot\text{H}$) by spin trapping. *J Am Chem Soc* 1982;104:3537–3539.
- [79] Li MY, Cline CS, Koker EB, Carmichael HH, Chignell CF, Bilski P. Quenching of Singlet Molecular Oxygen ($^1\text{O}_2$) by Azide Anion in Solvent Mixtures. *Photochem Photobiol* 2001;74:760–4. doi:10.1562/0031-8655(2001)074<0760:QOSMOO>2.0.CO;2.
- [80] Devasagayam TP, Sundquist AR, Di Mascio P, Kaiser S, Sies H. Activity of thiols as singlet molecular oxygen quenchers. *J Photochem Photobiol B* 1991;9:105–116.
- [81] Lafleur MVM, Hoorweg JJ, Joenje H, Westmijze EJ, Retèl J. The ambivalent role of glutathione in the protection of DNA against singlet oxygen. *Free Radic Res* 1994;21:9–17.
- [82] Miyoshi N, Tomita G. Fluorescein-photosensitized Furan Oxidation in Methanolic and Reversed Micellar Solutions, Part II Kinetic Analysis. *Z Für Naturforschung B* 1980;35:107–111.

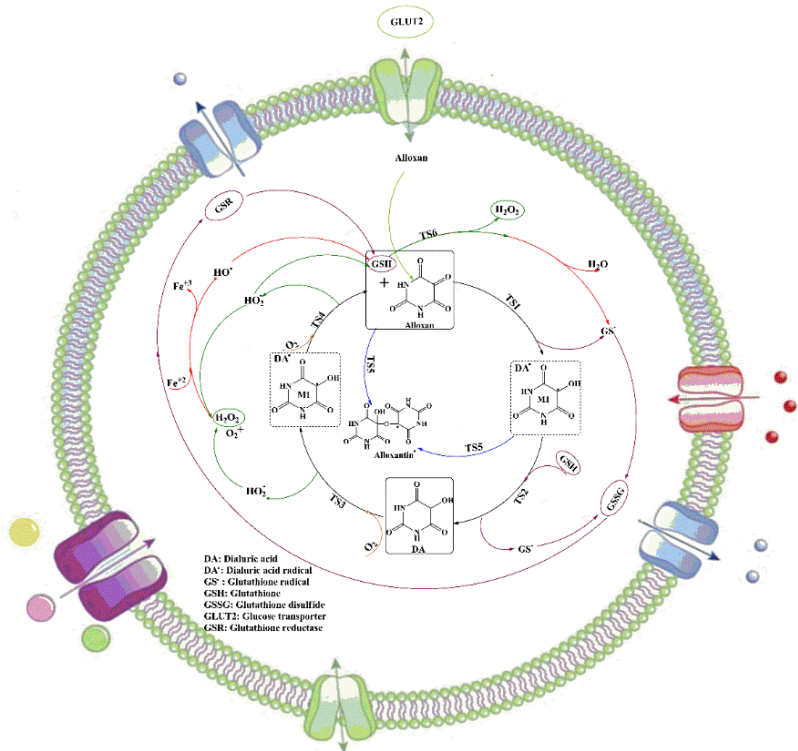
Jomana Al-Nu'airat



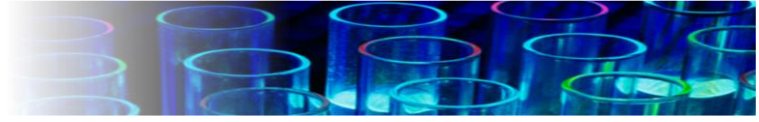


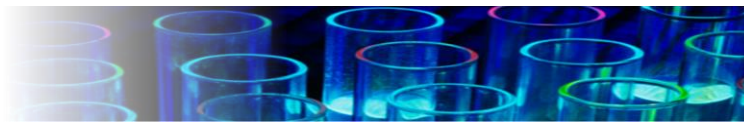
Chapter 8

Alloxan – Glutathione Redox Cycle



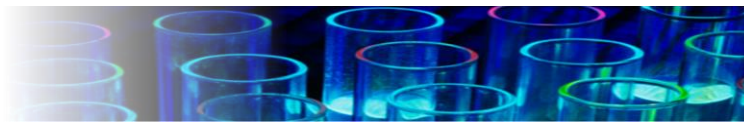
Chapter 8





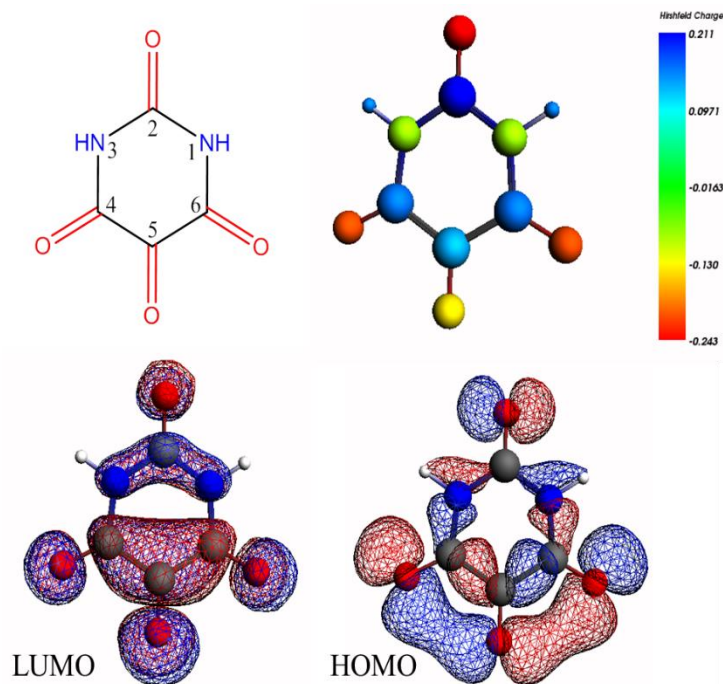
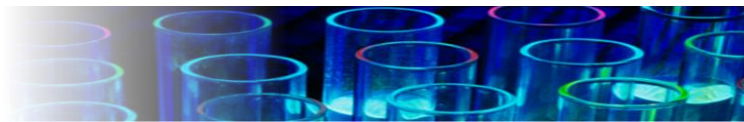
Abstract

Alloxan represents a cytotoxic analogue of glucose that has been widely applied to induce diabetes in laboratory animals. The glucose transporter (GLUT2) miscarries alloxan to the pancreas, where then, alloxan initiates a redox cycle with intercellular thiols (GSH) forming reactive oxygen species (ROS). ROS eventually cause necrosis of the pancreatic insulin-producing beta cells, prompting the insulin-dependent diabetes mellitus (IDDM). This contribution illuminates the mechanistic pathways governing the alloxan–GSH redox via accurate molecular modelling coupled with experimental determination of prominent reactive species. Combined electron paramagnetic resonance (EPR) and broad-scan UV-Vis spectroscopy identified the major products as well as the main intermediate radicals of the titled reaction. The EPR spectra proved for the first time the direct synchronised generation of dialuric acid radical (DA^{\cdot}) and glutathione radical (GS^{\cdot}), with g factors amounting to 2.00265 and 2.00252, respectively. Furthermore, applying of the 5,5-Dimethyl-1-Pyrroline-N-Oxide (DMPO) spin trap reveals also the generation of hydrogen peroxide (H_2O_2) and hydroxyl radical (HO^{\cdot}). Based on our combined modelling and experimental UV-Vis analysis, we assigned the nature of “compound 305” to the DA^{\cdot} - GS^{\cdot} complex. Results from this study explain the alloxan-induced diabetes on a precise molecular basis.



8.1 Introduction

The chemical induction of alloxan (Scheme 8.1) constitutes one of the most effective techniques to induce diabetes in laboratory rats [1–6]. Alloxan (2,4,5,6(1H, 3H)-pyrimidinetetrone) represents a cytotoxic analogue of glucose,[7] and, because of this structural similarity, GLUT2 (glucose transporter) miscarries alloxan to the plasma membrane in the pancreas. Where then, alloxan initiates a cyclic redox reaction with intercellular thiols [8,9], mainly tripeptide glutathione (GSH, cf. Figure 8.1) [10–12]. GSH reduces alloxan to dialuric acid (DA), then the reaction of DA with oxygen converts DA back to alloxan, generating reactive oxygen species (ROS) such as superoxide and hydroperoxyl radicals ($O_2^{\cdot-}$, HO_2^{\cdot}), hydrogen peroxide (H_2O_2) and hydroxyl radical (HO^{\cdot}) in the Fenton reaction [13–15]. The ROS terminates the pancreatic insulin-producing beta cells causing insulin-dependent diabetes mellitus (IDDM) or what is generally known as “alloxan diabetes” [16–18]. Consequently, following the discovery of its diabetogenic action in 1946, alloxan has been heavily applied to induce diabetes in laboratory animals [19].



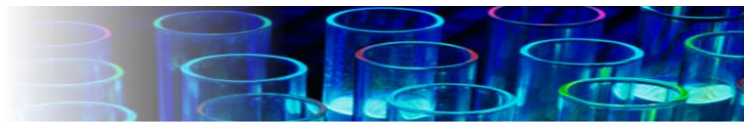
Scheme 8.1. Alloxan structure

Alloxan retains two proton donor sites (N–H) and four proton acceptor groups (C=O). For such a unique structure, alloxan parades several tautomeric forms that might lead to different biological activity [20–22]. In general, alloxan reacts readily with thiols and inhibits easily enzymes such as hexokinase and glucokinase [10]. Alloxan reacts with GSH, forming dialuric acid (DA) through an intermediate moiety of dialuric acid radical (DA[•]) that, under an aerobic condition, transforms back to alloxan [23,24]. However, large Gibbs free energy change of reaction make the one electron reduction of alloxan to DA[•] unfeasible thermodynamically [25,26]. Lagercrantz and Yhland [23] confirmed that, the radical species (DA[•]) generated in the reaction of alloxan with GSH matches the one formed during the oxidation of DA. Dialuric acid is nontoxic [12,13,27], however its ability to form ROS upon oxygenation, especially superoxide radicals (O₂^{•-}) and its protonated form of hydroperoxyl radical (HO₂[•]), renders it hazardous.



Studying the chemical reactivity of alloxan and GSH provides crucial information to understand their diabetogenic behaviour. However, in aqueous solutions, alloxan spontaneously disintegrates following a first order reaction with a half-life of only 0.9 min (37 °C, pH = 7.4) [12,28]. The involvement of other ROS and the emergence of parallel reactions make it even harder to elucidate precisely the redox pathways of alloxan. Moreover, the literature presents the following gaps: (i) One-electron reduction of alloxan to DA^{\bullet} is not thermodynamically favourable at physiological pH of 7.4 [25]. Nonetheless, alloxan shows remarkable reactivity towards GSH. (ii) Published results do not substantiate the direct formation of the two radicals (DA^{\bullet} , GS^{\bullet}) simultaneously. Various attempts, since the 1960s, have revealed the formation of DA^{\bullet} only. (iii) There are no models of the reaction of GSH with alloxan in literature. This might be as a result of complex structure of GSH, mandating massive computational cost. (iv) The previous spectroscopic (UV-Vis) measurement of the titled reaction was performed within a narrow wavelength window of 200 – 300 nm.

Therefore, the present study aims to address the aforementioned points. We combine the results from the electron paramagnetic resonance (EPR) spectroscopy and broad-scan UV-Vis spectroscopy to identify the major products as well as the main intermediate radicals of the reaction of GSH with alloxan. Furthermore, our contribution illuminates the mechanistic pathways governing the alloxan–GSH redox cycle within the density functional theory (DFT) framework. In particular, we map out the reaction routes, assessing their relative feasibility based on the computed reaction rate constants and the Gibbs free energy change of relevant reactions.

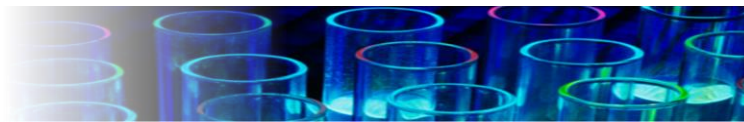


8.2 Methodology

8.2.1 Analytical techniques

The presented EPR spectra represent averages of five scans at a resonant frequency of 9.76 GHz using a EMXPlus 10/2.7 spectrometer fitted with an ER 4102ST general purpose rectangular X-band cavity equipped with cooling side-plates. We placed samples in a 10.5 mm flat cell (WG-812-Q) and scanned them with the spectrometer typically set to the following parameters: microwave power, 20 mW; modulation frequency, 100 kHz; modulation amplitude 3 G; sweep width, 100 G; time constant, 0.01 ms; conversion time, 50 ms; sweep time, 100 s; receiver gain 2×10^5 ; number of data points, 10000; and, centre field 3490.0 G. The standard deviation in the relative EPR intensity corresponded to $\pm 10\%$.

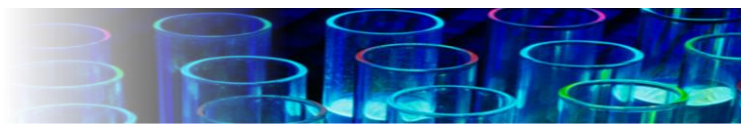
We obtained the glutathione and alloxan UV-Vis spectra using an Agilent Carry 5000 UV-Vis-NIR spectrophotometer operated at a resolution of 1 nm. For alloxan-glutathione solutions, phosphate buffers served to obtain the biological pH of 7.4 along with a pH of 6.4. We obtained the absorption profiles in situ by scanning the samples for time intervals of 0–10 h and corrected the baseline by subtracting the spectra of the corresponding blank buffer solutions. We selected the ratio of alloxan to glutathione as 1 : 10 based on a previous study of Patterson et al. [28] Sigma Aldrich supplied glutathione and alloxan with the highest commercial purity available of more than $> 98\%$. We prepared all solutions using ultrapure water with resistivity $> 18 \text{ M}\Omega \text{ cm}$, tapped from an Arium Pro-Sarburis milli-Q (Millipore) water purification system. In each experiment we prepared fresh solutions containing alloxan or glutathione prior to analysis in a 25°C temperature-controlled laboratory.

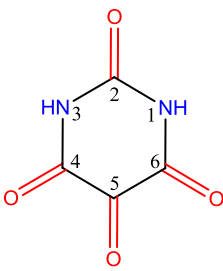


8.2.2 Computational details

The Gaussian 09 [29] suite of programs affords all structural optimisations and energy calculations ($\Delta^\ddagger H^\circ_{298}$, $\Delta_r H^\circ_{298}$, $\Delta^\ddagger G^\circ_{298}$, and $\Delta_r G^\circ_{298}$). The theoretical methodology comprises the meta-hybrid M062X[30] functional supplemented with the polarised basis set of 6-311+G(d,p)[31] and the well-known complete-basis-set CBS-QB3 composite functional. The M062X method has been parameterised to provide accurate and cost-effective performance for general application in organic chemistry, as well documented in literature [30,32–34]. The complex chemistry model of CBS-QB3 provides the most accurate estimates of geometries and enthalpies, especially for hydrogen abstraction reactions [35–38]. We base the discussion on Gibbs free energy and enthalpy values calculated at 298.15 K.

Simulating the aqueous-phase reactions based on gas phase model represents satisfactory approximation of reactions occurring in aqueous media under the proviso that Fukui coefficients in these solvents do not change significantly [39]. However, in this contribution we simulated the redox cycle reactions in both aqueous and gaseous media. We modelled reactions in the aqueous phase by deploying the polarisable continuum model (PCM) with the dielectric constant (ϵ) equal to 78.39 at 298.15 K [40]. Attempts to investigate the catalytic effect of discrete water molecules [41–43], rather than using PCM, did not yield viable pathways. In Table 8.1, that presents the validation of the computational method, we compare the values of both lengths and bond angles for the alloxan molecule, as computed from M062X, CBS-QB3 and CBS-QB3 (solvation) models with the results of experimental measurements. We selected the CBS-QB3 (solvation) model based on a mean unsigned errors (MUE) of 0.007 Å for bond length and 0.68° for bond angles.

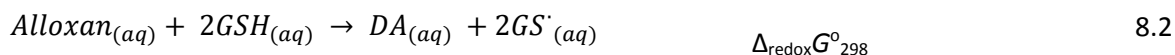
**Table 8.1.** Validation of computational methods

	Distances (Å)	M06-2X	CBS-QB3		Experimental [22,74–76]	
		Gas	Gas	Solvation (PCM)		
	C(5)-O(5)	1.187	1.195	1.197	[1.198]	
	C(5)-C(4)	1.543	1.546	1.542	[1.529]; 1.537	
	C(4)-O(4)	1.194	1.201	1.206	[1.212]	
	C(4)-N(3)	1.384	1.388	1.378	[1.365]; 1.371	
	N(3)-C(2)	1.392	1.395	1.393	1.374	
	N(3)-H(3)	1.014	1.014	1.015	[1.021]	
	MUE	0.012	0.011	0.007		
	Angles (°)					
	C(4)-C(5)-O(5)	120.79	120.78	120.73	[120.7]	
	C(4)-C(5)-C(6)	118.42	118.44	118.55	[118.7]; 113.8	
	C(5)-C(4)-N(3)	114.61	114.56	114.69	[115.3]; 117.4	
	C(5)-C(4)-O(4)	122.10	122.36	121.64	[120.8]; 121.7	
	N(3)-C(4)-O(4)	123.29	123.08	123.67	[123.9]	
	C(4)-N(3)-C(2)	128.43	128.63	128.14	[126.5]; 126.7	
	C(4)-N(3)-H(3)	116.87	116.71	117.08	[117.9]; 118.0	
C(4)-N(3)-H(3)	114.70	114.65	114.79	[115.5]		
N(3)-C(2)-O(2)	122.25	122.41	122.09	[121.1]; 121.4		
N(3)-C(2)-N(1)	115.49	115.18	115.81	[117.8]		
MUE	0.89	1.03	0.68			

Equation 8.3 describes the calculation of the standard Gibbs free energy change for the alloxan redox reaction, $\Delta_{\text{redox}}G^{\circ}_{298}$; where Equations 8.1 and 8.2 stand for the reactions taking place in gaseous and aqueous phases respectively, i.e., $\Delta_{\text{g}}G^{\circ}_{298}$ and $\Delta_{\text{redox}}G^{\circ}_{298}$. $\Delta_{\text{solv}}G^{\circ}_{298}$ expresses the difference between the solvation energy and the gas phase energy at 1 M. The conversion of the standard states from the gaseous (1 atm, 25 °C) to aqueous phase (1 M) requires the



correction term of ($RT\ln(24.46)$), but as Equation 8.3 comprises the same number of molecules of reactants and products, this correction cancels out.



$$\begin{aligned} \Delta_{\text{redox}}G^{\circ}_{298} = & \Delta_{\text{g}}G^{\circ}_{298} + \Delta_{\text{solv}}G^{\circ}_{298}(\text{DA}) + 2\Delta_{\text{solv}}G^{\circ}_{298}(\text{GS}^{\cdot}) - \Delta_{\text{solv}}G^{\circ}_{298}(\text{Alloxan}) \\ & - 2\Delta_{\text{solv}}G^{\circ}_{298}(\text{GSH}) \end{aligned} \quad 8.3$$

We calculated the redox potential (E°_{298}) by dividing the Gibbs free energy of reaction ($\Delta_{\text{redox}}G^{\circ}_{298}$) by negative nF ; where, n denotes the number of electron engaged (i.e., two), and F represents the Faraday constant ($96.487 \text{ kJ mol}^{-1} \text{ V}^{-1}$) relatively to the IUPAC standard hydrogen electrode, 4.44 V [44]. The UV-Vis absorption spectra were simulated using time-dependent DFT (TDDFT) calculations for the ground and excited states [45–49]. The ADF code [50,51] facilitated the computation of the Hirshfeld atomic charges [52]. The choice of the Hirshfeld scheme stems from its superior performance in estimating atomic charges in reference to other approaches, such as the commonly deployed Mulliken population analysis [53] that often displays severe sensitivity to the implemented basis set. Finally, the KiSTheLP package estimated reaction rate constants at the temperature of $298.15 (\pm 20\%) \text{ K}$ [54], based on the conventional transition state theory with the inclusion of one dimensional Eckart barrier, accounting for the contribution of the quantum tunnelling effect.

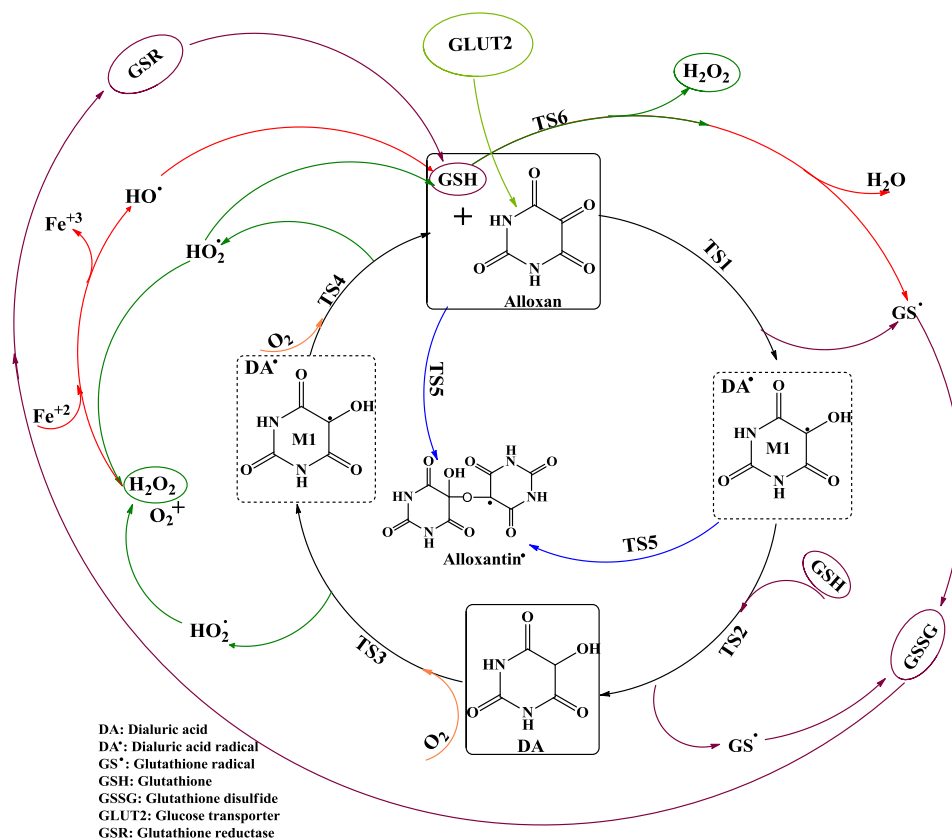
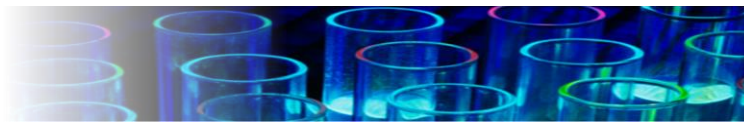
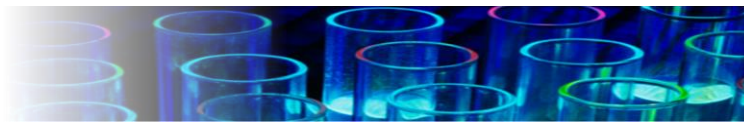


Figure 8.1. Alloxan and dialuric acid redox cycling reactions; GSH denotes glutathione, GSSG indicates glutathione disulfide, GS^{*} represents glutathione radical, and DA^{*} stands for dialuric acid radical.

8.3 Results and Discussion

Figure 8.1 illustrates the overall reaction network of alloxan action and Table 8.2 shows the Arrhenius kinetic parameters of the main reactions. Alloxan mechanism consists of the following consecutive chemical events: (i) A two-step reactions of alloxan with the SH groups in the GSH, producing a dialuric acid (DA) via the dialuric acid radical (DA^{*}). (ii) Re-oxidation of the dialuric acid back into alloxan. This redox cycle generates ROS species, most notably superoxide radicals (O₂⁻). (iii) Generation of the ferric ions (III) from the reaction of the



ferrous ions (II) with the superoxide radicals. (iv) Formation of hydroxyl radicals through dismutation of superoxide into hydrogen peroxide (H₂O₂).

Table 8.2. Arrhenius rate parameters at 298 K, 1 M; $A_{\text{solvation}}$ and $E_{\text{a-solvation}}$ are in M⁻¹ s⁻¹ and kJ mol⁻¹ respectively

Reaction	CBS-QB3	
	$A_{\text{solvation}}$	$E_{\text{a-solvation}}$
Alloxan + GSH → DA [•] + GS [•]	4.19×10^{10}	141.8
DA [•] + GSH → DA + GS [•]	4.18×10^{12}	48.9
DA + O ₂ → DA [•] + HO ₂ [•]	2.19×10^{12}	36.9
DA [•] + O ₂ → Alloxan + HO ₂ [•]	7.35×10^7	10.9
Alloxan + DA [•] → Alloxantin	1.89×10^7	38.7
GSH + HO ₂ [•] → GS [•] + H ₂ O ₂	5.34×10^5	6.6

8.3.1 Hydrogen atom transfer to alloxan

Scheme 8.1 illustrates the highest occupied molecular orbital (HOMO, -0.274 Ha), the lowest unoccupied molecular orbital (LUMO, -0.213 Ha), and the Hirshfeld charge map for the alloxan molecule. Alloxan HOMO displays nonbonding orbitals localised on the oxygen and nitrogen atoms in contrast to pyrimidine in which the HOMO normally contains π orbitals. Pyrimidine moiety, in general, holds high LUMO and HOMO energies (i.e. -0.06 and -0.269 Ha, respectively). Comparing these values to those of alloxan (pyrimidinetetrone) indicates that, alloxan constitutes an efficient electron acceptor.



Alloxan LUMO centre on C(4)O, C(5)O, and C(6)O, the nodes indicate a π^* orbital. Hence, the C(5)O site should be the most reactive towards a nucleophilic attack. Furthermore, the maximum Hirshfield charges on oxygens in alloxan fall on the oxygen atom bound to C(5); cf. Scheme 8.1. For this reason, we expect the first nucleophilic attack to result in a DA \cdot isomer that displays a hydroxyl group attached to C(5). Moreover, the reaction of the O(2) and O(4) generates less stable radicals, for instance, the DA \cdot formed by hydrogen addition to O(2) site requires 128 kJ mol $^{-1}$ higher Gibbs free energy than the one formed at the O(5) atom [55,56]. Hydrogen bonding with the neighbouring carbonyl oxygen C(4)O and C(6)O further stabilises the hydrogen added onto the O(5) site. This might explain why alloxan is diabetogenic whereas ninhydrin, barbituric acid and violuric acid are not; i.e., they exhibit similar structures to alloxan with an exception of the C(5)O site.

The prime action of alloxan rests in its great affinity toward the SH positions in GSH. Figure 8.2 presents potential energy surfaces for the formation of DA via two single hydrogen abstraction reactions from the thiol groups in two molecules of GSH. The first step signifies abstraction of a thiol H atom by one of the phenoxy-type O atoms in the alloxan molecule producing the DA \cdot adduct. This step forms an unknown compound characterised by a maximum absorption band at 305 nm; presumably containing the thiyl radical GS \cdot . This reaction displays endothermicity of 84 kJ mol $^{-1}$ and requires an activation enthalpy of 145 kJ mol $^{-1}$ to overcome the barrier associated with the formation of the transition structure TS1. Clearly, this reaction will not proceed under ambient conditions. Metal ions, such as Ca $^{+2}$, may act as a catalyst to speed up the reaction. The radical site in the DA \cdot moiety is centred on C5. Abstraction of another H atom from the SH group in the GSH by this radical centre demands a significantly lower activation enthalpy of 51 kJ mol $^{-1}$. Clearly, the noticeable difference in



the activation energy between TS1 and TS2 stems from the open-shell character of the former in reference to the closed-shell of the latter.

The two-step channel depicted in Figure 8.2 produces DA and results in the appearance of two S radical centres, thus contributing to deactivation of the enzyme. The relatively high barriers for TS1 and TS2 do not support the reported vulnerability of SH-containing compounds due to the attack by alloxan to DA[•]. Furthermore, Rosso et al. [25], and Kokkar and Bhandari [55] reported that thermodynamics prohibit the one-electron reduction of alloxan to DA[•]. This means that, DA[•] forms by oxidation of DA. Our calculated redox potential E°_{298} of -781 mV (SHE, -177 mV), corresponding to the Gibbs free energy change of this reaction $\Delta_{\text{redox}}G^{\circ}_{298}$ of 151 kJ mol⁻¹, reveals the nonspontaneous nature of this reaction.

The autoxidation of biomolecules such as dialuric acid, ascorbate, alloxan, or thiols is spin forbidden implying a serious kinetic limitation ($< 10^{-5} \text{ M}^{-1}\text{s}^{-1}$) [57]. However, many biomolecules including those listed above have been reported to react spontaneously with oxygen forming ROS such as superoxide radicals ($\text{O}_2^{\bullet-}$) and hydrogen peroxide (H_2O_2). Based on the law of conservation of spin angular momentum, it is not possible to couple unpaired electrons with the same spin (triplet oxygen) with the two spin paired electrons in the singlet biocompounds. Triplet oxygen must then convert to singlet oxygen to overcome the spin restriction ($E_a \cong 94 \text{ kJ mol}^{-1}$) [57], e.g. DA gaseous reaction with oxygen mandates $\Delta_r G^{\circ}_{298} = 93 \text{ kJ mol}^{-1}$. This implements the strong involvement of catalyst in such reactions when they reported to happen spontaneously [58–60].

Two types of catalysts should be involved in alloxan redox cycle water and transition metals such as iron and copper. In our pervious modelling study [43] on the catalytic effect of water



in reactions involving hydrogen atom transfer between molecules, we found that the reaction barriers reduced dramatically in the presence of only two water molecules. In experimental practice, there are two inescapable encountered problems while studying alloxan and glutathione reaction first, the contamination of reagents including buffers with trace amounts of metals and second, the metal ligation (chelation) of those contaminants to the reactants. Where in the first, it is possible that a significant amount of $O_2^{\cdot-}$ would form as a result of the reaction of contaminate (Fe^{+2}) in the buffer solution which can be evidenced by the formation of H_2O_2 radical without encountering SOD. At physiological pH, iron and copper (most predominant transition metals in vivo) have a low solubility and mostly chelated to a carrier [61]. It is strongly suggested that GSH is a strong iron [62] and copper chelator persuasively reducing the redox potential. The shift in redox potential is a result of orbitals overlapping between the ligand (Alloxan or GSH) and the metal [57]. Furthermore, other in vivo reducing agents, including dithiols, cysteine, and ascorbic acid may contribute as well to the reduction of alloxan [18,63].

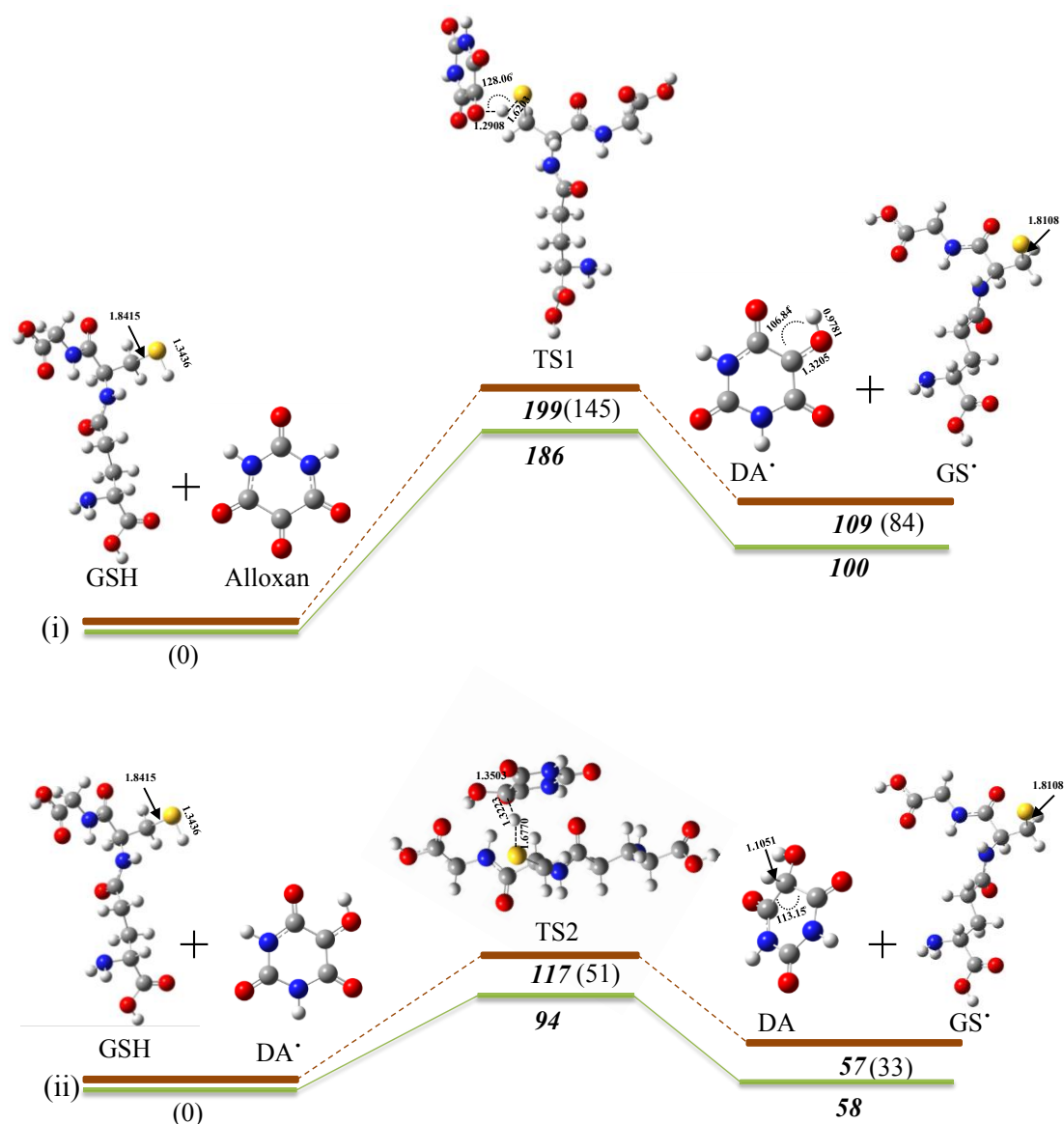
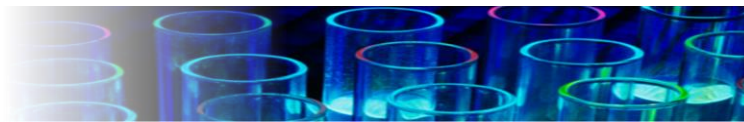


Figure 8.2. Enthalpies of activation and reaction ($\Delta^\ddagger H^\circ_{298}$, $\Delta_r H^\circ_{298}$) in parentheses and Gibbs free energies of reaction and activation ($\Delta^\ddagger G^\circ_{298}$, $\Delta_r G^\circ_{298}$) in bold italic of alloxan reaction with glutathione forming dialuric acid radical (DA[•]) (i) followed by a second stage protonation of DA[•] via glutathione (GSH) to generate dialuric acid and glutathione radical (GS[•]) (ii). Solid green lines indicate the gas analogues. All values are in kJ mol⁻¹ at 298.15 K.

8.3.2 UV-Vis and EPR analysis

Alloxan conversion to dialuric acid is extremely sensitive to changes in pH, especially those within the physiological limits of pH. When the acidity decreases (or the alkalinity increases),



the reaction rate increases [64,65]. This is related to alloxan dissociation constant of $pK_a = 6.63$. The channels illustrated Figure 8.3 (i) and (ii) show alloxan converting to alloxanic acid by reacting with one molecule of water and forming a monohydrate intermediate. The reaction barrier for the overall reaction amounts to 186 kJ mol^{-1} .

In Figure 8.4a, dialuric acid shows an absorption band at around 278 nm at pH = 7.4 and 272 nm at pH 6.4 after 6 min. Winterbourn and Munday [27] reported that, the addition of alloxan to a neutral solution of GSH at a molar ratio of 1 : 100 leads to an immediate increase in absorption at 273 nm, characteristic of dialuric acid. With time, another peak appears at around 315 nm, generally associated with the so-called “compound 305”. We have detected this peak at both biological pH of 7.4 and at pH of 6.4. At long reaction times, such as in excess of 6 h, the reaction of alloxan and glutathione induces the appearance pink colour linked to a second peak around 520 nm, as illustrated in Figure 8.4c. We assigned this peak to alloxantin', a hemiacetal species formed in the reaction of alloxan with its reduced radical form ($DA\cdot$), involving conversion of the carbonyl group to a hydroxyl group; see Figure 8.5. Figure 8.4d illustrates the spectrum of the fully developed reaction after 10 h at pH of 7.4, where, the two peaks at 315 and 520 nm becomes more significant. An overlapping with the computed UV-Vis spectra (based on the oscillatory strength) reveals $DA\cdot - GS\cdot$ at 315 nm and alloxantin' at 520 nm.

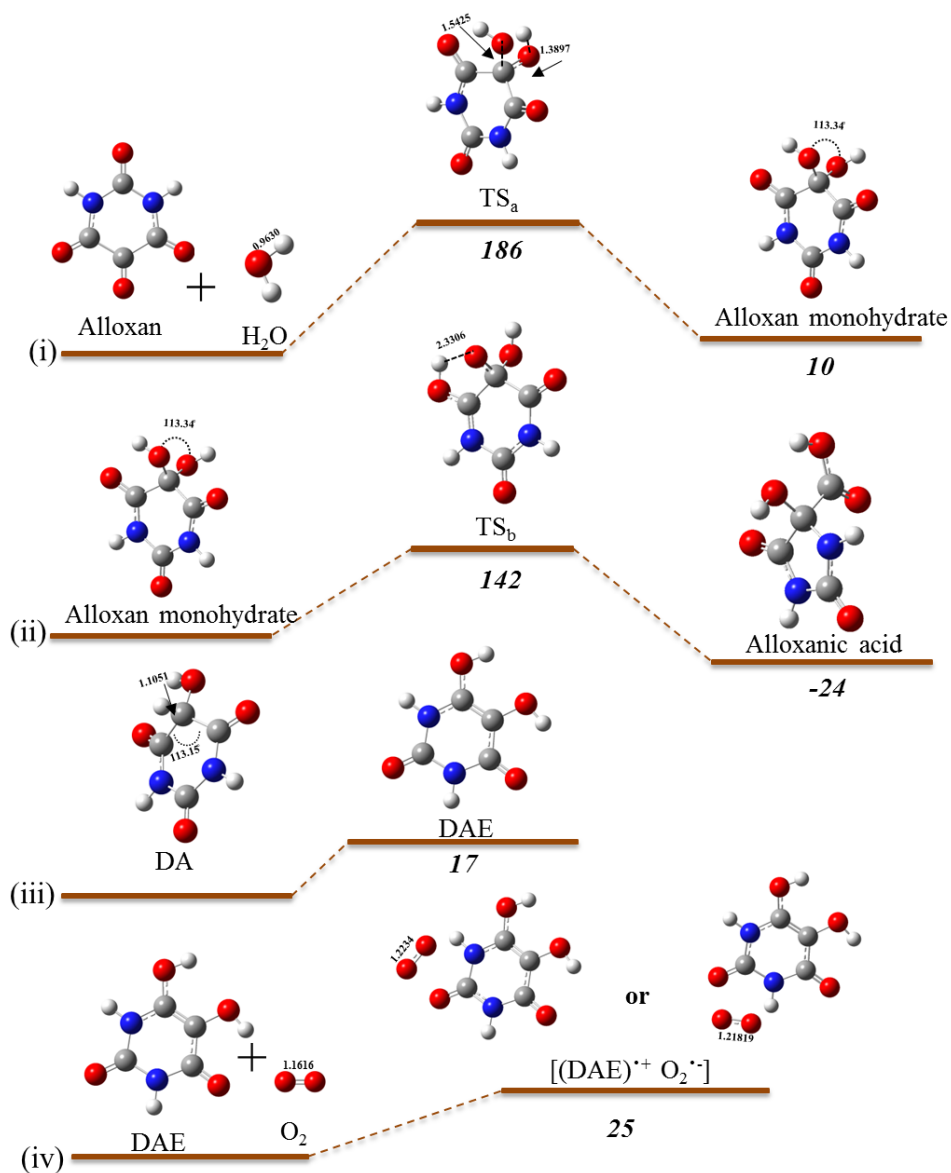


Figure 8.3. Gibbs free energies of reaction and activation ($\Delta^\ddagger G_{298}^0$, $\Delta_r G_{298}^0$) in bold italic of channels (i) and (ii) illustrating the formation of alloxanic acid through the formation of alloxan monohydrate, routes (iii) and (iv) shows the unimolecular isomeration of DA to DAE followed by charged radical complex formation by coupling with oxygen. All values are in kJ mol⁻¹ at 298.15 K.

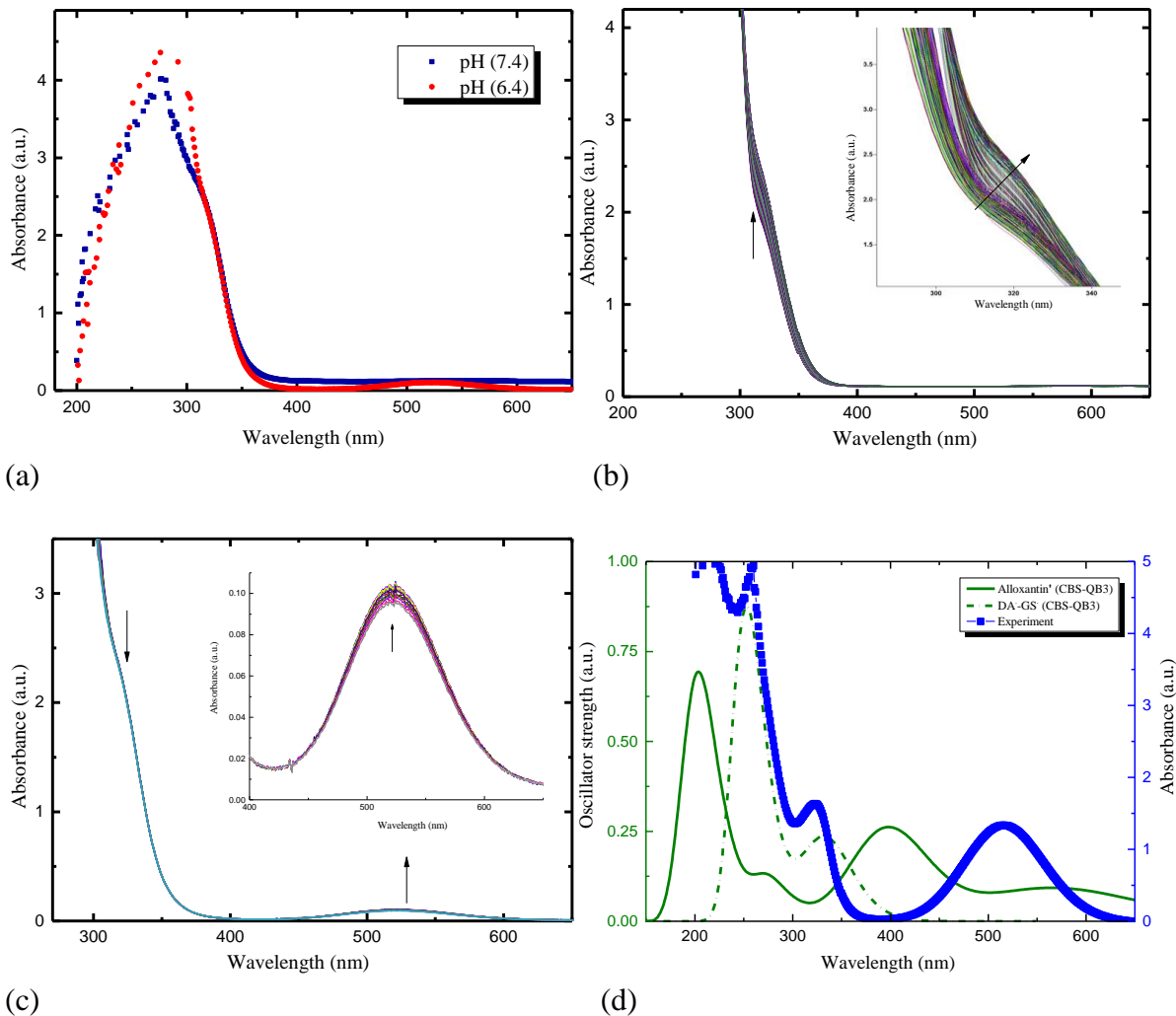
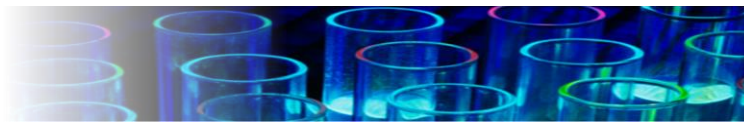


Figure 8.4: Time evolution UV-Vis spectra of alloxan and GSH solution; a: full scan covering the UV-Vis region after 6 min, b: pH = 7.4 recorded for 1-30 min, c: pH = 6.4 covering the reaction from 6 to 8 h, d: pH = 7.4 after the reaction is fully developed at 10 h compared to the theoretically computed UV-Vis spectra for alloxantin and DA⁻-GS⁻ complex. Ordinate axes show absorbance in arbitrary unit.

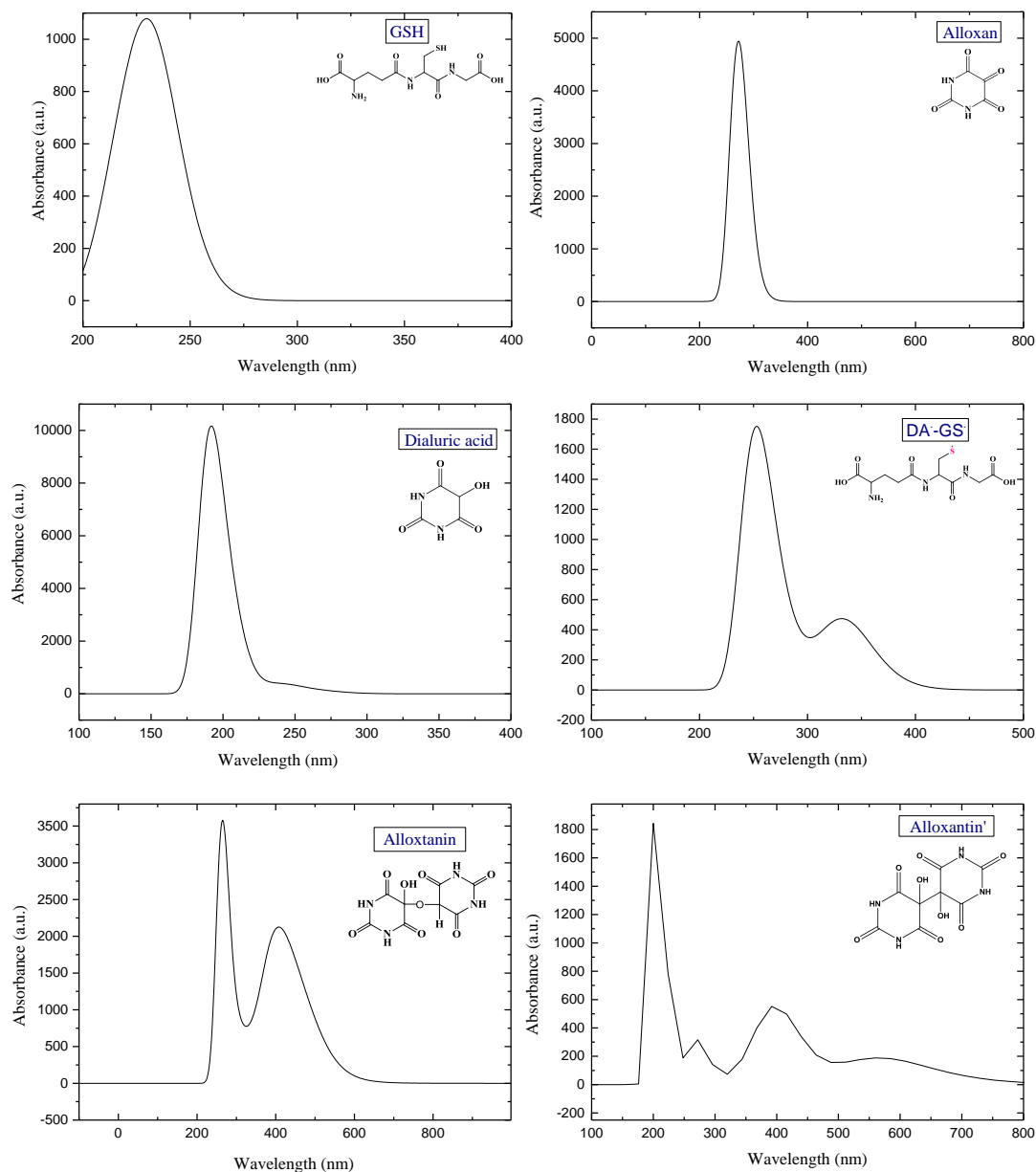
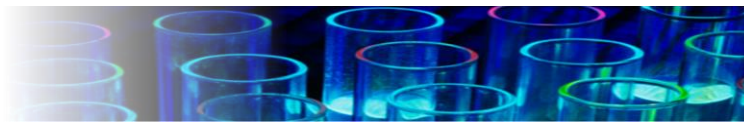


Figure 8.5. UV-Vis spectra calculated based on CBS-QB3 solvation model for reactants, intermediates, and products involved in the redox cycle.

Figure 8.6 illustrates the EPR spectrum of a buffered solution of alloxan and glutathione recorded in situ at 25 °C; application of spin traps was unnecessary in this case. The spectrum reveals the simultaneous formation of DA[•] and GS[•] radicals. Brömme et al. [24] recorded the ESR spectra of DA[•] of solutions of water and deuterium oxide, reporting no detection of the GS[•] radical. The appearance of the DA[•] spectrum is associated with either a one-electron



reduction of alloxan by hydrogen transfer from glutathione or oxidation of dialuric acid. Dialuric acid represents the reduction product of alloxan, with one of the hydroxyl groups being replaced by hydrogen atom. The hydrogen atom interacts with the radical on the neighbouring carbon (C5) forming a 1 : 1 hyperfine coupling EPR signal with a g -factor of $g = 2.03039$ at 3432 G. On the other hand, GS^{\cdot} radical shows a strong peak with g -factor of 2.00252 and a centre field of 3490 G.

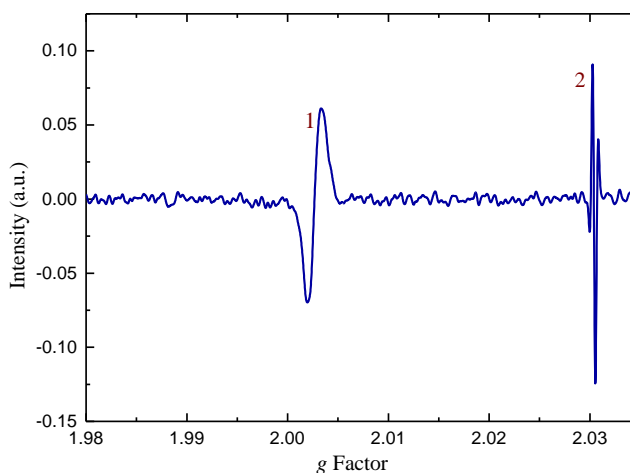


Figure 8.6. EPR signal of two radicals formed from in a sample containing 1 mM alloxan, 1 mM glutathione in 50 % methanol solution, at pH = 7.4 after 1 min. Values of the g factor correspond to GS^{\cdot} (1) of 2.00252 and 2.03039 for DA^{\cdot} (2) radicles, respectively.

8.3.3 Oxygenation of dialuric acid and its radical

Figure 8.7 depicts the reactions that conclude the redox cycle of alloxan. In the first step, a molecule of oxygen at its triplet ground state abstracts a H atom from the $H(C_5)OH$ site in DA, leading to the formation of a potent ROS of HO_2^{\cdot} . This route proceeds via an accessible activation enthalpy of 44 kJ mol^{-1} (TS3) and affords the DA^{\cdot} adduct. Oxidation of DA^{\cdot} back into alloxan features the abstraction of hydroxyl H by another oxygen molecule. Formation of



alloxan occurs via a trivial activation enthalpy of 10 kJ mol^{-1} with a rate constant of $9.12 \times 10^5 \text{ M}^{-1}\text{s}^{-1}$. For comparison, Rosso et al. [25] reported a rate constant of $6\text{-}8 \times 10^5 \text{ M}^{-1}\text{s}^{-1}$. The two oxidation reactions in Figure 7 are noticeably exothermic by 81 kJ mol^{-1} and 132 kJ mol^{-1} . The HO_2^\cdot emerging from these channels constitutes a precursor for the very active oxidising agents, i.e., hydroxyl HO^\cdot and superoxide $\text{O}_2^{\cdot-}$ radicals. The impact of oxygen concentration on the redox cycle has been studied elsewhere [63,66], where the authors reported the maximum decomposition of GSH at oxygen levels of $250 \mu\text{mol L}^{-1}$ and found that by reducing the oxygen levels to $25 \mu\text{mol L}^{-1}$ (i.e. intra-cellular oxygen concentration) more DA can be formed.

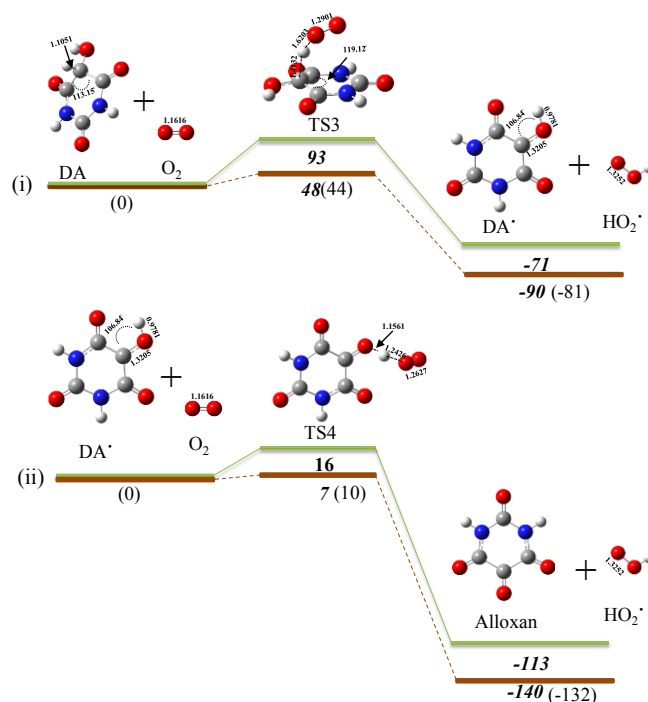


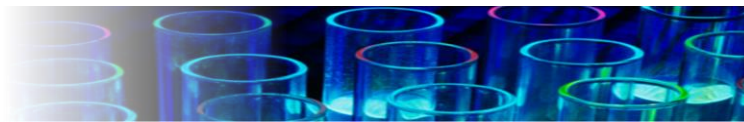
Figure 8.7. Oxygenation reaction potential diagram ($\Delta^\ddagger H^\circ_{298}$, $\Delta_r H^\circ_{298}$) in parentheses and Gibbs free energies of reaction and activation ($\Delta^\ddagger G^\circ_{298}$, $\Delta_r G^\circ_{298}$) in bold italic of (i) dialuric acid (DA) and (ii) dialuric acid radical (DA[•]) leading back to alloxan. Solid green lines indicate the gas analogues. All values are in kJ mol^{-1} at 298.15 K.



Figure 8.3 demonstrates that, DA can easily isomerise intermolecularly to form an enol analogue (DAE). Czerwinska et al. [67] reported that the enol form of DA forms [DAE^{•+} O₂^{•-}] radical complex reducing the overall activation energy for the cycle. Our modelled [DAE^{•+} O₂^{•-}] route in channel (iv) of Figure 8.3 demand a $\Delta_r G^{\circ}_{298} = 25 \text{ kJ mol}^{-1}$.

8.3.4 Formation of ROS

The upper panel in Figure 8 illustrates the pathway for the formation of H₂O₂ via the abstraction of a thiol H atom from the GSH molecule. This reaction comprises a very low activation enthalpy of 11 kJ mol⁻¹ and a relatively high Gibbs free energy change of 30 kJ mol⁻¹. The latter makes the reaction non-spontaneous thermodynamically and operating at low conversion. In vivo, however, the glutathione peroxidases enzyme (GPx) catalyses this reaction [68]. Moreover, the subsequent reaction consumes GS[•] ensuring the driving force for this reaction to proceed. The H₂O₂ molecule readily dissociates into two hydroxyl groups in the presence of a metal catalyst (typically iron oxide). Catalase, an enzyme that inactivates hydrogen peroxide, inhibits this step. Channel (ii) in Figure 8.8 illustrates how a hydroxyl radical abstracts a hydrogen atom from the SH group in GSH without encountering a reaction barrier. The presence of glucose may partially reduce the generation of HO[•] from H₂O₂, increasing the recirculation of GSH and thus diverting HO₂[•] away from the thiol position. It has also been reported that, in vitro generation of HO[•] radicals depends on the concentration of GSH, with low concentration of GSH increasing the rate of HO[•] formation [18]. Despite the fact that, superoxide radical dismutase (SOD) suppresses the main oxidation route of DA, it also presents a major source of hydrogen peroxide through the global reaction (O₂^{•-} + O₂^{•-} + 2H⁺ → H₂O₂ + O₂). This explains that, complete protection against alloxan diabetes necessitates the presence



of both SOD and catalase to stop the redox cycle. Figure 8.9 illustrates the EPR spectra for alloxan reaction with GSH in the presence of SOD9, where the GS^\bullet and DA^\bullet radicals disappear completely after 6 min.

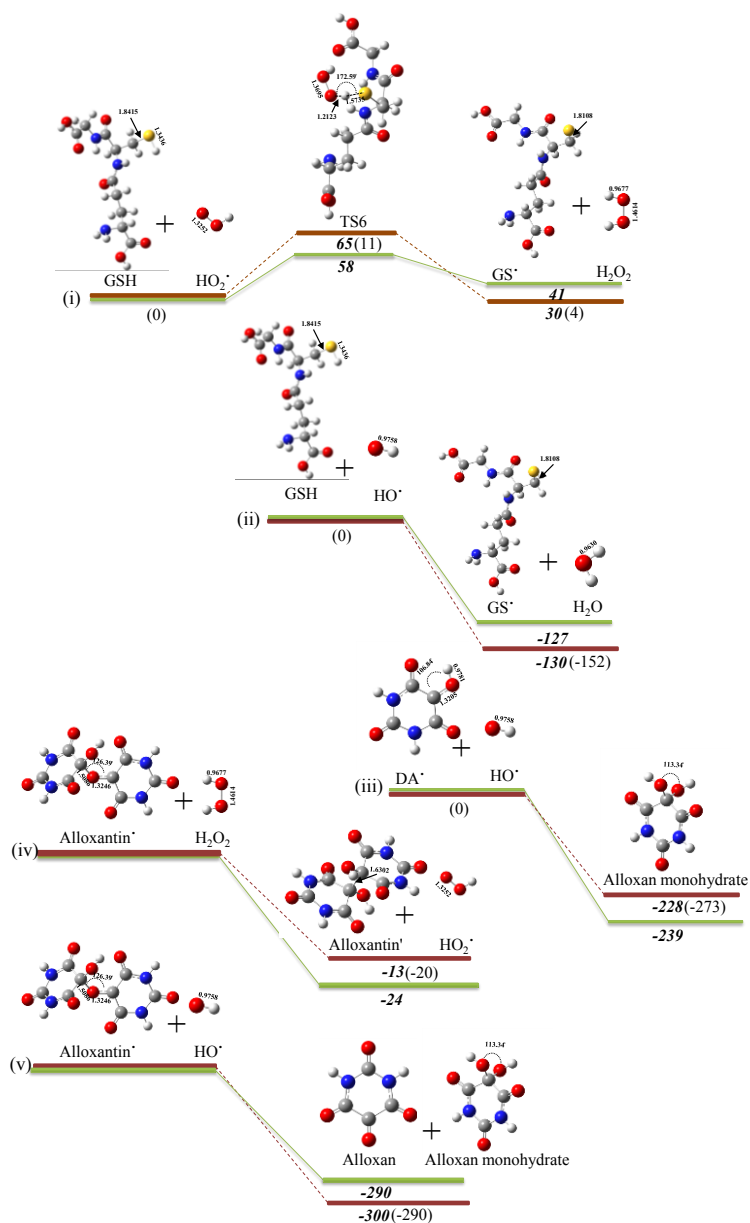


Figure 8.8. Glutathione quenching of (i) hydroperoxide and (ii) hydroxyl radicals. Values represent enthalpies of activation and reaction ($\Delta^\ddagger H^\circ_{298}$, $\Delta_r H^\circ_{298}$) in parentheses and Gibbs free energies of reaction and activation ($\Delta^\ddagger G^\circ_{298}$, $\Delta_r G^\circ_{298}$) in bold italic both in kJ mol⁻¹ calculated at 298.15 K. Solid green lines indicate the gas analogues.

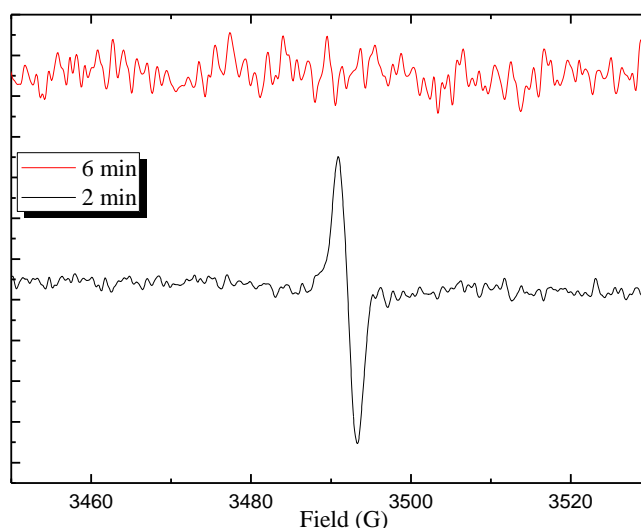


Figure 8.9. EPR spectra, measured in situ, as obtained from reaction of 1 μM alloxan, 10 μM glutathione and 5 μM superoxide radical dismutase (SOD) in buffered solution (pH = 7.4) after 2 and 6 min. Ordinate axis shows intensities in arbitrary unit.

8.3.5 Dimerisation reactions

The unique structure of alloxan and its derived radicals enable them to undergo dimerisation reactions, producing the corresponding ether or keto-keto structures. The two upper panels in Figure 8.10 represent the sink pathways for DA^\bullet and alloxan through the dimerisation reactions. Addition of alloxan to the radical site in DA^\bullet forms the radical alloxantin' through an activation enthalpy of 34 kJ mol^{-1} . Self-condensation of DA^\bullet adducts into alloxantin' (channel ii) disturbs the alloxan redox cycle. Self-addition of two thiyl GS^\bullet radicals at their SH centres affords the GSSG structure [69]. The latter also arises through a channel that minimises the formation of HO^\bullet from H_2O_2 : $2\text{HO}^\bullet + 2\text{GSH} \rightarrow \text{GSSG} + 2\text{H}_2\text{O}$. In Figure 8.11, we applied an EPR spin trap 5,5-Dimethyl-1-Pyrroline-N-Oxide (DMPO) to examine the disappearance of GS^\bullet radicals. The spectrum of $\text{DMPO}^\bullet\text{-SG}$ radical is conspicuously different and easy to distinguish displaying a 1 : 1 : 1 : 1 signal with a g factor of 2.00345 [70]. The



time evolution of the DMPO[•]-SG EPR spectra indicates the change in the strength of the signal due to the consumption of the GS[•] radical in the dimerisation reaction (GSSG); this occurs within 90 min reaction time of 1 μM alloxan, 10 μM glutathione and 10 μM DMPO in 50 % buffered methanol solution (pH = 7.4). Figure 8.11b shows the extracted radicals spectra that overlap with the DMPO[•]-SG EPR spectrum. Which are as follow, DMPO-H₂O₂ (1: 2: 2: 1), DMPO-DA (1: 1: 1), and DMPO-OH (1: 2: 2: 1) with *g* factors amount to 2.00601, 2.00606, and 2.00532, respectively.

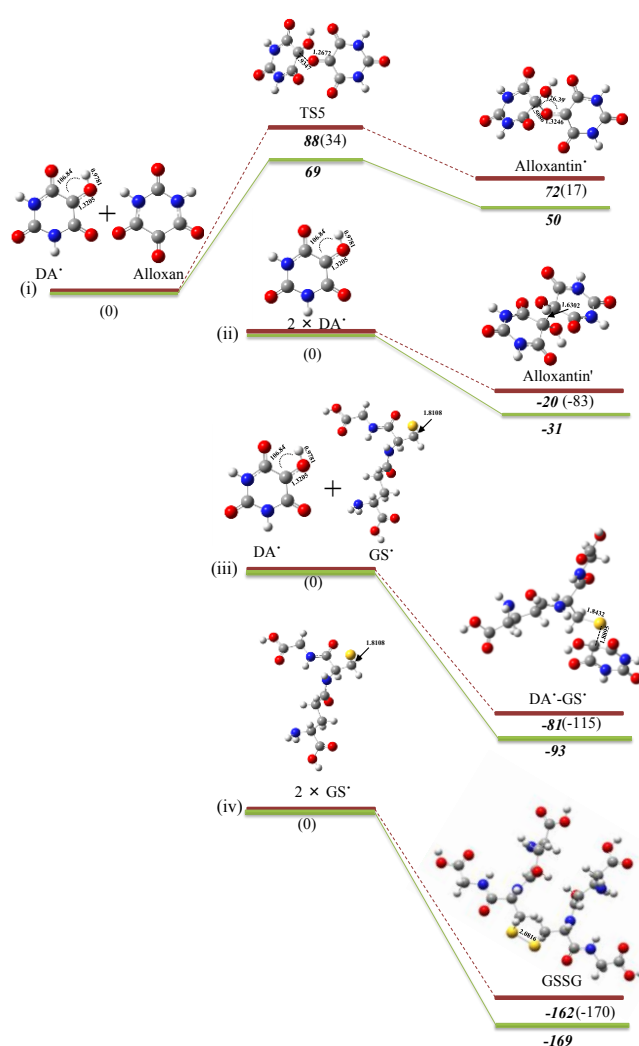


Figure 8.10. Enthalpies of activation and reaction ($\Delta^\ddagger H^{\circ}_{298}$, $\Delta_r H^{\circ}_{298}$) in parentheses and Gibbs free energies of reaction and activation ($\Delta^\ddagger G^{\circ}_{298}$, $\Delta_r G^{\circ}_{298}$) in bold italic for the dimerisation reactions of (i) alloxan with dialuric acid radical, (ii) dialuric acid radicals, (iii) dialuric acid radical with glutathione radical, (iv) glutathione radicals. Solid green lines indicate the gas analogues. All values are in kJ mol⁻¹ at 298.15 K.

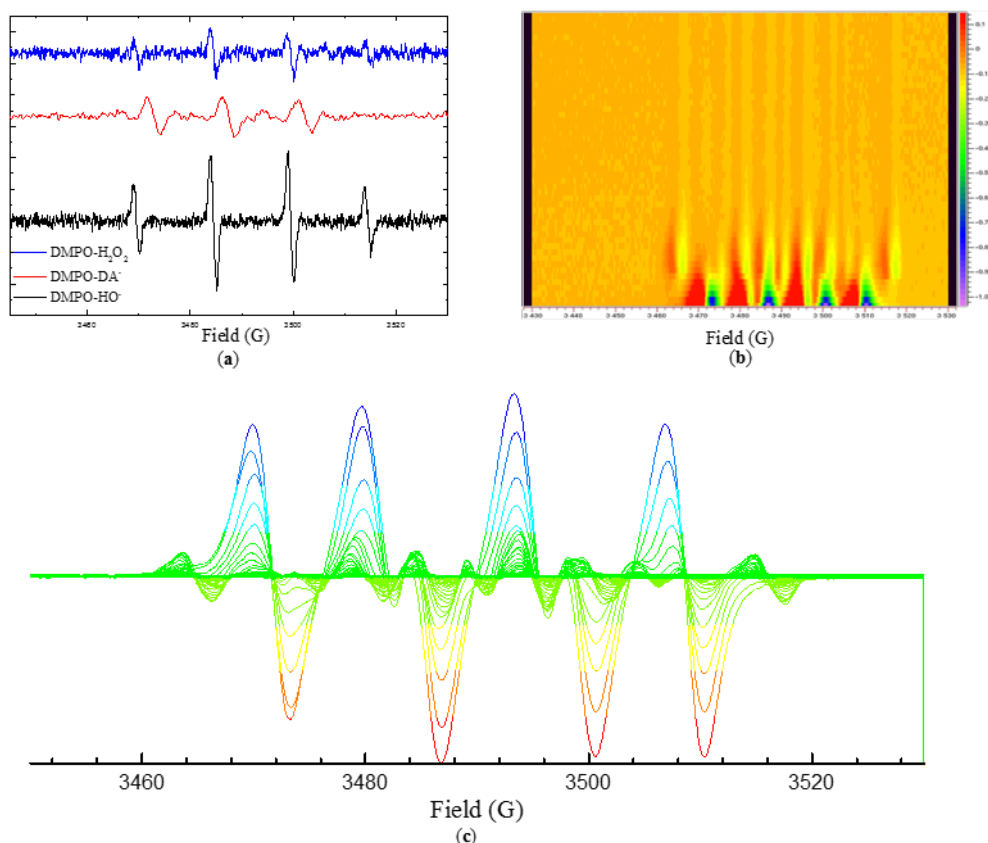
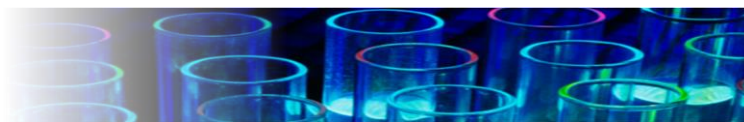


Figure 8.11. Time evolution of EPR spectra, measured in situ, as obtained from reaction of 1 μM alloxan, 10 μM glutathione and 10 μM DMPO in 50 % buffered methanol solution (pH = 7.4) for 90 min. DMPO-SG radical displays 1 : 1 : 1 spectrum with $g = 2.00345$. (a) The extracted spectra for DMPO- H_2O_2 , DMPO- DA^\bullet , and DMPO- HO^\bullet with g factors amount to 2.00601, 2.00606, and 2.00532, respectively, (b) presents the density plot for the reaction time course. Ordinate axis shows intensities in arbitrary unit.

Panel (iii) of Figure 8.10 illustrates that the addition of DA^\bullet to the GSH radical forms the $\text{DA}^\bullet\text{-GS}^\bullet$ complex. The modelled UV-Vis spectra for species involved in the redox cycle, as depicted in Figure 8.4, show a hypochromic shift of 50 nm if compared to the experimentally reported UV-Vis spectra [27,28,48]. This prompts us to conclude that, the peak appearing at 315 nm, known as “compound 305” [12,14,71,72], represents a complex of DA^\bullet and GS^\bullet ($\text{DA}^\bullet\text{-GS}^\bullet$; cf. Figure 8.3d). This explains the observation of Brömme et al. and Resnik and Wolff



that generation of “compound 305” mandates the formation of both DA[•] and GS[•] radicals [14,73].

8.4 Conclusion

Alloxan is applied universally as a diabetogenic agent in laboratory rats. In the presence of glutathione (GSH), alloxan along with its reduced form dialuric acid (DA[•]) act as a redox couple with redox potential $E^{\circ}_{298} = -781$ mV (corresponding to the Gibbs free energy change of the reaction ($\Delta_{\text{redox}}G^{\circ}_{298}$) of 151 kJ mol^{-1}). The time resolved EPR spectra confirm the concurrent generation of DA[•] and GS[•] radicals and the appearance of hydrogen peroxide (H₂O₂) and hydroxyl radical (HO[•]) when applying DMPO spin trap supporting the results of the molecular modelling.

8.5 References

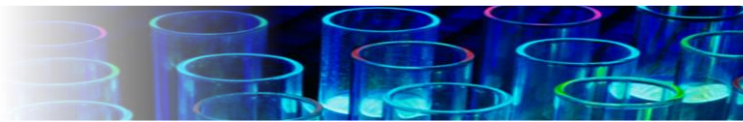
- [1] Rohilla A, Ali S. Alloxan induced diabetes: mechanisms and effects. *International Journal of Research in Pharmaceutical and Biomedical Sciences* 2012;3:819–823.
- [2] Etuk EU, others. Animals models for studying diabetes mellitus. *Agric Biol JN Am* 2010;1:130–134.
- [3] Weaver DC, McDaniel ML, Naber SP, Barry CD, Lacy PE. Alloxan stimulation and inhibition of insulin release from isolated rat islets of Langerhans. *Diabetes* 1978;27:1205–1214.
- [4] Bonner-Weir S, Weir GC. New sources of pancreatic β -cells. *Nat Biotech* 2005;23:857–61. doi:10.1038/nbt1115.



- [5] Baeyens L, Lemper M, Leuckx G, De Groef S, Bonfanti P, Stangé G, et al. Transient cytokine treatment induces acinar cell reprogramming and regenerates functional beta cell mass in diabetic mice. *Nat Biotech* 2014;32:76–83. doi:10.1038/nbt.2747.
- [6] Jemai H, El Feki A, Sayadi S. Antidiabetic and Antioxidant Effects of Hydroxytyrosol and Oleuropein from Olive Leaves in Alloxan-Diabetic Rats. *J Agric Food Chem* 2009;57:8798–804. doi:10.1021/jf901280r.
- [7] Lenzen S, Panten U. Alloxan: history and mechanism of action. *Diabetologia* 1988;31:337–342.
- [8] Holley RW. Glutathione. *J Am Chem Soc* 1955;77:3171–3171. doi:10.1021/ja01616a100.
- [9] Miller GL. Glutathione. *J Am Chem Soc* 1960;82:4439–40. doi:10.1021/ja01501a090.
- [10] Lenzen S, Freytag S, Panten U. Inhibition of glucokinase by alloxan through interaction with SH groups in the sugar-binding site of the enzyme. *Molecular Pharmacology* 1988;34:395–400.
- [11] Lenzen S, Mirzaie-Petri M. Inhibition of glucokinase and hexokinase from pancreatic B-cells and liver by alloxan, alloxantin, dialuric acid, and t-butylhydroperoxide. *Biomedical Research* 1991;12:297–307.
- [12] Lenzen S, Munday R. Thiol-group reactivity, hydrophilicity and stability of alloxan, its reduction products and its N-methyl derivatives and a comparison with ninhydrin. *Biochemical Pharmacology* 1991;42:1385–1391.
- [13] Elsner M, Gurgul-Convey E, Lenzen S. Relative importance of cellular uptake and reactive oxygen species for the toxicity of alloxan and dialuric acid to insulin-producing cells. *Free Radical Biology and Medicine* 2006;41:825–834.
- [14] Resnik RA, Wolff AR. The reaction of alloxan with glutathione and protein. *Archives of Biochemistry and Biophysics* 1956;64:33–50.
- [15] Heikkila RE, Winston B, Cohen G, Barden H. Alloxan-induced diabetes—evidence for hydroxyl radical as a cytotoxic intermediate. *Biochemical Pharmacology* 1976;25:1085–1092.
- [16] Dunn JS, McLetchie NGB. Experimental alloxan diabetes in the rat. *The Lancet* 1943;242:384–387.



- [17] McLetchie NGB. Alloxan diabetes: the sorcerer and his apprentice. *Diabetologia* 1982;23:72–75.
- [18] Lenzen S. The mechanisms of alloxan-and streptozotocin-induced diabetes. *Diabetologia* 2008;51:216–226.
- [19] Worchel HN, Magnuson MA. Cytokine-driven beta-cell production in vivo. *Nat Biotech* 2014;32:63–4. doi:10.1038/nbt.2788.
- [20] Elroby SA, Aziz SG, Hilal RH. The electronic structure of alloxan monohydrate. Spectroscopic and density functional synergic approach. *Journal of Molecular Structure* 2017;1130:487–96. doi:10.1016/j.molstruc.2016.10.069.
- [21] Allehyani BH, Elroby SA, Aziz SG, Hilal RH. Electronic structure of alloxan and its dimers: QM/QD simulations and quantum chemical topology analysis. *Journal of Biomolecular Structure and Dynamics* 2015;33:2121–2132.
- [22] Bolton W. The crystal structure of alloxan. *Acta Crystallographica* 1964;17:147–152.
- [23] Lagercrantz C, Yhland M. Free radicals in the reaction of alloxan with glutathione and ascorbic acid. *Acta Chem Scand* 1963;17:1677–1682.
- [24] Brömme HJ, Mörke W, Peschke E. Transformation of barbituric acid into alloxan by hydroxyl radicals: interaction with melatonin and with other hydroxyl radical scavengers. *Journal of Pineal Research* 2002;33:239–47. doi:10.1034/j.1600-079X.2002.02936.x.
- [25] Rosso JA, Astorga MA, Mártire DO, Gonzalez MC. Alloxan-dialuric acid cycling: A complex redox mechanism. *Free Radical Research* 2009;43:93–99.
- [26] Kakkar R, Bhandari M, Gaba R. Tautomeric transformations and reactivity of alloxan. *Computational and Theoretical Chemistry* 2012;986:14–24. doi:10.1016/j.comptc.2012.01.038.
- [27] Winterbourn CC, Munday R. Glutathione-mediated redox cycling of alloxan: mechanisms of superoxide dismutase inhibition and of metal-catalyzed OH formation. *Biochemical Pharmacology* 1989;38:271–277.
- [28] Patterson JW, Lazarow A, Levey S, others. Alloxan and dialuric acid: their stabilities and ultraviolet absorption spectra. *Journal of Biological Chemistry* 1949;177:187–196.



- [29] Frisch M, Trucks GW, Schlegel HB, Scuseria GE, Robb MA, Cheeseman JR, et al. Gaussian 09, Revision A. 02, Gaussian, Inc, Wallingford, CT 2009;200.
- [30] Zhao Y, Truhlar DG. The M06 suite of density functionals for main group thermochemistry, thermochemical kinetics, noncovalent interactions, excited states, and transition elements: two new functionals and systematic testing of four M06-class functionals and 12 other functionals. *Theoretical Chemistry Accounts* 2008;120:215–241.
- [31] Montgomery Jr JA, Ochterski JW, Petersson GA. A complete basis set model chemistry. IV. An improved atomic pair natural orbital method. *The Journal of Chemical Physics* 1994;101:5900–5909.
- [32] Zhao Y, Truhlar DG. Exploring the Limit of Accuracy of the Global Hybrid Meta Density Functional for Main-Group Thermochemistry, Kinetics, and Noncovalent Interactions. *J Chem Theory Comput* 2008;4:1849–68. doi:10.1021/ct800246v.
- [33] Zeinali N, Altarawneh M, Li D, Al-Nu'airat J, Dlugogorski BZ. New Mechanistic Insights: Why Do Plants Produce Isoprene? *ACS Omega* 2016;1:220–225.
- [34] Al-Nu'airat J, Altarawneh MK, Gao X, Westmoreland PR, Dlugogorski BZ. Reaction of Aniline with Singlet Oxygen ($O_2^1\Delta_g$). *The Journal of Physical Chemistry A* 2017.
- [35] Vandeputte AG, Reyniers M-F, Marin GB. A theoretical study of the thermodynamics and kinetics of small organosulfur compounds. *Theoretical Chemistry Accounts* 2009;123:391–412.
- [36] Vandeputte AG, Sabbe MK, Reyniers M-F, Van Speybroeck V, Waroquier M, Marin GB. Theoretical study of the thermodynamics and kinetics of hydrogen abstractions from hydrocarbons. *The Journal of Physical Chemistry A* 2007;111:11771–11786.
- [37] Casanovas R, Frau J, Ortega-Castro J, Salvà A, Donoso J, Muñoz F. Simplification of the CBS-QB3 method for predicting gas-phase deprotonation free energies. *International Journal of Quantum Chemistry* 2010;110:323–330.
- [38] Zeng Z, Altarawneh M, Oluwoye I, Glarborg P, Dlugogorski BZ. Inhibition and Promotion of Pyrolysis by Hydrogen Sulfide (H_2S) and Sulfanyl Radical (SH). *J Phys Chem A* 2016;120:8941–8. doi:10.1021/acs.jpca.6b09357.



- [39] Morales J, Günther G, Zanocco AL, Lemp E. Singlet Oxygen Reactions with Flavonoids. A Theoretical – Experimental Study. *PLOS ONE* 2012;7:e40548. doi:10.1371/journal.pone.0040548.
- [40] Mennucci B. Polarizable continuum model. *Wiley Interdisciplinary Reviews: Computational Molecular Science* 2012;2:386–404.
- [41] Dorado JB, Dlugogorski BZ, Kennedy EM, Mackie JC, Gore J, Altarawneh M. Decomposition of S-nitroso species. *RSC Adv* 2015;5:29914–23. doi:10.1039/C5RA03292J.
- [42] Dorado JB, Dlugogorski BZ, Kennedy EM, Mackie JC, Gore J, Altarawneh M. S-Nitrosation of Aminothiones. *J Org Chem* 2015;80:6951–8. doi:10.1021/acs.joc.5b00313.
- [43] Rayson MS, Altarawneh M, Mackie JC, Kennedy EM, Dlugogorski BZ. Theoretical study of the ammonia- hypochlorous acid reaction mechanism. *The Journal of Physical Chemistry A* 2010;114:2597–2606.
- [44] Rabinowitz JD, Vacchino JF, Beeson C, McConnell HM. Potentiometric Measurement of Intracellular Redox Activity. *J Am Chem Soc* 1998;120:2464–73. doi:10.1021/ja973560f.
- [45] Yao L, Lin S-H. The anharmonic effect study of coupled Morse oscillators for the unimolecular reaction. *Science in China Series B: Chemistry* 2008;51:1146–1152.
- [46] Zhu C, Liang KK, Hayashi M, Lin SH. Theoretical treatment of anharmonic effect on molecular absorption, fluorescence spectra, and electron transfer. *Chemical Physics* 2009;358:137–146.
- [47] Yang L, Zhu C, Yu J, Lin SH. Anharmonic Franck–Condon simulation of the absorption and fluorescence spectra for the low-lying S1 and S2 excited states of pyrimidine. *Chemical Physics* 2012;400:126–136.
- [48] Atac A, Karabacak M, Karaca C, Kose E. NMR, UV, FT-IR, FT-Raman spectra and molecular structure (monomeric and dimeric structures) investigation of nicotinic acid N-oxide: A combined experimental and theoretical study. *Spectrochimica Acta Part A: Molecular and Biomolecular Spectroscopy* 2012;85:145–154.
- [49] Ramalingam S, Karabacak M, Periandy S, Puviarasan N, Tanuja D. Spectroscopic (infrared, Raman, UV and NMR) analysis, Gaussian hybrid computational investigation (MEP



maps/HOMO and LUMO) on cyclohexanone oxime. *Spectrochimica Acta Part A: Molecular and Biomolecular Spectroscopy* 2012;96:207–220.

[50] Te Velde G t, Bickelhaupt FM, Baerends EJ, Fonseca Guerra C, van Gisbergen SJ, Snijders JG, et al. Chemistry with ADF. *Journal of Computational Chemistry* 2001;22:931–967.

[51] Guerra CF, Snijders JG, te Velde G t, Baerends EJ. Towards an order-N DFT method. *Theoretical Chemistry Accounts* 1998;99:391–403.

[52] Hirshfeld FL. Bonded-atom fragments for describing molecular charge densities. *Theoretica Chimica Acta* 1977;44:129–138.

[53] Fonseca Guerra C, Handgraaf J-W, Baerends EJ, Bickelhaupt FM. Voronoi deformation density (VDD) charges: Assessment of the Mulliken, Bader, Hirshfeld, Weinhold, and VDD methods for charge analysis. *Journal of Computational Chemistry* 2004;25:189–210.

[54] Canneaux S, Bohr F, Henon E. KiSThelP: A program to predict thermodynamic properties and rate constants from quantum chemistry results†. *Journal of Computational Chemistry* 2014;35:82–93.

[55] Kakkar R, Bhandari M. Theoretical investigation of the alloxan–dialuric acid redox cycle. *Int J Quantum Chem* 2013;113:2060–9. doi:10.1002/qua.24441.

[56] D’Mello JF. *Handbook of plant and fungal toxicants*. CRC Press; 1997.

[57] Miller DM, Buettner GR, Aust SD. Transition metals as catalysts of “autoxidation” reactions. *Free Radical Biology and Medicine* 1990;8:95–108.

[58] Buettner GR, Czapski PG. Ascorbate autoxidation in the presence of iron and copper chelates. *Free Radical Research Communications* 1986;1:349–353.

[59] Legrand Y-M, Gray M, Cooke G, Rotello VM. Model Systems for Flavoenzyme Activity: Relationships between Cofactor Structure, Binding and Redox Properties. *J Am Chem Soc* 2003;125:15789–95. doi:10.1021/ja036940b.

[60] Hasford JJ, Rizzo CJ. Linear Free Energy Substituent Effect on Flavin Redox Chemistry. *J Am Chem Soc* 1998;120:2251–5. doi:10.1021/ja972992n.

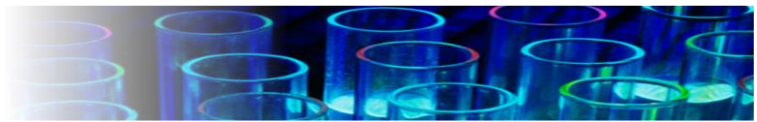


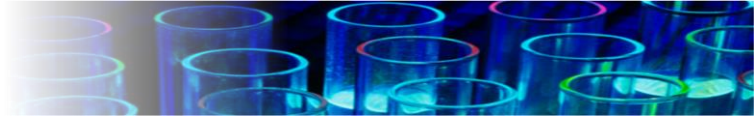
- [61] Li NC, Gawron O, Bascuas G. Stability of Zinc Complexes with Glutathione and Oxidized Glutathione. *J Am Chem Soc* 1954;76:225–9. doi:10.1021/ja01630a058.
- [62] Qi W, Li J, Chain CY, Pasquevich GA, Pasquevich AF, Cowan JA. Glutathione Complexed Fe–S Centers. *J Am Chem Soc* 2012;134:10745–8. doi:10.1021/ja302186j.
- [63] Elsner M, Gurgul-Convey E, Lenzen S. Relative importance of cellular uptake and reactive oxygen species for the toxicity of alloxan and dialuric acid to insulin-producing cells. *Free Radical Biology and Medicine* 2006;41:825–834.
- [64] Klebanoff SJ. Factors affecting the activity of alloxan in vitro. *Canadian Journal of Biochemistry and Physiology* 1955;33:780–791.
- [65] Dixon M, Zerfas LG. The role of coenzymes in dehydrogenase systems. *Biochemical Journal* 1940;34:371.
- [66] Brömme HJ, Weinandy R, Peschke E. Influence of oxygen concentration on redox cycling of alloxan and dialuric acid. *Hormone and Metabolic Research* 2005;37:729–733.
- [67] Czerwinska M, Sikora A, Szajerski P, Adamus J, Marcinek A, Gebicki J, et al. Mechanistic Aspects of Alloxan Diabetogenic Activity: A Key Role of Keto- Enol Inversion of Dialuric Acid on Ionization. *The Journal of Physical Chemistry A* 2006;110:7272–7278.
- [68] Mugesh G, Panda A, Singh HB, Punekar NS, Butcher RJ. Glutathione Peroxidase-like Antioxidant Activity of Diaryl Diselenides: A Mechanistic Study. *J Am Chem Soc* 2001;123:839–50. doi:10.1021/ja994467p.
- [69] McMahon BK, Gunnlaugsson T. Selective Detection of the Reduced Form of Glutathione (GSH) over the Oxidized (GSSG) Form Using a Combination of Glutathione Reductase and a Tb(III)-Cyclen Maleimide Based Lanthanide Luminescent ‘Switch On’ Assay. *J Am Chem Soc* 2012;134:10725–8. doi:10.1021/ja300887k.
- [70] Scott MJ, Billiar TR, Stoyanovsky DA. *N-tert*-butylmethanimine *N*-oxide is an efficient spin-trapping probe for EPR analysis of glutathione thiyl radical. *Scientific Reports* 2016;6:srep38773. doi:10.1038/srep38773.
- [71] Patterson JW, Lazarow A, Levey S, others. Reactions of alloxan and dialuric acid with the sulfhydryl group. *Journal of Biological Chemistry* 1949;177:197–204.



- [72] Washburn MP, Wells WW. Glutathione dependent reduction of alloxan to dialuric acid catalyzed by thioltransferase (glutaredoxin): a possible role for thioltransferase in alloxan toxicity. *Free Radical Biology and Medicine* 1997;23:563–570.
- [73] Brömme HJ, Mörke W, Weinandy R, Peschke D, Peschke E. Formation of Compound 305 Requires the Simultaneous Generation of Both Alloxan and GSH Radicals. *Hormone and Metabolic Research* 2002;34:62–6. doi:10.1055/s-2002-20527.
- [74] Harrowfield JM, Skelton BW, Soudi AA, White AH. Crystal Structure of Alloxan Monohydrate: A Redetermination. *Australian Journal of Chemistry* 1989;42:1795–1798.
- [75] Singh C. The structure of the pyrimidines and purines. VIII. The crystal structure of alloxan $C_4H_4N_2O_5$. *Acta Crystallographica* 1965;19:759–767.
- [76] Bolton W. The crystal structure of triketoindane (anhydrous ninhydrin). A structure showing close CO- C interactions. *Acta Crystallographica* 1965;18:5–10.


Jomana Al-Nu'airat

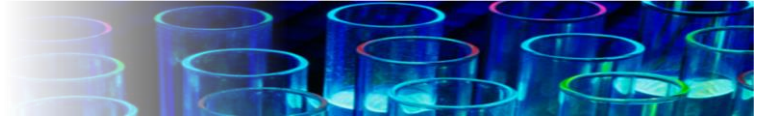




Chapter 9

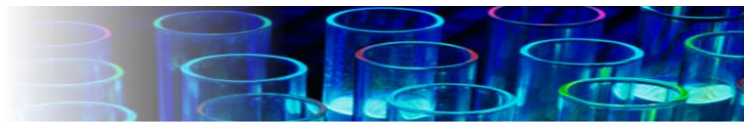
Conclusion and Recommendations





Chapter 9

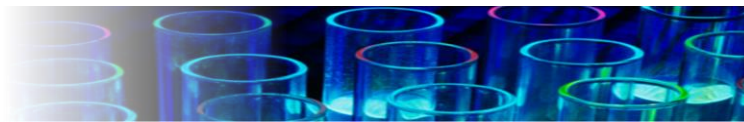
1



9.1 Conclusion

This dissertation collates ab initio and experimental studies pertaining to the reactions of reactive oxygen species (ROS) with various hydrocarbons, focusing on respective occurrences in three thematic areas, i.e., enhancement of combustion, destruction of organic pollutants in water, and mammalian stress signalling. The physico-chemical analyses, involving both kinetics and thermodynamics, have identified the role of ROS, mainly singlet oxygen, in tuning the initiation channels during oxidation of organic materials.

The first aspect of this thesis elaborates the interaction of ROS with hydrocarbons in combustion systems. This can be advantageous in internal combustion (IC) engines; it was found that the addition of singlet oxygen enhances the performance of oxy-fuel engines. From an application point of view, the mechanistic and kinetic results of interaction of singlet oxygen with toluene (presented in Chapter 4) elucidate the heightened performance of oxy-fuel engines via singlet oxygen surcharge. The innovative concept of this study resolves the relative reactivity of singlet oxygen with aromatic hydrocarbons, following the order of $\text{OH} > \text{H} > \text{CH}_3 > {}^1\text{O}_2 > \text{HO}_2 > {}^3\text{O}_2$, and the formation of *p*-quinonemethide (4-methylenecyclohexa-2,5-dienone) and *o*-quinonemethide (6-methylenecyclohexa-2,4-dienone), respectively (i.e., very reactive intermediates). These indicate that the systematic addition of singlet oxygen into combustion engine can enhance the ignition, reduce the enthalpic requirements and result in an energetically improved combustion process. On the other hand, interaction of ROS in combustion systems could have advert effects in terms of its disadvantages, e.g. in spontaneous ignitions, as it has been recorded in Chapter 5; formation of ROS on the surfaces of nano-components causes the formation of phenoxy radical, an environmentally persistent free radical (EPFR), in the initiation channels. Moreover, this thesis has demonstrated that, the oxidation



of aryl-alkyl ethers present in coal matrix, in reactions catalysed by particles of $\alpha\text{-Fe}_2\text{O}_3$, may be responsible for the initiation of spontaneous fires of coal seams, mined coal and cleaning rejects from coal processing.

Secondly, this thesis has discussed the photo-induced reaction of singlet oxygen with trace water pollutants such as phenol and aniline. Addition of $\text{O}_2(^1\Delta_g)$ to the phenol/aniline molecule branches into two competing 1,4-cycloaddition and *ortho ene*-type routes. By coupling the experimental and theoretical results, the water reaction model reveals that the unimolecular rearrangements of the 1,4-endoperoxide proceed in a facile exothermic reaction to form *para*-benzoquinone (via cycloaddition of singlet oxygen to the *ipso-para* site) as the predominant product over the *ortho*-benzoquinone (*ene*-route of singlet oxygen addition to the *ipso-ortho* site) product. Moreover, the findings resolved the lack of consensus on literature regarding the expected products, their selectivity ratios and reaction mechanism of aniline with $\text{O}_2(^1\Delta_g)$ (Chapter 6). The mechanistic maps presented in Chapter 7 are supported by the in-situ detection of *para*-semibenzoquinone anion (PSBQ) in the electron paramagnetic resonator (EPR) and by the results of singlet-oxygen spin trapping and experiments involving $\text{O}_2(^1\Delta_g)$ and $\text{HO}\cdot$ scavengers. Furthermore, Chapter 7 contrasts the experimental and modelled profiles of concentration of singlet oxygen in water, the former obtained from the EPR spin-trapping technique and the latter from the solution of the coupled ordinary differential equations that describe the kinetics of the process, as coded in the POLYMATH software. The measured trend correlates well with the kinetic approximation, indicating an expected concentration of singlet oxygen between $(3 - 4) \times 10^{-6}$ M in response to 3 h illumination by 24 V LED light. The combined insights from these sections of the thesis should apply equally to decomposition of other biologically active phenolic entities, typically occurring in aqueous media.



The final focus of this thesis highlights the formation of other forms of ROS in biologically-related environments. Such ROS can terminate the pancreatic insulin-producing beta cells causing insulin-dependent diabetes mellitus (IDDM) or what is generally known as “alloxan diabetes”. The EPR spectra proved that, the direct synchronised generation of dialuric acid radical (DA \cdot) and glutathione radical (GS \cdot), with *g* factors amounting to 2.00265 and 2.00252, respectively. Furthermore, applying of the 5,5-Dimethyl-1-Pyrroline-N-Oxide (DMPO) spin trap confirms the generation of hydrogen peroxide (H₂O₂) and hydroxyl radical (HO \cdot), supporting the results of the molecular modelling. Based on the synergistic computational and experimental analyses, Chapter 8 assigns the nature of “compound 305” to the DA \cdot -GS \cdot complex, and hence explains the alloxan-induced diabetes on a precise molecular basis.

9.2 Recommendation and Future Directions

This dissertation had led to number of intriguing research questions. The following paragraphs provide some recommendations for future research directions.

- The current IC systems apply laser as a source of singlet oxygen, leading to the formation of other ROS like ozone (O₃) and O atoms. Therefore, it would be beneficial to test selectively the enhancement effect of singlet oxygen in IC. That could be achieved by applying photosensitisation gasouse-based techniques. Furthermore, in this dissertation, we showed that the activated oxygen on the surface of iron oxides nanoparticles implemented in the coal matrix has a significant effect on initiating spontaneous combustion and the formation of environmentally persistent free radicals (EPFR). Future work should test this on different types of coal residues. Moreover,



the question remains, what are the other likely source, effects, and implications of other ROS such as singlet oxygen on the spontaneous ignition of coal. These efforts will eliminate the risks and economic losses associated with spontaneous fires of valuable organic products.

- Regarding the reaction of singlet oxygen with hydrocarbons in aqueous solution, it will be interesting to test the use of actual dissolved organic materials (for generating singlet O_2 , as opposed to rose bengal used in this thesis). As dissolved organic matter transpires in waste water in varying concentrations, future work should quantitate their effectiveness in generating singlet oxygen, and subsequent destruction of trace organics in an actual wastewater stream (e.g., septic ponds) using direct sunlight. Furthermore, it be interesting to test the role of singlet oxygen, i.e., kinetically, in breaking down other persistent organic pollutant occurring in water. This class of contaminants should include brominated flame retardants (BFR), polychlorinated biphenyls (PCBs) and mixed halogenated dioxins/furans, and polyfluoroalkyl substances (PFAS). Moreover, the correlations of EPFRs formation with dioxins and other unintentional dioxin-like compounds might reveals ROS interactions.
- Finally, the autoxidation of biomolecules such as dialuric acid, ascorbate, alloxan, or thiols is spin forbidden implying a serious kinetic limitation ($< 10^{-5} M^{-1}s^{-1}$). However, many biomolecules including those listed above have been reported to react spontaneously with oxygen forming ROS such as superoxide radicals ($O_2^{\cdot-}$) and hydrogen peroxide (H_2O_2). This implements the strong involvement of catalyst in such reactions when they reported to happen spontaneously, and therefore, future research involving both experimental practice and computational mapping are necessary to



further improve our knowledge of such observation. In addition to the qualitative study provided in Chapter 8, detailed quantitative experimental investigation will be of significance. In such, the experimental and modelled profiles of reactants, intermediates ROS, and products in water should be compared and combined. Reactants and products profiles can be obtained through an in situ high performance liquid chromatography (HPLC) analysis where the ROS time course can be obtained from EPR spin-trapping technique. The mechanistic maps obtained earlier in Chapter 8 can then be implemented to describe the kinetics of the process, if coded in the POLYMATH software.

“The question is – if you die today what ideas, what dreams, what abilities, what talents, what gifts, would die with you?”

– Les Brow

Jomana Al-Nu'airat





Chapter 10

Supplementary Document

Chapter 10





Appendix I: Supporting Information for Chapter 4

Table S4.1 Relative rates for toluene oxidation by singlet and triplet oxygen.

T (K)	Triplet oxygen concentration (molecule cm^{-3}) based on the ideal gas law	Singlet oxygen concentration (molecule cm^{-3})	Rate constant: Singlet ($\text{cm}^3 \text{ molecule}^{-1} \text{ s}^{-1}$)	Rate constant: Triplet ($\text{cm}^3 \text{ molecule}^{-1} \text{ s}^{-1}$)	Rate: Singlet (s^{-1})	Rate: Triplet (s^{-1})
300	5.14×10^{24}	6.06×10^{14}	1.54×10^{-9}	2.15×10^{-38}	9.30×10^5	1.10×10^{-13}
350	4.40×10^{24}	5.19×10^{14}	2.13×10^{-10}	1.99×10^{-33}	1.11×10^5	8.78×10^{-9}
400	3.85×10^{24}	4.54×10^{14}	4.83×10^{-11}	1.11×10^{-29}	2.20×10^4	4.28×10^{-5}
450	3.42×10^{24}	4.04×10^{14}	1.53×10^{-11}	9.41×10^{-27}	6.17×10^3	3.22×10^{-2}
500	3.08×10^{24}	3.64×10^{14}	6.07×10^{-11}	2.13×10^{-24}	2.21×10^3	6.56×10^0
550	2.80×10^{24}	3.31×10^{14}	2.86×10^{-12}	1.84×10^{-22}	9.44×10^2	5.16×10^2
600	2.57×10^{24}	3.03×10^{14}	1.52×10^{-12}	7.71×10^{-21}	4.61×10^2	1.98×10^4
650	2.37×10^{24}	2.80×10^{14}	8.94×10^{-13}	1.85×10^{-19}	2.50×10^2	4.38×10^5
700	2.20×10^{24}	2.60×10^{14}	5.67×10^{-13}	2.85×10^{-18}	1.47×10^2	6.27×10^6
750	2.05×10^{24}	2.42×10^{14}	3.82×10^{-13}	3.09×10^{-17}	9.25×10^1	6.34×10^7
800	1.93×10^{24}	2.27×10^{14}	2.70×10^{-13}	2.51×10^{-16}	6.14×10^1	4.84×10^8



Thermochemical data in NASA database format

Toluene H8 C7 0 0g 300.00 5000.00 1000.00 1
 1.17332177E+01 2.89791785E-02 -1.13076234E-05 2.02196836E-09 -1.35979445E-13 2
 3.38780288E+04 -3.64134849E+01 -2.74821970E+0 5.97970532E-02 -2.09598217E-05 3
 -1.58996004E-08 1.10422510E-11 3.83925924E+04 4.07841876E+01 4

M1 H8 C7 O2 0g 300.00 5000.00 1000.00 1
 1.73071546E+01 3.05364821E-02 -1.19773783E-05 2.14991146E-09 -1.44993515E-13 2
 3.42886973E+04 -6.51761775E+01 -6.51737656E+00 9.92591146E-02 -8.24013825E-05 3
 2.93410928E-08 -1.87796040E-12 4.07530579E+04 5.72299038E+01 4

M2 H8 C7 O2 0g 300.00 5000.00 1000.00 1
 1.54240798E+01 3.24607944E-02 -1.27661585E-05 2.29545132E-09 -1.54988734E-13 2
 3.48818277E+04 -5.53745348E+01 -6.08172327E+00 8.85213109E-02 -5.87881400E-05 3
 9.12118994E-09 4.41443860E-12 4.10537126E+04 5.66863262E+01 4

M3 H8 C7 O2 0g 300.00 5000.00 1000.00 1
 1.72099313E+01 2.81253071E-02 -1.08750185E-05 1.93303283E-09 -1.29470731E-13 2
 3.46324743E+04 -5.96145764E+01 -2.92796778E+00 8.80334787E-02 -7.59589446E-05 3
 3.06832303E-08 -3.62375253E-12 4.00037459E+04 4.33948484E+01 4

M4 H8 C7 O2 0g 300.00 5000.00 1000.00 1
 1.75135384E+01 2.71377147E-02 -1.05585653E-05 1.88544714E-09 -1.26718413E-13 2



									3
									4
M5	H7	C7	0	0g	300.00	5000.00	1000.00		1
									2
									3
									4
M6	H8	C7	O2	0g	300.00	5000.00	1000.00		1
									2
									3
									4
M7	H8	C7	O2	0g	300.00	5000.00	1000.00		1
									2
									3
									4
M8	H8	C7	O2	0g	300.00	5000.00	1000.00		1
									2
									3
									4
M9	H6	C7	O1	0g	300.00	5000.00	1000.00		1
									2



2.79446135E+04-4.52282966E+01-2.80126051E+00 7.08417011E-02-5.18454460E-05 3
1.37310347E-08 9.56479129E-13 3.27200667E+04 4.25274596E+01 4

M10 H7 C7 O1 0g 300.00 5000.00 1000.00 1
1.50044030E+01 2.69301420E-02 -1.05372540E-05 1.88830854E-09 -1.27204318E-13 2
3.03401144E+04-5.05547267E+01-4.13080433E+00 7.96310121E-02-5.96508127E-05 3
1.61038573E-08 1.14664447E-12 3.56680506E+04 4.84022631E+01 4

M11 H6 C7 O1 0g 300.00 5000.00 1000.00 1
1.40790028E+01 2.50101993E-02 -9.79789625E-06 1.75737898E-09 -1.18462631E-13 2
2.79789227E+04-4.51607946E+01-2.86263451E+00 7.02275065E-02-4.95502312E-05 3
1.11258304E-08 1.93399786E-12 3.27919016E+04 4.28689626E+01 4

**Cartesians Coordinates (M06/6-311+G(d,p))****Toluene**

0 1

C	-2.91811861	1.23693378	0.00000000
C	-2.91715961	0.53729178	-1.19888100
C	-2.91811861	1.23693378	-2.39776200
C	-2.91811861	2.62459178	-2.39474700
C	-2.91391761	3.33913278	-1.19888100
C	-2.91811861	2.62459178	-0.00301500
H	-2.92309761	0.69892378	0.94355500
H	-2.92040461	-0.54847722	-1.19888100
H	-2.92309761	0.69892378	-3.34131700
H	-2.92338261	3.16750978	-3.33756000
H	-2.92338261	3.16750978	0.93979800
C	-2.88211561	4.83684178	-1.19888100
H	-3.37530161	5.24820178	-0.31308300
H	-1.85050361	5.20858978	-1.19888100
H	-3.37530161	5.24820178	-2.08467900

Benzene

0 1

C	0.16550523	0.47038327	0.00000000
C	-0.46765577	-0.76559373	0.00003200
C	0.28612223	-1.93182173	-0.00001600
C	1.67315723	-1.86215573	0.00000600



C	2.30627223	-0.62626673	0.00001500
C	1.55244223	0.54004427	-0.00002500
H	-0.42404577	1.38219227	-0.00001400
H	-1.55209177	-0.82014773	-0.00002000
H	-0.20869777	-2.89831873	-0.00006200
H	2.26258123	-2.77404573	-0.00002400
H	3.39070023	-0.57156873	0.00002700
H	2.04739423	1.50647427	-0.00002300

M1-4

0 1

C	0.16550523	0.06968641	0.00000000
C	1.40499723	-0.49298559	0.64151100
C	2.65246523	0.05151541	-0.00030000
C	2.66233723	1.37831741	0.00000400
C	1.42284523	1.94098541	0.64151500
C	0.17537823	1.39648841	-0.00029600
H	-0.66065977	-0.55928059	-0.30981400
H	3.46926023	-0.58946759	-0.31031700
H	3.48850223	2.00728441	-0.30981000
H	1.43075523	3.02394741	0.77100800
H	-0.64141777	2.03747041	-0.31031400
O	1.41910623	1.44107441	2.01479600
O	1.40873523	0.00691541	2.01479000
H	1.39708723	-1.57594859	0.77099100

**M1**

0 1

C	0.75783976	1.67247384	0.00000000
C	0.16091076	0.43204384	0.61441900
C	0.75783976	-0.80838916	0.00000700
C	2.08350676	-0.81072616	0.04148500
C	2.61580676	0.43204384	0.69942900
C	2.08350676	1.67481684	0.04149200
H	0.12887276	2.49547384	-0.32479600
H	0.12887276	-1.63139216	-0.32478400
H	2.72663276	-1.63466716	-0.24424900
H	3.69415876	0.43204384	0.86476100
H	2.72663176	2.49875984	-0.24423700
O	2.07069376	0.43204084	2.05572700
O	0.63992076	0.43204684	2.00864900
C	-1.33749024	0.43204384	0.72652400
H	-1.68413024	1.32108384	1.26012000
H	-1.77441524	0.43204084	-0.27736700
H	-1.68413024	-0.45699316	1.26012600

M2

0 1

C	0.37456448	2.09059230	0.00000000
C	1.27566048	0.93915230	0.38087200
C	2.33531048	0.69059130	-0.65569000



C	3.03863648	1.78889730	-0.90092800
C	2.56120948	2.94831130	-0.06772500
C	1.08857948	3.18463330	-0.24658000
H	0.73410748	0.04601230	0.70307700
H	2.54470548	-0.29888070	-1.04470500
H	3.92120448	1.85049130	-1.52687000
H	3.17658548	3.84557630	-0.14668000
H	0.67707148	4.16992930	-0.43891400
O	2.75139148	2.53644930	1.32304200
O	1.97381548	1.36006730	1.59112600
C	-1.10089352	1.95240330	0.06006300
H	-1.42122952	1.66292030	1.06848100
H	-1.60096052	2.88828530	-0.20273500
H	-1.45476052	1.16925830	-0.62209500

M3

0 1

H	-1.05400702	0.62717769	0.00000000
O	-1.07755302	-0.05240131	0.68810700
O	0.25793798	-0.53754531	0.67455500
C	1.25620998	1.52978869	1.45648900
C	2.47582598	1.84197969	0.73142700
C	0.98533898	0.07849169	1.76315000
C	3.47594398	0.95030469	0.65573200
H	2.57493098	2.83472269	0.29928200



C	2.21986798	-0.75601631	1.85839000
H	0.35905698	-0.01479031	2.66017000
C	3.36294098	-0.34746031	1.29987700
H	4.39914398	1.20031169	0.14239900
H	2.12859198	-1.73337031	2.32020100
H	4.23978498	-0.98831931	1.32800700
C	0.38156498	2.47766969	1.81212200
H	-0.50213102	2.24299369	2.39751200
H	0.53608398	3.51707269	1.53396800

M4

0 1

C	0.94947740	0.54006968	0.00000000
C	0.04642640	-0.59374032	0.15410300
C	-1.25684960	-0.43732432	0.38842700
C	-1.89737260	0.90465268	0.51839100
C	-0.95842360	2.04085968	0.29725300
C	0.34337540	1.86359768	0.07194900
H	0.47682840	-1.58936332	0.07036300
H	-1.90863460	-1.29830432	0.50818900
H	-1.39429260	3.03492068	0.33405800
H	0.99740640	2.72149668	-0.06627700
O	-2.94153960	1.09603068	-0.45072700
C	2.26350140	0.37579668	-0.20934200
O	-4.03873460	0.26902068	-0.06159800



H	-4.12937360	-0.29681732	-0.83896400
H	2.70669940	-0.61341232	-0.26890600
H	2.92742740	1.22647568	-0.32758000
H	-2.37502360	1.00116668	1.50894700

M5

0 2

C	-0.47095345	2.50788476	0.31558021
C	-0.47094445	3.20957576	-0.89058179
C	-0.47095345	2.50788476	-2.09674379
C	-0.47096445	1.12999176	-2.10319679
C	-0.47096445	0.39219676	-0.89058179
C	-0.47096445	1.12999176	0.32203321
H	-0.47095245	3.05131376	1.25586321
H	-0.47092345	4.29496576	-0.89058179
H	-0.47095245	3.05131376	-3.03702679
H	-0.47097345	0.58554376	-3.04416379
H	-0.47097345	0.58554376	1.26300021
C	-0.47095445	-1.00541824	-0.89058179
H	-0.47094945	-1.56452924	0.03923821
H	-0.47094945	-1.56452924	-1.82040179

M6

0 1

C	-0.51376116	2.83972121	-0.01345332
---	-------------	------------	-------------



C	-1.43110816	1.74009521	-0.38812232
C	-0.86525316	0.38597821	-0.58179032
C	0.60843384	0.18548521	-0.37945532
C	1.46387984	1.33657821	-0.00488132
C	0.79566584	2.65303021	0.16461068
H	-0.94014616	3.83052421	0.09989468
H	-2.33085816	2.01534221	-0.92945332
H	1.43227284	3.49482721	0.42065668
O	1.10224684	0.32087421	0.93269668
O	-1.63307616	0.69102521	0.55580968
H	1.05795184	-0.61643079	-0.96015732
H	-1.34086016	-0.28165879	-1.29458932
C	2.92474684	1.36629721	-0.36905432
H	3.07881184	1.91912421	-1.29808732
H	3.49764784	1.85498421	0.42312068
H	3.30413784	0.35140521	-0.49075532

M7

01

C	-0.37456448	3.36236929	0.00000000
C	0.33003652	4.64193529	0.21034900
C	-0.48962348	5.88627629	0.17040000
C	-1.82352948	5.86990629	0.16764700
C	-2.59230448	4.60208829	0.14148800
C	-1.85224548	3.34041229	-0.27539500



H	0.20098152	2.53194429	-0.40317200
H	0.04819752	6.83030929	0.17449800
H	-2.41266448	6.77915129	0.20031400
H	-2.01408948	3.22663029	-1.35351500
H	-2.33207348	2.49001129	0.21351100
O	-3.77687748	4.57977129	0.37664900
O	0.02005752	3.76407829	1.29896900
C	1.79556852	4.78658629	-0.09730600
H	2.26533052	5.46227629	0.62167000
H	2.29120952	3.81782829	-0.03456900
H	1.93890052	5.19504729	-1.10008700

M8

0 1

C	1.76829277	2.33449474	0.00000000
C	1.11061677	3.71341174	-0.12083900
C	1.99354777	4.85081874	-0.43668400
C	3.32668277	4.70456474	-0.49566500
C	4.00725477	3.45564174	-0.15303600
C	3.17536577	2.42392674	0.56488300
H	1.13065777	1.71857874	0.64234700
H	1.50494777	5.78916774	-0.67183100
H	3.94898377	5.53681274	-0.81241400
H	3.09682277	2.71649374	1.61849300
H	3.64807877	1.44128474	0.52109300

Chapter 10



O	1.86075677	1.77614074	-1.30140700
H	0.97309877	1.70712774	-1.66629200
O	-0.09425523	3.82149274	-0.05643900
C	5.30077477	3.28569774	-0.43623400
H	5.81322177	2.35995574	-0.20196000
H	5.87643377	4.06710074	-0.91966700

M9

0 1

C	0.58362372	2.87456442	0.00000000
C	0.58362372	1.62473542	-0.76015400
C	0.58362372	0.37490642	0.00000000
C	0.58362372	0.36647942	1.33922200
C	0.58362372	1.62473542	2.11698200
C	0.58362372	2.88299142	1.33922200
H	0.58362372	3.80266342	-0.56269100
H	0.58362372	-0.55319258	-0.56269100
H	0.58362372	-0.55214558	1.91364500
H	0.58362372	3.80161642	1.91364500
O	0.58362372	1.62473542	3.33239200
C	0.58362372	1.62473542	-2.10224100
H	0.58362372	2.55144242	-2.66453700
H	0.58362372	0.69802842	-2.66453700

M10



0 2

O	-0.30487806	3.67595813	0.00000000
C	0.66577494	5.90058713	0.21248500
C	1.92937894	6.63910113	0.23637700
C	0.75823794	4.39678513	0.46317300
C	3.11307894	6.01195413	0.15936300
H	1.87548094	7.72242313	0.25581500
C	2.09843894	3.79417513	0.10867000
H	0.65137794	4.25757413	1.56732500
C	3.18922694	4.55626813	0.01200600
H	4.03349194	6.58330213	0.14485600
H	2.12198094	2.71733113	-0.01179300
H	4.15208194	4.10656613	-0.20175000
C	-0.50961706	6.49651313	0.00212900
H	-1.42669906	5.92320413	-0.04811100
H	-0.56693106	7.57019113	-0.13539900

M11

0 1

O	0.47909410	1.77700346	0.00000000
C	-0.39762090	3.99458046	-0.00009900
C	-1.62111290	4.78813946	-0.00008700
C	-0.50431890	2.48935946	-0.00025900
C	-2.82811290	4.19973846	-0.00007300
H	-1.52449790	5.86873046	-0.00006000



C	-1.86946790	1.93894146	-0.00006600
C	-2.94404690	2.74733446	-0.00003600
H	-3.73352590	4.79373246	-0.00003800
H	-1.95490190	0.85921346	0.00000300
H	-3.93974190	2.31638246	0.00003900
C	0.82010510	4.55304046	-0.00002200
H	1.70369110	3.92527746	-0.00009300
H	0.94496910	5.63022246	0.00002800

TS1-4

0 1

C	1.08885023	2.90940762	0.00000000
C	1.53691023	1.57872062	0.33968100
C	2.84860723	1.17461162	-0.03557300
C	3.78361623	2.15067862	0.00004700
C	3.33554223	3.48135462	0.33974900
C	2.02386123	3.88547662	-0.03554500
H	3.10372923	0.12530562	-0.12318600
H	4.84510523	1.94480362	-0.07676700
H	4.08923423	4.24141762	0.51878300
H	1.76874223	4.93478662	-0.12312900
O	2.99186123	2.86142462	2.08936200
O	1.88049423	2.19857862	2.08931300
H	0.78320923	0.81865062	0.51865100
H	0.02736323	3.11528662	-0.07685200

**TS1**

0 1

C	0.75783976	3.41463410	0.00000000
C	0.09199176	2.20920110	0.37305600
C	0.72400976	0.95370410	0.02550500
C	2.07310376	0.91303410	-0.03675600
C	2.73415476	2.11975610	0.32564200
C	2.10902476	3.37966910	0.00613200
H	0.19972776	4.34314110	-0.06502200
H	0.10936076	0.06022810	-0.03489600
H	2.62348876	-0.01521190	-0.13341100
H	3.80875776	2.10675410	0.47689000
H	2.71392776	4.27563910	-0.07347400
O	2.10779276	2.29282810	2.09552900
O	0.84272176	2.01902410	2.12036200
C	-1.36871424	2.20595610	0.65755200
H	-1.70162224	3.17095610	1.04563400
H	-1.93395024	1.98100610	-0.25467100
H	-1.60304324	1.43251110	1.39539100

TS2

0 1

C	1.68118475	4.18118461	0.00000000
C	2.50375475	3.00850061	0.05074300



C	3.78539575	3.00363461	-0.61004900
C	4.45778575	4.17777061	-0.63815900
C	3.81134075	5.26634561	0.00464100
C	2.37656475	5.34287761	0.00700300
H	4.23790575	2.06291161	-0.90166000
H	5.49654575	4.24783661	-0.93831100
H	4.37311375	6.17625861	0.19021300
H	1.88900575	6.29901861	0.16987100
O	3.73079375	4.47872361	1.79883600
O	3.32574975	3.25337661	1.67666300
H	2.01233275	2.05187061	0.21263400
C	0.21239975	4.07736161	0.22597100
H	-0.27589725	3.47516961	-0.54801700
H	0.01190875	3.59203261	1.18913800
H	-0.25894025	5.06324261	0.23952500

TS3

0 1

H	0.13066203	-0.15679442	0.00000000
O	-0.06105497	-1.27135342	-0.46537400
O	1.09051303	-1.83751142	-0.55837600
C	2.04461903	0.08123758	0.67825400
C	3.01813703	0.70966658	-0.14169300
C	2.29456003	-1.24372842	1.11863900
C	4.19793003	0.08350158	-0.42014800



H	2.81300903	1.70552858	-0.52465000
C	3.53219703	-1.85727142	0.85823300
H	1.58588903	-1.71234642	1.79417200
C	4.45854103	-1.21017042	0.08674700
H	4.94541303	0.57719658	-1.03298700
H	3.72855703	-2.85151842	1.24404100
H	5.40689603	-1.68820242	-0.13883700
C	0.75430003	0.62725758	0.87630400
H	0.21906903	0.35231558	1.78355300
H	0.57079803	1.64224958	0.52563400

TS4

0 1

C	-0.79268297	0.05226481	0.00000000
C	-1.55647297	0.64421181	-1.07240300
C	-0.99728697	1.82572681	-1.71730200
C	0.32470203	1.83961281	-1.88173500
C	1.11175403	0.70178181	-1.32599000
C	0.54505203	0.18947681	-0.05221300
H	-1.29571497	-0.59361919	0.71373200
H	-1.66603297	2.53626181	-2.19366500
H	0.81847903	2.58947581	-2.49237000
H	2.17865903	0.92694481	-1.26119900
H	1.19904303	-0.33306419	0.63682500
O	1.09166503	-0.43401819	-2.26682600



O	-0.15729197	-1.03741919	-2.36965800
H	-1.51653197	-0.44957519	-2.42572800
C	-2.55410497	-0.04039919	-1.78350800
H	-3.00620797	-0.92055019	-1.33082500
H	-3.17664697	0.52655181	-2.47210400

TS5

0 1

C	-1.29790947	-0.43554006	0.00000000
H	-0.67445547	0.34824294	-0.87775800
H	-0.76242047	-0.15974506	0.90681500
H	-1.11387347	-1.45046206	-0.35059600
O	-0.48205447	1.46171594	-1.34303200
O	-1.63320747	2.02883894	-1.43614500
C	-2.58821447	0.11023594	-0.19861000
C	-3.56103847	-0.51843306	-1.01921000
C	-2.83914547	1.43478694	0.24225300
C	-4.74096347	0.10730694	-1.29821600
H	-3.35523247	-1.51408106	-1.40236600
C	-4.07661247	2.04796794	-0.01893600
H	-2.13057147	1.90395594	0.91748600
C	-5.00233047	1.40068594	-0.79119800
H	-5.48787847	-0.38655206	-1.91161400
H	-4.27359347	3.04206794	0.36693500
H	-5.95069047	1.87847694	-1.01727800

**TS6**

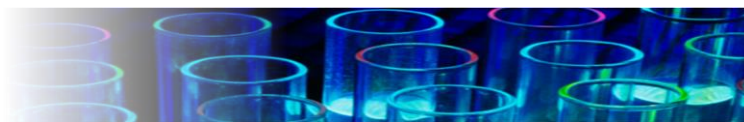
0 1

C	-0.04355401	0.08710801	0.00000000
C	0.68573599	1.40588301	0.25206200
C	-0.07961501	2.67589801	0.21864300
C	-1.41029701	2.68183301	0.18649200
C	-2.19385801	1.43324801	-0.08814600
C	-1.42752201	0.23195501	-0.34647000
H	0.52472099	-0.77358399	-0.35149500
H	0.49994099	3.59375901	0.29742900
H	-1.98764301	3.59800001	0.26280200
H	-2.41104001	1.64366101	-1.22063700
H	-1.98569201	-0.57814299	-0.80970900
O	-3.25349501	1.11293401	0.62523700
O	0.31957399	0.54077201	1.29285300
C	2.14315799	1.45732701	-0.08150500
H	2.29234099	1.82428501	-1.10084100
H	2.64886999	2.14654901	0.60397500
H	2.60772299	0.47356801	0.01851300

TS7

0 1

C	-0.51393731	0.94076654	0.00000000
C	0.04443469	2.33165754	0.01161400



C	-0.81731731	3.45430254	0.27661500
C	-2.15000531	3.30967554	0.35200700
C	-2.81398131	1.98581554	0.25680500
C	-1.99944831	0.85854054	-0.31108100
H	0.04506569	0.27868854	-0.68903700
H	-0.35179031	4.42755054	0.41610600
H	-2.80442931	4.14992354	0.56706300
H	-2.14625131	0.89061854	-1.40152900
H	-2.41068031	-0.08903246	0.04642500
O	-3.96665931	1.86627354	0.60076100
O	-0.20779631	0.75316654	1.33333800
H	1.05626869	1.51980554	1.12202800
C	1.43776169	2.34100454	0.19521800
H	1.93124869	3.25497554	0.51082200
H	2.02458469	1.66545454	-0.42921900

TS8

01

C	-3.38850191	0.59233449	0.00000000
C	-4.29855991	1.55701049	-0.59720900
C	-3.74405091	2.88970149	-0.91169900
C	-2.30776991	3.07949049	-0.93400200
C	-1.42185691	1.99631149	-0.53982800
C	-2.06772391	0.79769749	0.05165200
H	-3.82575891	-0.32964151	0.37774900

Chapter 10



H	-4.34980291	3.47754249	-1.60206800
H	-1.89231091	3.81646949	-1.61659900
H	-2.78706091	3.78514149	0.24326000
H	-1.39012091	0.05943149	0.47035600
O	-0.20759291	2.04120149	-0.65620200
H	-4.42871191	4.62286949	0.47097200
O	-3.95191891	3.78527849	0.56431700
C	-5.57156291	1.26459149	-0.88328700
H	-6.23212991	1.99002549	-1.34822400
H	-5.98670791	0.28590149	-0.66314400



Frequencies (VIB) and rotational constants (GHZ) (M06/6-311+G(d,p))

Benzene

GHZ 5.747220 5.746810 2.873510
VIB 404.4 404.4 613.3 613.8 679.1 715.2 857.4 857.6 983.8 984.0 1005.8 1012.0 1021.7
1058.0 1058.5 1147.4 1177.0 1177.4 1346.6 1353.2 1498.2 1498.7 1647.2 1648.3 3144.0
3152.8 3153.8 3167.8 3168.6 3177.9

M1-4

GHZ 2.912360 2.898460 2.776860
VIB 268.5 385.9 390.9 438.6 474.9 639.6 679.1 695.4 714.3 730.6 832.5 850.1 931.4 941.0
942.3 949.7 968.5 993.7 1026.4 1061.2 1083.3 1140.3 1266.6 1274.6 1278.3 1292.9 1344.2
1363.8 1660.1 1704.8 3105.3 3108.0 3174.2 3175.5 3196.9 3199.4

TS1-4

GHZ 2.758500 2.716030 2.698430
VIB -486.4 151.3 224.1 304.8 381.8 451.7 550.9 585.2 627.0 671.8 740.6 762.1 919.5 953.7
971.4 978.9 1003.5 1004.7 1043.4 1066.9 1133.6 1133.8 1163.5 1200.0 1329.3 1381.0 1428.6
1509.5 1562.3 1655.6 3162.6 3167.1 3176.4 3182.0 3192.9 3197.2

Toluene

GHZ 5.587940 2.541970 1.766350
VIB 59.5 207.5 346.4 408.8 469.1 526.0 627.9 707.2 738.3 802.7 851.7 905.9 981.1 991.6
999.6 1010.2 1046.5 1050.2 1101.8 1155.9 1183.5 1238.1 1325.4 1345.2 1393.6 1447.0 1459.3
1482.9 1519.6 1637.6 1661.4 3010.8 3079.5 3102.5 3136.2 3137.0 3151.1 3160.5 3172.2



M1

GHZ 2.853540 1.830130 1.775760
VIB 224.5 262.0 288.5 296.1 393.3 402.4 459.6 490.3 566.9 640.2 695.6 707.6 712.4 757.6
840.7 861.8 918.5 941.1 947.8 950.6 966.4 994.5 1014.2 1081.5 1108.9 1130.8 1222.7 1253.9
1274.9 1288.8 1342.0 1373.2 1398.0 1448.4 1465.4 1658.2 1709.2 3023.4 3103.6 3108.9
3118.4 3160.6 3162.0 3190.8 3193.3

M2

GHZ 2.844580 1.679530 1.643960
VIB 138.5 192.4 261.8 303.0 379.6 431.5 446.9 521.8 570.3 672.0 707.8 722.2 798.1 826.5
842.5 874.4 931.7 943.9 957.6 966.1 1002.0 1028.7 1047.5 1058.4 1109.9 1195.5 1249.4
1271.3 1275.1 1293.3 1344.0 1354.7 1392.7 1445.9 1455.6 1675.6 1736.3 3000.4 3062.7
3085.1 3104.1 3106.2 3170.5 3173.0 3196.4

M3

GHZ 2.550530 1.568980 1.134650
VIB 77.2 137.4 189.9 217.6 282.9 370.2 386.0 409.7 483.1 530.3 607.1 670.7 708.3 760.5
788.4 820.6 932.4 945.4 961.7 977.1 983.1 983.8 995.5 998.3 1057.5 1156.0 1179.3 1292.7
1314.9 1333.5 1381.0 1383.3 1417.1 1445.1 1632.1 1672.6 1717.5 3022.9 3113.8 3142.9
3149.9 3169.1 3179.5 3211.1 3794.2

M4

GHZ 4.347960 1.034870 0.874630



VIB 56.4 121.7 211.4 229.4 245.6 357.3 376.0 405.7 469.1 547.2 595.0 672.1 693.2 791.0
800.2 808.7 912.3 918.5 952.3 960.4 980.9 997.5 1002.7 1038.9 1078.4 1143.2 1186.7 1301.3
1312.5 1361.3 1366.8 1387.5 1433.6 1441.8 1660.4 1683.1 1743.6 2957.3 3122.6 3136.7
3140.1 3163.1 3166.4 3217.9 3826.2

M5

GHZ 5.579120 2.730090 1.833090

VIB 195.8 359.9 383.7 469.6 504.1 528.7 619.0 674.1 697.7 768.6 823.8 834.3 892.3 957.2
973.2 984.1 988.4 1034.8 1105.3 1149.0 1166.4 1286.1 1323.2 1346.2 1460.1 1462.0 1492.7
1584.4 1601.7 3119.3 3143.4 3145.2 3156.6 3163.3 3175.1 3225.3

M6

GHZ 3.313120 1.643250 1.288990

VIB 160.6 176.7 205.1 313.3 350.8 396.5 486.6 508.7 577.6 680.3 728.5 750.1 822.2 861.9
868.0 914.2 950.2 997.8 1008.6 1030.0 1062.1 1082.6 1109.2 1125.2 1147.2 1222.0 1250.3
1294.6 1336.7 1389.7 1417.3 1440.7 1473.3 1486.5 1493.5 1516.2 1730.8 3065.5 3136.4
3147.7 3158.4 3163.3 3171.2 3182.7 3208.6

M7

GHZ 3.656570 1.342540 1.104920

VIB 72.2 189.2 233.3 246.4 315.6 363.6 417.6 464.0 492.8 600.3 632.9 707.7 745.5 771.6
837.7 888.6 925.7 964.8 1009.1 1024.9 1064.0 1102.3 1132.7 1174.4 1224.3 1254.1 1269.5
1338.9 1367.1 1417.3 1426.6 1446.1 1481.6 1494.9 1520.3 1722.0 1829.6 3066.0 3066.7
3127.2 3136.6 3144.8 3161.5 3183.5 3221.2



M8

GHZ 2.889620 1.446260 1.118990
VIB 67.4 110.2 224.2 289.2 329.8 359.7 387.5 433.9 473.7 517.6 608.9 680.3 745.3 776.1
789.6 871.8 909.9 956.8 967.1 971.9 1029.7 1035.4 1114.5 1150.2 1219.7 1230.1 1284.9
1341.1 1363.7 1372.8 1415.9 1429.6 1458.2 1471.8 1673.5 1731.8 1817.4 3055.9 3074.6
3129.7 3168.5 3184.2 3221.1 3258.6 3882.1

M9

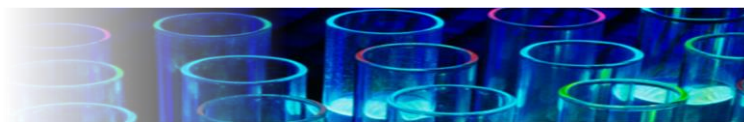
GHZ 5.246300 1.655290 1.258280
VIB 93.7 238.4 348.5 355.5 461.4 462.5 484.6 611.5 685.6 743.8 779.9 802.1 815.5 876.0
966.8 977.2 977.3 1003.5 1017.9 1126.0 1184.2 1272.1 1363.2 1375.1 1457.4 1464.2 1667.9
1673.5 1741.9 1790.3 3172.5 3194.4 3195.8 3227.1 3228.7 3265.2

M10

GHZ 3.179850 2.332030 1.378260
VIB 66.5 214.7 320.5 380.5 426.9 462.1 477.8 557.4 669.9 679.0 754.7 800.0 835.8 861.8
951.8 960.1 989.0 1006.0 1010.7 1064.0 1096.9 1124.9 1178.5 1185.2 1227.6 1320.9 1388.0
1417.1 1459.2 1659.6 1697.9 1740.2 2830.2 3174.4 3195.3 3201.9 3219.4 3226.1 3269.9

M11

GHZ 3.306600 2.406040 1.392670
VIB 77.6 228.5 347.9 420.4 445.3 464.0 528.5 573.4 676.3 722.7 760.3 821.3 877.0 880.8
960.4 1002.6 1006.8 1024.0 1029.8 1160.7 1184.4 1216.5 1343.5 1384.8 1433.0 1469.4 1639.0
1675.7 1721.1 1798.4 3168.4 3193.8 3198.4 3226.0 3230.4 3268.2



TS1

GHZ 2.692940 1.720550 1.718140
VIB -456.7 132.8 165.1 206.0 262.7 284.8 356.0 392.0 454.0 537.2 569.4 601.3 664.7 754.7
757.8 779.8 925.9 951.4 979.2 984.7 994.5 1004.9 1038.9 1096.2 1133.8 1147.9 1199.3 1257.4
1299.9 1369.0 1389.3 1438.3 1454.7 1459.2 1507.7 1557.9 1666.3 3016.3 3091.5 3120.9
3159.6 3162.6 3167.8 3186.9 3191.4

TS2

GHZ 2.639860 1.645730 1.623970
VIB -480.4 126.5 145.2 164.5 185.1 303.8 340.1 396.8 495.0 524.6 557.6 619.0 674.9 743.6
807.4 844.3 934.4 968.2 981.3 991.1 1028.0 1039.4 1049.1 1073.0 1136.5 1148.9 1188.3
1230.4 1303.8 1378.6 1388.1 1412.0 1448.6 1462.1 1520.2 1581.8 1672.5 3007.4 3073.5
3109.6 3146.1 3162.1 3172.5 3179.6 3194.7

TS3

GHZ 2.757050 1.436930 1.183710
VIB -1108.3 113.1 141.4 169.2 280.6 345.2 398.0 416.7 505.1 525.5 561.3 619.5 667.4
702.7 762.5 831.6 845.3 943.2 981.9 982.7 998.7 1003.0 1033.4 1064.7 1103.6 1165.4 1178.7
1184.0 1311.6 1327.2 1373.4 1410.1 1452.4 1467.6 1514.8 1542.1 1600.7 1665.6 3088.7
3150.5 3158.3 3165.7 3173.2 3180.7 3183.0

TS4

GHZ 2.472850 1.821700 1.673050
VIB -1958.5 160.2 194.7 246.0 319.3 357.1 401.4 442.5 465.7 547.3 599.5 666.9 698.6
734.1 762.3 792.5 838.4 893.6 917.0 942.0 960.9 970.1 983.5 1007.1 1045.2 1127.0 1153.5



1269.0 1290.0 1320.8 1350.2 1354.4 1409.7 1416.5 1472.8 1543.6 1590.0 1694.7 3088.7
3093.9 3154.8 3157.6 3174.7 3186.5 3192.0

TS5

GHZ 4.025780 0.746440 0.680850
VIB -983.4 34.5 50.7 97.2 189.3 203.9 354.4 362.5 405.3 496.1 543.2 621.7 680.1 751.8
768.4 837.5 844.3 926.9 973.6 987.1 990.9 1001.6 1009.0 1045.0 1108.6 1159.9 1180.0 1211.6
1280.2 1328.7 1359.5 1362.3 1456.9 1472.5 1513.5 1611.3 1640.2 2328.6 3080.4 3149.9
3153.2 3162.0 3171.7 3180.2 3208.5

TS6

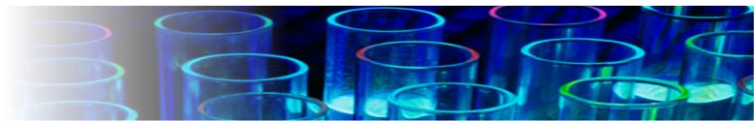
GHZ 3.590760 1.396320 1.157410
VIB -771.0 118.4 173.0 208.8 299.0 329.9 380.9 447.1 466.4 558.7 587.7 654.4 691.4 749.4
798.6 820.2 871.9 942.8 962.6 988.1 1025.5 1031.6 1045.3 1049.1 1112.4 1161.4 1234.2
1254.0 1283.4 1328.2 1384.6 1396.8 1410.9 1438.9 1448.3 1464.2 1690.9 2350.0 3020.1
3099.1 3103.6 3123.8 3130.9 3167.8 3171.9

TS7

GHZ 3.278710 1.402260 1.113070
VIB -2296.5 72.1 163.5 259.9 293.6 349.9 372.6 462.2 500.0 529.6 598.8 628.4 638.7 750.2
755.0 816.6 897.2 925.5 927.7 962.6 1011.7 1025.9 1090.7 1146.9 1185.8 1229.3 1251.6
1271.9 1303.2 1329.2 1348.4 1399.6 1410.6 1421.6 1518.2 1656.8 1780.8 1801.3 2907.5
3005.5 3084.5 3100.2 3138.5 3166.9 3191.9

TS8

Chapter 10



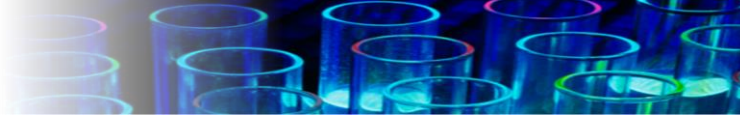
GHZ 2.681590 1.411520 1.068090

VIB -1546.0 85.4 134.8 210.0 295.8 351.2 382.2 404.7 455.3 472.5 516.1 561.5 620.0 691.7

715.2 779.4 785.5 827.3 859.3 876.8 941.7 954.4 981.6 1001.4 1061.9 1143.8 1166.7 1246.7

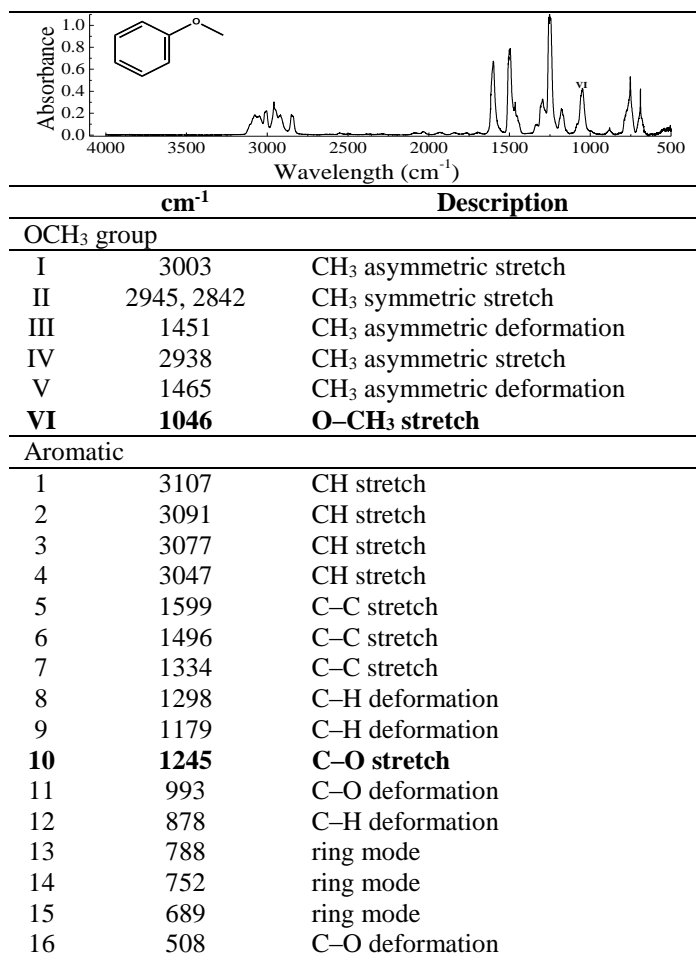
1315.9 1341.4 1349.7 1384.9 1431.3 1434.2 1654.4 1705.3 1718.0 1748.8 3107.6 3120.9

3135.3 3155.7 3169.9 3216.3 3806.9



Appendix II: Supporting Information for Chapter 5

Table S5.1. IR bands of vaporised anisole, 1000 ppm in 2.4 m path-length gas cell



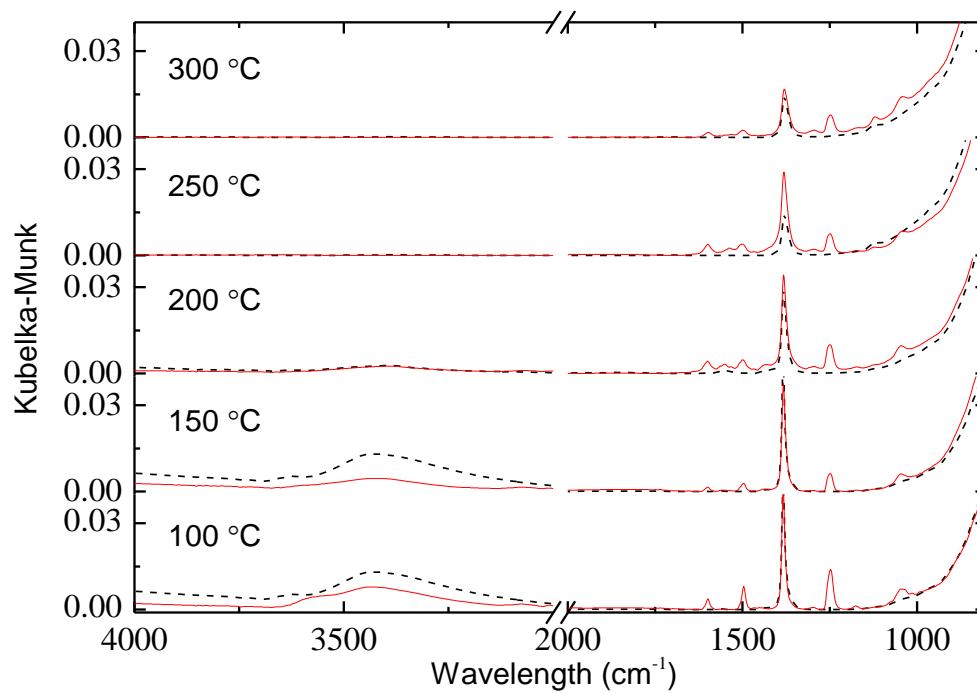
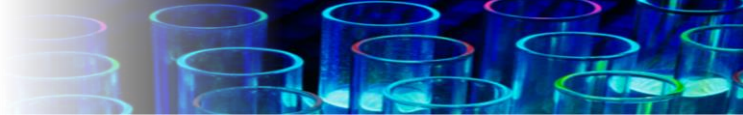


Figure S5.2. Full range DRIFTS adsorption spectra of anisole on Fe_2O_3 surface (control) after 3 h at different temperatures.

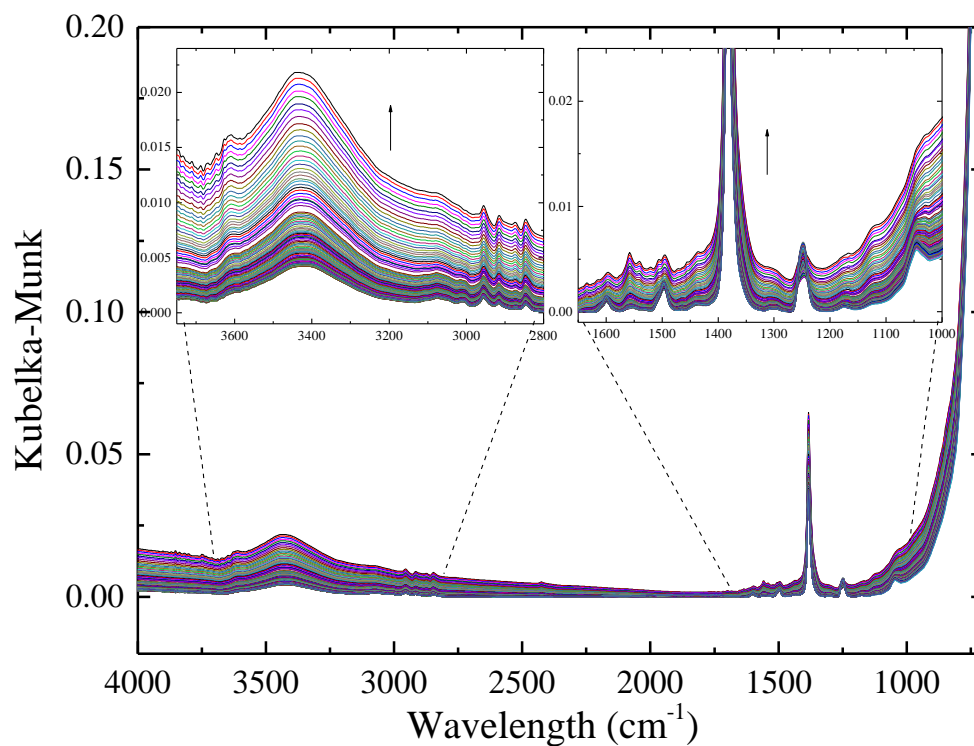


Figure S5.3. Full range DRIFTS adsorption spectra of anisole on Fe_2O_3 surface (control) (0-3 h) at 150 °C. The arrows indicate the direction of the temporal change of the spectrum.

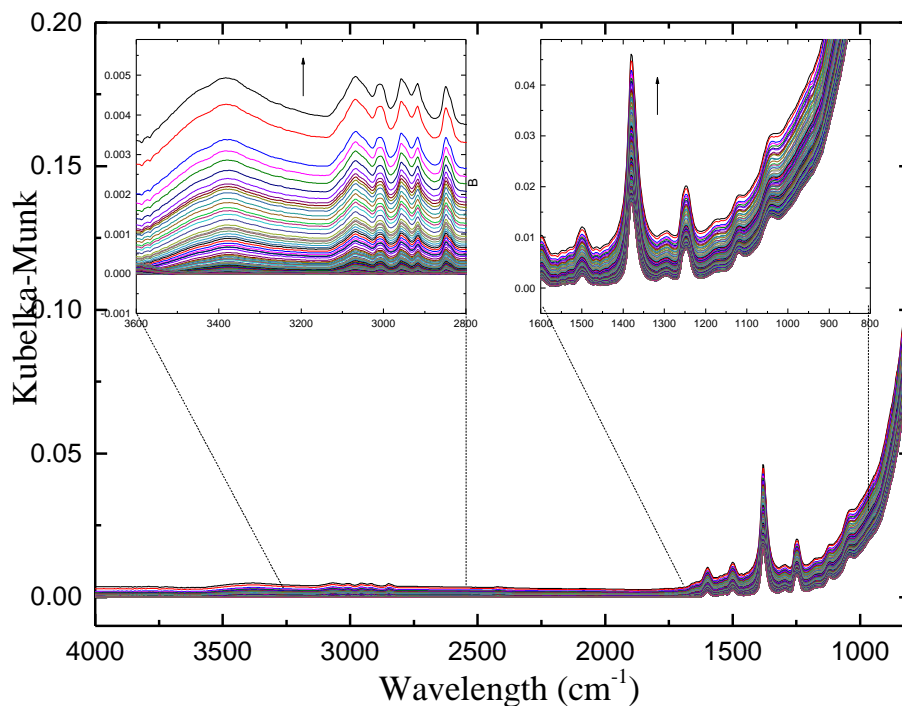
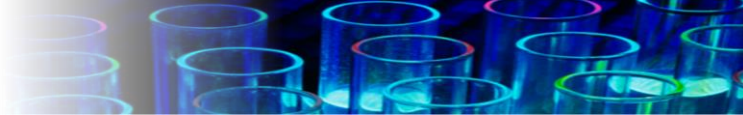


Figure S5.4. Full range DRIFTS adsorption spectra of anisole on Fe_2O_3 surface (control) (0-3) h at 200 °C. The arrows indicate the direction of the temporal change of the spectrum.

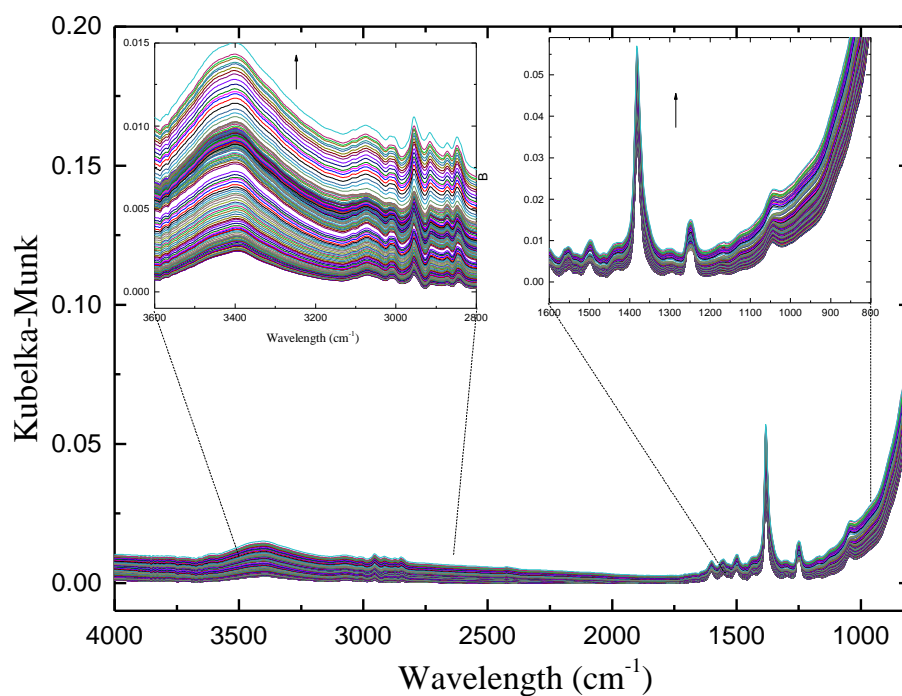


Figure S5.5. Full range DRIFTS adsorption spectra of anisole on Fe_2O_3 surface (control) (0-3) h at 300 °C. The arrows indicate the direction of the temporal change of the spectrum.



Appendix III: Supporting Information for Chapter 6

Table S6.1: Singlet enthalpy H_{Singlet} , triplet energy H_{Triplet} and spin unrestricted $H_{(\text{Singlet}, \text{Guess}=\text{Mix})}$ energy calculated by B3LYP, HSEH1PBE, B3PW91, CAM-B3LYP, and M06 for O, O₂, NH, NF, C, and Si diradicals, in addition to the spin contaminations S^2_{Singlet} and S^2_{Triplet} for singlet and triplet states, respectively. All energy values are in kJ/mol at 298.15 K.

Molecule	Method	S^2_{Triplet}	S^2_{Singlet}	H_{Singlet}	H_{Triplet}	H_{Singlet} <i>Guess=Mix</i>
C	B3LYP ^a	2.003143	1.003854	-99216.49	-99388.07	-99349.41
	HSEH1PBE ^b	2.002981	1.004918	-99067.87	-99257.12	-99215.74
	B3PW91 ^b	2.003621	1.006867	-99146.20	-99330.92	-99290.29
	CAM-B3LYP ^b	2.003600	1.005861	-99154.52	-99329.67	-99289.67
	M06 ^a	2.002636	1.002451	-99156.03	-99249.58	-99302.05
NF	B3LYP ^a	2.00675	1.003275	-405403.45	-405595.20	-405544.41
	HSEH1PBE ^b	2.008081	1.005725	-405037.48	-405243.75	-405193.37
	B3PW91 ^b	2.007336	1.005011	-405254.50	-405456.04	-405404.20
	CAM-B3LYP ^b	2.00722	1.004732	-405308.31	-405501.52	-405450.48
	M06 ^a	2.000032	1.001584	-405212.53	-405316.80	-405395.46
NH	B3LYP ^a	2.005538	1.002283	-144796.40	-145007.44	-144952.21
	HSEH1PBE ^b	2.006337	1.004696	-144621.01	-144853.05	-144796.23
	B3PW91 ^b	2.006206	1.004454	-144724.06	-144951.67	-144893.01
	CAM-B3LYP ^b	2.00569	1.003552	-144731.00	-144943.26	-144888.57
	M06 ^a	2.007998	1.001192	-144702.68	-144817.74	-144902.55
O₂	B3LYP ^a	2.008759	1.004213	-394617.81	-394779.10	-394736.05
	HSEH1PBE ^b	2.009991	1.006042	-394261.54	-394431.33	-394389.45
	B3PW91 ^b	2.008947	1.005107	-394478.36	-394644.63	-394602.12
	CAM-B3LYP ^b	2.009797	1.005412	-394522.20	-394685.34	-394641.66
	M06 ^a	2.007585	1.001743	-394411.08	-394500.74	-394566.97
Si	B3LYP ^a	2.002006	1.005428	-759690.30	-759798.25	-759775.82
	HSEH1PBE ^b	2.005461	1.016211	-759338.85	-759463.20	-759438.59



	B3PW91 ^b	2.004945	1.014981	-759537.21	-759657.71	-759633.23
	CAM-B3LYP ^b	2.004582	1.013743	-759650.51	-759759.42	-759740.05
	M06 ^a	2.001256	1.004103	-759600.35	-759659.34	-759688.55
	<hr/>					
	B3LYP ^a	2.0034910	1.001746	-196877.20	-197142.30	-197072.47
O	HSEH1PBE ^b	2.0037310	1.003587	-196672.77	-196960.00	-196889.00
	B3PW91 ^b	2.0037490	1.003360	-196780.55	-197062.97	-196989.96
	CAM-B3LYP ^b	2.003843	1.002890	-196817.28	-197084.81	-197015.27
	M06 ^a	2.005748	1.00105	-196787.16	-196941.34	-197044.43
	<hr/>					
	Basis set; a: 6-311G+(d,p), b: 6-311G++(3df,2p)					

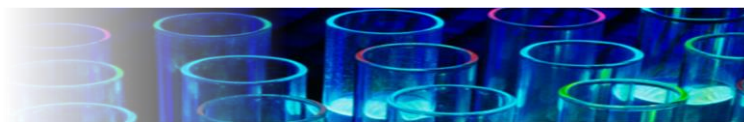


Table S6.2: Spin-projected (singlet-triplet) gap enthalpy ($\Delta G H_{298}^{S-T}$) for O, O₂, NH, NF, C, and Si diradicals and the normal (singlet-triplet) gap energy $\Delta G H_{298}$ for spin unrestricted B3LYP, HSEH1PBE, B3PW91, CAM-B3LYP, and M06 functionals.

All energy values are in kJ/mol.

Molecule	Method	Experimental $\Delta G H_{298}[1]$	$\Delta G H_{298}$	$\Delta G H_{298}^{S-T}$
C	B3LYP ^a		172	78
	HSEH1PBE ^b		189	83
	B3PW91 ^b	122	185	82
	CAM-B3LYP ^b		175	80
	M06 ^a		146	105
NF	B3LYP ^a		192	102
	HSEH1PBE ^b		206	101
	B3PW91 ^b	144	202	104
	CAM-B3LYP ^b		193.	102
	M06 ^a		183	158
NH	B3LYP ^a		211	110
	HSEH1PBE ^b		232	114
	B3PW91 ^b	150	228	118
	CAM-B3LYP ^b		212	110
	M06 ^a		200	169
O₂	B3LYP ^a		161	86
	HSEH1PBE ^b		170	84
	B3PW91 ^b	95	166	85
	CAM-B3LYP ^b		163	87
	M06 ^a		156	132
Si	B3LYP ^a		108	46
	HSEH1PBE ^b		124	50
	B3PW91 ^b	72	121	50



	CAM-B3LYP ^b		109	39
	M06 ^a		88	59
	B3LYP ^a		265	140
O	HSEH1PBE ^b		287	142
	B3PW91 ^b	190	282	146
	CAM-B3LYP ^b		268	139
	M06 ^a		257	206

Basis set; a: 6-311G+(d,p), b: 6-311G++(3df,2p)

[1] Slipchenko LV, Krylov AI. Singlet-triplet gaps in diradicals by the spin-flip approach: A benchmark study. *The Journal of Chemical Physics* 2002;117:4694–4708.

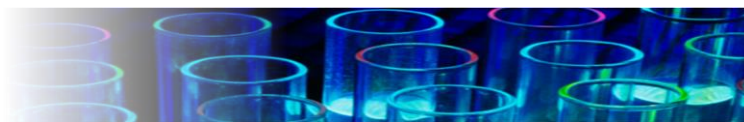


Table S6.3. Enthalpies and Gibbs free energies of activation and reaction ($\Delta^{\#}H^{\circ}_{298}$, $\Delta_r H^{\circ}_{298}$, $\Delta^{\#}G^{\circ}_{298}$ and $\Delta_r G^{\circ}_{298}$) calculated based on gas-phase (B3LYP in italic and M06 in in brackets) and solvation (M06) models. All values are in kJ/mol at 298.15 K

$(\Delta_r H^{\circ}_{298})$										
<i>M1</i>	<i>M2</i>	<i>M3</i>	<i>M4</i>	<i>M5</i>	<i>M6</i>	<i>M7</i>	<i>M8</i>	<i>M9</i>	<i>M10</i>	<i>M11</i>
47	54	-18	-16	140	-196	-285	-304	-311	131	-285
<i>[-19]</i>	<i>[37]</i>	<i>[-98]</i>	<i>[-94]</i>	<i>[101]</i>	<i>[-237]</i>	<i>[-386]</i>	<i>[-365]</i>	<i>[-388]</i>	<i>[120]</i>	<i>[-355]</i>
-34	-56	-108	-108	86	-258	-397	-405	-407	104	-403
$(\Delta^{\#}H^{\circ}_{298})$										
<i>TS1</i>	<i>TS2</i>	<i>TS3</i>	<i>TS4</i>	<i>TS5</i>	<i>TS6</i>	<i>TS7</i>	<i>TS8</i>			
79	101	75	240	154	18	-157	-94			
<i>[10]</i>	<i>[23]</i>	<i>[16]</i>	<i>[154]</i>	<i>[113]</i>	<i>[-95]</i>	<i>[-253]</i>	<i>[-178]</i>			
-22	-4	-9	110	96	-210	-319	-193			
$(\Delta_r G^{\circ}_{298})$										
<i>M1</i>	<i>M2</i>	<i>M3</i>	<i>M4</i>	<i>M5</i>	<i>M6</i>	<i>M7</i>	<i>M8</i>	<i>M9</i>	<i>M10</i>	<i>M11</i>
-3	-8	-79	-78	52	-208	-341	-383	-434	81	-403
<i>[-39]</i>	<i>[-44]</i>	<i>[-110]</i>	<i>[-100]</i>	<i>[15]</i>	<i>[-246]</i>	<i>[-378]</i>	<i>[-420]</i>	<i>[-471]</i>	<i>[45]</i>	<i>[-440]</i>
-76	-81	-148	-148	-21	-282	-415	-457	-508	7.6	-477
$(\Delta^{\#}G^{\circ}_{298})$										
<i>TS1</i>	<i>TS2</i>	<i>TS3</i>	<i>TS4</i>	<i>TS5</i>	<i>TS6</i>	<i>TS7</i>	<i>TS8</i>			
34	56	40	184	127	-68	-228	-154			
<i>[-3]</i>	<i>[19]</i>	<i>[4]</i>	<i>[147]</i>	<i>[90]</i>	<i>[-105]</i>	<i>[-264]</i>	<i>[-191]</i>			
-39	-17	-33	110	54	-142	-301	-228			



Table S6.4. PolyMath [2] ordinary differential equations (ODEs) and parameters for the solvation model at 313 K

	Variable	Polymath Equation
Explicit Equations (L/ (mol s))	<i>K1</i>	$K1=1.85\times 10^9$
	<i>K6</i>	$K6= 20.18\times 10^{14}$
	<i>K7</i>	$K7=4.3\times 10^{26}$
	<i>K8</i>	$K8=323$
Integration Variables (mol/ L)	Aniline	Aniline(0)= 1×10^{-3}
	Singlet Oxygen	SingletOxygen(0) = 18.2×10^{-6}
	<i>M6</i>	$M6(0)=0$
	<i>M7</i>	$M7(0)=0$
	<i>M8</i>	$M8(0)=0$
	<i>M9</i>	$M9(0)=0$
ODE Equations	d(Aniline)/d(<i>t</i>)	d(Aniline)/d(<i>t</i>) = $-K1\times \text{Aniline}\times \text{Oxygen}$
	d(SingletOxygen)/d(<i>t</i>)	d(SingletOxygen)/d(<i>t</i>) = 0
	d(<i>M6</i>)/d(<i>t</i>)	d(<i>M6</i>)/d(<i>t</i>) = $K1\times \text{Aniline}\times \text{SingletOxygen}- K6\times M6$
	d(<i>M7</i>)/d(<i>t</i>)	d(<i>M7</i>)/d(<i>t</i>) = $K6\times M6- K7\times M7$
	d(<i>M8</i>)/d(<i>t</i>)	d(<i>M8</i>)/d(<i>t</i>) = $K7\times M7- K8\times M8$
	d(<i>M9</i>)/d(<i>t</i>)	d(<i>M9</i>)/d(<i>t</i>) = $K8\times M8$
Independent Variable (s)	<i>t</i>	$t(0)= 0 ; t(f)= 1800$

[2] POLYMATH is copyrighted by Shacham, M.; Cutlip, M. B; Elly M. POLYMATH, <http://www.polymath-software.com/>, (accessed Feb 23, 2016)

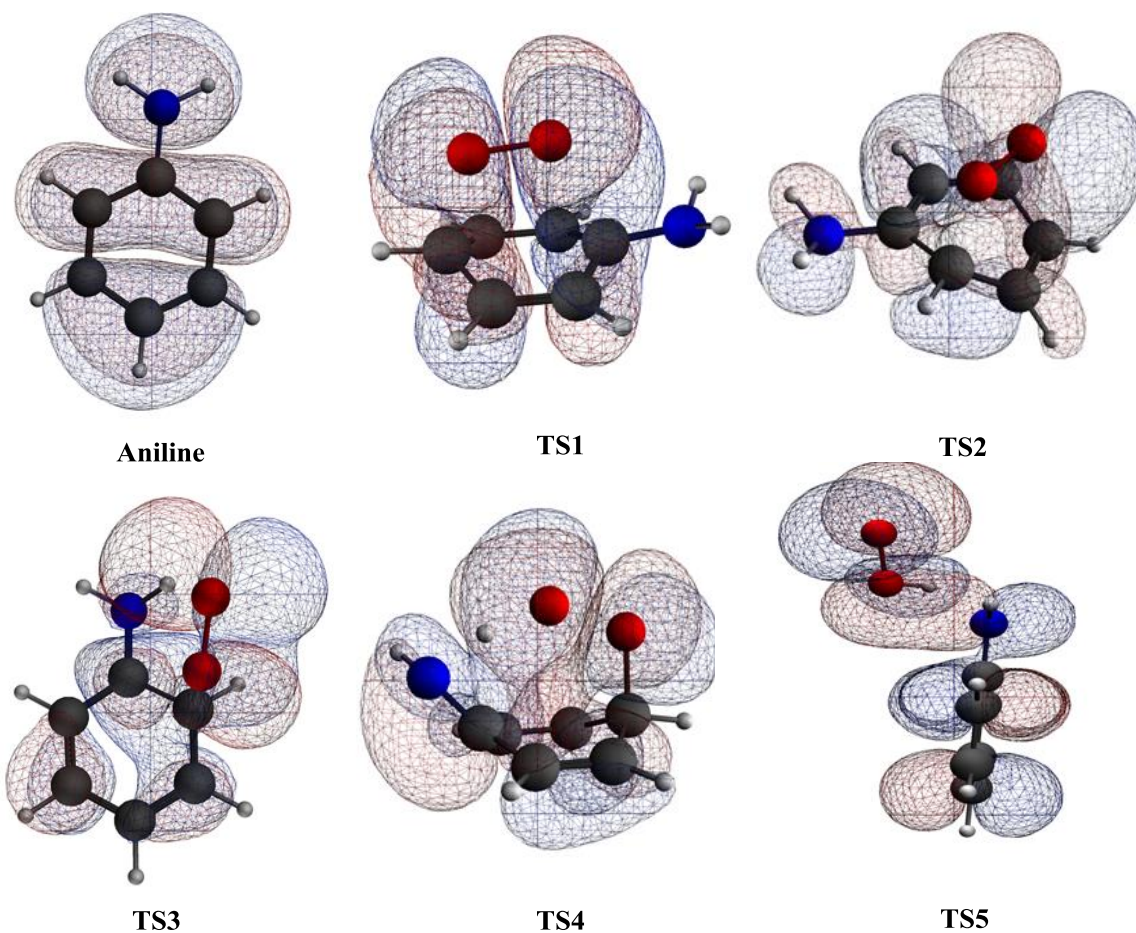


Figure S6.1. B3LYP-HOMO maps of the transition states for the initial channels in the reaction of $O_2^1\Delta_g$ with aniline.

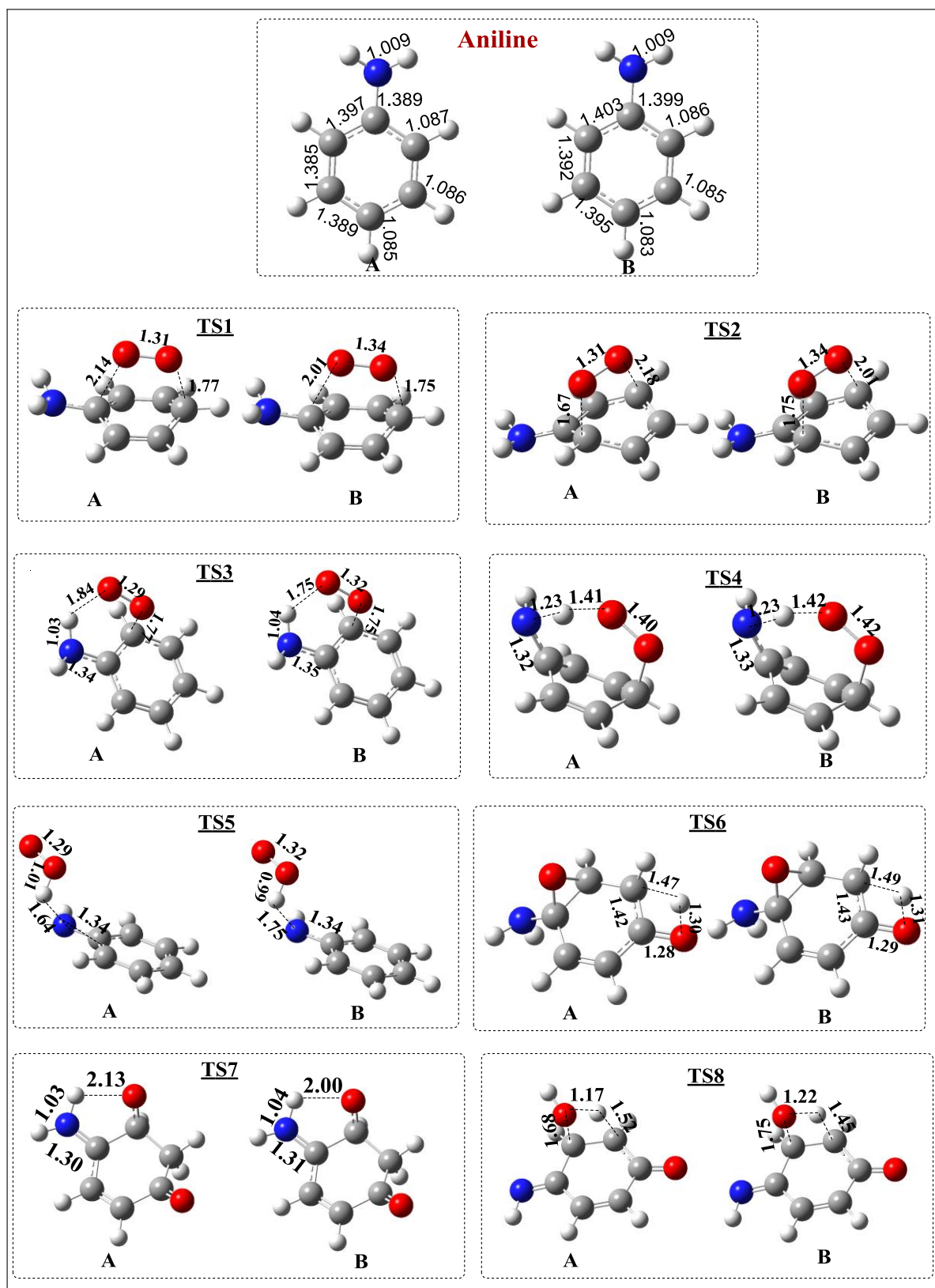


Figure S6.2. Optimised structures of transition states of aniline oxidation by singlet oxygen with A: M06 and B: B3LYP (distances are in Å).

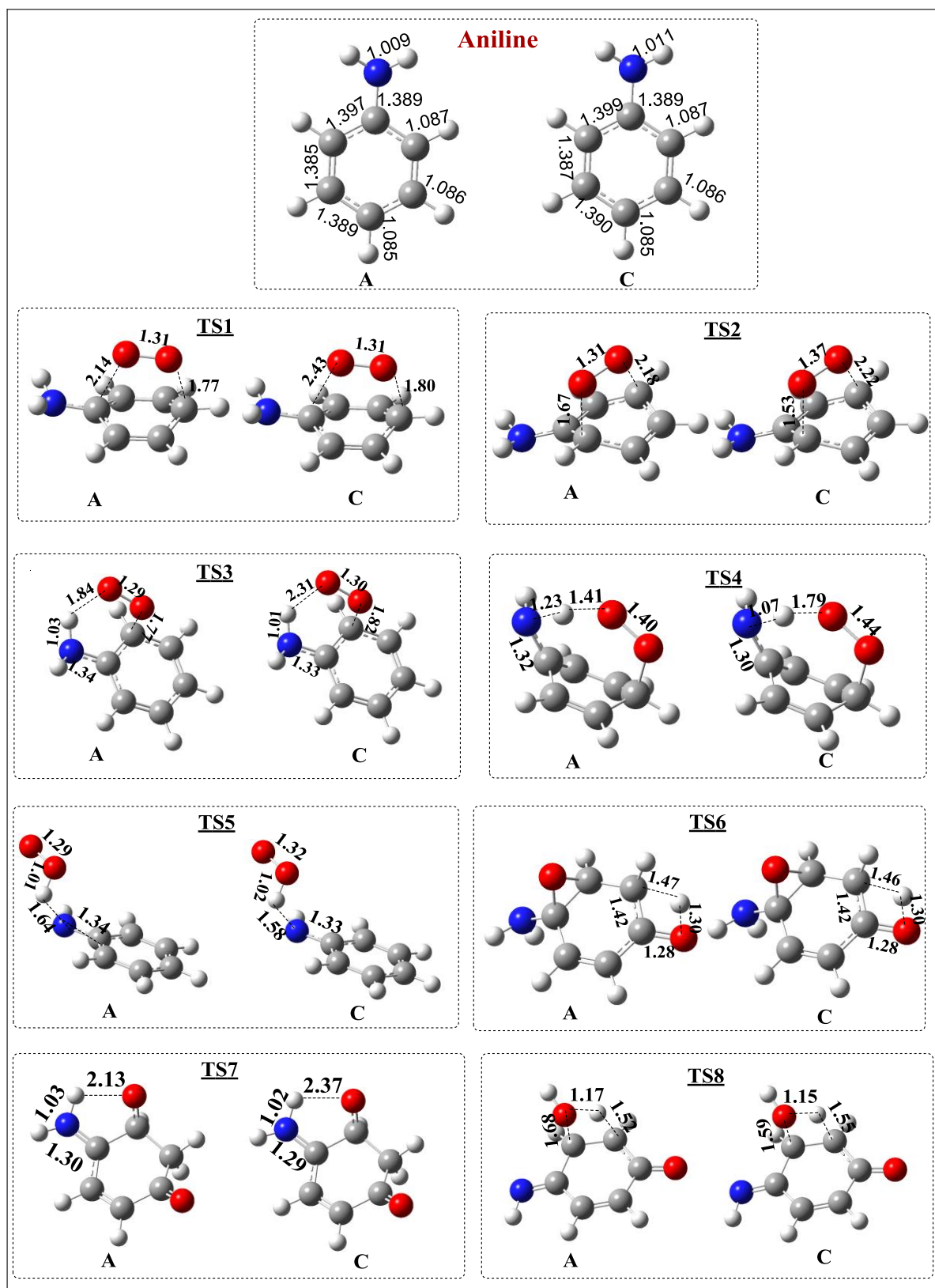


Figure S6.3. Optimised structures of transition states of aniline oxidation by singlet oxygen with A: M06/6-311+G(d,p) and C: M06/6-311+G(d,p) solvation (distances are in Å).

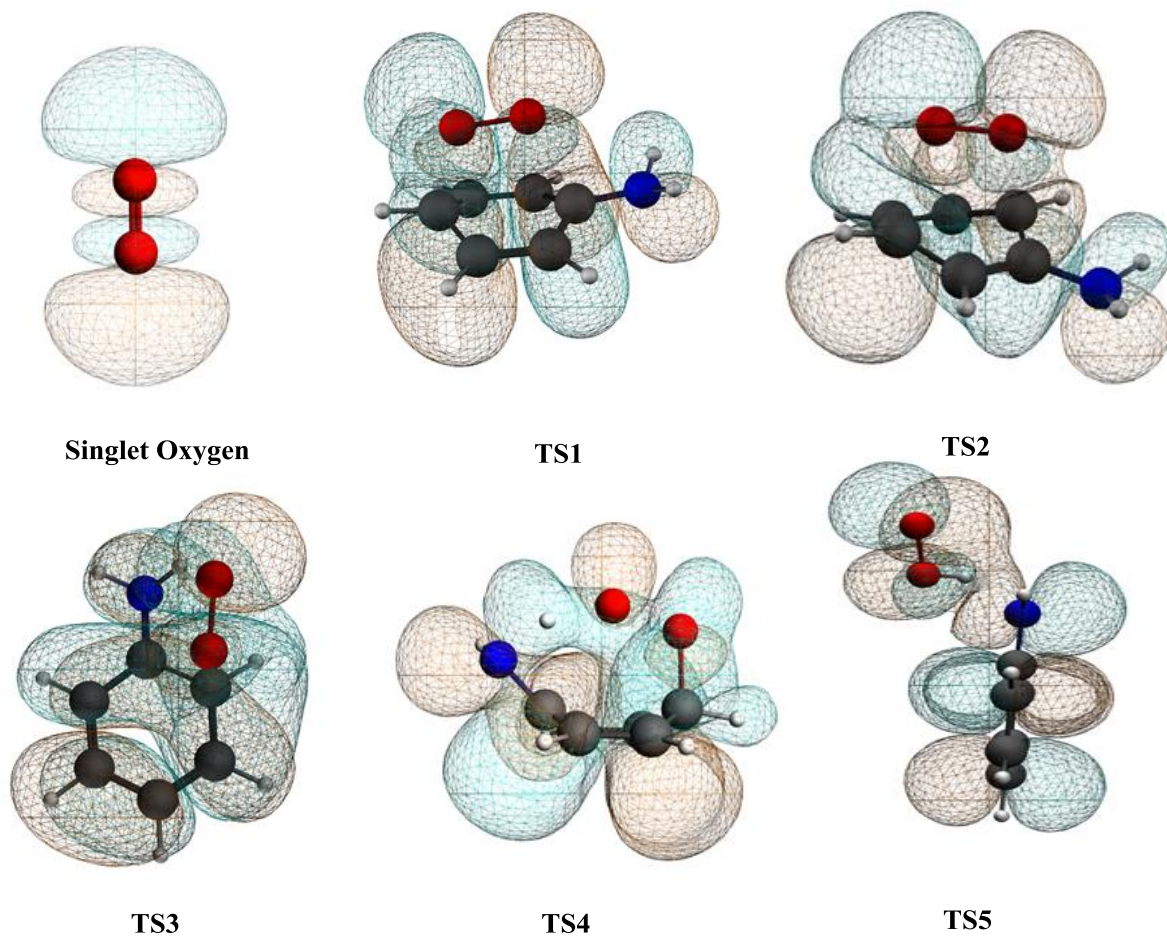


Figure S6.4. B3LYP (6-311+G(d,p))-LUMO maps of transition states for the initial channels in the reaction of $O_2\ ^1\Delta_g$ with aniline.

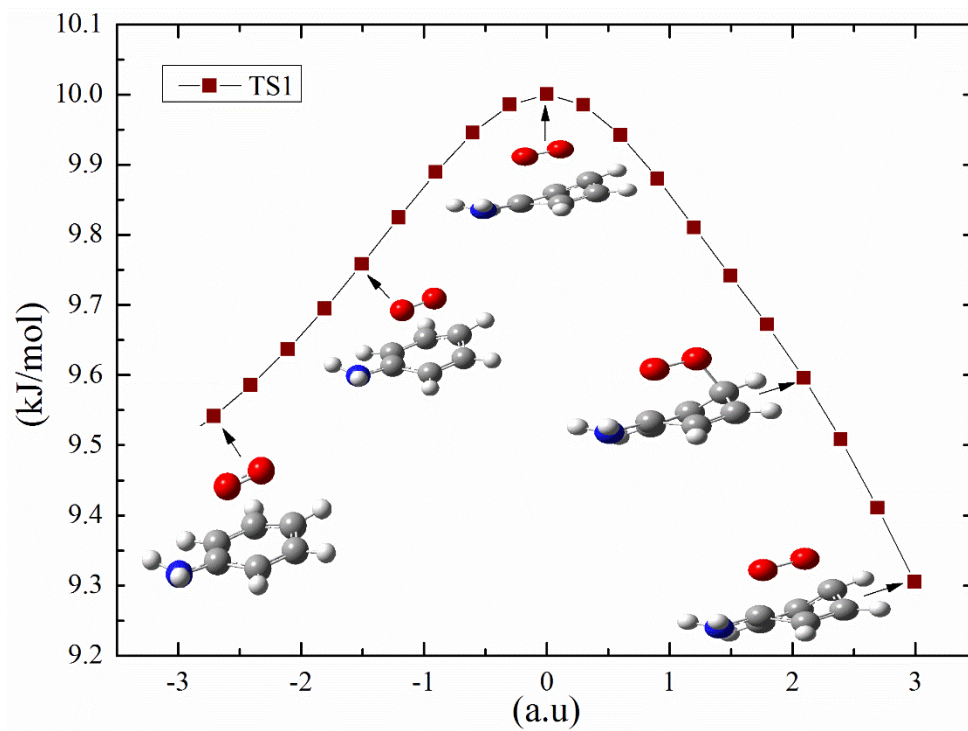


Figure S6.5. IRC calculation (M06/6-311+G(d,p)) for reaction pathway of aniline with singlet oxygen via TS1.

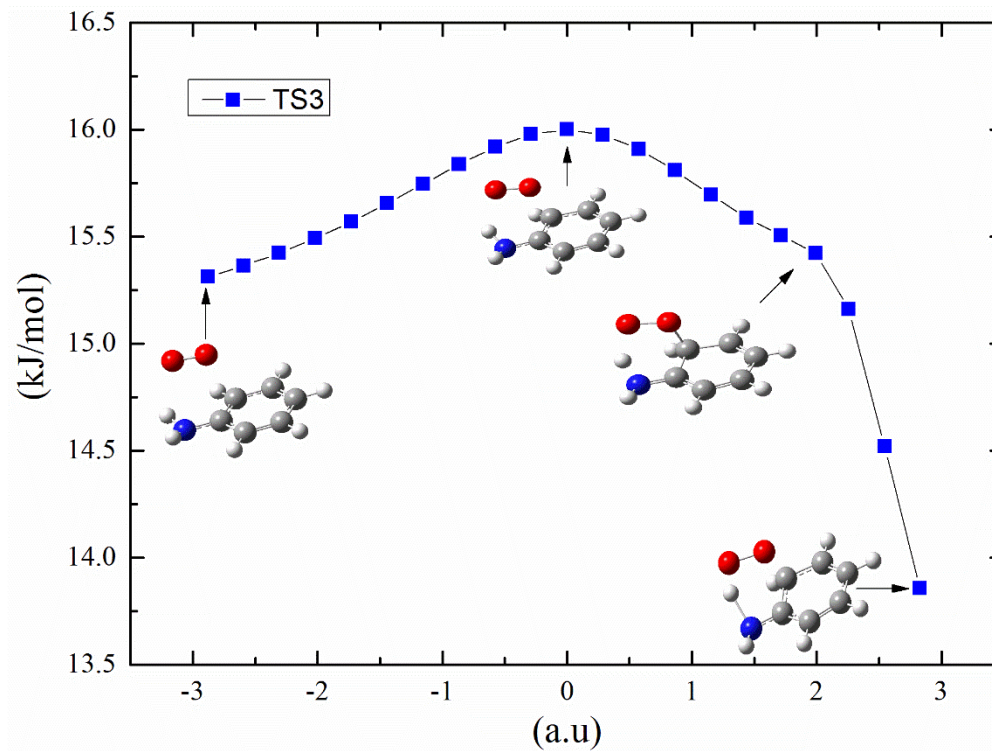


Figure S6.6. IRC calculation (M06/6-311+G(d,p)) for the reaction pathway of aniline with singlet oxygen via TS3.

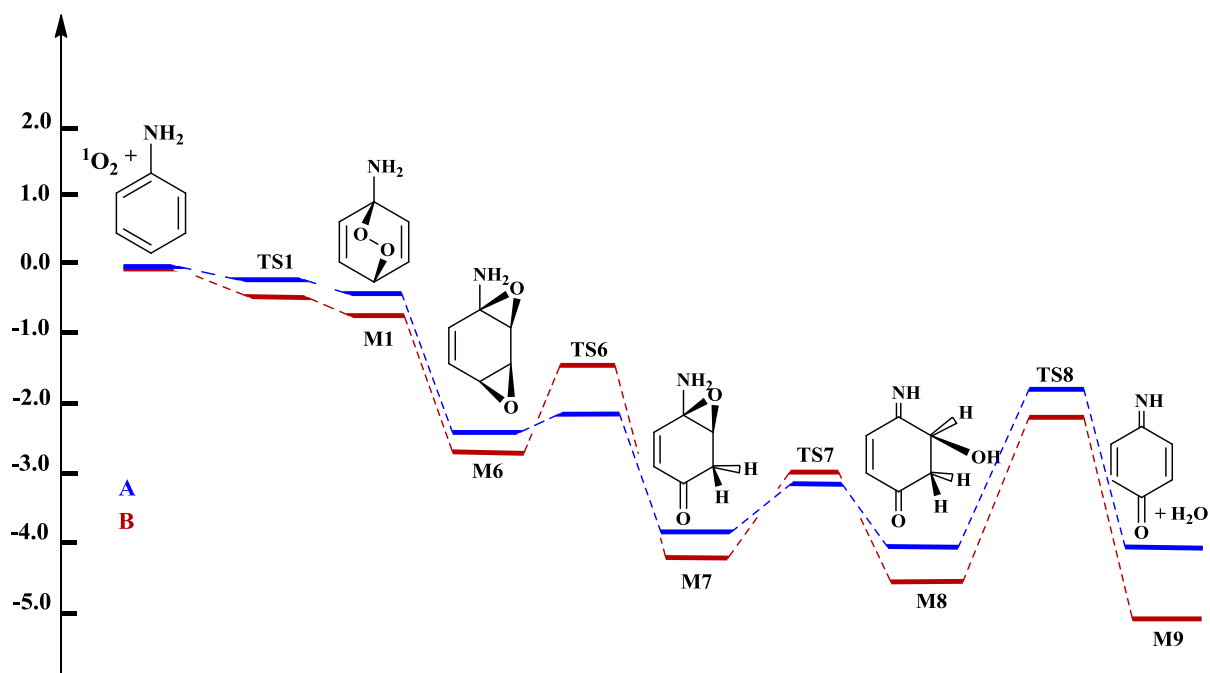


Figure S6.7. Enthalpy map (blue) and Gibbs free energy map (red) for the formation of *para*-iminobenzoquinone from the reaction of singlet oxygen with aniline using M06/6-311+G(d,p) (solvation) model. All values are in $\text{kJ/mol} \times 10^{-2}$ at 298.15

K.

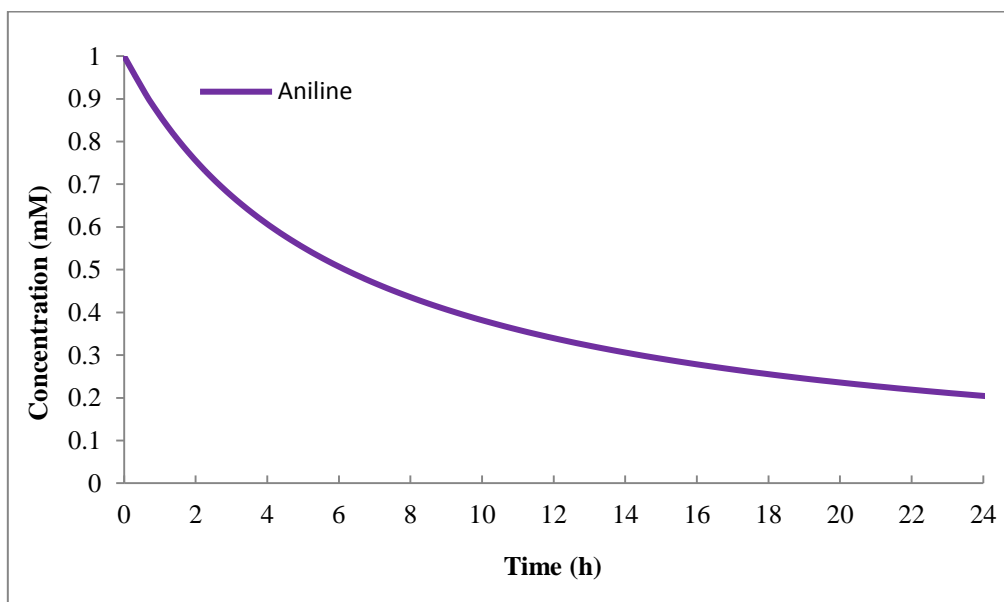


Figure S6.8. Concentration profile for aniline photoreaction with singlet oxygen via the water-solvation model- M06/6-311+G(d,p) at 313 K.



Cartesians Coordinates (M06/6-311+G(d,p), (solvation))

Aniline

0 1

C	-0.93488300	-0.00000300	-0.00854700
C	-0.22066400	1.20271200	-0.00505700
C	1.16585900	1.19695500	0.00336500
C	1.87318100	0.00000200	0.00705100
C	1.16586400	-1.19695100	0.00336500
C	-0.22066100	-1.20271400	-0.00506700
H	-0.76454400	2.14434800	-0.00885800
H	1.69990800	2.14304600	0.00873800
H	2.95829700	0.00000600	0.01492600
H	1.69991400	-2.14304200	0.00873500
H	-0.76453500	-2.14435400	-0.00888500
N	-2.32197700	-0.00001000	-0.07412900
H	-2.77368500	0.83799100	0.26668900
H	-2.77369500	-0.83792500	0.26688700

Oxygen (singlet)

0 1

O	0.00000000	0.00000000	0.59573200
O	0.00000000	0.00000000	-0.59573200

Oxygen (triplet)

0 3

O	0.00000000	0.00000000	0.59770900
O	0.00000000	0.00000000	-0.59770900

Oxygen (singlet-mix HOMO and LOMO orbitals)



0 1

O	0.00000000	0.00000000	0.59605300
O	0.00000000	0.00000000	-0.59605300

TS1

0 1

C	-0.53797000	1.23909200	-0.51265600
C	-1.18799000	0.00000000	-0.20370400
C	-0.53797000	-1.23909100	-0.51265800
C	0.77883900	-1.23142200	-0.81420100
C	1.49728300	0.00000100	-0.65957700
C	0.77883900	1.23142400	-0.81419800
H	-1.11565300	2.15704300	-0.46211500
H	-1.11565200	-2.15704200	-0.46211900
H	1.32077100	-2.15155100	-1.00055300
H	2.56017000	0.00000200	-0.87769500
H	1.32077000	2.15155400	-1.00054900
O	1.55575600	-0.00000200	1.14287800
O	0.35483700	-0.00000100	1.66880300
N	-2.45023300	-0.00000100	0.21800600
H	-2.92484600	0.86222400	0.44275300
H	-2.92484600	-0.86222500	0.44275100

TS2

0 1

C	-1.13955400	0.25437900	-0.20598200
C	-0.26703100	-0.89813100	-0.54956700
C	0.94345600	-0.55078100	-1.29949100
C	1.58515400	0.51835800	-0.81643600
C	0.91569300	1.30779900	0.20889000



C	-0.46700600	1.37157300	0.26657400
H	1.35965800	-1.22624900	-2.03627300
H	2.57726200	0.81187600	-1.14343500
H	1.50047400	2.05606400	0.73510100
H	-0.98142400	2.15027900	0.81950800
O	1.15457900	-0.55108200	1.39745600
O	0.10921000	-1.27282200	0.88694000
H	-0.81416900	-1.77072100	-0.90829700
N	-2.46007700	0.07739300	-0.15812000
H	-3.06517400	0.77043200	0.25791400
H	-2.89066700	-0.76138300	-0.51678100

TS3

0 1

H	-2.14955800	0.95088800	1.01873300
O	-2.35044100	-0.64178800	-0.63996800
O	-1.14154100	-1.12427000	-0.68168500
C	-0.22632300	0.78287800	0.37273400
C	0.85294500	1.38096100	-0.32930900
C	-0.14865800	-0.59721600	0.75406500
C	1.99248100	0.66841100	-0.53815900
H	0.75613800	2.40678500	-0.67080600
C	1.10764700	-1.26602800	0.60570100
H	-0.84154000	-0.95199800	1.51276000
C	2.12732900	-0.66966800	-0.06127700
H	2.82080400	1.12631500	-1.06899500
H	1.20783900	-2.27388300	0.99353200
H	3.06467900	-1.19338200	-0.21578500
N	-1.37098600	1.42223500	0.57793100
H	-1.55813100	2.31206200	0.13572900

**TS4**

0 1

C	1.67942900	-0.50791000	0.40443500
C	1.04295500	0.65038600	-0.23693000
C	0.32399700	0.38017200	-1.48726100
C	-0.54671900	-0.61244700	-1.36200400
C	-0.62896100	-1.21760500	0.00778000
C	0.77555000	-1.47978400	0.53586900
H	2.67828000	-0.49325600	0.82187300
H	0.42025100	1.04555600	-2.33691600
H	-1.25838200	-0.87778100	-2.13472300
H	-1.23887000	-2.12674900	0.01553000
H	0.98540300	-2.38897000	1.09016200
O	-1.20563700	-0.26565700	0.95866500
O	-1.75182900	0.95401000	0.41907900
N	0.76283400	1.74831400	0.39166700
H	1.13575800	1.85692400	1.33137200
H	-0.28006100	1.96237800	0.27775100

TS5

0 1

N	1.08252000	0.19071800	0.89233300
H	1.41169300	1.15864400	0.93545800
H	2.20466600	-0.63427400	0.14681300
O	2.72309500	-0.31313700	-0.66571800
O	3.89594500	0.12927800	-0.25415300
C	-0.17596300	0.12718800	0.45723800
C	-0.94463000	1.27739000	0.11368100
C	-0.78212700	-1.15753300	0.34534000



C	-2.24548600	1.13987700	-0.30175600
H	-0.48223800	2.25701300	0.19435300
C	-2.07987900	-1.27755000	-0.08891000
H	-0.18993400	-2.02618200	0.61615000
C	-2.81521400	-0.13368200	-0.40978100
H	-2.83332400	2.01571800	-0.55363100
H	-2.53879500	-2.25615700	-0.17594600
H	-3.84224300	-0.23305300	-0.74543400

TS6

0 1

C	0.52465800	-1.17237100	-0.16354100
C	1.24531800	0.09882500	-0.02393100
C	0.45601000	1.33397300	0.25511200
C	-0.88382000	1.35999500	0.29909600
C	-1.57452100	0.12947800	0.01042600
C	-0.95327400	-1.14200900	-0.10605600
H	1.01562500	-1.96131500	-0.73226600
H	1.02107700	2.25767400	0.36236800
H	-1.44489800	2.28006200	0.42361700
H	-2.25869400	-1.07084900	-0.76700700
H	-1.39985200	-1.87211400	0.57783800
O	-2.79959700	0.04002900	-0.36405600
O	1.23056800	-0.84538000	1.04731400
N	2.48397200	0.26098200	-0.68824300
H	2.38760300	0.21080500	-1.69591000
H	2.95733600	1.12432400	-0.44363500

TS7

0 1



C	-0.72278400	-0.96680100	0.38448800
C	-1.14826900	0.48085000	0.13259800
C	-0.24885900	1.61104400	0.15875900
C	1.06650600	1.38703200	0.05429800
C	1.61427200	0.00336100	-0.01364600
C	0.80357200	-1.02439100	0.69092100
H	-1.22058300	-1.18089500	1.37109300
H	-0.66091000	2.61665400	0.12886200
H	1.77149400	2.20390200	-0.06964600
H	0.96599200	-0.84235800	1.76363300
H	1.16928200	-2.02665100	0.45836600
O	2.65729300	-0.20289200	-0.59853400
O	-1.13679500	-1.74129200	-0.61777500
H	-2.93339200	-0.20125900	-0.36894900
N	-2.38011400	0.64213500	-0.22017300
H	-2.78170100	1.54256300	-0.45619500

TS8

0 1

C	-0.36580300	-1.49199200	0.39303400
C	-1.27304000	-0.51569600	-0.20837700
C	-0.71789300	0.86011200	-0.43703200
C	0.74606500	1.02641800	-0.48562800
C	1.60051500	-0.05657300	-0.11825800
C	0.95091800	-1.27209000	0.45034900
H	-0.80276100	-2.41981800	0.75561000
H	-1.30204800	1.40691200	-1.17669200
H	1.15185700	1.78111600	-1.15409300
H	0.19248500	1.74020000	0.77396100
H	1.62716400	-2.01371700	0.86755300



O	2.83273500	-0.04576500	-0.22383800
H	-1.47755400	2.42604300	0.84269600
O	-0.94484500	1.61682800	0.92964300
N	-2.48318700	-0.72867400	-0.54344300
H	-2.75453400	-1.68958400	-0.31589500

M1

0 1

C	-1.19142700	-0.24284500	0.00026500
C	-0.51543900	-0.48270500	1.22243900
C	0.80064000	-0.86119600	1.21512200
C	1.49398000	-0.97193400	0.00128500
C	0.80056100	-0.86452400	-1.21287600
C	-0.51559600	-0.48637800	-1.22123600
H	-1.05344400	-0.33938500	2.15505700
H	1.32654900	-1.01504200	2.15141000
H	2.54730200	-1.23001200	0.00159800
H	1.32645800	-1.02101000	-2.14873400
H	-1.05366400	-0.34591400	-2.15425300
N	-2.48171300	0.14481400	-0.00019800
H	-2.94453500	0.39474700	0.86007300
H	-2.94468600	0.39224300	-0.86111300
O	1.52978100	1.42400500	-0.00225400
O	0.33668200	1.77701500	-0.00182700

M2

0 1

C	-1.18334200	0.16707000	-0.18758300
C	-0.29534600	-1.00527200	0.16571400
C	0.76131500	-1.23716900	-0.87384700



C	1.47153800	-0.13678000	-1.09253000
C	0.99873700	1.01162700	-0.24021000
C	-0.46355000	1.27498100	-0.41540300
H	-0.84966400	-1.89694100	0.46631500
H	0.94811300	-2.21760800	-1.29475900
H	2.34482500	-0.06066000	-1.73014900
H	1.62369100	1.90300100	-0.30127000
H	-0.86272100	2.27171500	-0.55969900
O	1.21335400	0.55054200	1.14842400
O	0.39573700	-0.60923600	1.39376900
N	-2.53998100	0.01906900	-0.05480100
H	-3.11103500	0.78078300	-0.39622000
H	-2.92217800	-0.89095900	-0.27500100

M3

0 1

H	-2.50370500	0.62420300	-0.00130800
O	-2.67127500	-0.32071900	0.22526200
O	-1.54131300	-0.93548000	-0.39024900
C	-0.02747900	0.92838300	0.03242300
C	1.38316700	1.27990800	0.10979600
C	-0.37160100	-0.52572500	0.29302900
C	2.32584400	0.32456700	0.03563400
H	1.64490600	2.33445400	0.12457300
C	0.71805100	-1.49029800	-0.02983500
H	-0.56114100	-0.60565100	1.38303100
C	1.98768800	-1.08339100	-0.09705800
H	3.37526400	0.60369600	0.02870600
H	0.43543900	-2.53461400	-0.11756700
H	2.78854800	-1.79785500	-0.25456600



N	-0.98790700	1.73324300	-0.22333800
H	-0.65728800	2.69199200	-0.34353700

M4

0 1

C	1.03622700	-1.22997100	-0.06501700
C	1.76067700	0.03351600	0.10937200
C	0.99245700	1.26349600	-0.10053900
C	-0.28081200	1.24060700	-0.49013800
C	-1.00837700	-0.02867100	-0.77961400
C	-0.23794600	-1.26226100	-0.45088700
H	1.58138400	-2.14786700	0.14305500
H	1.51535400	2.19811600	0.08189900
H	-0.84267900	2.16011400	-0.63589500
H	-1.27195400	-0.05210200	-1.85080900
H	-0.76989700	-2.20356000	-0.56268800
O	-2.31190300	-0.04682100	-0.18843900
O	-2.16177100	-0.07327400	1.22970700
N	2.99535800	0.12455100	0.44527500
H	3.39846100	-0.80849500	0.56375100
H	-2.36213600	0.84241000	1.47455500

M5

0 2

C	-0.01099000	-1.80955200	0.00000000
C	-0.01186500	-1.10829700	1.19914800
C	-0.01186500	0.27931100	1.20734000
C	-0.00037700	0.98177500	0.00000000
C	-0.01186500	0.27931100	-1.20734000
C	-0.01186500	-1.10829700	-1.19914800



H	-0.01376300	-2.89463800	0.00000000
H	-0.01632800	-1.64438400	2.14352100
H	-0.01972100	0.82949400	2.14347000
H	-0.01972100	0.82949400	-2.14347000
H	-0.01632800	-1.64438400	-2.14352100
N	-0.06395300	2.38124300	0.00000000
H	0.88649500	2.77021900	0.00000000

M6

0 1

C	-0.81470300	1.56418000	0.00835900
C	-1.72530900	0.46695000	-0.37015700
C	-1.16847100	-0.88063500	-0.54950700
C	0.30179200	-1.07913200	-0.33853100
C	1.14841600	0.06815100	-0.00712400
C	0.49572100	1.38293200	0.17326400
H	-1.24374000	2.55521000	0.12465100
H	-2.62209500	0.74233900	-0.92141200
H	1.14168600	2.22161200	0.42292500
N	2.48605300	0.13744300	-0.44379700
H	3.06907300	0.65685000	0.20612600
H	2.89217400	-0.78166900	-0.58428900
O	0.79752100	-0.93110500	0.98060900
O	-1.94385500	-0.57407400	0.58594700
H	0.74647400	-1.89652700	-0.90769200
H	-1.63995000	-1.55315200	-1.26400200

M7

0 1

C	0.56363400	-1.14153300	-0.18799900
---	------------	-------------	-------------



C	1.25143200	0.13251800	-0.01580500
C	0.43195200	1.36689800	-0.02454000
C	-0.90201500	1.33868600	-0.02779700
C	-1.65781600	0.07955700	-0.06924900
C	-0.91028500	-1.17786500	-0.44457600
H	1.13615600	-1.97431600	-0.59940900
H	0.96729600	2.31378400	-0.01180100
H	-1.48995400	2.25064600	0.01485500
H	-1.08037900	-1.33072500	-1.51929200
H	-1.37946500	-2.02745200	0.06274800
O	-2.85682700	0.05331400	0.13890900
O	0.97481100	-0.73572700	1.11324500
N	2.58021900	0.31591700	-0.43295600
H	3.07847100	0.98004800	0.15211000
H	3.10106100	-0.55367500	-0.46595400

M8

0 1

C	-0.68385400	-0.98533800	0.27511800
C	-1.36414500	0.37608100	0.17150100
C	-0.50956400	1.50961700	-0.20159800
C	0.82357400	1.39722400	-0.25544400
C	1.53121000	0.16549700	0.11307000
C	0.71758900	-0.87480400	0.83046500
H	-1.30448000	-1.63004400	0.91029600
H	-1.01533600	2.43769300	-0.45223100
H	1.44541500	2.22721100	-0.58092200
H	0.65144400	-0.57891000	1.88607500
H	1.21356000	-1.84972400	0.79236000
O	-0.58201000	-1.51281700	-1.03846800



H	-1.46499700	-1.71561100	-1.36547100
O	-2.56664100	0.48500800	0.30804100
N	2.77495000	0.08818200	-0.15581600
H	3.15008700	-0.81507600	0.14536000

M9

0 1

C	1.16438100	-0.81065400	0.00000000
C	1.25771300	0.65185300	0.00000000
C	0.00000000	1.40778400	0.00000000
C	-1.18340000	0.78789600	0.00000000
C	-1.28032200	-0.68243400	0.00000000
C	-0.01641900	-1.43614800	0.00000000
H	2.10519900	-1.35322700	0.00000000
H	0.07097100	2.49281500	0.00000000
H	-2.12211700	1.33344700	0.00000000
H	-0.09845400	-2.51863300	0.00000000
O	-2.36294700	-1.24747600	0.00000000
N	2.42119000	1.18679800	0.00000000
H	2.34793100	2.20804200	0.00000000

M10

0 2

O	-1.72832500	-1.36666000	-0.15487300
C	-0.63918900	0.79292700	0.02703300
C	0.66248400	1.44505600	0.04905300
C	-0.62174500	-0.73960500	0.25183000
C	1.80344700	0.73857200	-0.00711200
H	0.66313000	2.53101900	0.05383900
C	0.68290400	-1.41784200	-0.02338500

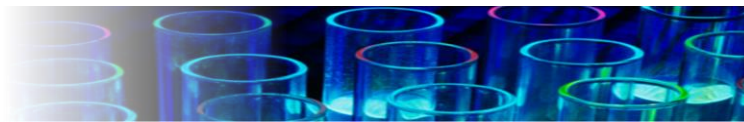


H	-0.71442300	-0.77004500	1.37826500
C	1.81469100	-0.71178500	-0.10080500
H	2.75605700	1.25946200	-0.02283300
H	0.66131300	-2.50040400	-0.10455200
H	2.76395100	-1.21289400	-0.26184000
N	-1.71434700	1.45216200	-0.12351800
H	-2.51854200	0.81707100	-0.11895400

M11

0 1

O	1.63102600	-1.49479200	0.00016200
C	0.69442200	0.70889600	-0.00003200
C	-0.56132300	1.45413300	-0.00002500
C	0.62117500	-0.81877200	-0.00041300
C	-1.74028900	0.81716100	-0.00000200
H	-0.50120200	2.53936900	0.00001900
C	-0.71439500	-1.40767600	-0.00000300
C	-1.81292600	-0.63412600	0.00007500
H	-2.66889300	1.37827600	0.00006400
H	-0.77149500	-2.49139600	0.00013800
H	-2.79723900	-1.09304300	0.00023500
N	1.85560800	1.23574100	0.00006600
H	1.78137800	2.25725600	0.00018800



Appendix IV: Supporting Information for Chapter 7

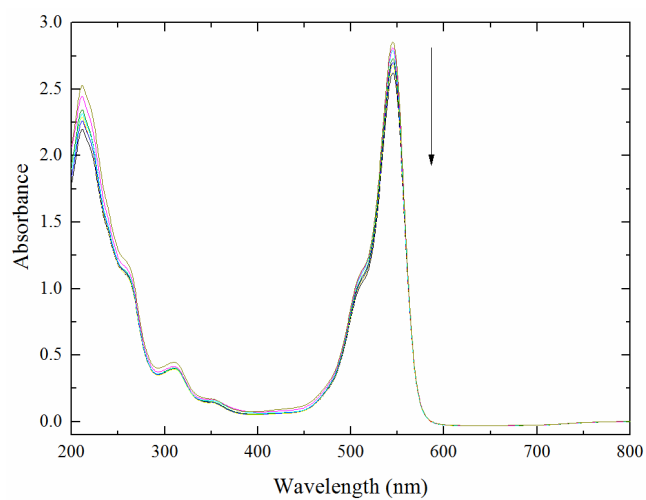


Figure S7.1. The time-course absorbance decay of rose bengal bleaching after illuminating for 0 - 24 h. Note that the results show minor bleaching of rose bengal over 24-h experiments.

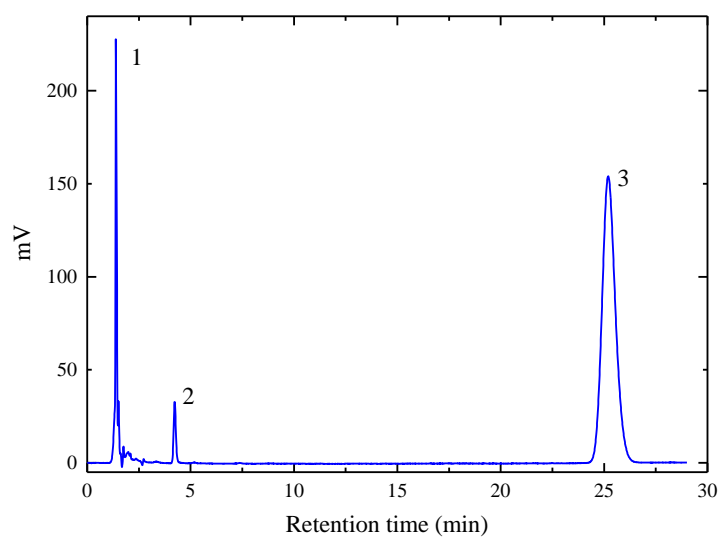


Figure S7.2. HPLC spectrum of (35 μ M RB, 1 mM phenol) illuminated sample in buffered solution (pH 6.2); 1: rose bengal, 2: para-benzoquinone, 3: phenol.

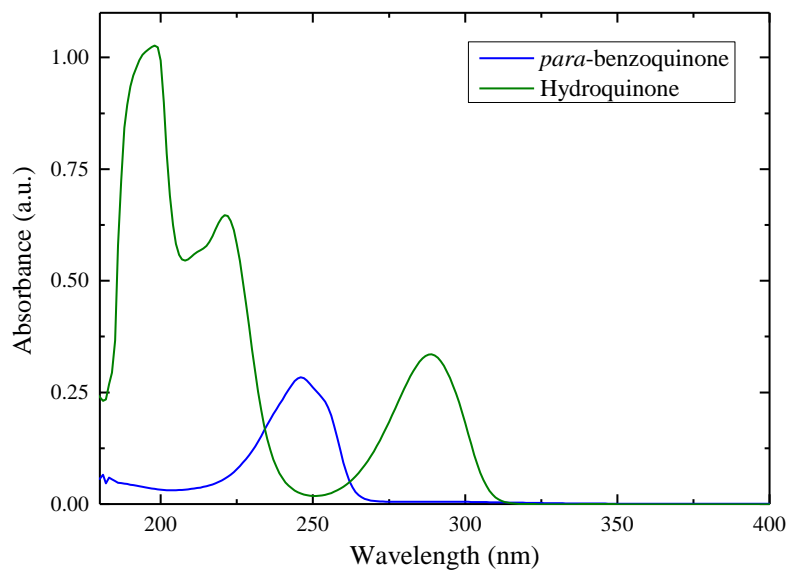
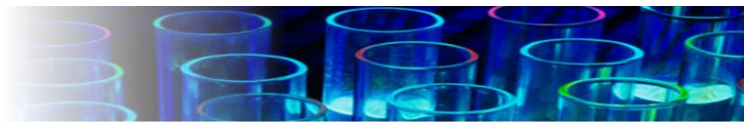


Figure S7.3. para-Benzoquinone (50 μM) and hydroquinone (50 μM) in 10 mM phosphate buffer solution (blank).

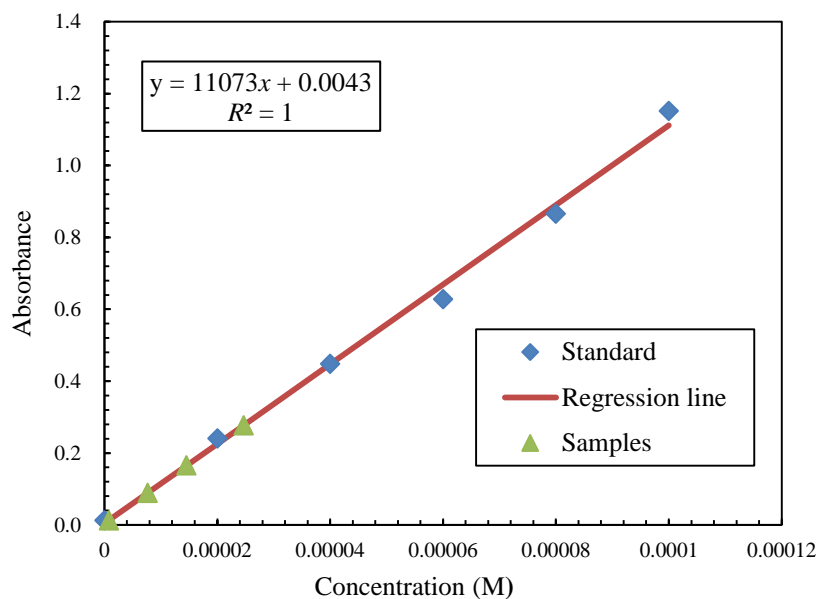


Figure S7.4. The absorbance values at 510 nm for ferrioxalate ($\text{K}_3\text{Fe}(\text{C}_2\text{O}_4)_3 \cdot 3\text{H}_2\text{O}$) standards (y-axis) at different concentrations (x-axis).

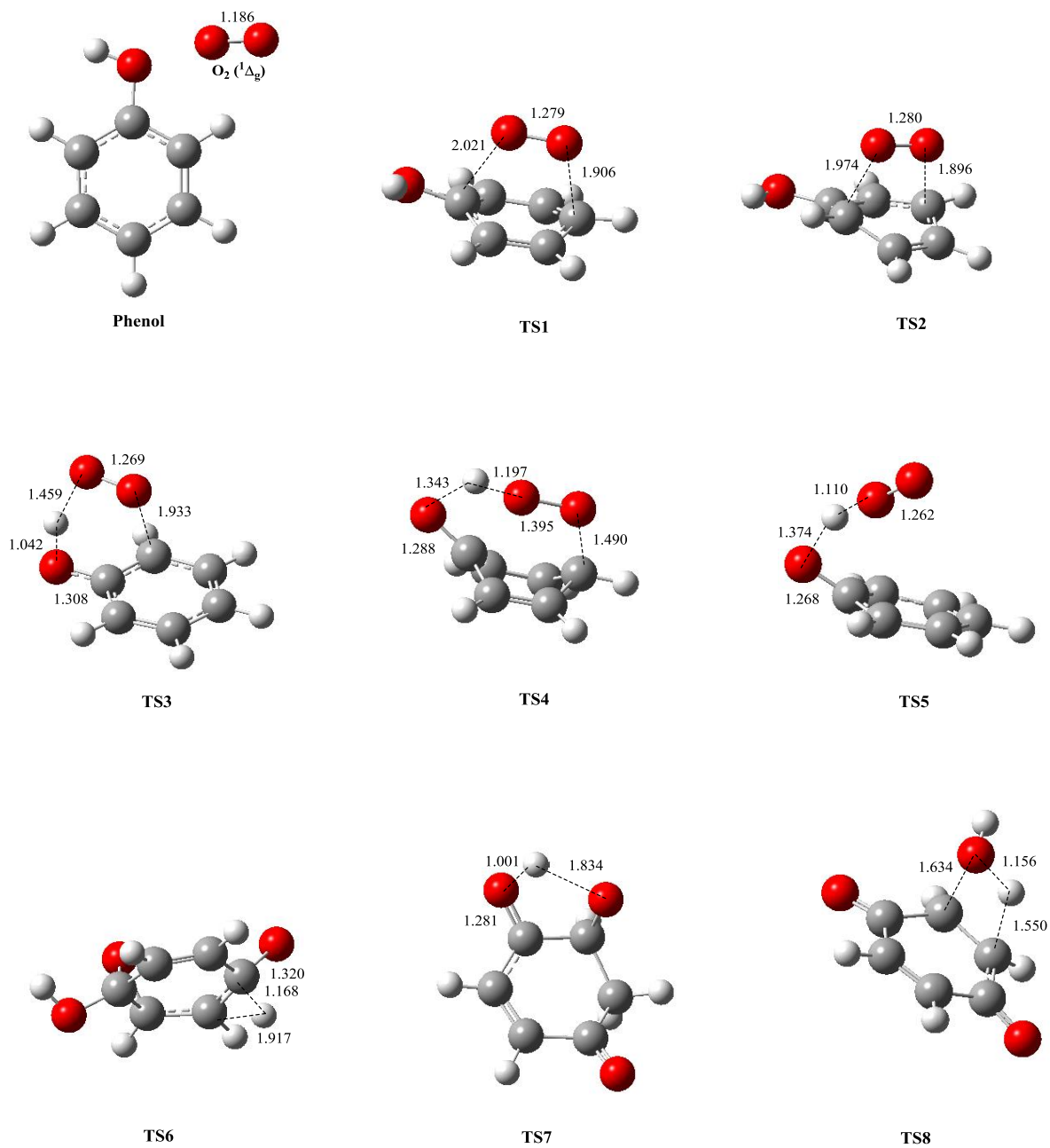


Figure S7.5. Optimised structures of transition states of phenol oxidation by singlet oxygen with M062X (distances are in Å).

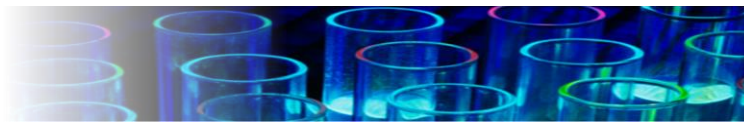
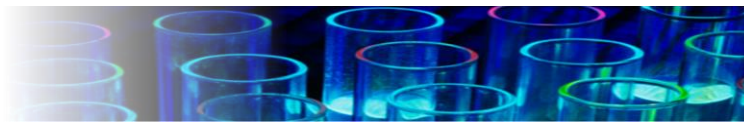


Table S7.1. Ordinary differential equations (ODEs) and parameters for the estimated singlet oxygen concentration profile at 298.15 K, as coded in the POLYMATH software [1]

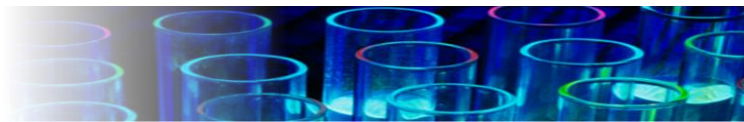
	Variable	Polymath Equation
Explicit Equations ($M^{-1} s^{-1}/L E^{-1}$ or s^{-1})	k_v	$k_v = 1 \times 10^{10}$
	k_b	$k_b = 0.856$
	k°	$k^\circ = 6.5 \times 10^3$
	k_t	$k_t = 1.2 \times 10^9$
	k_d	$k_d = 5 \times 10^5$
	k_{isc}	$k_{isc} = 1 \times 10^9$
Integration Variables ($M/L E^{-1} s^{-1}$)	${}^1\text{RB}$	${}^1\text{RB}(0) = 3.5 \times 10^{-5}$
	$h\nu(0)$	$h\nu(0) = 32.75 \times 10^{-5}$
	Oxygen	Oxygen(0) = 3.9×10^{-5}
	${}^1\text{RB}^*$	${}^1\text{RB}^*(0) = 0$
	${}^3\text{RB}^*$	${}^3\text{RB}^*(0) = 0$
	RB_b	$\text{RB}_b(0) = 0$
	Singlet oxygen	Singlet oxygen(0) = 0
ODE Equations	$d({}^1\text{RB})/d(t)$	$d({}^1\text{RB})/d(t) = -k_v \times {}^1\text{RB} \times h\nu - k_b \times {}^1\text{RB} \times h\nu + k_t \times {}^3\text{RB}^* \times \text{Oxygen} + k^\circ \times {}^3\text{RB}^*$
	$d(\text{SingletOxygen})/d(t)$	$d(\text{SingletOxygen})/d(t) = k_t \times {}^3\text{RB}^* \times \text{Oxygen} - k_d \times \text{SingletOxygen}$
	$d(h\nu)/d(t)$	$d(h\nu)/d(t) = 0$
	$d(\text{RB}_b)/d(t)$	$d(\text{RB}_b)/d(t) = k_b \times {}^1\text{RB} \times h\nu$
	$d(\text{Oxygen})/d(t)$	$d(\text{Oxygen})/d(t) = 0$
	$d({}^1\text{RB}^*)/d(t)$	$d({}^1\text{RB}^*)/d(t) = k_v \times {}^1\text{RB} \times h\nu - k_{isc} \times {}^1\text{RB}^*$
	$d({}^3\text{RB}^*)/d(t)$	$d({}^3\text{RB}^*)/d(t) = k_{isc} \times {}^1\text{RB}^* - k^\circ \times {}^3\text{RB}^* - k_t \times {}^3\text{RB}^* \times \text{Oxygen}$
Independent Variable (s)	t	$t(0) = 0 ; t(f) = 10800$



Shacham, M.; Cutlip, M. B; Elly M. POLYMATH, <http://www.polymath-software.com/>,
date of access: 23/2/2016.

Table S7.2. POLYMATH ordinary differential equations (ODEs) and parameters for the solvation model at 298.15 K. The rate constants k_1 to k_8 come from Table 7.1 in Chapter 7

	Variable	Polymath Equation
Explicit Equations ($M^{-1} s^{-1}/L$ E^{-1} or s^{-1})	k_v	$k_v = 1 \times 10^{10}$
	k_b	$k_b = 0.856$
	k°	$k^\circ = 6.5 \times 10^3$
	k_t	$k_t = 1.2 \times 10^9$
	k_d	$k_d = 5 \times 10^5$
	k_{isc}	$k_{isc} = 1 \times 10^9$
	k_1	$k_1 = 1.21 \times 10^4$
	k_6	$k_6 = 1.62 \times 10^{-2}$
	k_7	$k_7 = 2.91 \times 10^{-3}$
k_8	$k_8 = 3.47 \times 10^{-2}$	
Integration Variables ($M/L E^{-1} s^{-1}$)	${}^1\text{RB}$	${}^1\text{RB}(0) = 3.5 \times 10^{-5}$
	$h\nu(0)$	$h\nu(0) = 1.157 \times 10^{-9}$
	Oxygen	Oxygen(0) = 3.9×10^{-5}
	${}^1\text{RB}^*$	${}^1\text{RB}^*(0) = 0$
	${}^3\text{RB}^*$	${}^3\text{RB}^*(0) = 0$
	RB_b	$\text{RB}_b(0) = 0$
	Singlet oxygen	Singlet oxygen(0) = 0
	Phenol	Phenol(0) = 1×10^{-3}
	M_6	$M_6(0) = 0$
M_7	$M_7(0) = 0$	
M_8	$M_8(0) = 0$	



	$M9$	$M9(0) = 0$
ODE Equations	$d(^1RB)/d(t)$	$d(^1RB)/d(t) = -k_v \times ^1RB \times hv - k_b \times ^1RB \times hv + k_t \times ^3RB^* \times \text{Oxygen} + k^\circ \times ^3RB^*$
	$d(\text{SingletOxygen})/d(t)$	$d(\text{SingletOxygen})/d(t) = k_t \times ^3RB^* \times \text{Oxygen} - k_d \times \text{SingletOxygen} - k_1 \times \text{Phenol} \times \text{Oxygen} - k_q \times \text{Phenol} \times \text{Oxygen}$
	$d(hv)/d(t)$	$d(hv)/d(t) = 0$
	$d(RB_b)/d(t)$	$d(RB_b)/d(t) = k_b \times ^1RB \times hv$
	$d(\text{Oxygen})/d(t)$	$d(\text{Oxygen})/d(t) = 0$
	$d(^1RB^*)/d(t)$	$d(^1RB^*)/d(t) = k_v \times ^1RB \times hv - k_{isc} \times ^1RB^*$
	$d(^3RB^*)/d(t)$	$d(^3RB^*)/d(t) = k_{isc} \times ^1RB^* - k^\circ \times ^3RB^* - k_t \times ^3RB^* \times \text{Oxygen}$
	$d(\text{Phenol})/d(t)$	$d(\text{Phenol})/d(t) = -k_1 \times \text{Phenol} \times \text{Oxygen}$
	$d(M6)/d(t)$	$d(M6)/d(t) = k_1 \times \text{Phenol} \times \text{SingletOxygen} - k_6 \times M6$
	$d(M7)/d(t)$	$d(M7)/d(t) = k_6 \times M6 - k_7 \times M7$
	$d(M8)/d(t)$	$d(M8)/d(t) = k_7 \times M7 - k_8 \times M8$
	$d(M9)/d(t)$	$d(M9)/d(t) = k_8 \times M8$
Independent Variable (s)	t	$t(0) = 0 ; t(f) = 3000$



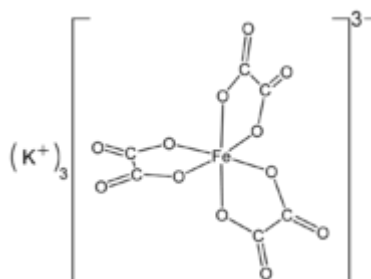
Actinometry Experiment

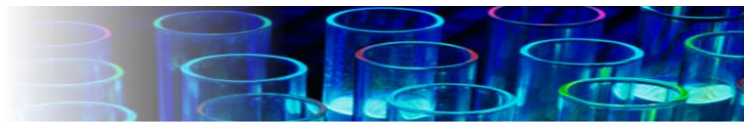
Materials:

1. Ferrous sulfate heptahydrate ($\text{FeSO}_4 \cdot 7\text{H}_2\text{O}$)
2. 1,10-phenanthroline monohydrate
3. Sulfuric acid-98% (H_2SO_4)
4. Ferric chloride (FeCl_3)
5. Potassium oxalate ($\text{K}_2\text{C}_2\text{O}_4 \cdot \text{H}_2\text{O}$)
6. Sodium acetate (CH_3COONa)
7. DI water
8. Heat gun
9. Thermometer
10. Vacuum filtration system

Procedure:

- Phase 1: Preparation of ferrioxalate crystals.

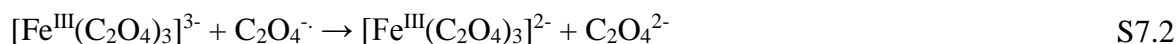
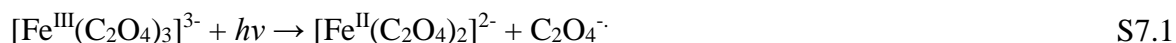


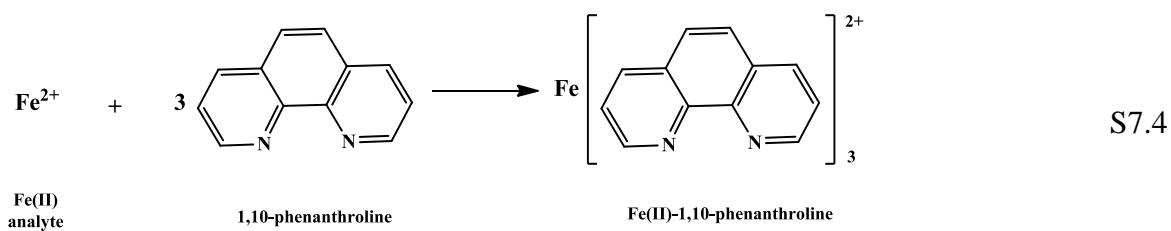
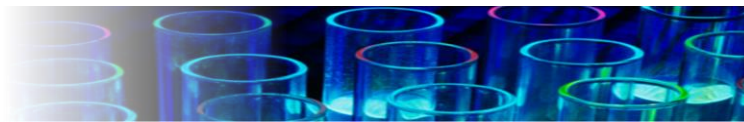


Ferrioxalate ferrioxalate ($\text{K}_3\text{Fe}(\text{C}_2\text{O}_4)_3 \cdot 3\text{H}_2\text{O}$) was prepared in the dark room by mixing three volumes of 1.5 M potassium oxalate ($\text{K}_2\text{C}_2\text{O}_4$) with one volume of 1.5 M ferric chloride (FeCl_3) in a 2L beaker. Solution of 1.5 M $\text{K}_2\text{C}_2\text{O}_4$ was made by introducing 139.58 g $\text{K}_2\text{C}_2\text{O}_4 \cdot \text{H}_2\text{O}$ in a 500 mL flask and filling the flask up to the mark with DI-water. Solution of 1.5 M FeCl_3 was prepared by the same way except for adding 101.37 g FeCl_3 . The solution was mixed under magnetic stirring in a stream of warm air by a heat gun. The solution temperature was monitored by a thermometer and controlled to be around 45° C by adjusting the wind speed and the distance between the heat gun and the beaker. The solution recrystallised three times in an ice bath. Between each recrystallisation, we washed the crystals with 600 mL water and then separated them using a vacuum filtration system. The resulting $\text{K}_3\text{Fe}(\text{C}_2\text{O}_4)_3 \cdot 3\text{H}_2\text{O}$ crystals appeared neon green in colour and were stored in an amber vial.

- **Phase 2: Photoreaction of potassium ferrioxalate.**

Exposure of potassium ferrioxalate ($\text{K}_3\text{Fe}(\text{C}_2\text{O}_4)_3 \cdot 3\text{H}_2\text{O}$) to green LEDs light results in the following reactions:



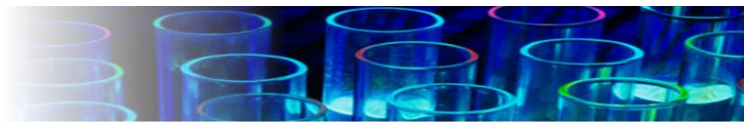


To prepare 0.15 M ferrioxalate solution for photolysis, we dissolved 7.368 g of the potassium ferrioxalate crystals in around 400 mL of DI-water in a 500mL flask. A volume of 50 mL 1N sulfuric acid is added and then diluted by DI-water by filling the beaker to the mark. For photolysis, in a photochemical reactor, 5 mL (V_1) solution was exposed to light generated by 24 LEDs. Dark control sample (blank) was processed exactly as the irradiated samples except covering it with aluminium foil. To produce sufficient ferrous iron, we irradiated the solution for 50 min.

For analysis, 2 mL (V_2) solution was taken from the reactor tube and mixed with buffer solution equal to $V_B = (V_2/2)$ to prevent solid precipitation, then 2 mL 0.1 wt % 1,10-phenanthroline was added in 50 mL (V_3) volumetric flasks and made up to the mark by adding DI-water. After around 30 min, the complex of ferrous iron and 1,10-phenanthroline was fully developed and ready for analysis. The complex concentration was determined on a UV-visible spectrophotometer at 510 nm using the calibration curve prepared in phase 3 below, see Figure S3.

- **Phase 3: Calibration curve**

Three solutions are needed to prepare the necessary standards for the calibration curve.



1. A buffer solution was made by mixing 600 mL 1 N Sodium acetate (CH_3COONa) (48.01 g) and 360 mL 1 N H_2SO_4 in a 1 L volumetric flask and diluted by DI-water until the level reaches the L-liter mark. Solution of 1 N H_2SO_4 was made by diluting 27.17 mL pure (98 %) sulfuric acid to 1 L by water.
2. Solution of 0.1 wt % 1,10-phenanthroline was prepared by adding 109.987 mg of 1,10-phenanthroline monohydrate to 100 mL by DI-water and stored in the dark.
3. Solution of 0.4 mM ferrous iron in 0.1 N H_2SO_4 was made freshly by diluting 0.1 M FeSO_4 in 0.1 N H_2SO_4 . For this, 2 mL 0.1 M FeSO_4 in 0.1 N H_2SO_4 was mixed with 50 mL 1 N H_2SO_4 and diluted to 500 mL by DI-water. Solution of 0.1 M FeSO_4 in 0.1 N H_2SO_4 was prepared by mixing 13.901 g $\text{FeSO}_4 \cdot 7\text{H}_2\text{O}$ and 50 mL 1 N H_2SO_4 in a 500 mL volumetric flask and filling the flask with DI-water to the mark.

Volume (X) 0, 1.25, 2.5, 3.75, 5, 6.25 mL of 0.4 mM FeSO_4 were added to a series of 25 mL volumetric flasks and mixed with (12.5-X) mL 0.1 N H_2SO_4 and 6.25 mL buffer solution. The resulting concentrations of ferrous iron ranged from 0 to 0.1 mM. We added 2.5 mL 0.1 wt % 1,10-phenanthroline monohydrate to the volumetric flasks and left the solution to sit for a least 30 min to let the complex of ferrous iron and 1,10-phenanthroline develop fully. Standard solutions were analysed on a UV-Vis spectrophotometer at 510 nm and the standard curve was prepared by plotting the absorbance at 510 nm of each solution against the concentration; see Figure 7.3 in Chapter 7.

**Cartesian Coordinates of Figure S5 structures (M06/6-311+G(d,p), (solvation))****Phenol**

0 1

C	0.88628766	0.23411371	0.00000000
C	-0.49825534	0.19871571	0.00005100
C	-1.21339734	1.39037471	0.00002500
C	-0.54350034	2.60791071	-0.00003500
C	0.84404266	2.62858571	0.00001000
C	1.56736666	1.44535171	0.00001000
H	1.43892466	-0.69615129	-0.00000100
H	-1.04147134	-0.73612829	0.00013600
H	-1.10733534	3.53369471	-0.00016600
H	1.35942166	3.57991771	0.00001900
H	2.64795066	1.46560871	0.00001300
O	-2.57061234	1.30561671	-0.00018200
H	-2.95388034	2.18554671	0.00129000

Oxygen (singlet)

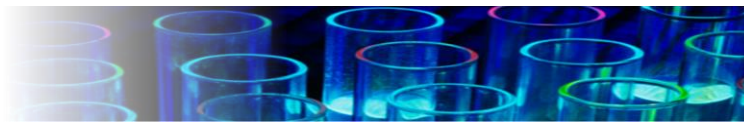
0 1

O	0.00000000	0.00000000	0.59573200
O	0.00000000	0.00000000	-0.59573200

Oxygen (triplet)

0 3

O	0.00000000	0.00000000	0.59770900
---	------------	------------	------------



O 0.00000000 0.00000000 -0.59770900

Oxygen (singlet-mix HOMO and LOMO orbitals)

0 1

O 0.00000000 0.00000000 0.59605300

O 0.00000000 0.00000000 -0.59605300

TS1

0 1

C -1.45484956 0.98662206 0.00000000

C -2.09378956 -0.26719894 0.23471200

C -1.48166656 -1.47698894 -0.20627000

C -0.13389056 -1.48007594 -0.30280300

C 0.54771944 -0.27675594 0.05374200

C -0.10899456 0.97733606 -0.11413800

H -2.04760056 1.88720806 0.06870600

H -2.07976056 -2.37427994 -0.30009600

H 0.42457444 -2.38771894 -0.47825400

H 1.62706544 -0.29371994 0.10767100

H 0.46602944 1.89088306 -0.14648500

O 0.09077044 -0.47328794 1.89419600

O -1.17838456 -0.40013494 2.03185000

H -3.71957256 -1.09788894 0.75616800

O -3.39446056 -0.21846794 0.54252200

TS2



0 1

C	1.77257532	0.68561872	0.00000000
C	2.53521132	-0.53599728	-0.02442300
C	3.78340932	-0.56568228	-0.69899800
C	4.48988332	0.58524772	-0.64983900
C	3.86245732	1.72298872	-0.03085900
C	2.45940032	1.85649472	-0.03282500
H	4.21632432	-1.50440728	-1.01002200
H	5.52952732	0.63866072	-0.93817100
H	4.46575332	2.60412272	0.13864700
H	1.97281432	2.79714272	0.17478300
O	4.08304832	0.73863572	1.66405700
O	3.14464632	-0.12928428	1.72465200
H	1.99894832	-1.46405828	0.13840800
O	0.44347932	0.66873872	0.21458000
H	0.11091332	-0.23172028	0.22136500

TS3

0 1

H	-2.09277500	0.71122200	0.19344900
O	-2.38636800	-0.51988300	-0.53244400
O	-1.21477600	-0.94352200	-0.77600800
C	-0.22515400	0.72469500	0.41051500
C	0.83491100	1.38564800	-0.25732000
C	-0.09136100	-0.64635200	0.76830200



C	1.99158200	0.71085200	-0.50196100
H	0.69150200	2.41683900	-0.54666500
C	1.14457900	-1.30525200	0.52366500
H	-0.81996000	-1.07900800	1.43826900
C	2.14692600	-0.65160900	-0.12072800
H	2.81003700	1.21258500	-1.00106700
H	1.26373800	-2.33149500	0.84141400
H	3.08012800	-1.15507500	-0.33199400
O	-1.36655300	1.32803500	0.61742300

TS4

0 1

C	-2.20735795	0.68561872	0.00000000
C	-2.87708995	1.88492772	-0.59178300
C	-2.20473195	3.17215972	-0.22587400
C	-0.88547195	3.11507272	-0.39428600
C	-0.33673095	1.80131972	-0.90740900
C	-0.88948595	0.64561472	-0.12546400
H	-2.84068295	-0.10935428	0.36787500
H	-2.77392895	4.05195772	0.03740500
H	-0.22872695	3.96314672	-0.26735600
H	0.74231705	1.79372172	-1.02096600
H	-0.26946295	-0.19779228	0.14320500
O	-0.82687795	1.54940972	-2.29122700
O	-2.18167595	1.87845972	-2.25153100



H	-3.23159395	1.31949272	-2.11446400
O	-4.04032895	1.71175272	-1.11696400

TS5

0 1

C	-2.44147167	0.98662206	0.00000000
C	-2.59093467	2.23633806	-0.72325000
C	-1.51957767	2.66769906	-1.56380400
C	-0.52638367	1.78664206	-1.84255000
C	-0.45766867	0.49495206	-1.22453200
C	-1.34773267	0.14300206	-0.25551200
H	-3.11959367	0.80487106	0.82191700
H	-1.60817667	3.62216106	-2.06266800
H	0.23466333	2.05109506	-2.56552900
H	0.35156433	-0.16893494	-1.49513900
H	-1.25752967	-0.79755394	0.26954900
O	-3.61786267	0.13892006	-2.48675500
O	-3.99020067	0.39111906	-1.30787600
H	-4.18357267	1.47437806	-1.16045500
O	-3.75857767	2.72725006	-0.78866400

TS6

0 1

C	-1.10367898	0.28428093	0.00000000
C	-0.38580998	1.60335693	0.24041200



C	-1.12793098	2.88869893	0.20728300
C	-2.45611298	2.89423793	0.18466100
C	-3.25024198	1.64014193	-0.06310200
C	-2.50104698	0.43223593	-0.31776100
H	-0.52686298	-0.56096007	-0.35176700
H	-0.53649798	3.79520793	0.25455700
H	-3.02666198	3.81147593	0.24937900
H	-3.49210998	1.82402693	-1.18868300
H	-3.06842798	-0.37753407	-0.76048500
O	-4.29768998	1.32311293	0.67526700
O	-0.71615698	0.75995493	1.29073100
H	1.44268002	2.11866093	0.48550500
O	0.92504902	1.60770993	-0.14602200

TS7

0 1

C	-1.25418065	0.25083612	0.00000000
C	-1.65896065	1.67862212	-0.20882600
C	-0.76979765	2.81160812	-0.27929800
C	0.53941435	2.56829012	-0.40047900
C	1.09963235	1.17509012	-0.41724700
C	0.26248635	0.09983212	0.21558900
H	-1.76384465	-0.13894088	0.90562900
H	-1.19939165	3.80153612	-0.36605300
H	1.25192735	3.36278812	-0.58603600



H	0.49235435	0.14287012	1.28622700
H	0.57633835	-0.87049388	-0.16245100
O	2.19236235	1.00248112	-0.88766700
O	-1.74940665	-0.21359088	-1.17420800
H	-3.13907565	0.92633912	-0.80736400
O	-2.88567665	1.86078812	-0.52875300

TS8

0 1

C	-0.68561876	0.83612039	0.00000000
C	-1.63471776	1.79557939	-0.59034300
C	-1.11635676	3.20320539	-0.84395500
C	0.31683324	3.44765739	-0.84855900
C	1.22109424	2.38311339	-0.47144800
C	0.61478224	1.11719539	0.06819400
H	-1.10427376	-0.10562361	0.33086100
H	-1.73749076	3.72086639	-1.56839300
H	0.71471724	4.21447639	-1.49939000
H	-0.31629976	4.10463939	0.40487500
H	1.33111124	0.41233839	0.47264700
O	2.43224124	2.44528339	-0.55562100
O	-2.77297076	1.51713939	-0.86655400
H	-2.00658176	4.73668839	0.47013700
O	-1.44980176	3.94983039	0.57080200





Appendix V: Risk Assessment and Hazard Analysis

Name of activities	Singlet oxygen generation and reactions
Form completed by	Jomana Al-Nu'airat

<i>Do the activities involve:</i>			<i>If yes, complete:</i>
1.	Chemical substances	Yes	Section 1
2.	Process	Yes	Section 2
3.	Analytical equipment	Yes	Section 3



1. CHEMICAL RISK ASSESSMENT

Chemical name	Class	Score*	Potential injury/illness	Control measures or action required
Sodium Azide	6.1	3	<ol style="list-style-type: none"> 1. Fatal if swallowed. 2. Fatal in contact with skin. 3. Very toxic to aquatic life with long lasting effects. 4. It is a combustible substance and may explode if heated. It is incompatible with acids, heavy metals/salts, benzoyl chloride + potassium hydroxide, bromine, barium carbonate, carbon disulfide, chlorides, dimethyl sulfate and hot water. 	<ol style="list-style-type: none"> 1. Do not get in eyes, on skin, or on clothing- Use PPE 2. Wash skin thoroughly after handling. 3. Do not eat, drink or smoke when using this product. 4. Avoid release to the environment. Use weighing scoop. 5. Perform under the fume hood. 6. IF SWALLOWED: Immediately call a POISON CENTER or doctor/ physician. 7. IF ON SKIN: Gently wash with plenty of soap and water immediately call a POISON CENTER or doctor/ physician. 8. Remove/Take off immediately all contaminated clothing. 9. Wash contaminated clothing before reuse. 10. Collect spillage (spillage kit) 11. Store in cool, dry, well ventilated area, removed from acids, heavy metals,



				<p>bromine, chlorides, barium carbonate, other incompatibilities, direct sunlight, heat sources and foodstuff.</p> <p>12. Note that metal shelves and other metal items used to handle sodium azide (i.e., spatulas) can also result in the formation of heavy metal azides and thus should be avoided.</p> <p>13. Solid sodium azide should be stored in a locked-secured cabinet away from metals and water.</p>
Phenol	6.1	5	<ol style="list-style-type: none"> 1. Toxic if swallowed. 2. Toxic in contact with skin. 3. Causes severe skin burns and eye damage. 4. Toxic if inhaled. 5. Suspected of causing genetic defects. 6. May cause damage to organs through prolonged or repeated exposure. 7. Phenol is incompatible with strong oxidizing agents, calcium hypochlorite, halogens, halogenated compounds, aluminum chloride, and nitrobenzene. Hot phenol can attack aluminum, lead, magnesium and zinc. It can react exothermally with peroxymonosulfuric acid, sodium nitrate, 1,3-butadiene and boron trifluoride diethyl ether. 	<ol style="list-style-type: none"> 8. Do not breathe dust/ fume/ gas/ mist/ vapours/ spray. 9. Wash skin thoroughly after handling. 10. Do not eat, drink or smoke when using this product. 11. Use a well-ventilated area. 12. Use PPE. 13. Perform under the fume hood 14. IF SWALLOWED: Immediately call a POISON CENTER or doctor/ physician. Rinse mouth. Do NOT induce vomiting. 15. IF ON SKIN (or hair): Remove/ Take off immediately all contaminated clothing. Rinse skin with water/ shower. 16. IF INHALED: Remove victim to fresh air and keep at rest in a position comfortable for breathing. 17. IF IN EYES: Rinse cautiously with water



				<p>for several minutes. Remove contact lenses, if present and easy to do. Continue rinsing.</p> <p>18. Remove/Take off immediately all contaminated clothing.</p> <p>19. Wash contaminated clothing before reuse</p>
Aniline	6.1	5	<ol style="list-style-type: none"> 1. Toxic if swallowed, in contact with skin or if inhaled 2. May cause an allergic skin reaction. 3. Causes serious eye damage. 4. Suspected of causing genetic defects. 5. Suspected of causing cancer. 6. Causes damage to organs (Blood) through prolonged or repeated exposure. 7. Very toxic to aquatic life with long lasting effects. 8. Incompatible with oxidizing agents, bases, acids, iron and iron salts, zinc, aluminium. 	<ol style="list-style-type: none"> 9. Do not breathe dust/ fume/ gas/ mist/ vapours/ spray. 10. Wash skin thoroughly after handling. 11. Avoid release to the environment. 12. Wear PPE. 13. Perform under the fume hood 14. IF SWALLOWED: Immediately call a POISON CENTER or doctor/physician. Rinse mouth. 15. IF ON SKIN: Wash with plenty of water. Call a POISON CENTER or doctor/physician if you feel unwell. 16. IF INHALED: Remove person to fresh air and keep comfortable for breathing. Call a POISON CENTER or doctor/physician. 17. IF IN EYES: Rinse cautiously with water for several minutes. Remove contact lenses, if present and easy to do. Continue rinsing.
2-Propanol	3	5	<ol style="list-style-type: none"> 18. Causes serious eye irritation. 19. May cause drowsiness or dizziness. 20. Highly flammable liquid and vapors. 	<ol style="list-style-type: none"> 21. Keep away from heat/sparks/open flames/hot surfaces. - No smoking. 22. Keep container tightly closed. 23. Avoid breathing dust/ fume/ gas/ mist/ vapours/ spray. 24. Wear PPE.



				<p>25. Perform under the fume hood</p> <p>26. IF ON SKIN (or hair): Remove/ Take off immediately all contaminated clothing. Rinse skin with water/ shower.</p> <p>27. IF INHALED: Remove victim to fresh air and keep at rest in a position comfortable for breathing. Call a POISON CENTER or doctor/ physician if you feel unwell.</p> <p>28. If eye irritation persists: Get medical advice/ attention.</p> <p>29. In case of fire: Use dry sand, dry chemical or alcohol-resistant foam for extinction.</p>
Sodium formate	NA	6	30. Not a hazardous substance	<p>31. If inhaled, move person into fresh air. If not breathing, give artificial respiration.</p> <p>32. In case of skin contact: Wash off with soap and plenty of water.</p> <p>33. In case of eye contact: Flush eyes with water as a precaution.</p> <p>34. If swallowed: Never give anything by mouth to an unconscious person. Rinse mouth with water.</p>
DL-Dithiothreitol	9	5	<p>35. Harmful if swallowed.</p> <p>36. Causes skin irritation.</p> <p>37. Causes serious eye irritation.</p> <p>38. May cause respiratory irritation.</p>	<p>39. Avoid breathing dust/ fume/ gas/ mist/ vapours/ spray.</p> <p>40. Wash skin thoroughly after handling.</p> <p>41. Do not eat, drink or smoke when using this product.</p> <p>42. Use PPE.</p> <p>43. Perform under the fume hood</p> <p>44. IF INHALED: Remove victim to fresh air and keep at rest in a position comfortable for breathing. Call a POISON CENTER or doctor/ physician if you feel unwell.</p>



				45. If eye irritation persists: Get medical advice/ attention.
L-Glutathione reduced	NA	6	1. Not a hazardous substance	<p>2. If inhaled If breathed in, move person into fresh air. If not breathing, give artificial respiration.</p> <p>3. In case of skin contact: Wash off with soap and plenty of water.</p> <p>4. In case of eye contact: Flush eyes with water as a precaution.</p> <p>5. If swallowed: Never give anything by mouth to an unconscious person. Rinse mouth with water.</p>
Tert-Butanol	3	5	<p>6. Highly flammable liquid and vapour.</p> <p>7. Causes serious eye irritation.</p> <p>8. May cause respiratory irritation</p>	<p>9. Keep away from heat/sparks/open flames/hot surfaces. - No smoking.</p> <p>10. Keep container tightly closed.</p> <p>11. Avoid breathing dust/ fume/ gas/ mist/ vapours/ spray.</p> <p>12. Perform under the fume hood</p> <p>13. Wash skin thoroughly after handling.</p> <p>14. Wear PEE.</p> <p>15. IF ON SKIN (or hair): Remove/ Take off immediately all contaminated clothing. Rinse skin with water/ shower.</p> <p>16. IF INHALED: Remove victim to fresh air and keep at rest in a position comfortable for breathing.</p> <p>17. IF IN EYES: Rinse cautiously with water for several minutes. Remove contact lenses, if present and easy to do. Continue rinsing.</p>



				<p>18. Call a POISON CENTER or doctor/physician if you feel unwell.</p> <p>19. If eye irritation persists: Get medical advice/ attention.</p> <p>20. In case of fire: Use dry sand, dry chemical or alcohol-resistant foam for extinction.</p>
Methylene blue	NA	6	<p>1. Harmful if swallowed.</p> <p>2. Causes skin irritation.</p> <p>3. Causes serious eye irritation.</p> <p>4. May cause respiratory irritation.</p>	<p>5. Avoid breathing dust/ fume/ gas/ mist/ vapours/ spray.</p> <p>6. Wash skin thoroughly after handling.</p> <p>7. Do not eat, drink or smoke when using this product.</p> <p>8. Use PPE.</p> <p>9. Perform under the fume hood</p> <p>10. IF SWALLOWED: Call a POISON CENTER or doctor/ physician if you feel unwell.</p> <p>11. IF ON SKIN: Wash with plenty of soap and water.</p> <p>12. IF INHALED: Remove victim to fresh air and keep at rest in a position comfortable for breathing.</p> <p>13. IF IN EYES: Rinse cautiously with water for several minutes. Remove contact lenses, if present and easy to do. Continue rinsing.</p> <p>14. Call a POISON CENTER or doctor/ physician if you feel unwell.</p> <p>15. If skin irritation occurs: Get medical advice/ attention.</p> <p>16. If eye irritation persists: Get medical advice/ attention.</p>



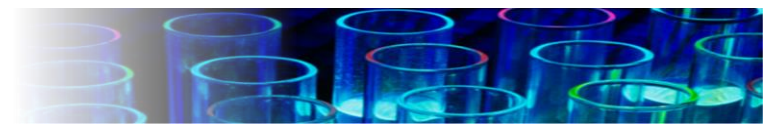
				17. Take off contaminated clothing and wash before reuse.
Compressed Air	NA	6	<ol style="list-style-type: none"> 1. Contains gas under pressure; may explode if heated. 2. May support combustion. 	<ol style="list-style-type: none"> 3. Check the compressor outlet pressure before opening the supply valve. 4. Check the pressure regulator.
Acetonitrile	3	5	<ol style="list-style-type: none"> 5. Highly flammable liquid and vapour. Harmful if swallowed. 6. Harmful in contact with skin. Causes serious eye irritation. 7. Harmful if inhaled. 	<ol style="list-style-type: none"> 8. Keep away from heat/sparks/open flames/hot surfaces. - No smoking. 9. Keep container tightly closed. 10. Avoid breathing dust/ fume/ gas/ mist/ vapours/ spray. Wear PEE. 11. Perform under the fume hood 12. IF ON SKIN (or hair): Remove/ Take off immediately all contaminated clothing. Rinse skin with water/ shower. IF INHALED: Remove victim to fresh air and keep at rest in a position comfortable for breathing. Call a POISON CENTER or doctor/ physician if you feel unwell. 13. If eye irritation persists: Get medical advice/ attention. In case of fire: Use dry sand, dry chemical or alcohol-resistant foam for extinction. 14. Store in a well-ventilated place. Keep cool. Dispose of contents in a waste container with a proper label.



Phosphate Buffer Solution	NA	6	1. Not a dangerous substance or mixture	2. If inhaled If breathed in, move person into fresh air. If not breathing, give artificial respiration. 3. In case of skin contact: Wash off with soap and plenty of water. 4. In case of eye contact: Flush eyes with water as a precaution. 5. If swallowed: Never give anything by mouth to an unconscious person. Rinse mouth with water.
Hydroquinone	9	5	1. Danger 2. Harmful if swallowed. 3. May cause an allergic skin reaction. 4. Causes serious eye damage. 5. Suspected of causing genetic defects. 6. Suspected of causing cancer. 7. Very toxic to aquatic life with long lasting effects	1. Avoid breathing dust/ fume/ gas/ mist/ vapours/ spray. 2. Avoid release to the environment. 3. Wear PPE. 4. Perform under the fume hood 5. IF IN EYES: Rinse cautiously with water for several minutes. Remove contact lenses, if present and easy to do. Continue rinsing. Immediately call a POISON CENTER or doctor/ physician. 6. IF exposed or concerned: Get medical advice/ attention. 7. If skin irritation or rash occurs: Get medical advice/ attention. 8. Wash contaminated clothing before reuse.
p-Benzoquinone	6.1	5	9. Toxic if swallowed. 10. Causes skin irritation. 11. Causes serious eye irritation. 12. Toxic if inhaled. 13. May cause respiratory irritation. 14. Very toxic to aquatic life.	15. Avoid breathing dust/ fume/ gas/ mist/ vapours/ spray. 16. Wash skin thoroughly after handling. 17. Do not eat, drink or smoke when using this product. 18. Use only in a well-ventilated area or under the fume hood.



				<p>19. Avoid release to the environment.</p> <p>20. Wear PPE.</p> <p>21. IF SWALLOWED: Immediately call a POISON CENTER or doctor/physician.</p> <p>22. IF ON SKIN: Wash with plenty of soap and water.</p> <p>23. IF INHALED: Remove victim to fresh air and keep at rest in a position comfortable for breathing.</p> <p>24. IF IN EYES: Rinse cautiously with water for several minutes. Remove contact lenses, if present and easy to do.</p> <p>25. If skin irritation occurs: Get medical advice/ attention.</p> <p>26. If eye irritation persists: Get medical advice/ attention.</p> <p>27. Take off contaminated clothing and wash before reuse.</p> <p>28. Collect spillage</p>
4-Aminophenol			<p>29. Harmful if swallowed.</p> <p>30. Harmful if inhaled.</p> <p>31. Suspected of causing genetic defects.</p> <p>32. Very toxic to aquatic life.</p>	<p>33. Avoid breathing dust/ fume/ gas/ mist/ vapours/ spray.</p> <p>34. Wash skin thoroughly after handling.</p> <p>35. Do not eat, drink or smoke when using this product.</p> <p>36. Avoid release to the environment.</p> <p>37. Wear PPE.</p> <p>38. Perform under the fume hood</p> <p>39. IF exposed or concerned: Get medical advice/ attention.</p> <p>40. Collect spillage.</p>



				41. Dispose of contents/ container to an approved waste disposal plant.
--	--	--	--	---

*Determine the risk score for each hazard from the Risk Ranking table.

Risk Ranking (score)

How severely could it hurt someone? or How ill could it make someone?	How likely is it to be that bad?			
	Very likely could happen anytime	Likely could happen sometime	Unlikely could happen but very rarely	Very unlikely could happen but probably never will
Kill or cause permanent disability or ill health	1	1	2	3
Long term illness or serious injury	1	2	3	4
Medical attention and several days off work	2	3	4	5
First aid needed	3	4	5	6

Actions:

- 1: Stop work until the risk is reduced
- 2: Reduce the risk urgently
- 3: Reduce the risk as a priority
- 4/5/6: Reduce the risk



42. HAZARD IDENTIFICATION OF WORKPLACE / PROCESS

Activities	Hazard	Score*	Possible injury/harm	Control measures or action required
Illumination of Methylene blue in a solution of aromatic (Phenol, Aniline), and buffer.	<ol style="list-style-type: none"> Toxicity of chemicals. Exposure of Singlet oxygen. Break of the glass reactor. 	4	<ol style="list-style-type: none"> Refer to chemicals section. Singlet oxygen can penetrate organic matters. Skin injury and contact with hazardous chemicals. 	<ol style="list-style-type: none"> Use PPE Perform activities under the fume hood. Keep away the flammable materials. Present in the lab during experiments. Carry out experiment with care and attention.
Use of LED lamp	<ol style="list-style-type: none"> Electricity 	6	<ol style="list-style-type: none"> Electric shock 	<ol style="list-style-type: none"> Wear safety glasses Make sure all the wires are perfectly insulated
Use of purge Air	<ol style="list-style-type: none"> Compressor pressure regulator failure. 	6	<ol style="list-style-type: none"> May cause severe injuries and damages in case of reactor breakage 	<ol style="list-style-type: none"> Perform leak and blockage check before experiments. Check the outlet compressor pressure and the pressure regulator before starting the experiments.
Reactor	<ol style="list-style-type: none"> Breakage due to mechanical stress Leakage from connections. May fall down as it will be held above the ground 	6	<ol style="list-style-type: none"> Possible release of singlet oxygen. Toxicity and corrosiveness of chemicals if broken. Physical injury. 	<ol style="list-style-type: none"> Make sure the reactor is properly held using retort stand Handle with care and put a caution note next to the reactor during the experiment Perform leak check before running any experiments Perform under the fume hood.



Reactor and glass ware cleaning	5. Glass wares	6	1. Breakage may happen during cleaning. May cause injuries.	2. Handle with care, clean, dry and return to storage shelves after use. 3. Wear suitable PPE
Analysis using GC-MS	4. Injection port, column or oven heat. 5. Sample injection syringe. 6. Toxicity of chemicals.	6	1. Heat from injection port, column or oven can burn. 2. Skin puncture by sample injection syringe. 3. Exposure to toxic gaseous compounds.	1. Use auto sampler for injection and avoid touching metal component if manual injection is necessary. Avoid opening at high operation temperature. 2. Use auto sampler where possible. Avoid placing fingers in the place of auto injection. Don't change sample when auto injector is working, and/or manually inject sample very carefully.

*Determine the risk score for each hazard from the **Risk Ranking** table.

Note: More detailed HAZOP analysis is found in HAZOP analysis document

3. RISK TO THE ANALYTICAL EQUIPMENT

Activities	Equipment	Potential risk to the equipment	Control measures or action required
GC-MS Triple Quad	Shimadzu GC/MS triple quad.	1. No carrier gas flow can cause damage of the equipment. 2. Leak can destroy the column and filament.	9. Always connect vacuum pump exhaust to proper vent.



		<p>3. Oven temperature set up in the method exceeds the maximum isothermal temperature of the column can destroy the column.</p> <p>4. The filament on during the elution of solvent can break the filament.</p> <p>5. Septa used more than 100 times injections can cause leak to the system and septa bleed in the result.</p> <p>6. Liner which is not cleaned after 200 times injections can cause contamination in the result.</p> <p>7. Too high concentration of sample can cause the column and ion source dirty which will affect the result.</p> <p>8. Certain types of samples can damage the column.</p>	<p>10. Check the carrier gas flow and amount in the cylinder at the start of the day before analyzing.</p> <p>11. Record the volume of the carrier gas in the cylinder once a week.</p> <p>12. Ensure there is no leak in the system by checking the vacuum pressure, as well as performing air and water check.</p> <p>13. Create the oven temperature profile with the maximum temperature lower than the maximum isothermal temperature of the column.</p> <p>14. Ensure that the filament is off during the solvent peak elution time.</p> <p>15. Record the number of injections and replace septa after 50 – 100 injections.</p> <p>16. Record the number of injections and clean the liner after 100 – 200 injections.</p> <p>17. Dilute the sample to about 100 ppm and use split ratio of 100 to 1 initially.</p> <p>18. Do not inject water, acetone, strong acids, strong bases and heavy metals, as well as samples that react with the stationary phase of the column</p>
19. HPLC	20. SHIMADZU PROMINENCE HPLC	<p>21. Aqueous mobile phases containing buffers may grow algae over time and block the system.</p> <p>22. Beware of injecting a sample made up in an organic solvent while running mobile phases containing buffers. This may cause precipitates,</p>	<p>24. Make mobile phase in a clean bottle and vacuum filter using 0.45 μm membrane.</p> <p>25. Ensure these buffers are stored in the fridge between uses or are made fresh on the day.</p>



		<p>blockages, chromatography issues and column damage.</p> <p>23. Failure to open the purge valve before pushing the purge button will cause damage to the pump.</p>	<p>26. Try mixing a small amount of sample and mobile phase in a beaker and check for precipitation or cloudiness before running on the HPLC. ALWAYS filter your sample through a 0.45 μm membrane before injecting into the HPLC system.</p> <p>27. Whenever possible make up your sample using mobile phase or a similar solution</p> <p>28. Turn the purge valve anti clockwise one quarter of a turn to open it and press the button labelled purge.</p> <p>29. When HPLC Turned off, connect the mobile phase you wish to store the instrument and column in, this is usually 50:50 MeOH: H₂O. If you have used a mobile phase containing salt buffers you will need to first purge the system with a salt free version of your mobile phase. Failure to do so will most likely lead to precipitation and blockages in the system</p>
--	--	--	---